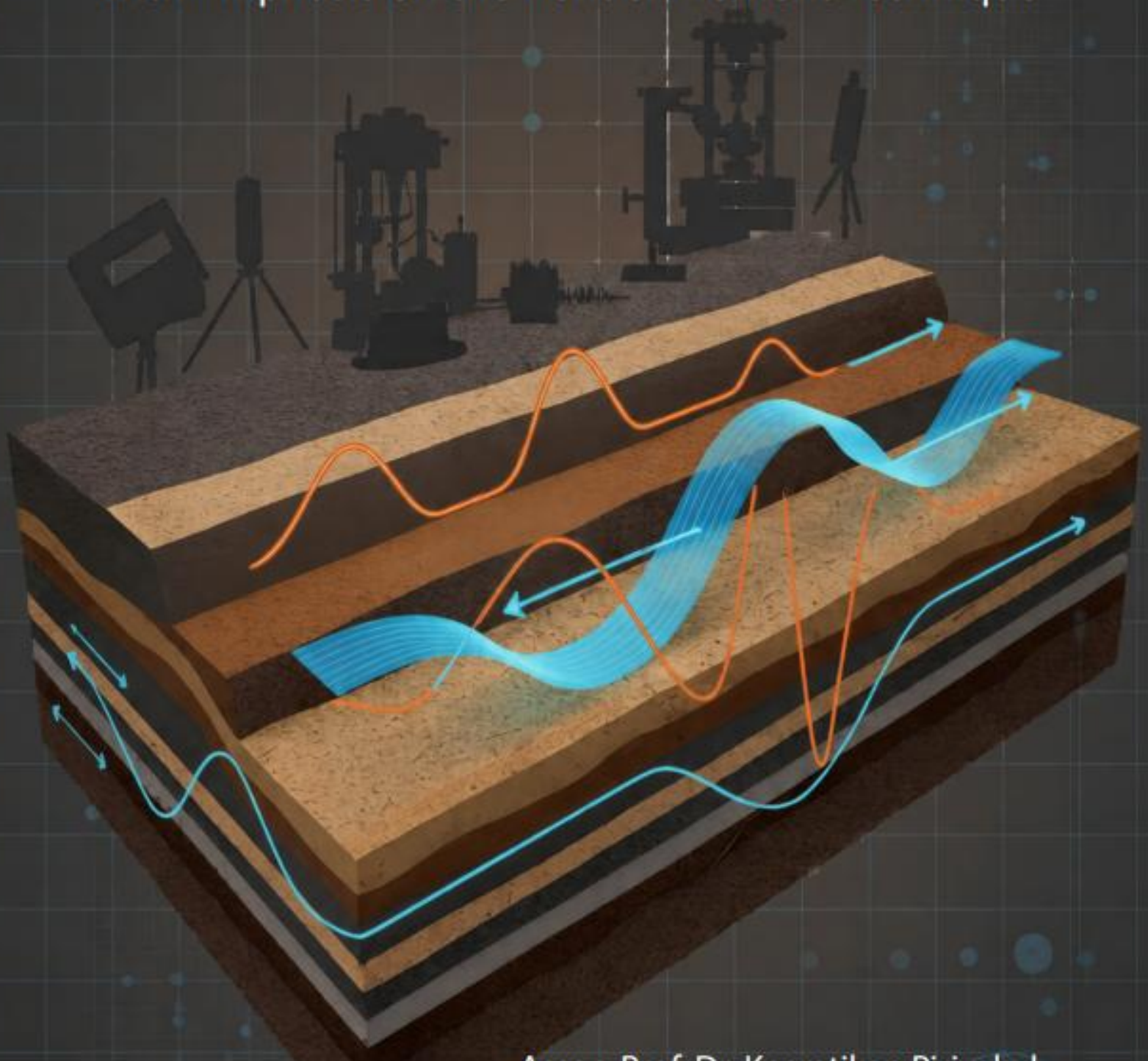
INTERNATIONAL EDITION

ENGINEERING APPLICATION OF SHEAR WAVES

in Advanced Soil Mechanics and Testing Method with Emphasis on the Bender Element Technique



Assoc. Prof. Dr. Keeratikan Piriyakul

INTERNATIONAL
EDITION

ENGINEERING APPLICATION OF SHEAR WAVES

in Advanced Soil Mechanics and Testing Method
with Emphasis on the Bender Element Technique

Assoc. Prof. Dr. Keeratikan Piriyakul

Engineering Application of Shear Waves in Advanced Soil Mechanics and Testing Method with Emphasis on the Bender Element Technique

All rights reserved.
No part of this publication may be reproduced, stored in a retrieval system, or transmitted in any form or by any means — electronic, mechanical, photocopying, recording, or otherwise without the prior written permission of the copyright owner.

ข้อมูลทางบรรณานุกรมของสำนักหอสมุดแห่งชาติ
National Library of Thailand Cataloging in Publication Data
Keeratikan Piriyakul.
Engineering Application of Shear Waves in Advanced Soil Mechanics and Testing Method with Emphasis on the Bender Element Technique.-- Bangkok : Textbook Publishing and Digital Publication Center King Mongkut's University of Technology North Bangkok, 2026.
208 p.

1. Soil mechanics. 2. Engineering. I. Title.

624.151
ISBN 978-616-637-177-2

Edited and Published by Assoc. Prof. Dr. Keeratikan Piriyakul

First Edition : August, 2026 100 Copies

Printed at Textbook Publishing and Digital Publication Center
King Mongkut's University of Technology North Bangkok
1518 Pracharat 1 Road, Wongsawang, Bangsue Bangkok 10800, Thailand
Tel: +66-2555-2000 Ext. 1436, 1437
E-mail: textbook_digital@op.kmutnb.ac.th

Price : 350 Baht

ตำรา/หนังสือเล่มนี้ได้ผ่านการประเมินโดยคณะผู้ทรงคุณวุฒิในสาขาวิชา
ได้รับการรับรองคุณภาพจากคณะกรรมการรับรองคุณภาพตำราหรือหนังสือ
มหาวิทยาลัยเทคโนโลยีพระจอมเกล้าพระนครเหนือ

Preface

Engineering Application of Shear Waves in Advanced Soil Mechanics and Testing Method with Emphasis on the Bender Element Technique is a comprehensive reference that explores the fundamental and applied aspects of shear wave propagation in geomaterials. This book is written for graduate students, as well as researchers and professionals in geology, geophysics, civil engineering, and related disciplines. This volume provides an up-to-date synthesis of recent developments in shear wave propagation. It serves as an indispensable resource for those seeking to deepen their understanding of this critical area of geotechnical and geophysical engineering.

The book begins with a clear exposition of the fundamental principles of shear wave propagation, addressing the classification of shear waves and their underlying physical properties. It then advances to methods of characterization and measurement, including laboratory testing, field investigations, and mathematical modeling. Each technique is presented in detail, with practical guidance on selecting the most suitable approach for specific applications.

A distinctive feature of this work is its emphasis on the applied dimensions of shear wave propagation in geomaterials for ground improvement. Particular attention is devoted to the role of shear waves in the non-destructive evaluation of soils and treated soils. Applications across multiple domains—geotechnical engineering, environmental geology, civil engineering, and geophysics—are comprehensively reviewed. The discussion includes the Bender Element Testing (BET) method, a widely adopted approach for determining shear wave velocity and initial shear modulus.

In addition to its practical orientation, the book examines state-of-the-art research advances in shear wave propagation. Topics include innovations in instrumentation and measurement, as well as emerging techniques for signal interpretation and analysis. By integrating both experimental and theoretical perspectives, the authors highlight the evolving methodologies that continue to expand the frontiers of this field.

The closing chapters address future research directions, exploring the potential of shear wave applications in developing novel geotechnical engineering practices and advancing the fundamental understanding of wave–material interactions in geomaterials.

Overall, this book offers a rigorous and accessible treatment of the subject. Its combination of theoretical depth, practical application, and coverage of cutting-edge research makes it an essential resource for graduate students, researchers, and practitioners engaged in the study of shear wave behavior in soils and geomaterials.

I am grateful to following reviewers who offered many valuable suggestions for improving this book:

- Prof. Wim Haegeman, Ghent University and VIVES University College, Belgium.
- Prof. Dennes T. Bergado, Professor Emeritus of Civil (Geotechnical) Engineering, Asian Institute of Technology, Thailand.

Keeratikan Piriyakul

Table of Contents (Continued)

		Page
Chapter 5: Applications of Shear Wave Testing in Geopolymeric Materials		**5-1**
5.1	Introduction of Geopolymeric Materials	5-1
5.2	Geopolymeric Materials and Methods	5-3
5.3	Results and Discussions	5-6
Summary		5-15
Questions and Problems		5-16
Chapter 6: Applications of Shear Wave Testing in Biocemented Sand		**6-1**
6.1	Introduction of Biocement	6-1
6.2	Principle of MICP Process	6-3
6.3	Biocemented Materials and Methods	6-5
6.4	Results and Discussions	6-12
Summary		6-25
Questions and Problems		6-26
Chapter 7: Applications of Shear Wave Testing in Bangkok Clay mixed with Cement and Industrial Waste		**7-1**
7.1	Introduction of Bangkok Clay mixed with Cement and Industrial Waste	7-1
7.2	Materials	7-3
7.3	Methods	7-4
7.4	Results and Discussions	7-6
Summary		7-17
Questions and Problems		7-18
Chapter 8: Applications of Shear Wave Testing in Bangkok Clay mixed with Cement and Fibers		**8-1**
8.1	Introduction of Bangkok Clay mixed with Cement and Fibers	8-1
8.2	Fiber Materials and Methods	8-3
8.3	Results and Discussions	8-9
Summary		8-23
Questions and Problems		8-24
Reference		**R-1**
Index		**I-1**

List of Figures

		Page
Figure 1-1	P-wave illustration.	1-2
Figure 1-2	S-wave illustration.	1-2
Figure 1-3	Rayleigh wave illustration.	1-3
Figure 1-4	Love wave illustration.	1-3
Figure 1-5	Variation of stiffness with strain measured with different laboratory tests after Piriyakul (2009).	1-5
Figure 1-6	Spectral Analysis of Surface Wave (SASW) test configuration.	1-6
Figure 1-7	Seismic Cone Penetration Test (SCPT) configuration after ConeTec. (2025).	1-7
Figure 1-8	a) Bender Element Test (BET) configuration and b) Schematic diagram after Piriyakul (2010).	1-8
Figure 2-1	Motion of shear wave (S-wave).	2-1
Figure 2-2	Motion of compressional wave (P-wave).	2-1
Figure 2-3	Differential stress elements for simple longitudinal stress.	2-4
Figure 2-4	Differential stress elements for simple shear stress.	2-5
Figure 2-5	Stress along the x-axis acting upon a 3D differential element.	2-7
Figure 2-6	A cross-anisotropy model.	2-9
Figure 2-7	Damping ratio in function of shear strain.	2-11
Figure 3-1	Overview of possible shear strain amplitudes after Studer et al. (2008).	3-2
Figure 3-2	a) Series and b) Parallel connected bender elements after Iamchaturapatr et al. (2022).	3-2
Figure 3-3	Piezoelectric sensors: a) Series and b) Parallel types.	3-3
Figure 3-4	Schematic of bender element test after Iamchaturapatr et al. (2022).	3-3
Figure 3-5	Installation of bender element sensors on a soil sample.	3-4
Figure 3-6	Bender element test setup at the KMUTNB campus.	3-4
Figure 3-7	Cyclic triaxial test at the KMUTNB campus.	3-5
Figure 3-8	Parts of cyclic triaxial apparatus after Controls Group (2025).	3-6
Figure 3-9	Schematic of cyclic simple shear apparatus after VJ Tech (2025).	3-7
Figure 3-10	a) Consolidation phase and b) Shearing phase.	3-7
Figure 3-11	Schematic of resonant column test.	3-8
Figure 3-12	Schematic of the free torsion pendulum test after Karl (2005).	3-10
Figure 3-13	Displacement record of free torsion pendulum test.	3-11
Figure 3-14	Stress path triaxial test at the KMUTNB campus.	3-13
Figure 3-15	K_0 consolidation and shearing in stress path triaxial test after Controls Group (2025).	3-14
Figure 3-16	a) K_0- and b) K-consolidation flow charts after Piriyakul & Haegeman (2005).	3-14
Figure 3-17	Part of the stress path triaxial test after Controls Group (2025).	3-15
Figure 3-18	Hall effect on sample transducers after Controls Group (2025).	3-16
Figure 3-19	a) Seismic cross-hole test, b) seismic up-hole test, c) seismic downhole test after Mok et al. (1988).	3-17
Figure 3-20	Ray paths for the seismic refraction test after Kramer (1996).	3-18
Figure 3-21	Time arrival diagram as result of a seismic refraction test after Kramer (1996).	3-19
Figure 3-22	Ray paths for the seismic reflection test after Kramer (1996).	3-20
Figure 3-23	Typical configuration of source and receivers in a SASW test after Kramer (1996).	3-21
Figure 3-24	SCPT test.	3-22

List of Figures (Continued)

		Page
Figure 4-1	Set-up of bender elements after Petcherdchoo et al. (2023).	4-1
Figure 4-2	Schematic of piezoelectric bender element and associated electronics after Piriyakul (2010).	4-3
Figure 4-3	Near field effect on the shear wave arrival in a clay specimen with different frequencies after Piriyakul (2010).	4-4
Figure 4-4	Calibration of bender element testing.	4-5
Figure 4-5	Calibration of bender element with a single period sinusoidal waveform	4-7
Figure 4-6	Calibration of bender element with a 5-period sinusoidal waveform.	4-7
Figure 4-7	Calibration of bender element with a period triangle waveform.	4-8
Figure 4-8	Calibration of bender element with a 5-period triangle waveform.	4-8
Figure 4-9	Calibration of bender element with a single period rectangle waveform.	4-9
Figure 4-10	Calibration of bender element with a 5-period rectangle waveform.	4-9
Figure 4-11	Measurement of shear velocity with a single period sinusoidal waveform.	4-11
Figure 4-12	Measurement of shear velocity with a 5-period sinusoidal waveform.	4-11
Figure 4-13	Measurement of shear velocity with a single period triangle waveform.	4-12
Figure 4-14	Measurement of shear velocity with a 5-period triangle waveform.	4-12
Figure 4-15	Measurement of shear velocity with a single period rectangle waveform.	4-13
Figure 4-16	Measurement of shear velocity with a 5-period rectangle waveform.	4-13
Figure 4-17	Example of measurement of a continue sinusoidal waveform of the soil-cement sample.	4-14
Figure 4-18	Calibration of bender element with a single period sinusoidal waveform ASTM D8295–19.	4-15
Figure 4-19	Measurement of shear velocity with a single period sinusoidal waveform according to ASTM D8295–19.	4-15
Figure 4-20	Generalized Bangkok soil and shear wave velocity profiles after Warnitchai et al. (2000).	4-17
Figure 4-21	Measurement of shear wave velocity of Bangkok clay at 4.0 m depth (Frequency=12,000 Hz) after Piriyakul (2013a).	4-18
Figure 4-22	Measurement of shear wave velocity of Bangkok clay at 5.0 m depth (Frequency=12,000 Hz) after Piriyakul (2013a).	4-19
Figure 4-23	Measurement of shear wave velocity of Bangkok clay at 13.0 m depth (Frequency=12,000 Hz) after Piriyakul (2013a).	4-20
Figure 4-24	Results of shear wave velocity both laboratory and in-situ tests with depth of Bangkok clay formation after Piriyakul (2013a).	4-20
Figure 4-25	The relationship between $\frac{1}{V_s}$ and $\frac{1}{t}$ after Piriyakul (2013b).	4-23
Figure 4-26	The relationship between $\frac{1}{G_0}$ and $\frac{1}{t}$ after Piriyakul (2013b).	4-23
Figure 4-27	The relationship between $\frac{1}{S_u}$ and $\frac{1}{t}$ after Piriyakul (2013b).	4-24
Figure 4-28	The relationship between V_s and S_u after Piriyakul (2013b).	4-24
Figure 4-29	The relationship between G_0 and S_u after Piriyakul (2013b).	4-25
Figure 4-30	Measurement of calibration time for 1 sinusoidal signal.	4-27
Figure 4-31	Measurement of shear velocity of 1 sinusoidal signal.	4-27

List of Figures (Continued)

		Page
Figure 4-32	Measurement of calibration time for 5 sinusoidal signal.	4-28
Figure 4-33	Measurement of shear velocity of 5 sinusoidal signal.	4-28
Figure 4-34	Measurement of calibration time for 1 triangle signal.	4-29
Figure 4-35	Measurement of shear velocity of 1 triangle signal.	4-29
Figure 4-36	Measurement of calibration time for 5 triangle signal.	4-30
Figure 4-37	Measurement of shear velocity of 5 triangle signal.	4-30
Figure 4-38	Measurement of calibration time for 1 square signal.	4-31
Figure 4-39	Measurement of shear velocity of 1 square signal.	4-31
Figure 4-40	Measurement of calibration time for 5 square signal.	4-32
Figure 4-41	Measurement of shear velocity of 5 square signal.	4-32
Figure 4-42	A continuously sinusoidal waveform.	4-33
Figure 4-43	The offset time (t_c).	4-36
Figure 4-44	The total recorded time (t_t).	4-36
Figure 5-1	Thermal treatment of kaolin at the calcined temperatures: (a) 200°C; (b) 800°C; (c) 1000°C; (d) 1200°C after Iamchaturapatr et al. (2022b).	5-3
Figure 5-2	The Vicat needle apparatus after Iamchaturapatr et al. (2022b).	5-4
Figure 5-3	The shear wave velocity varied with elapsed time for thermal treatment after Iamchaturapatr et al. (2022b).	5-6
Figure 5-4	The penetration varied with elapsed time for the thermal treatment after Iamchaturapatr et al. (2022b).	5-7
Figure 5-5	The shear wave velocity varied with elapsed time for the mixing of geopolymer solution after Iamchaturapatr et al. (2022b).	5-8
Figure 5-6	The penetration varied with elapsed time for the mixing of geopolymer solution after Iamchaturapatr et al. (2022b).	5-9
Figure 5-7	The shear wave velocity varied with elapsed time for the mixing proportion between the metakaolin treated at 800°C and the geopolymer solution after Iamchaturapatr et al. (2022b).	5-10
Figure 5-8	The shear wave velocity varied with elapsed time for the mixing proportion between the metakaolin treated at 1000°C and the geopolymer solution after Iamchaturapatr et al. (2022b).	5-10
Figure 5-9	The penetration varied with elapsed time for the mixing proportion between the metakaolin treated at 800°C and the geopolymer solution after Iamchaturapatr et al. (2022b).	5-11
Figure 5-10	The penetration varied with elapsed time for the mixing proportion between the metakaolin treated at 1000°C and the geopolymer solution after Iamchaturapatr et al. (2022b).	5-11
Figure 5-11	Relationship between the shear wave velocity and the penetration after Iamchaturapatr et al. (2022b).	5-12
Figure 5-12	CBR test results for different mixing methods and conditions: (a) unsoaked (b) soaked (c) swelling after Iamchaturapatr et al. (2022b).	5-13
Figure 6-1	Biocementation process via MICP after Petcherdchoo et al. (2025).	6-5
Figure 6-2	Particle size distribution of sandy soils after Petcherdchoo et al. (2025).	6-6
Figure 6-3	Biocement Sand Reactor (BSR) after Petcherdchoo et al. (2025).	6-7
Figure 6-4	Setting-up of bender element testing for BSR after Petcherdchoo et al. (2025).	6-8
Figure 6-5	Relationship between pH and G_0 varied with Time after Petcherdchoo et al. (2025).	6-9

List of Figures (Continued)

Page

Figure 6-6 MICP treatment with the surface percolation methods for sandy soil samples (a) pour all the biocement solution at one time with the rate of 157.5 mL/h (b) continue drop the biocement solution with the rate of 3.3 mL/h, and (c) periodically drop the biocement solution of 79 mL/day with the rate of 13.5 mL/h for 4 days after Petcherdchoo et al. (2025). 6-11
Figure 6-7 MICP treatment with the injection method for a sandy soil by periodically injection after Petcherdchoo et al. (2025). 6-11
Figure 6-8 Contour of shear wave velocity for sample no.1 at cross section X-X′ after Petcherdchoo et al. (2025). 6-13
Figure 6-9 Contour of shear wave velocity for sample no.1 at cross section Y-Y′ after Petcherdchoo et al. (2025). 6-14
Figure 6-10 Contour of shear wave velocity for sample no.2 at cross section X-X′ after Petcherdchoo et al. (2025). 6-15
Figure 6-11 Contour of shear wave velocity for sample no.2 at cross section Y-Y′ after Petcherdchoo et al. (2025). 6-16
Figure 6-12 Contour of shear wave velocity for sample no.3 at cross section X-X′ after Petcherdchoo et al. (2025). 6-17
Figure 6-13 Contour of shear wave velocity for sample no.3 at cross section Y-Y′ after Petcherdchoo et al. (2025). 6-18
Figure 6-14 Contour of shear wave velocity for sample no.4 at cross section X-X′ after Petcherdchoo et al. (2025). 6-19
Figure 6-15 Contour of shear wave velocity for sample no.4 at cross section Y-Y′ after Petcherdchoo et al. (2025). 6-20
Figure 6-16 Initial shear modulus (G_0) of untreated and treated sandy soils with surface percolation and injection techniques after Petcherdchoo et al. (2025). 6-21
Figure 6-17 SEM image of the biocemented sandy soil at 250x after Petcherdchoo et al. (2025). 6-22
Figure 6-18 SEM image of the biocemented sandy soil at 1000x after Petcherdchoo et al. (2025). 6-23
Figure 6-19 X-ray Diffractometer (XRD) result after Petcherdchoo et al. (2025). 6-24
Figure 7-1 Flow chart for sample preparation and tests after Petcherdchoo et al. (2023). 7-5
Figure 7-2 Development of V_s with curing time of FA stabilized Bangkok soft clay after Petcherdchoo et al. (2023). 7-6
Figure 7-3 Development of G_0 with curing time of FA stabilized Bangkok soft clay after Petcherdchoo et al. (2023). 7-7
Figure 7-4 Development of q_u with curing time of FA stabilized Bangkok soft clay after Petcherdchoo et al. (2023). 7-7
Figure 7-5 Variation of V_s and FA contents of stabilized Bangkok soft clay after Petcherdchoo et al. (2023). 7-8
Figure 7-6 Variation of G_0 and FA contents of stabilized Bangkok soft clay after Petcherdchoo et al. (2023). 7-8
Figure 7-7 Variation of q_u and FA contents of stabilized Bangkok soft clay after Petcherdchoo et al. (2023). 7-9
Figure 7-8 Relationships between q_u/q_{28} and curing time after Petcherdchoo et al. (2023). 7-11

List of Figures (Continued)

Page

Figure 7-9 Relationships between $G_0/G_{0(28)}$ and q_u/q_{28} after Petcherdchoo et al. (2023). 7-13
Figure 7-10 Relationships between G_0 and q_u after Petcherdchoo et al. (2023). 7-14
Figure 7-11 SEM image of 20% FA sample at 28 days after Petcherdchoo et al. (2023). 7-16
Figure 8-1 SEM image of OPC after Piriyakul et al. (2026). 8-4
Figure 8-2 EDx result of OPC after Piriyakul et al. (2026). 8-5
Figure 8-3 Polyester fiber after Piriyakul et al. (2026). 8-6
Figure 8-4 Michaelis-Menten Kinetics (a) curve (b) invert of curve after Piriyakul et al. (2026). 8-9
Figure 8-5 UCS *vs* Curing time (a) 0% polyester fiber (b) 1% polyester fiber and (c) 20% polyester fiber after Piriyakul et al. (2026). 8-10
Figure 8-6 UCS *vs* Curing time (a) 10% cement and (b) 20% cement after Piriyakul et al. (2026). 8-11
Figure 8-7 Normalized UCS *vs* Curing time (a) 10% cement and (b) 20% cement after Piriyakul et al. (2026). 8-12
Figure 8-8 G_0 *vs* Curing time (a) 2% cement (b) 10% cement and (c) 20% cement after Piriyakul et al. (2026). 8-13
Figure 8-9 G_0 *vs* Curing time (a) 0% fiber (b) 1% fiber and (c) 20% fiber. 8-14
Figure 8-10 G_0 *vs* Fiber content (a) 1-20% cement (b) 1-2% cement and (c) 5-20% cement after Piriyakul et al. (2026). 8-16
Figure 8-11 G_f *vs* Fiber content (a) 1-20% cement and (b) 5-20% cement after Piriyakul et al. (2026). 8-18
Figure 8-12 G_f *vs* OPC content after Piriyakul et al. (2026). 8-19
Figure 8-13 G_0 *vs* W/C after Piriyakul et al. (2026). 8-20
Figure 8-14 G_0 *vs* UCS (a) 5% cement (b) 10% cement and (c) 20% cement after Piriyakul et al. (2026). 8-22

List of Tables

		Page
Table 1-1	Typical Values of V_s for Various Materials.	1-4
Table 4-1	Pattern of different wave forms.	4-6
Table 4-2	presents the measurement of the V_s and the G_0 out of different waveforms.	4-10
Table 4-3	Shear moduli of a clay specimen.	4-14
Table 4-4	Engineering properties of Bangkok clay.	4-16
Table 4-5	Shear wave velocity and shear modulus results of Bangkok clay with depth.	4-21
Table 4-6	Percent error of shear wave velocity.	4-21
Table 4-7	Test results of Bangkok clay.	4-25
Table 4-8	Number of wavelengths and frequencies in phase of a clay specimen.	4-33
Table 4-9	Number of wavelengths, f, V_s, and G_0 of a clay specimen.	4-34
Table 5-1	Chemical composition of kaolin.	5-5
Table 5-2	Basic engineering properties of kaolin.	5-5
Table 7-1	Chemical compositions of Bangkok clay, ordinary Portland cement and Fly ash (class F).	7-3
Table 7-2	Properties of Bangkok soft clay in this study.	7-3
Table 7-3	Mixing proportions of Bangkok clay samples.	7-4
Table 8-1	Chemical compositions of Bangkok clay and Ordinary Portland Cement (OPC).	8-4
Table 8-2	Properties of Bangkok soft clay.	8-5
Table 8-3	Parameters of specimens with polyester fibers.	8-7
Table 8-4	Calibrated fitting functions of G_0-W/C relationships of cemented Bangkok clay.	8-20

List of Abbreviations

A

AAS	Alkali-Activated Slag
ANFIS	Adaptive Neuro-Fuzzy Inference System
ASTM	American Society for Testing and Materials

B

B	Binder concentration
BA	Biomass Ash
BET	Bender Element Testing
BSR	Biocemented Sand Reactor

C

C	Cement
CBR	California Bearing Ratio
CCR	Calcium Carbide Residue
CF	Coconut Fiber
CSH	Calcium Silicate Hydrate

D

DMC	Deep Mixing Columns

E

E	Young's Modulus
EDS	Energy Dispersive Spectroscopy
EDx	Energy Dispersive X-ray
EICP	Enzyme-Induced Carbonate Precipitation

F

FA	Fly Ash
FEM	Finite Element Method
FTIR	Fourier Transform Infrared Spectroscopy

G

G	Shear Modulus
G_0	Initial Shear Modulus
GR	Garnet Residues

K

KMUTNB	King Mongkut's University of Technology North Bangkok

L

LI	Liquidity Index
LL	Liquid Limit

M

MCS	Microbial Cemented Sand
MICP	Microbially Induced Calcite Precipitation

N

NDT	Non-Destructive Testing
NEHRP	National Earthquake Hazards Reduction Program
NS	Nano-Silica

O

OMC	Optimum Moisture Content
OPC	Ordinary Portland Cement

P

PET	Polyethylene Terephthalate
PL	Plastic Limit
P-wave	Primary Wave

S

SASW	Spectral Analysis of Surface Wave
SC	Soft Clay
SCPT	Seismic Cone Penetration Test
SEM	Scanning Electron Microscope
SF	Sisal Fiber
SSM	Shallow Soil Mixing
S-wave	Shear Wave or Secondary Wave

T

TDA	Tire-Derived Aggregates
TGA	Thermo Gravimetric Analysis

U

UCS	Unconfined Compressive Strength

V

V	Wave Velocity
V_p	Primary Wave Velocity
V_s	Shear Wave Velocity

X

XCT	X-ray Computed Tomography
XRD	X-Ray Diffractometer

Z

ZS	Zinc Sludge

Chapter 1: Introduction to Shear Wave Propagation in Geomaterials

1.1 Overview of Elastic Waves

The study of elastic wave propagation in geomaterials constitutes a foundational area in geotechnical engineering and earthquake seismology, as it provides essential insights into the mechanical behavior of earth materials under dynamic loading conditions. Elastic waves are generally categorized into two principal groups: body waves, which penetrate through the interior of a medium, and surface waves, which are constrained to the outer boundary of a medium and decay in amplitude with depth as described in Piriyakul (2009).

Body waves are further divided into primary waves (P-waves) and secondary waves (S-waves). P-waves are longitudinal in nature, and the particle motion occurs in the same direction as the wave propagation. This characteristic, illustrated in Figure 1-1, explains why P-waves are the fastest seismic waves, traveling at higher velocities than other wave types. Because of their longitudinal motion, P-waves are capable of propagating through solids, liquids, and gases. They are, therefore, the first waves detected during seismic events, making them of great importance in seismology for the rapid identification of earthquake occurrence as described in Heisey et al. (1982).

S-waves, by contrast, are transverse waves in which particle motion occurs perpendicular to the direction of wave propagation, as illustrated in Figure 1-2. These waves travel more slowly than P-waves and, crucially, can only propagate through solids, since fluids do not support shear stresses. The distinction between the propagation properties of P-waves and S-waves has made them valuable diagnostic tools for identifying subsurface conditions, particularly the stiffness and density of geomaterials as described in Nazarian et al. (1983).

Surface waves, unlike body waves, are confined near the Earth's free surface and decrease in amplitude with depth. Two main types of surface waves are commonly recognized. Rayleigh waves, shown in Figure 1-3, induce elliptical particle motion in a retrograde fashion within a vertical plane. Their combined vertical and horizontal motion often results in severe shaking of structures at the surface. Love waves, illustrated in Figure 1-4, involve horizontally polarized shear motion perpendicular to the propagation direction and require a layered medium for their existence. Although surface waves typically travel more slowly than body waves, they possess greater amplitudes and longer durations. This makes them responsible for most of the observed damage during earthquakes, particularly because of their prolonged ground-shaking effects as described in Nazarian & Stokoe (1985).

While all types of seismic waves contribute to understanding the behavior of geomaterials, this book focuses specifically on shear wave propagation because of its fundamental relevance to soil and rock characterization in geotechnical engineering.

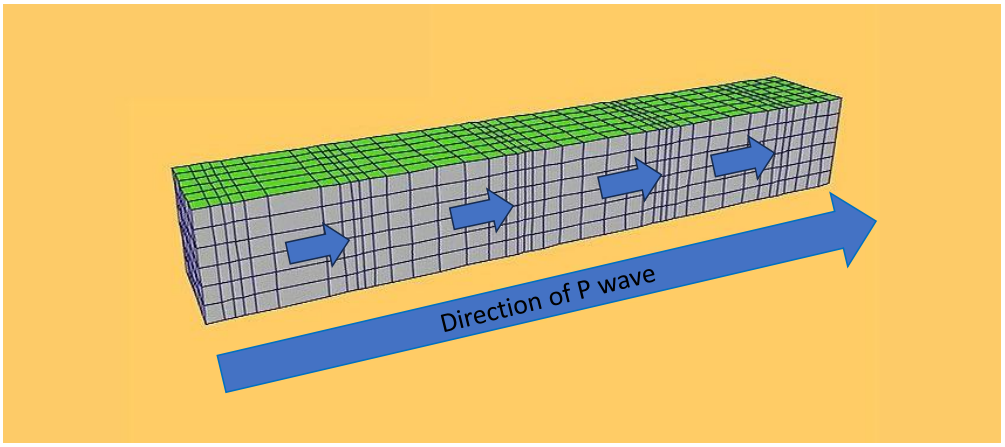


Figure 1-1 P-wave illustration.

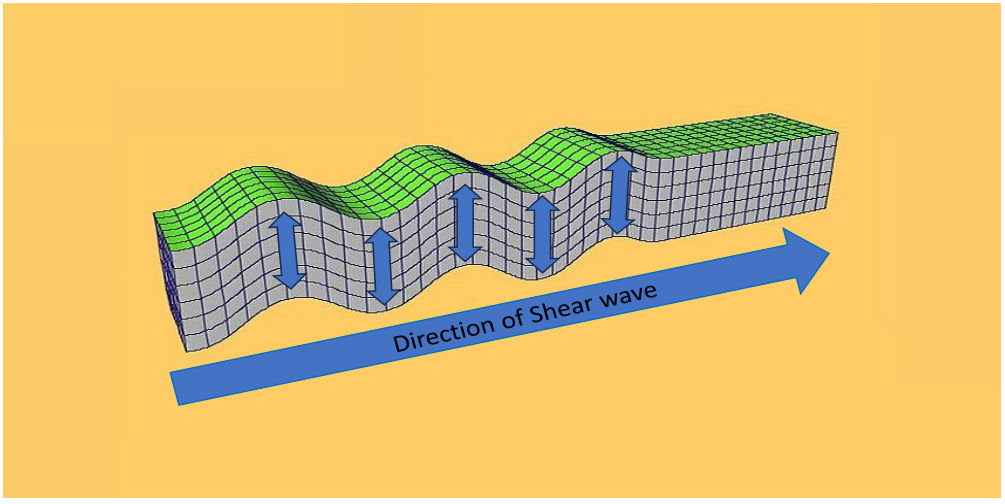


Figure 1-2 S-wave illustration.

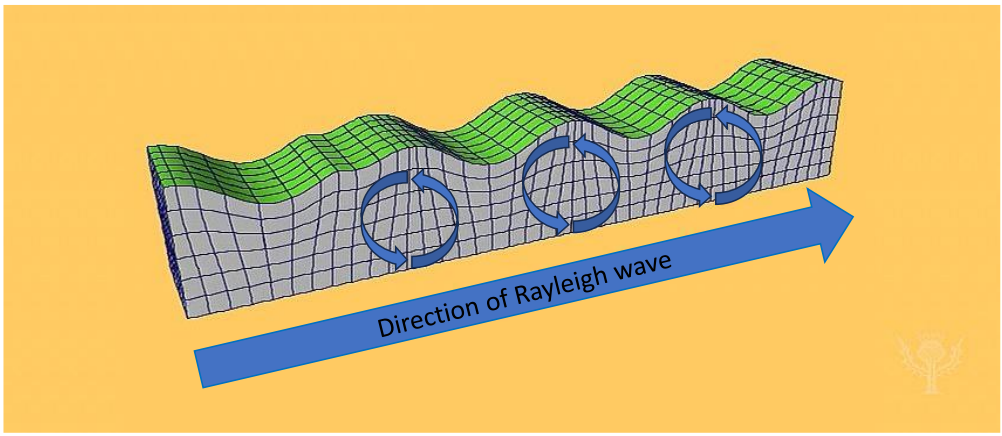


Figure 1-3 Rayleigh wave illustration.

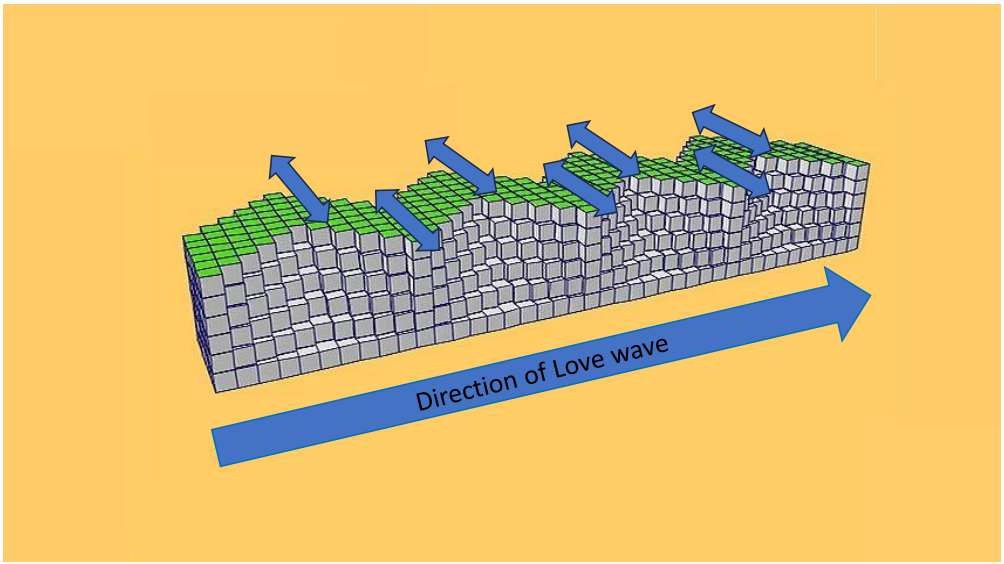


Figure 1-4 Love wave illustration.

1.2 Introduction to Shear Wave Propagation

Shear waves (commonly referred to as S-waves or secondary waves) are of critical significance in both seismology and geotechnical engineering. They are generated during seismic events and propagate exclusively through solid materials, transmitting vital information about subsurface conditions as described in Tokimatsu et al. (1992). As they pass through geomaterials, shear waves cause particles to move perpendicular to the direction of wave travel, producing shear stresses within the material. These stresses result in shearing deformations that provide information about the stiffness, density, and overall dynamic behavior of the subsurface.

The velocity of shear waves (V_s) is directly associated with the initial shear modulus (G_0) and the density of the medium. Therefore, by measuring V_s, engineers can determine the stiffness of soils and rocks in situ without disturbing their natural state. This makes V_s an important parameter for site characterization, seismic response analysis, and the evaluation of liquefaction potential as described in Gucunski & Woods (1992). Typical ranges of V_s for various geomaterials are presented in Table 1-1. For example, very soft soils generally have V_s values between 85–105 m/s, soft soils range between 106–135 m/s, and stiff soils exhibit values between 186–275 m/s. In contrast, rocks typically range between 761–1500 m/s, and hard rocks exceed 1500 m/s. Engineered materials such as concrete exhibit even higher velocities, with typical values in the range of 2286–2438 m/s as described in Ganji et al. (1998).

The variation of stiffness with respect to strain is an important concept in soil dynamics. As illustrated in Figure 1-5, conventional triaxial testing measures stiffness at strain levels near 1%, while advanced triaxial methods such as resonant column testing extend this range down to approximately 10^{-2}%. However, the most reliable insight into the very small strain domain—less than 10^{-3}%—is provided by geophysical methods and bender element testing.

This domain is particularly important because it corresponds to the initial shear modulus, G_0, which governs the initial response of soils during seismic loading as described in Piriyakul (2009) and Karray (1999). Understanding and quantifying G_0 through V_s measurements are indispensable for seismic design and modeling ground response as described in Lefebvre & Karray (1998).

Table 1-1 Typical Values of V_s for Various Materials.

Materials	Shear wave velocity, V_s (m/s)
Very soft clay/ Very soft soil	85-105
Soft clay/ Soft soil	106-135
Medium clay/ Medium soil	136-185
Stiff clay/ Stiff soil	186-275
Very stiff clay/ Very stiff soil	276-365
Soft rock	366-760
Typical rock	761-1500
Hard rock	>1500
Concrete/ Cementitious material	2286-2438

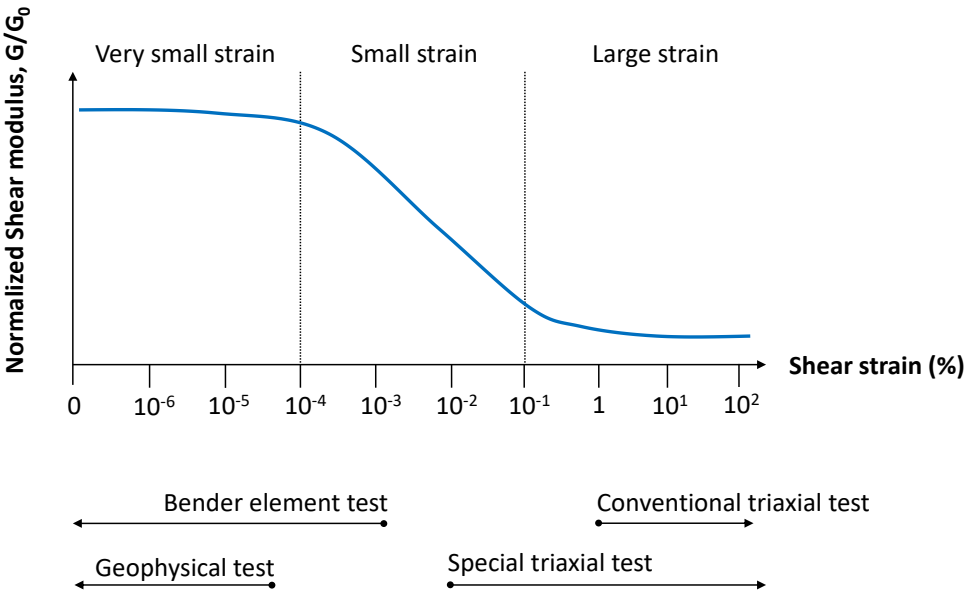


Figure 1-5 Variation of stiffness with strain measured with different laboratory tests after Piriyakul (2009).

1.3 Historical Development of Shear Wave Testing

1.3.1 Spectral Analysis of Surface Waves (SASW)

The Spectral Analysis of Surface Waves (SASW) method was pioneered in the early 1980s and has since become one of the most widely adopted techniques for in situ shear wave velocity measurement as explained in Heisey et al. (1982), Nazarian et al. (1983) and Nazarian & Stokoe (1985). The method involves generating waves at the ground surface using an impact source and recording their propagation with two receivers. The resulting signals are analyzed in the frequency domain to construct dispersion curves, which are then inverted to obtain shear wave velocity profiles. A schematic of this testing arrangement is provided in Figure 1-6.

Initially, it was assumed that only the fundamental Rayleigh mode contributed significantly to the dispersion curve. However, later investigations revealed that higher Rayleigh modes could also influence dispersion characteristics, leading to inaccuracies if not properly accounted for Tokimatsu et al. (1992), Gucunski & Woods (1992) and Ganji et al. (1998). To overcome these limitations, refinements in SASW methodology were introduced, including procedures to isolate or eliminate higher mode contributions during data processing. Such advances have improved the accuracy and reliability of SASW testing, making it a valuable tool in geotechnical site investigations as described in Karray (1999), Lefebvre & Karray (1998), Karray & Lefebvre (2000), Karray et al. (2010), Park et al. (1999) and Foti (2000).

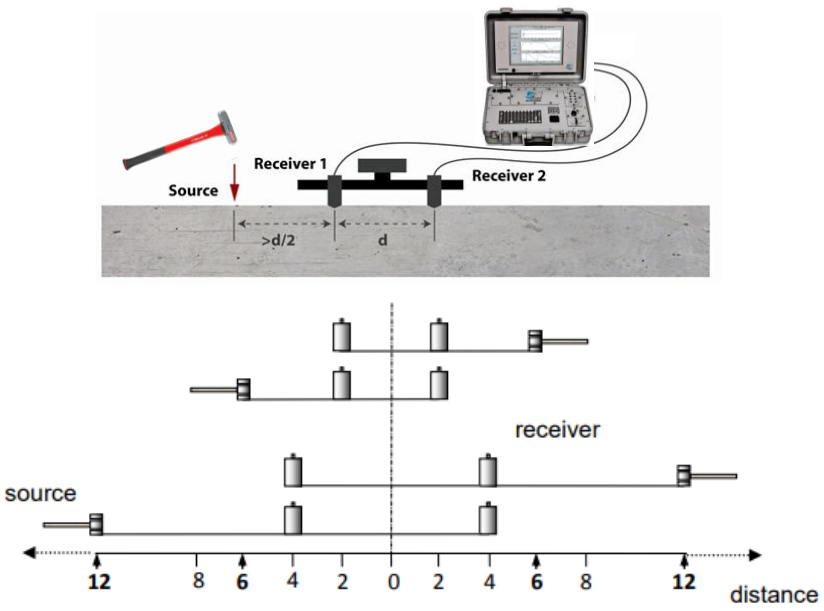


Figure 1-6 Spectral Analysis of Surface Wave (SASW) test configuration.

1.3.2 Seismic Cone Penetration Test (SCPT)

The Seismic Cone Penetration Test (SCPT) integrates traditional cone penetration testing with seismic wave velocity measurement, thereby offering both stratigraphic and stiffness information in a single test as described in ConeTec. (2025). In this method, the cone penetrometer is advanced into the soil while seismic waves are generated at the ground surface using an impact source. The waves are detected by a geophone embedded within the cone, as illustrated in Figure 1-7.

The SCPT provides real-time information about soil stratigraphy, stiffness, and strength, and is especially useful for site classification and liquefaction potential assessment. Its non-destructive nature ensures minimal disturbance to soil structure, and its ability to deliver immediate results enhances its cost-effectiveness compared to traditional geotechnical methods. Consequently, SCPT is now widely regarded as a standard tool in site investigations for seismic design and foundation engineering.

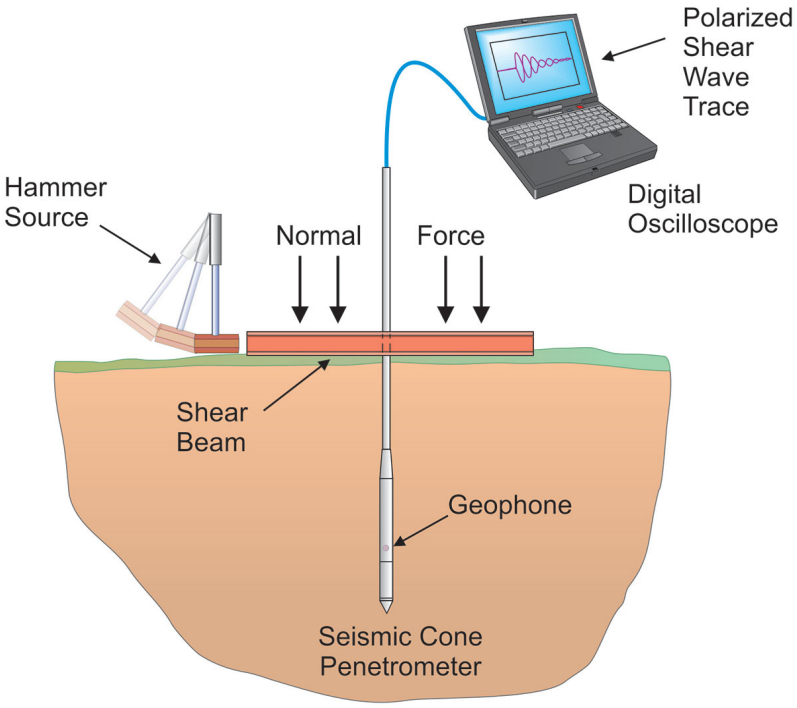
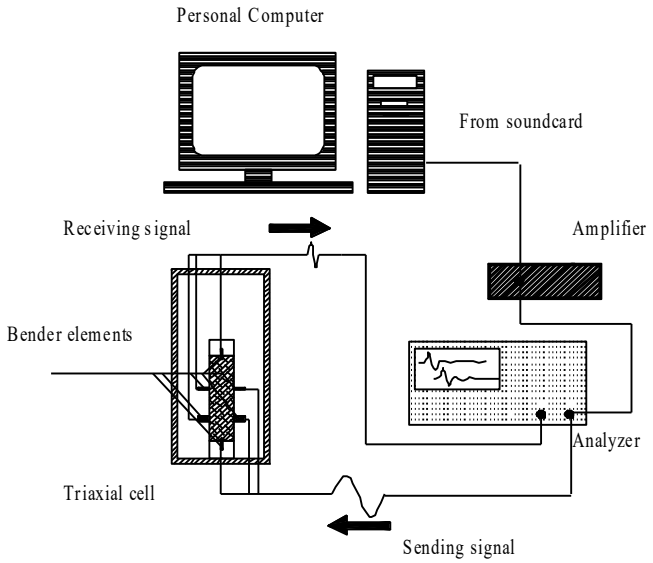


Figure 1-7 Seismic Cone Penetration Test (SCPT) configuration after ConeTec. (2025).

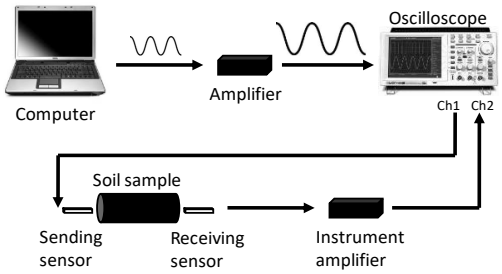
1.3.3 Bender Element Testing (BET)

The Bender Element Testing (BET) is a laboratory method designed to determine small-strain shear modulus (G_0) and damping properties of soils and rocks. The test employs piezoelectric bender elements, one functioning as a transmitter and the other as a receiver, which are embedded in a specimen to generate and capture shear waves. Figure 1-8a shows the laboratory configuration of the test, while Figure 1-8b illustrates the schematic arrangement.

By measuring the travel time of shear waves across the specimen, V_s can be calculated under controlled laboratory conditions, including varying confining pressures and saturation states. BET is valued for its non-destructive nature, repeatability, and ability to replicate in situ conditions. Furthermore, it has been increasingly used in the study of modified geomaterials such as fly ash and cement admixed Bangkok clay, demonstrating its versatility and relevance in contemporary soil mechanical research as described in Petcherdchoo et al. (2023).



(a)



(b)

Figure 1-8 a) Bender Element Testing (BET) configuration and b) Schematic diagram after Piriyakul (2010).

1.4 Importance of Shear Waves in Geomaterials

Shear wave testing plays a critical role in geotechnical engineering, as V_s provides a direct measure of the stiffness of soils and rocks at small strains. The determination of G_0 from V_s forms the basis of seismic site classification, site response analysis, and liquefaction assessment. Liquefaction, in particular, poses a severe risk in sandy and silty soils during strong seismic shaking. V_s-based correlations with cyclic resistance ratio (CRR) are widely used to evaluate liquefaction potential without requiring invasive testing as described in Ganji et al. (1998).

In addition, shear wave velocity profiling offers insight into subsurface stratigraphy and material contrasts, which are crucial for seismic hazard assessment and international seismic design standards such as National Earthquake Hazards Reduction Program (NEHRP) and Eurocode 8. Beyond geotechnical applications, shear wave techniques are also central to geophysical exploration, where they aid in imaging subsurface features such as aquifers, bedrock depth, and fault zones. Applications in rock mechanics, slope stability analysis, and underground construction further emphasize the multidisciplinary importance of V_s as described in Karray (1999), Lefebvre & Karray (1998), Karray & Lefebvre (2000), Karray et al. (2010), Park et al. (1999) and Foti (2000).

1.5 Objectives of this Book

The primary goal of this book is to provide a comprehensive understanding of shear wave propagation into geomaterials. It offers an extensive exploration of shear wave fundamentals and behaviors. The book covers the measurement and determination of shear wave velocity, followed by the characterization of the site.

Additionally, the book delves into the enhancement of geomaterials' strength and other engineering properties through the incorporation of binders, such as ordinary Portland cement, bio-cement, and geopolymer. The overall outline of this book can be summarized as follows:

Chapter 1 provides a comprehensive overview of shear wave propagation in geomaterials. The historical development of shear wave testing in both field and laboratory settings is explained, highlighting the evolution of modern shear wave testing techniques. This chapter emphasizes the significance of shear wave propagation in geomaterials and its importance in geotechnical engineering applications.

In Chapter 2, the fundamentals of shear wave theory and behavior are thoroughly explored. This chapter provides a clear and detailed explanation of all the basic theories of shear wave propagation. Shear wave behavior in both homogeneous and heterogeneous media is carefully studied. Moreover, the relationship between shear wave velocity, stiffness, and material damping is discussed in depth.

Chapter 3 presents a comprehensive and clear explanation of the methods of shear wave measurement and testing. The chapter delves deep into both field and laboratory tests for shear wave velocity, providing a detailed understanding of the measurement techniques. Additionally, the chapter covers advanced topics in shear wave measurement and testing, offering insights into cutting-edge developments in the field.

Chapter 4 is dedicated to the analysis and interpretation of shear wave data. It begins with an introduction to shear wave data analysis and interpretation. Signal processing techniques for shear wave data are thoroughly discussed, along with the consideration of near field effects on shear waves. This chapter covers various methods for the analysis of shear wave data, shedding light on the integration of shear wave data with other geotechnical data. Site characterization of Bangkok clay formation at the KMUTNB campus by using shear wave data is also elaborated in detail. Moreover, it explores the interpretation of shear wave data for engineering applications and integration of shear wave data with other geotechnical data.

Chapters 5 to 8 showcase the cutting-edge research on shear wave propagation conducted at KMUTNB. The latest advances in the field are presented, with a specific focus on characterizing various geomaterials, including clayey soils, sandy soils, geopolymeric materials, composite materials and fibers. These advancements are made possible by employing bender element testing, a highly accurate and sophisticated technique for shear wave characterization.

Summary

The book commences with a comprehensive introduction to the fundamental principles of shear wave propagation, encompassing various shear wave types and their physical characteristics. The authors then delve into a thorough exploration of methods used for characterizing and measuring shear waves, including laboratory testing, field measurements, and mathematical modeling. The book offers valuable insights into selecting the most suitable method for specific applications.

A prominent strength of the book lies in its emphasis on practical applications of shear wave propagation in geomaterials, notably in non-destructive evaluations. Readers gain a comprehensive understanding of the diverse domains where shear waves find use, such as geotechnical engineering, environmental geology, mining engineering, and geophysics. Additionally, the authors shed light on the widely adopted Bender Element Testing (BET) method, an essential technique for assessing shear modulus and shear wave velocity in soil and geomaterials non-destructively.

This book offers a rigorous and accessible treatment of the subject. Its combination of theoretical depth, practical application, and coverage of cutting-edge research makes it an essential resource for graduate students, researchers, civil and earthquake engineers engaged in the study of shear wave behavior in soils and geomaterials.

Questions and Problems

1. Provide a general explanation of shear wave propagation in geomaterials.
2. Explore the historical background of shear wave propagation in geomaterials.
3. Describe the process of conducting SCPT testing to obtain shear wave velocity.
4. Explain the procedure for using the Bender Element Test (BET) method to determine shear wave velocity.
5. Discuss the significance and relevance of shear wave propagation in geomaterials.

Chapter 2: Fundamentals of Shear Wave Theory and Behavior

2.1 Introduction to Shear Waves

Shear or S-waves, with their unique transverse motion as seen in Figure 2-1 and ability to propagate through various media, hold a significant place in the realm of wave phenomena. As they traverse through solid domains, their distinct characteristics open a world of possibilities for scientific exploration and practical applications. In solid materials, such as rocks, soils, and geomaterials, shear waves showcase their prowess in revealing the structural integrity and mechanical properties of substances. Achenbach (2012) explained clearly the basic wave propagation in elastic solids. When an external force is applied to the medium in a manner that induces shearing motion, these waves come into existence, propagating through the material like ripples in a pond. This fascinating behavior sets them apart from their longitudinal counterparts, the compressional waves (P-waves), where particles oscillate in the same direction as the wave's motion shown in Figure 2-2.

One of the most intriguing aspects of shear waves lies in their velocity, a property intricately tied to the mechanical and elastic attributes of the medium they traverse. Materials with higher shear moduli display sturdiness against shear deformation, leading to swifter shear wave propagation compared to materials with lower shear moduli. As these waves encounter boundaries or interfaces between different materials, their journey is marked by reflections, refractions, and scattering, offering valuable insights into the subsurface geology and material composition.

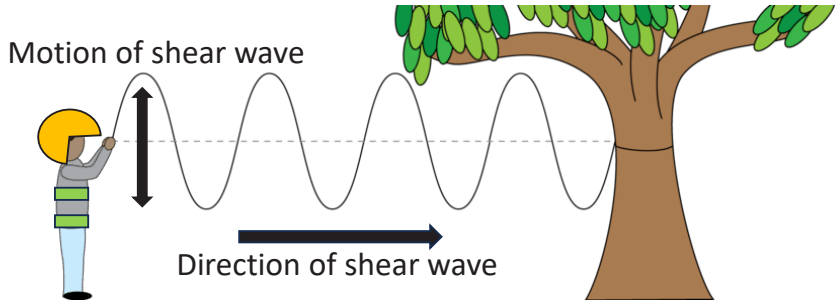


Figure 2-1 Motion of shear wave (S-wave).

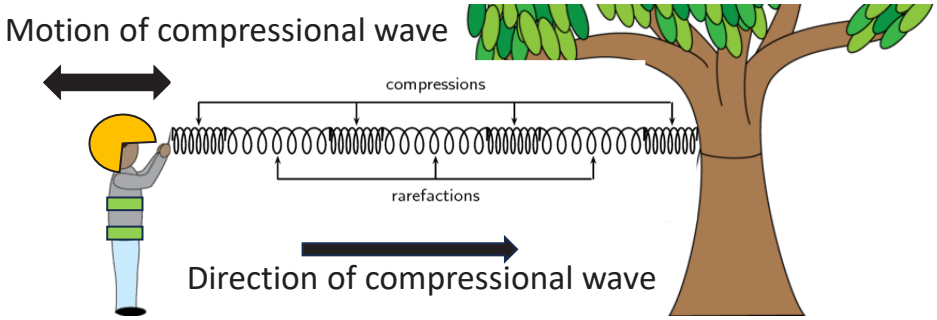


Figure 2-2 Motion of compressional wave (P-wave).

The seismic exploration and engineering communities have harnessed the potential of shear waves to an impressive degree. Employed extensively in geophysics, they play a pivotal role in mapping the subterranean structures, deciphering the Earth's crust, and even detecting subsurface hydrocarbon reserves. In geotechnical engineering, shear wave measurements serve as a potent tool for evaluating soil and rock properties, essential for constructing stable foundations and assessing potential geological hazards.

The realm of earthquake seismology finds shear waves indispensable, as they contribute significantly to the understanding of seismic activity and earthquake mechanisms. Materials testing and characterization also heavily rely on the discerning nature of shear waves, facilitating the analysis of material strength, homogeneity, and response to mechanical stresses.

In essence, shear waves occupy a central position in our comprehension of the behavior and properties of materials, contributing indispensably to the scientific understanding and engineering applications across diverse disciplines. From peering into the heart of the Earth to engineering safer structures, these waves unravel the mysteries hidden beneath the surface, forging a profound link between theoretical exploration and practical advancements in the world of science and technology.

2.2 Basic Theory of Shear Wave Propagation

The basic theory of shear wave propagation forms the foundation for understanding the behavior of shear waves as they travel through different mediums, particularly in solid materials like rocks, soils, and geomaterials as described in Blake (1961). This theory involves the principles of wave mechanics, elastic properties of materials, and the unique characteristics of shear waves. Shear wave propagation in an elastic continuum is a function of:

1) *Transverse motion:* Shear waves, also known as S-waves, exhibit transverse motion, which means the particles in the medium move perpendicular to the direction of shear wave propagation. As the wave advances forward, the particles oscillate sideways or in a transverse direction. This is in contrast to compressional waves (P-waves), where particles move in the same direction as the wave's motion.

2) *Elastic properties:* The propagation of shear waves is intimately related to the mechanical and elastic properties of the medium they traverse. The shear modulus (also called the rigidity modulus) is an essential material property that measures the resistance of a material to shear deformation. Materials with higher shear moduli transmit shear waves faster than those with lower shear moduli.

3) *Shear wave velocity:* The shear wave velocity is determined by the elastic properties and density of the medium. In general, shear waves travel at a slower pace than compressional waves, with their velocity being a significant fraction of the compressional wave velocity. This difference in velocity allows for the separation of shear and compressional waves during seismic measurements.

4) *Propagation in solid media:* Shear waves are particularly prevalent in solid materials, where the intermolecular forces allow for shear deformation to occur. When an external force is applied to the medium in a manner that induces shearing motion, shear waves are generated and propagate through the material, transmitting energy.

5) *Boundaries and reflection:* As shear waves encounter boundaries or interfaces between different materials, they undergo reflection, refraction, and scattering. These interactions provide valuable information about the subsurface structures, material boundaries, and variations in geological formations.

6) *Seismic applications:* Shear waves play an important role in seismic exploration and engineering. Seismologists use the distinct velocity and behavior of shear waves to detect and analyze subsurface geological features, identify geological layers, and study earthquake mechanisms. Engineers employ shear wave measurements to assess the mechanical properties of materials for construction and stability evaluations.

The basic theory of shear wave propagation is essential for various scientific, engineering, and geophysical studies. By understanding the unique behavior and characteristics of shear waves, researchers and professionals can unravel the mysteries hidden beneath the Earth's surface and make informed decisions in fields such as geophysics, geotechnical engineering, earthquake seismology, and materials testing.

2.3 Shear Wave Behavior in Isotropic Media

Shear waves, or S-waves, represent a captivating facet of wave propagation, particularly when they traverse isotropic continuum media. These media, characterized by uniform properties in all directions, offer a fertile ground for delving into the intricate behavior of shear waves. By delving deeper into the mathematical equations that govern their motion and interaction with material properties, we can gain a profound understanding of their behavior and applications in various scientific and engineering domains.

Shear waves, much like other forms of elastic waves, propagate through solid media by generating sinusoidal oscillations of particles. In this mode of propagation, the displacement of particles occurs in a direction perpendicular to the path of the wave, while compressional or longitudinal waves produce displacements that are aligned with the direction of travel. As the waves move through the medium, particle motion varies simultaneously with time and spatial position. Therefore, any theoretical representation of wave motion must account for frequency dependence in both temporal and spatial domains. The concept of angular frequency, ω, as defined in Equation 2.1, describes the oscillatory behavior of the wave with respect to time.

$$\omega = 2\pi f \tag{2.1}$$

The wave number, k, as defined in Equation 2.2, represents the spatial frequency of the propagating wave.

$$k = \frac{\omega}{v} \tag{2.2}$$

Here, f denotes the frequency of the wave expressed in Hertz, and v represents the wave velocity [m/s].

The analysis of a simplified one-dimensional wave provides a clearer foundation for understanding the fundamental nature of wave propagation within a three-dimensional medium. For the basic case of a one-dimensional wave moving along an arbitrary axis, x, the ultrasonic wave model is expressed in Equation 2.3.

$$u(x,t) = u_0 \cos(\omega t - kx) \tag{2.3}$$

In this expression, u_0 represents the maximum amplitude of displacement u. The displacement may be considered either parallel to the x-axis or perpendicular to it, which ensures that the model is applicable to both shear and longitudinal waves. By differentiating $u(x,t)$ twice with respect to the spatial coordinate, the relation presented in Equation 2.4 is obtained.

$$\frac{\partial^2 u}{\partial x^2} = -u_0(-k)^2 \cos(\omega t - kx) \tag{2.4}$$

Similarly, when the function $u(x,t)$ is differentiated twice with respect to time, the resulting expression corresponds to that given in Equation 2.5.

$$\frac{\partial^2 u}{\partial x^2} = -u_0(\omega)^2 \cos(\omega t - kx) \tag{2.5}$$

Equations 2.4 and 2.5 may be reformulated in relation to the original expression presented in Equation 2.3, yielding the following form as shown in Equation 2.6.

$$\frac{\partial^2 u}{\partial t^2} = -\omega^2 u(x,t) \tag{2.6}$$

$$\frac{\partial^2 u}{\partial x^2} = -k^2 u(x,t) \tag{2.7}$$

By rearranging Equation 2.4 and equating the resulting expressions, the one-dimensional wave equation is obtained, as presented in Equation 2.8.

$$\frac{\partial^2 u}{\partial x^2} - \frac{1}{c^2}\frac{\partial^2 u}{\partial t^2} = 0 \tag{2.8}$$

Next, a small differential element subjected to an uniaxial normal stress, σ_{xx}, as illustrated in Figure 2-3, is examined. The corresponding representation of differential elements under simple shear stress is shown in Figure 2-4.

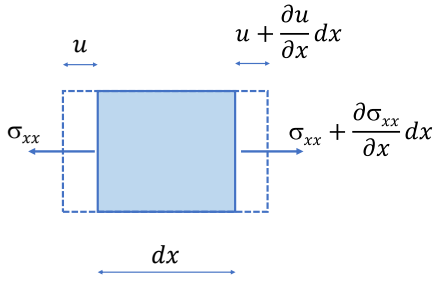


Figure 2-3 Differential stress elements for simple longitudinal stress.

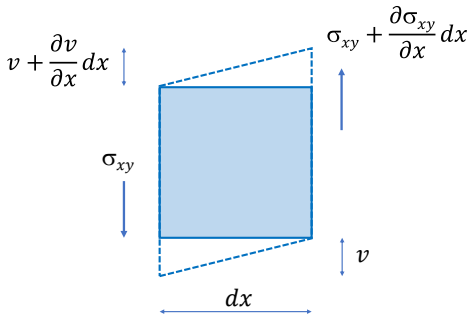


Figure 2-4 Differential stress elements for simple shear stress.

Applying Newton's First Law, a force balance may be established for this differential element under the assumption of a uniform cross-sectional area A, which leads to the expression shown in Equation 2.9.

$$A\left[\left(\sigma_x + \frac{\partial \sigma_x}{\partial x} dx\right) - \sigma_x\right] = \frac{d}{dt}\left[m \frac{\partial u}{\partial t}\right] \tag{2.9}$$

By assuming that the mass, m, is constant, it can be expressed in terms of the density, ρ, and taken outside of the derivative, resulting in the form given in Equation 2.10.

$$A \frac{\partial \sigma_x}{\partial x} dx = \rho dx A \frac{\partial^2 u}{\partial t^2} \tag{2.10}$$

Lastly, the preceding expression can be reduced to the simplified form presented in Equation 2.11.

$$\frac{\partial \sigma_x}{\partial x} = \rho \frac{\partial^2 u}{\partial t^2} \tag{2.11}$$

Since the material undergoes elastic deformation in a single dimension, the longitudinal stress and strain are linked through the elastic modulus of isotropic materials, as expressed in Equation 2.12.

$$\sigma_x = E\varepsilon = E \frac{\partial u}{\partial x} \tag{2.12}$$

Here, E represents the elastic modulus and ε denotes the strain. Differentiating the above relation with respect to x produces the expression presented in Equation 2.13.

$$\frac{\partial \sigma_x}{\partial x} = E \frac{\partial^2 u}{\partial x^2} \tag{2.13}$$

Equations 2.11 and 2.13 can be combined and reformulated to obtain a representation consistent with the one-dimensional wave equation.

$$\frac{\partial^2 u}{\partial x^2} - \frac{1}{V^2} \frac{\partial^2 u}{\partial t^2} = 0 \tag{2.14}$$

By comparing Equations 2.13 and 2.14, the velocity of sound in the longitudinal case can be expressed in terms of the elastic properties of the material, as shown in Equation 2.15.

$$V_p = \sqrt{\frac{E}{\rho}} \tag{2.15}$$

Here, V_p denotes the longitudinal wave velocity. A similar procedure can be applied to shear waves, as illustrated in Figure 3-1b. For shear wave propagation, the relationship between stress and strain is governed by the shear modulus G, which leads to the expression for wave velocity given in Equation 2.16.

$$V_s = \sqrt{\frac{G}{\rho}} = \sqrt{\frac{E}{2\rho(1+\nu)}} \tag{2.16}$$

In this equation, ν designates the Poisson's ratio, which is dimensionless.

When a three-dimensional differential element is analyzed in a comparable way, deflections arising from Poisson's effects are also observed. Thus, when a longitudinal stress is applied along the x-axis, the resulting displacements include u along the x-axis, v along the y-axis, and w along the z-axis. By incorporating these additional deformations together with the assumption of isotropy, the relationship between stress and strain for a three-dimensional body is established as expressed in Equations 2.17 and 2.18.

$$\varepsilon_{ii} = \frac{1}{E}\sigma_{ii} - \frac{\nu}{E}(\sigma_{jj} + \sigma_{kk}) \tag{2.17}$$

$$\varepsilon_{ij} = \varepsilon_{ji} = \frac{1}{2G}\sigma_{ij} \tag{2.18}$$

In this context, the dummy variables i, j, and k are employed to denote the x, y, and z directions. Expanding Equations 2.15 and 2.16 yields six distinct expressions, in which each of the six strain components is written as a function of the corresponding six stress components. For the present analysis, it is more convenient to formulate stress in terms of strain. Accordingly, the preceding equations can be rearranged into the form shown in Equation 2.19, while the shear stress is represented in Equation 2.20 as follows:

$$\sigma_{ii} = \frac{E(1-\nu)}{(1+\nu)(1-2\nu)}\varepsilon_{ii} + \frac{\nu E}{(1+\nu)(1-2\nu)}(\varepsilon_{jj}+\varepsilon_{kk}) \tag{2.19}$$

$$\sigma_{ij} = \frac{E}{(1+\nu)}\varepsilon_{ij} = \frac{E}{(1+\nu)}\varepsilon_{ji} \tag{2.20}$$

At this stage, retaining the previously introduced coefficients becomes increasingly complex and raises the likelihood of mathematical errors. To simplify the formulation, the Lamé coefficients are introduced, which allow the stress–strain relationships to be expressed in a more concise form, as presented in Equations 2.21 and 2.22.

$$\lambda = \frac{\nu E}{(1+\nu)(1-2\nu)} \tag{2.21}$$

$$\mu = \frac{E}{2(1+\nu)} \tag{2.22}$$

By employing the Lamé coefficients, the relationship between stresses and strains can be expressed in a simplified manner, as demonstrated in Equation 2.23.

$$\begin{bmatrix}\sigma_{xx}\\ \sigma_{yy}\\ \sigma_{zz}\\ \sigma_{yz}\\ \sigma_{xz}\\ \sigma_{xy}\end{bmatrix} = \begin{bmatrix}2\mu+\lambda & \lambda & \lambda & 0 & 0 & 0\\ \lambda & 2\mu+\lambda & \lambda & 0 & 0 & 0\\ \lambda & \lambda & 2\mu+\lambda & 0 & 0 & 0\\ 0 & 0 & 0 & 2\mu & 0 & 0\\ 0 & 0 & 0 & 0 & 2\mu & 0\\ 0 & 0 & 0 & 0 & 0 & 2\mu\end{bmatrix} \cdot \begin{bmatrix}\varepsilon_{xx}\\ \varepsilon_{yy}\\ \varepsilon_{zz}\\ \varepsilon_{yz}\\ \varepsilon_{xz}\\ \varepsilon_{xy}\end{bmatrix} \tag{2.23}$$

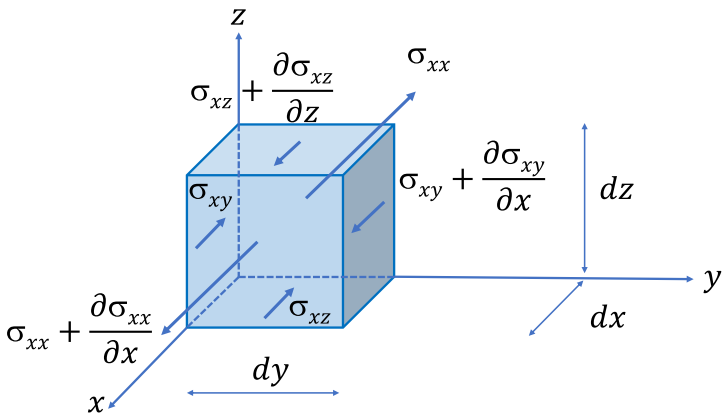


Figure 2-5 Stress along the x-axis acting upon a 3-D differential element.

Figure 2-3 illustrates a differential element subjected to stresses in the x-direction as a result of an ultrasonic wave. By applying Newton's Second Law, the corresponding force balance leads to the expression given in Equation 2.24.

$$\begin{aligned}\frac{\partial^2 u}{\partial t^2}\,\rho\,dx\,dy\,dz = &\left(\sigma_{xx}+\frac{\partial\sigma_{xx}}{\partial x}dx\right)dy\,dz-\sigma_{xx}dy\,dz+\\ &\left(\sigma_{xy}+\frac{\partial\sigma_{xy}}{\partial y}dy\right)dx\,dz\;-\sigma_{xy}dx\,dy+\\ &\left(\sigma_{xz}+\frac{\partial\sigma_{xz}}{\partial z}dz\right)dx\,dy\;-\sigma_{xz}dx\,dz\end{aligned} \tag{2.24}$$

The same approach can also be extended to deflections in the remaining two directions. Upon simplification, this process yields the relations presented in Equations 2.25 through 2.27.

$$\rho\frac{\partial^2 u}{\partial t^2} = \frac{\partial\sigma_{xx}}{\partial x}+\frac{\partial\sigma_{xy}}{\partial y}+\frac{\partial\sigma_{xz}}{\partial z} \tag{2.25}$$

$$\rho\frac{\partial^2 v}{\partial t^2} = \frac{\partial\sigma_{xy}}{\partial x}+\frac{\partial\sigma_{yy}}{\partial y}+\frac{\partial\sigma_{yz}}{\partial z} \tag{2.26}$$

$$\rho\frac{\partial^2 w}{\partial t^2} = \frac{\partial\sigma_{xz}}{\partial x}+\frac{\partial\sigma_{yz}}{\partial y}+\frac{\partial\sigma_{zz}}{\partial z} \tag{2.27}$$

The stress terms in the preceding equation can be reformulated in terms of the internal strains by substituting the appropriate expressions from Equation 2.23 into Equation 2.24. After regrouping and combining like terms, the three-dimensional wave equations are obtained, as expressed in Equations 2.28 through 2.30.

$$\rho\frac{\partial^2 u}{\partial t^2} = (\mu + \lambda)\left[\frac{\partial}{\partial x}\left(\frac{\partial u}{\partial x} + \frac{\partial v}{\partial y} + \frac{\partial w}{\partial z}\right)\right] + \mu\left[\frac{\partial^2 u}{\partial x^2} + \frac{\partial^2 u}{\partial y^2} + \frac{\partial^2 u}{\partial z^2}\right] \quad (2.28)$$

$$\rho\frac{\partial^2 v}{\partial t^2} = (\mu + \lambda)\left[\frac{\partial}{\partial y}\left(\frac{\partial u}{\partial x} + \frac{\partial v}{\partial y} + \frac{\partial w}{\partial z}\right)\right] + \mu\left[\frac{\partial^2 v}{\partial x^2} + \frac{\partial^2 v}{\partial y^2} + \frac{\partial^2 v}{\partial z^2}\right] \quad (2.29)$$

$$\rho\frac{\partial^2 w}{\partial t^2} = (\mu + \lambda)\left[\frac{\partial}{\partial z}\left(\frac{\partial u}{\partial x} + \frac{\partial v}{\partial y} + \frac{\partial w}{\partial z}\right)\right] + \mu\left[\frac{\partial^2 w}{\partial x^2} + \frac{\partial^2 w}{\partial y^2} + \frac{\partial^2 w}{\partial z^2}\right] \quad (2.30)$$

At this point, it is essential to consider the fundamental nature of the wave under study. Both longitudinal and shear waves exhibit oscillatory motion as they propagate through a material, with these oscillations dependent on both spatial position and time. The principal distinction between the two types lies in the orientation of their oscillatory displacements, ω. If the wave is propagating in the longitudinal mode so that all of its energy is traveling in the x-direction, then any of the cross derivatives will go to zero leaving only the $\frac{\partial^2 u}{\partial x^2}$ terms. Therefore, Equation 2.24 shows that the wave velocity traveling in this function will have a shear wave velocity.

$$V_p = \sqrt{\frac{2\mu+\lambda}{\rho}} = \sqrt{\frac{E(1-\nu)}{\rho(1+\nu)(1-2\nu)}} \quad (2.31)$$

In a similar manner, Equations 2.31 and 2.32 indicate that a shear wave propagating along the x-direction possesses a corresponding wave velocity.

$$V_s = \sqrt{\frac{\mu}{\rho}} = \sqrt{\frac{G}{\rho}}\sqrt{\frac{E}{2\rho(1+\nu)}} \quad (2.32)$$

With the velocities of both P-waves and S-waves expressed as functions of the elastic properties, the inverse relationship can be obtained through straightforward algebraic manipulation. By solving for Young's modulus and Poisson's ratio, the final expressions are derived as follows Equations 2.33 and 2.34:

$$E = \rho \cdot V_s^2\left(\frac{3V_p^2 - 4V_s^2}{V_p^2 - V_s^2}\right) \quad (2.33)$$

$$\nu = \frac{1-2\left(\frac{V_s}{V_p}\right)^2}{2-2\left(\frac{V_s}{V_p}\right)^2} \quad (2.34)$$

2.4 Shear Wave Behavior in Anisotropic Media

Shear wave behavior in heterogeneous media introduces complexities due to variations in material properties, composition, and structure throughout the medium. Heterogeneous media are materials with non-uniform properties, such as varying shear modulus, density, and structural characteristics. In such environments, shear waves encounter a range of behaviors and interactions, leading to interesting phenomena not observed in homogeneous media. Pickering (1970) proposed the relationship stress and strain for a material with a single vertical axis of symmetry which is called the cross-anisotropy in Figure 2-6 is described in Equation 2.35. Piriyakul (2006) studied the anisotropic behavior of Belgian Boom clay and well defined all elastic properties of this clay.

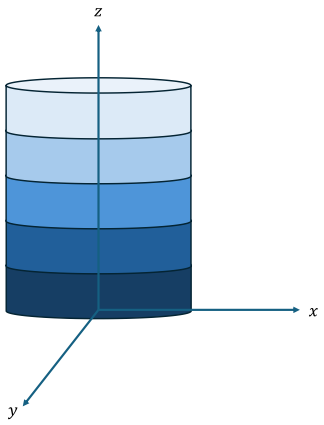


Figure 2-6 A cross-anisotropy model.

$$\begin{bmatrix}\sigma_{xx}\\ \sigma_{yy}\\ \sigma_{zz}\\ \sigma_{yz}\\ \sigma_{xz}\\ \sigma_{xy}\end{bmatrix} = \begin{bmatrix} E_h & \frac{E_h}{-\nu_{hh}} & \frac{E_v}{-\nu_{vh}} & 0 & 0 & 0\\ \frac{E_h}{-\nu_{hh}} & E_h & \frac{E_v}{-\nu_{vh}} & 0 & 0 & 0\\ \frac{E_h}{-\nu_{hv}} & \frac{E_h}{-\nu_{hv}} & E_v & 0 & 0 & 0\\ 0 & 0 & 0 & G_{hv} & 0 & 0\\ 0 & 0 & 0 & 0 & G_{hv} & 0\\ 0 & 0 & 0 & 0 & 0 & G_{hh}\end{bmatrix} \cdot \begin{bmatrix}\varepsilon_{xx}\\ \varepsilon_{yy}\\ \varepsilon_{zz}\\ \varepsilon_{yz}\\ \varepsilon_{xz}\\ \varepsilon_{xy}\end{bmatrix} \quad (2.35)$$

In this formulation, the stress and strain increments are expressed with respect to rectangular Cartesian axes, where the z-axis is oriented vertically. This representation makes it possible to distinguish between the horizontal directions, while still assuming that the material properties are identical in both of them. The seven elastic parameters appearing in Equation 2.35 are defined as follows:

G_{hv} = Shear modulus in vertical plane
G_{hh} = Shear modulus in horizontal plane
E_v = Young's modulus in the vertical direction
E_h = Young's modulus in the horizontal direction
ν_{vh} = Poisson's ratio for horizontal strain due to vertical stress
ν_{hv} = Poisson's ratio for vertical strain due to horizontal stress
ν_{hh} = Poisson's ratio for horizontal strain due to horizontal stress at right angles

2.5 Shear Wave Velocity and Stiffness

Shear wave velocity and stiffness are closely related properties that play a significant role in understanding the behavior of materials, particularly in the context of seismic wave propagation and geotechnical engineering.

2.5.1 Shear Wave Velocity (V_s)

Shear wave velocity refers to the speed at which shear waves propagate through a medium, such as rocks, soils, or other geomaterials. It is a measure of how quickly the transverse motion is transmitted through the material. Shear wave velocity is denoted by the symbol "V_s". The shear wave velocity of a material is influenced primarily by its shear modulus (also known as the shear modulus or G), which represents the material's resistance to shear deformation. For isotropic (uniform in all directions) homogeneous materials, the relationship between shear wave velocity and shear modulus is given by Equation 2.36:

$$G = \rho \cdot V_s^2 \tag{2.36}$$

where:
V_s = Shear wave velocity
G = Shear modulus
ρ = Density of the material

In general, materials with higher shear moduli have higher shear wave velocities, indicating that they transmit shear waves more rapidly. Consequently, materials with higher shear wave velocities are often considered stiffer, as they resist deformation caused by shear forces more effectively.

2.5.2 Stiffness and Young's Modulus (E)

Stiffness is a broader term used to describe the resistance of a material to deformation under applied forces. It is a measure of how much a material resists being stretched or compressed. Young's modulus (E), also known as the elastic modulus or the modulus of elasticity, is a fundamental material property that represents the stiffness of a material. Young's modulus measures the ratio of stress to strain in a material under tensile or compressive loads and is given by Equation 2.37:

$$E = \frac{Stress}{Strain} = \frac{\sigma}{\varepsilon} \tag{2.37}$$

where:
E = Young's modulus
Stress = Applied force per unit area
Strain = Deformation or change in length relative to the original length

For isotropic (uniform in all directions) homogeneous materials, the relationship between compression wave velocity and Young's modulus is given by Equation 2.38:

$$E = \rho \cdot V_p^2 \tag{2.38}$$

Young's modulus is related to the shear modulus (G) for isotropic materials through the Poisson's ratio (ν), which represents the lateral contraction of a material when subjected to axial strain. The relationship between Young's modulus, shear modulus, and Poisson's ratio is given by Equation 2.39:

$$G = \frac{E}{2(1+\nu)} \tag{2.39}$$

In geotechnical engineering and seismic studies, both shear wave velocity and stiffness (represented by Young's modulus) are essential parameters for assessing the mechanical behavior and integrity of geomaterials. By understanding these properties, engineers and geophysicists can make informed decisions for various applications, including foundation design, earthquake hazard assessment, and subsurface exploration.

2.6 Damping and Attenuation of Shear Waves

Damping and attenuation are essential concepts in understanding the behavior of shear waves as they propagate through materials as described by Ishibashi & Zhang (1993). These phenomena are crucial in seismic studies, engineering applications, and material characterization, as they determine how shear wave energy dissipates as the waves travel through a medium. Figure 2-7 depicts damping ratio, D, in function of shear strain, showing that the damping ratio, D, increases with increasing the shear strain, γ. Damping is a very important factor in shear wave behavior, especially in the context of seismic signals, as it affects the wave's amplitude and ability to transmit information. In seismic exploration and earthquake seismology, understanding damping is crucial for accurate interpretation of seismic data and assessing the geological properties of subsurface formations. Many researchers such as Schaeffer et al. (2013), Amaral et al. (2013), Chan (2012) and Patel et al. (2012) studied the dynamic parameters and damping of geomaterials by triaxial test and bender element test as described in Lee & Santamarina (2005).

Ishibashi & Zhang (1993) developed a closed expression for damping ratio based on the shear modulus reduction, $\frac{G}{G_0}$, and the plasticity index, I_p.

$$D = \frac{0.333(1+e^{-0.0145I_p^{1.3}})}{2}\left\{0.586\left(\frac{G}{G_0}\right)^2 - 1.547\frac{G}{G_0} + 1\right\} \tag{2.40}$$

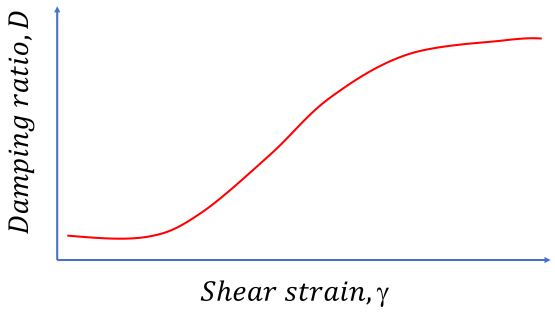


Figure 2-7 Damping ratio in function of shear strain.

In soil dynamics, vibration theory, and earthquake geotechnics, damping is properly defined as follows:

1) *Damping:* Damping refers to the gradual loss of energy in a propagating wave, leading to a decrease in its amplitude over distance. In the context of shear waves, damping occurs due to various internal and external factors that convert mechanical energy into other forms of energy, such as heat.

2) *Internal Damping:* Internal damping in a material arises from the interactions between its constituent particles or internal structural elements. These interactions may involve friction, viscoelastic behavior, material microstructure, and other dissipative processes. Materials with higher internal damping tend to absorb more shear wave energy, leading to greater attenuation.

3) *External Damping:* External damping is influenced by the medium in which the shear waves propagate. For example, if the shear wave travels through a viscoelastic material or encounters fluids or other dissipative elements, external damping contributes to energy dissipation and attenuation.

4) *Attenuation:* Attenuation refers to the decrease in amplitude or energy of a wave as it propagates through a medium. In the case of shear waves, attenuation results from damping, scattering, and other energy dissipation mechanisms. The attenuation rate quantifies the loss of wave energy over a given distance. The rate of attenuation of shear waves is influenced by various factors, including the material properties of the medium, frequency of the wave, and the distance traveled. High-frequency shear waves tend to attenuate more rapidly than low-frequency ones, and materials with higher damping properties show higher attenuation rates. In seismic studies, attenuation is a fundamental parameter for characterizing the properties of the subsurface, such as the quality of hydrocarbon reservoirs, the presence of fractures, and other geological features. It also plays a significant role in assessing the seismic hazard potential of regions prone to earthquakes.

So, damping and attenuation are fundamental aspects of shear wave behavior that govern the loss of energy as the waves propagate through materials. Understanding these phenomena is essential for various scientific, engineering, and geophysical applications, as they provide valuable insights into material properties, seismic exploration, and the integrity of geological formations.

Exercise 2.1 From Figure 2-8 calculate the angular wave number.

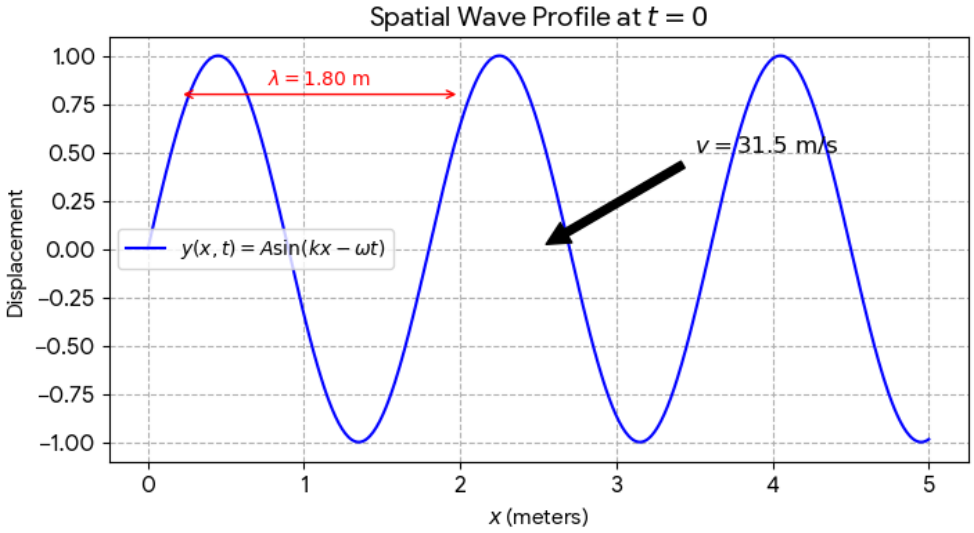


Figure 2-8 Example of wave form.

Solution

The angular wave number k represents the spatial frequency of the wave (radians per unit distance). It is calculated using the wavelength, λ :

Given λ =1.8 m:

$$k = \frac{2\pi}{1.8} = 3.49 \qquad \text{m}^{-1}$$

The result is correctly rounded to 3.49 m^{-1}.

Ans.

Exercise 2.2 From Figure 2-8 calculate the wave velocity.

Solution

The wave velocity v can be determined from the relationship between its angular frequency ω and its angular wave number k:
Given ω = 110 rad/s and k=3.49 m^{-1}

$v = \frac{110}{3.49}$=31.5 m/s

The wave velocity, v, is correctly rounded to 31.5 m/s.

Ans.

Exercise 2.3 A wave has frequency of 50 Hz and a wavelength of 10 m. What is the velocity of the wave?

Solution
f = 50 Hz
λ = 10 m
$v = f$ x λ = 50 x 10 = 500 m/s

Ans.

Exercise 2.4 A wave has frequency of 5 Hz and a velocity of 25 m/s. What is the wavelength?

Solution
f = 5 Hz
v = 25 m/s
λ = v / f = 25/5 = 5 m

Ans.

Exercise 2.5 A wave has a wavelength of 10 m and a velocity of 340 m/s. What is the frequency of the wave?

Solution
λ = 10 m
v = 340 m/s
$f = v$ / λ = 340/10 = 34 Hz

Ans.

Exercise 2.6 A ground has a shear wave velocity,V_s, of 50 m/s and a P-wave velocity,V_p, of 122 m/s. What is the poison's ratio?

Solution
V_s= 50 m/s
V_p = 122 m/s

From Equation 2.34, $\nu = \frac{1-2\left(\frac{V_s}{V_p}\right)^2}{2-2\left(\frac{V_s}{V_p}\right)^2} = \frac{1-2\left(\frac{50}{122}\right)^2}{2-2\left(\frac{50}{122}\right)^2}$

$$\nu = 0.4$$

Ans.

Exercise 2.7 A ground has a Young's modulus, E, of 1100 MPa and a Poison's ratio of 0.4. What is the shear modulus, G?

Solution
E = 1100 MPa
$\nu = 0.4$

From Equation 2.39, $G = \frac{E}{2(1+\nu)} = \frac{1100}{2(1+0.4)}$

G = 380 MPa

Ans.

Exercise 2.8 A ground has a shear wave velocity, V_s, of 100 m/s and a Poison's ratio of 0.4. What is the P-wave velocity, V_p?

Solution

V_s= 100 m/s

$\nu = 0.4$

From Equation 2.34, $\nu = \frac{1-2\left(\frac{V_s}{V_p}\right)^2}{2-2\left(\frac{V_s}{V_p}\right)^2}$

$$0.4 = \frac{1-2\left(\frac{100}{V_p}\right)^2}{2-2\left(\frac{100}{V_p}\right)^2}$$

V_p = 245 m/s

Ans.

Exercise 2.9 A ground has a P-wave velocity, V_p of 980 m/s and a Poison's ratio of 0.4. What is the shear wave velocity, V_s?

Solution

V_p= 980 m/s

$\nu = 0.4$

From Equation 2.34, $\nu = \frac{1-2\left(\frac{V_s}{V_p}\right)^2}{2-2\left(\frac{V_s}{V_p}\right)^2}$

$$0.4 = \frac{1-2\left(\frac{V_s}{980}\right)^2}{2-2\left(\frac{V_s}{980}\right)^2}$$

V_s = 400 m/s

Ans.

Exercise 2.10 A ground has a shear wave velocity,V_s, of 50 m/s and a mass density of 2373 kg/m^3. What is the shear modulus, G?

Solution

V_s= 50 m/s

$\rho = 2373$ kg/m^3

From Equation 2.16, $V_s = \sqrt{\frac{G}{\rho}}$

$$50 = \sqrt{\frac{G}{2373}}$$

G = 5.9 MPa

Ans.

Exercise 2.11 A ground has a p-wave velocity, V_p, of 490 m/s and a mass density of 2373 kg/m^3. What is the Young's modulus, E?

Solution

V_p= 490 m/s

ρ = 2373 kg/m^3

From Equation 2.15, $V_p = \sqrt{\frac{E}{\rho}}$

$$490 = \sqrt{\frac{E}{2373}}$$

E = 270 MPa

Ans.

Exercise 2.12 A ground has a p-wave velocity, V_p, of 1960 m/s, a mass density of 2373 kg/m^3 and a shear wave velocity,V_s, of 800 m/s. What is the Young's modulus, E?

Solution

V_p= 1960 m/s

V_s = 800 m/s

ρ = 2373 kg/m^3

From Equation 2.33, $E = \rho \cdot V_s^2 \left(\frac{3V_p^2 - 4V_s^2}{V_p^2 - V_s^2}\right)$

$$E = 2373 \cdot [(800)^2] \left(\frac{3(1960)^2 - 4(800)^2}{(1960)^2 - (800)^2}\right)$$

E = 4300 MPa

Ans.

Summary

1. Shear waves are important for expanding our knowledge of the behavior and characteristics of materials and provide a fundamental basis for scientific research and innovative engineering in a variety of domains. These waves reveal hidden mysteries, bridging the gap between theoretical discovery and practical problems advancement in science and technology, from exploring the Earth's inner depths to creating safer structures.

2. Numerous scientific, engineering, and geophysical applications depend on an understanding of the basic theory of shear wave propagation. Researchers and professionals can discover the hidden complexities beneath the Earth's surface and make well-informed decisions in fields like geophysics, geotechnical engineering, earthquake seismology, and materials testing by looking at the unique behavior and characteristics of shear waves.

3. The P-wave and S-wave velocities are expressed as functions of the elastic properties, it is easy to use algebraic manipulation to ascertain how these elastic properties relate to the wave velocity. We can solve for important elastic constants like Poisson's ratio and Young's modulus by rearranging the established relationships. These computations not only offer a more profound comprehension of the material's mechanical behavior, but they also directly link the intrinsic properties of the material with the characteristics of wave propagation. In the end, this procedure will produce explicit expressions for Poisson's ratio and Young's modulus, providing insightful information for a range of material science and geophysics applications.

4. The non-uniform nature of the material properties, composition, and structural variations within the medium introduces significant complexity into the behavior of shear waves in heterogeneous media. Analysis of wave propagation is made more difficult by heterogeneous media, which are defined by spatially varying characteristics like density, shear modulus, and microstructural features. Shear waves in these conditions interact with areas of contrasting properties, causing scattering, diffraction, and mode conversion. This can lead to phenomena that are not present in homogeneous media, like energy redistribution, wave attenuation, and the creation of secondary waves. Seismology, non-destructive material testing, and biomedical imaging are just a few of the many fields that depend on the study of shear wave behavior in heterogeneous materials because of these intricate interactions. Improved interpretations and applications in a variety of scientific and engineering fields are made possible by these analyses, which offer important insights into the mechanical and structural properties of materials.

5. Damping and attenuation are important variables that control energy loss as shear waves travel through materials. In contrast to attenuation, which includes energy absorption and scattering brought on by medium heterogeneities, damping results from internal friction and material breakdown. These mechanisms affect the frequency, amplitude, and travel distance of shear waves.

Questions and Problems

1. Explain the difference between the motion of shear wave (S-wave) and the motion of compressional wave (P-wave).
2. Explain the shear wave propagation in the isotropic domain.
3. Explain the shear wave propagation in the cross-anisotropic domain.
4. Explain the relationship between the shear wave velocity and the Elastic properties.
5. What are the Lame's coefficients and the use of them in the stress-strain relationship.

Chapter 3: Methods to determine Shear Wave Velocity and Shear Modulus

3.1 Introduction to Shear Wave Velocity and Shear Modulus

This chapter provides a comprehensive overview of the standard soil tests used to determine shear wave velocity and dynamic parameters, with particular emphasis on both laboratory and field-testing methods as described in Airey & Wood (1987). It explores the fundamental principles underlying these tests, their relevance in geotechnical engineering, and their application in evaluating the dynamic behavior of soils. The discussion covers a variety of commonly used techniques, highlighting their procedures, advantages, and limitations. Figure 3-1 presents the overview of possible shear strain amplitudes as described by Studer et al. (2008).

Laboratory tests such as shaking table, resonant column tests, cyclic triaxial tests, cyclic torsional shear tests, and bender element tests are described in detail, providing an understanding of their operational mechanisms and specific applications. For instance, the shaking table test offers insight into how soil samples respond to dynamic loading in a controlled environment, whereas the resonant column test is particularly useful in evaluating soil stiffness and damping properties under cyclic conditions. The cyclic triaxial test allows for the examination of soil behavior under repetitive loading, and the cyclic torsional shear test provides valuable data on shear modulus and damping ratios. The bender element test, on the other hand, is a non-destructive method used to measure shear wave velocity at very small strain levels.

Similarly, field methods such as seismic refraction and reflection tests, multichannel analysis of surface waves (MASW), dynamically loaded plates, and cross-hole or down-hole seismic testing are examined to provide insights into in-situ measurements. Seismic refraction and reflection tests, for instance, are critical for evaluating the subsurface stratigraphy and shear wave velocity profiles, while MASW techniques offer a non-invasive way to measure the shear wave velocity profile across larger areas. Dynamically loaded plates provide useful data on soil stiffness under actual loading conditions, and cross-hole or down-hole seismic testing allows for the measurement of shear wave velocity at different depths, providing a more detailed understanding of the soil's dynamic properties.

The chapter also addresses the importance of these advanced topics in shear wave measurement and testing, such as the limitations and challenges that practitioners may encounter in field and laboratory settings. These include issues related to soil heterogeneity, the accuracy of measurement techniques, the impact of environmental factors on testing conditions, and the calibration of equipment. Moreover, the chapter explores emerging technologies and innovative approaches to overcoming these challenges, offering insights into future directions in the field of soil dynamics. Additionally, the potential for integrating multiple testing methods for more comprehensive evaluations of soil behavior is discussed, emphasizing the need for a multidisciplinary approach in assessing the dynamic properties of soils and geomaterials.

Finally, this chapter outlines the key limitations in applying shear wave velocity within geotechnical engineering, emphasizing three main challenges: site-specific influences on testing accuracy, technical constraints of measurement equipment, and interpretational uncertainties in data analysis.

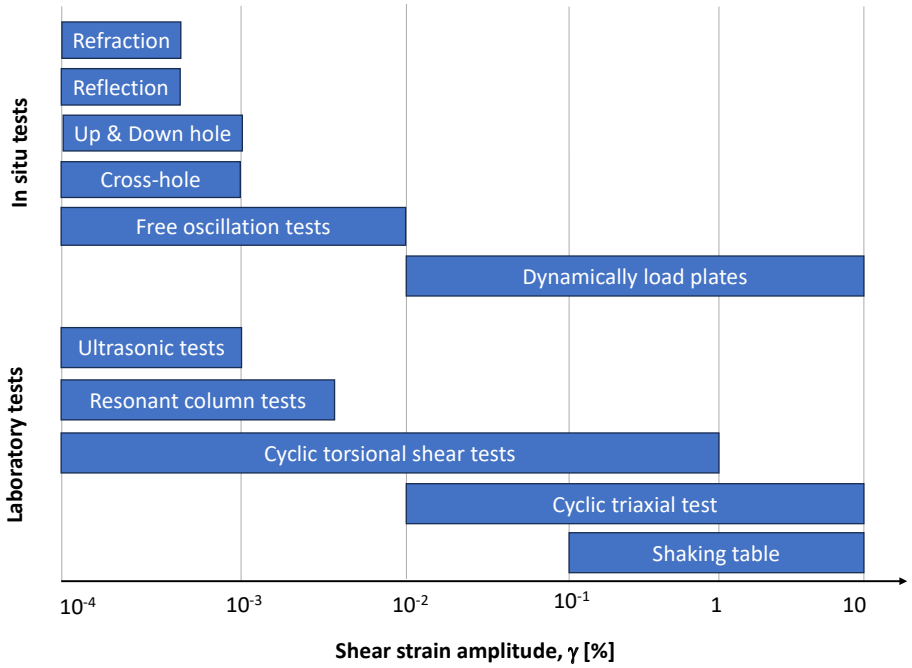


Figure 3-1 Overview of possible shear strain amplitudes after Studer et al. (2008).

3.2 Laboratory-Based Methods of Shear Wave Measurement and Testing

3.2.1 Bender Element Testing

The principle of bender elements is derived from the electromechanical properties of piezoelectric materials. When an electrical voltage is applied across two bonded piezoelectric components, one expands while the other contracts, which produces a bending motion of the entire element, as illustrated in Figure 3-2. Conversely, when the bender element is subjected to a lateral disturbance, a voltage is generated. This bidirectional property enables bender elements to operate both as transmitters and receivers of shear waves. The measurement of the travel time between the transmission and reception of a shear wave provides a means of determining shear wave velocity, a concept that has been demonstrated and validated in several studies as described in Dyvik & Madshus (1985) and Iamchaturapatr et al. (2022a).

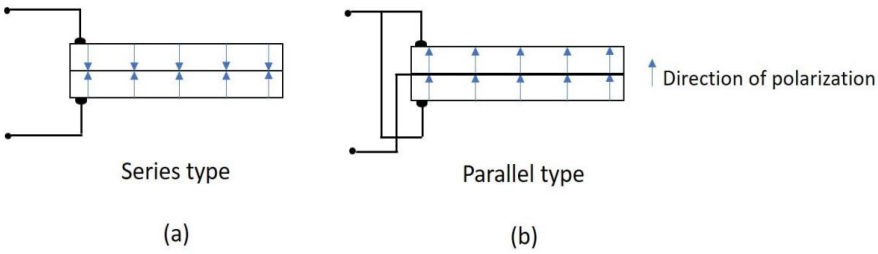
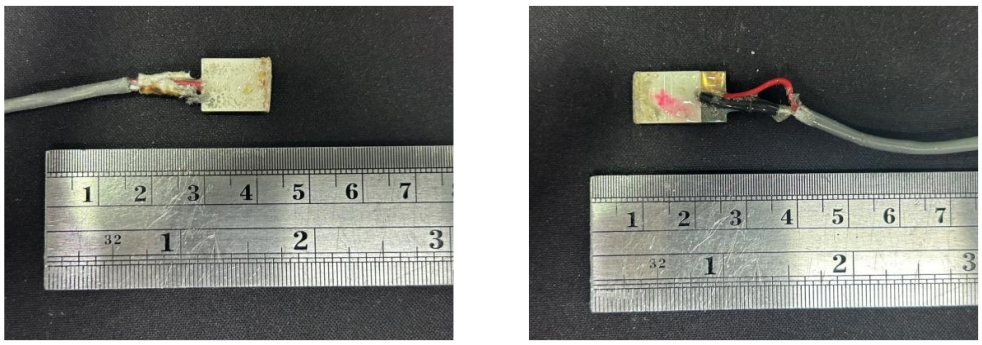


Figure 3-2 (a) Series and (b) Parallel connected bender elements after Iamchaturapatr et al. (2022a).



(a) (b)

Figure 3-3 Piezoelectric sensors: (a) Series and (b) Parallel types.

Piezoelectric bender elements are generally classified into two types: the series-connected configuration and the parallel-connected configuration. The series-connected bender element, illustrated in Figure 3-2a, is constructed with plates polarized in opposite directions, and electrical leads are attached to each of the outer electrode surfaces. The parallel-connected bender element, shown in Figure 3-2b, is arranged so that the polarization of both plates is aligned in the same direction. In this arrangement, the electrical connections are made such that the two outer electrode surfaces form one pole, while the center electrode functions as the opposite pole. To connect a wire to the center electrode, a portion of the element must be removed through grinding. In practical applications, the series-connected bender element is more effective as a receiver, whereas the parallel-connected configuration is typically preferred as a transmitter. In the present study, however, only the series type is employed for both transmitting and receiving functions, owing to its superior performance in capturing the received signal. Figure 3-3 depicts the piezoelectric sensors, used at the KMUTNB soil mechanics laboratory. The series one is shown in Figure 3-3a while the parallel type is expressed in Figure 3-3b. Both piezoelectric sensors were supplied by Fuji ceramic cooperation from Japan. The series type is the BM13*10*0.5(C-6)0.05P and the parallel sensor is the PM13*10*0.5(C-6)18*0.05P.

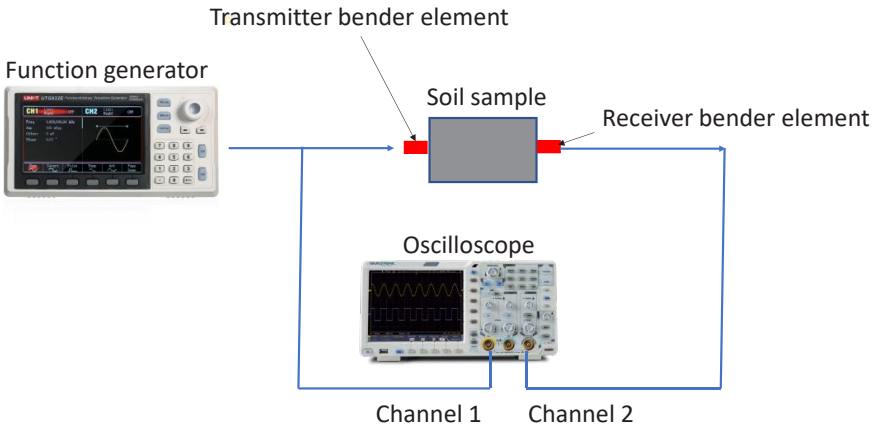


Figure 3-4 Schematic of bender element test after Iamchaturapatr et al. (2022).

Following the procedure outlined in ASTM D8295–19, which is the standard method for determining shear wave velocity and the initial shear modulus in soil specimens using bender elements, the shear wave is generated by a function generator producing a sinusoidal signal with a frequency range of 4 to 10 kHz and an amplitude of 20 $V_{p\text{-}p}$. The generated signal is delivered to the transmitting bender element, while the transmitted waveform is simultaneously monitored through channel 1 of the oscilloscope, as illustrated in Figure 3-4. For the transmitting element, the parallel connection is adopted because of its capability to produce large deformations and strong output signals. Once emitted, the shear wave propagates through the soil specimen, as depicted in Figure 3-5. On the receiving side, a series-connected bender element is employed owing to its higher sensitivity. The received signal is then recorded through channel 2 of the oscilloscope. More details about the development of bender element test is clearly explained by Piriyakul (2010). Figure 3-6 shows the bender element test setup at the KMUTNB soil mechanics laboratory.



Figure 3-5 Installation of bender element sensors on a soil sample.

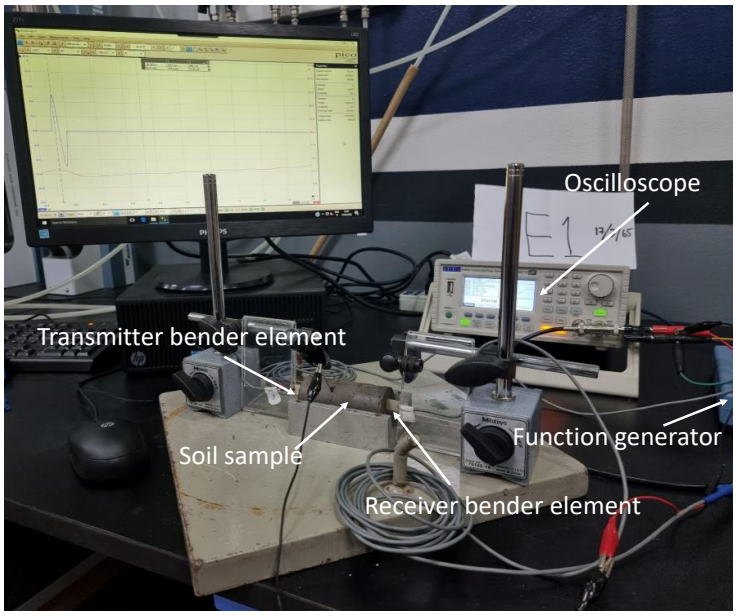


Figure 3-6 Bender element test setup at the KMUTNB campus.

3.2.2 Cyclic Triaxial Test

The testing apparatus is based on conventional triaxial equipment that is modified with an additional cyclic axial loading unit. In certain applications, the cell pressure may also be varied cyclically. Both isotropic and anisotropic initial stress states can be accommodated. The configuration of the cyclic triaxial testing device available at the KMUTNB soil mechanics laboratory is illustrated in Figure 3-7. Limitations caused by bedding errors and system compliance generally restrict measurements to shear strains greater than 10^{-2} %, although the use of local strain measurement devices allows accurate results to be obtained at strain levels as low as 10^{-4} %, as reported in previous investigations by Kramer (1996).

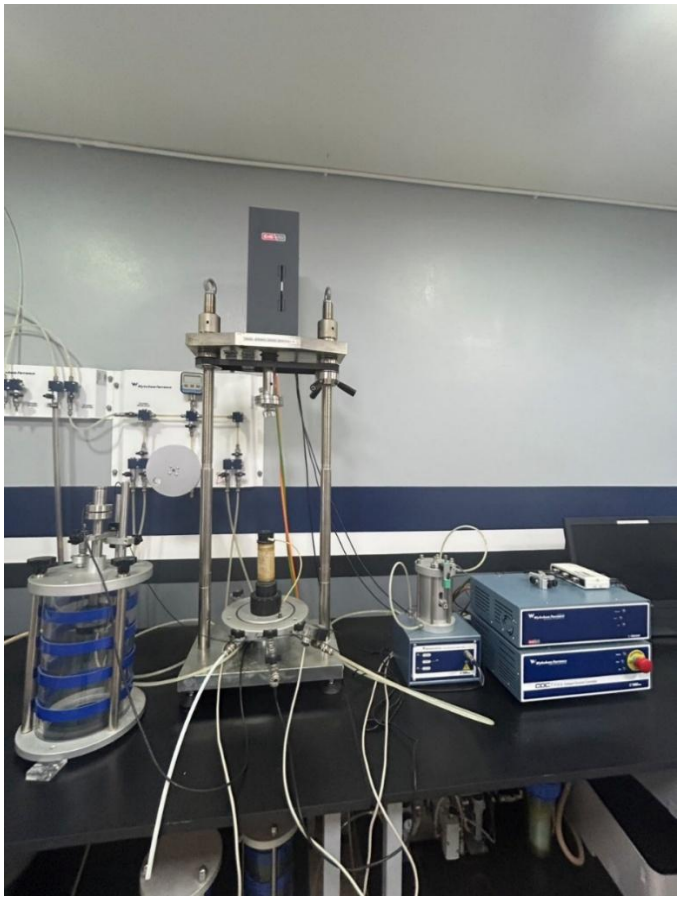


Figure 3-7 Cyclic triaxial test at the KMUTNB campus.

Cyclic Triaxial Test is a laboratory test used in geotechnical engineering to evaluate the behavior of soils under cyclic loading conditions, such as those caused by earthquakes, ocean waves, or repeated traffic loads. It is a variation of the standard triaxial test, where a soil sample is subjected to cyclic axial stresses while maintaining a constant confining pressure. This test is particularly useful in assessing the dynamic properties of soil, including its ability to withstand repeated loading without excessive deformation or failure. By simulating real-world cyclic forces, the test provides crucial insights into soil behavior under conditions that can lead to liquefaction, progressive deformation, or structural instability.

During the test, a cylindrical soil specimen—typically encased in a rubber membrane—is placed within a triaxial chamber and subjected to controlled cyclic axial loads while being confined under a predetermined pressure. The test can be performed under either stress-controlled or strain-controlled conditions, depending on the research objective. In stress-controlled tests, the cyclic stress amplitude remains constant, simulating real-world loads such as seismic vibrations or vehicle-induced stress variations. In strain-controlled tests, the strain amplitude is regulated to examine soil deformation characteristics under cyclic conditions. Figure 3-8 shows the cyclic triaxial test setup and the part details of this apparatus respectively. Fundamental parameters measured in the cyclic triaxial test include shear modulus, damping ratio, pore water pressure buildup, and the number of loading cycles required to induce liquefaction. These measurements are essential in evaluating the soil's resilience and susceptibility to failure under repeated loading. The test is widely used in geotechnical earthquake engineering, pavement design, and offshore engineering, where understanding soil behavior under cyclic forces is necessary for designing stable foundations and infrastructure.

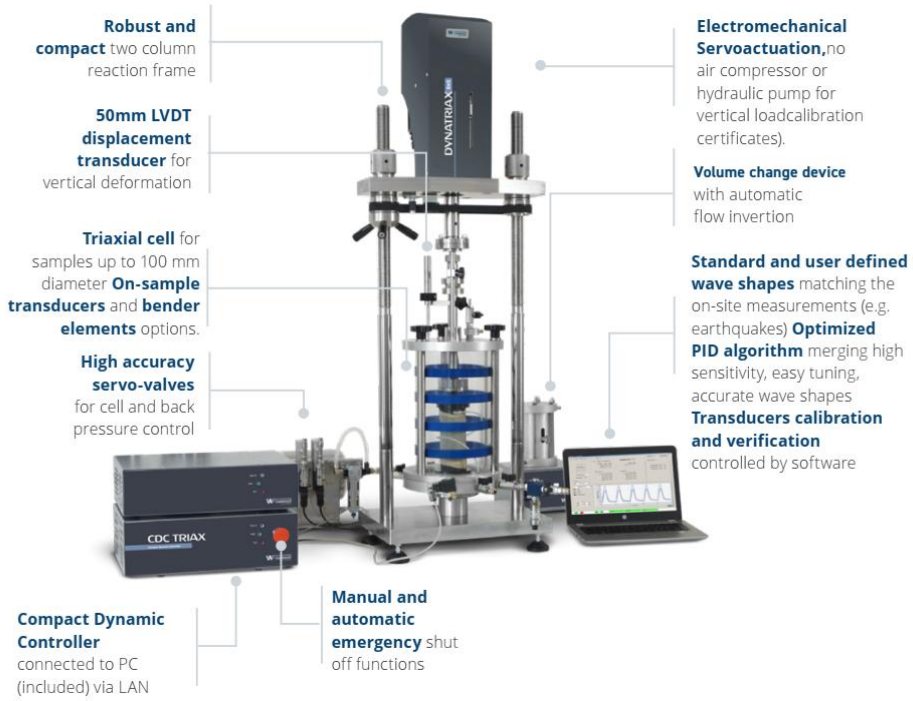


Figure 3-8 Parts of cyclic triaxial apparatus after Controls Group (2025).

3.2.3 Cyclic simple shear test

The cyclic simple shear apparatus is widely employed for the investigation of soil liquefaction. The configuration of this device is presented in Figure 3-9 after VJ Tech (2025). In this method, a short cylindrical specimen is laterally confined to prevent outward expansion. Cyclic horizontal shear stresses are then applied to either the top or bottom of the specimen, producing deformations that closely resemble those experienced by soil elements during the vertical propagation of shear waves. Advanced simple shear systems, which enable independent control of vertical and horizontal stresses, are capable of applying stress conditions beyond those corresponding to K_0 states, as reported in earlier studies by Airey & Wood (1987). The specimen during the consolidation stage of the cyclic simple shear test is illustrated in Figure 3-10a, while the shearing phase is shown in Figure 3-10b.

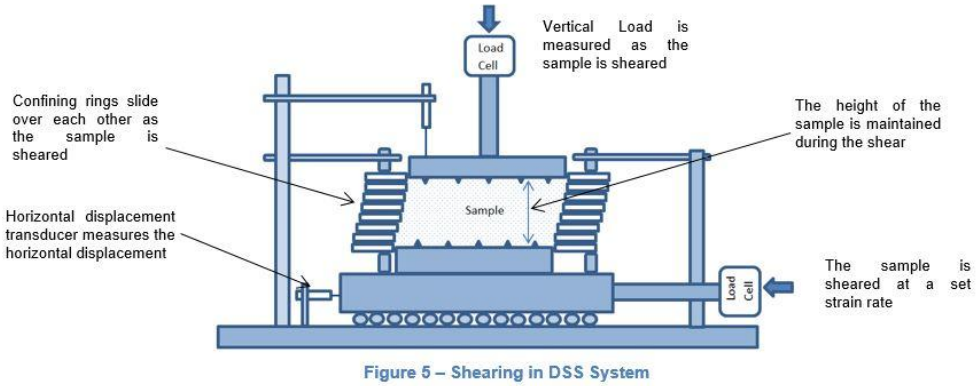


Figure 3-9 Schematic of cyclic simple shear apparatus after VJ Tech (2025).

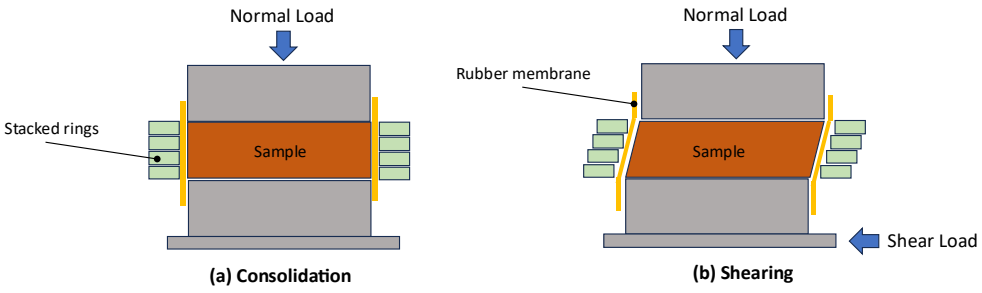


Figure 3-10 (a) Consolidation phase and (b) Shearing phase.

3.2.4 Resonant column test

The resonant column test is a widely recognized method for determining the dynamic shear modulus, the dynamic modulus of elasticity, and the damping ratio of soils. In this procedure, a specimen is mounted within a triaxial cell and subjected to either torsional or axial excitation at its upper end. The excitation is typically harmonic within a frequency range of 30 to 300 Hz, although alternative excitation forms such as random white noise as seen in Cascante & Santamarina (1997) or pulse signals as explained by Nakagawa et al. (1996) have also been employed. Equipment exists for both solid cylindrical and hollow cylindrical specimens, with the latter configuration reducing variations in shear strain amplitude across the sample during torsional excitation. An integrated accelerometer permits direct measurement of acceleration at the specimen's top, as illustrated in Figure 3-11.

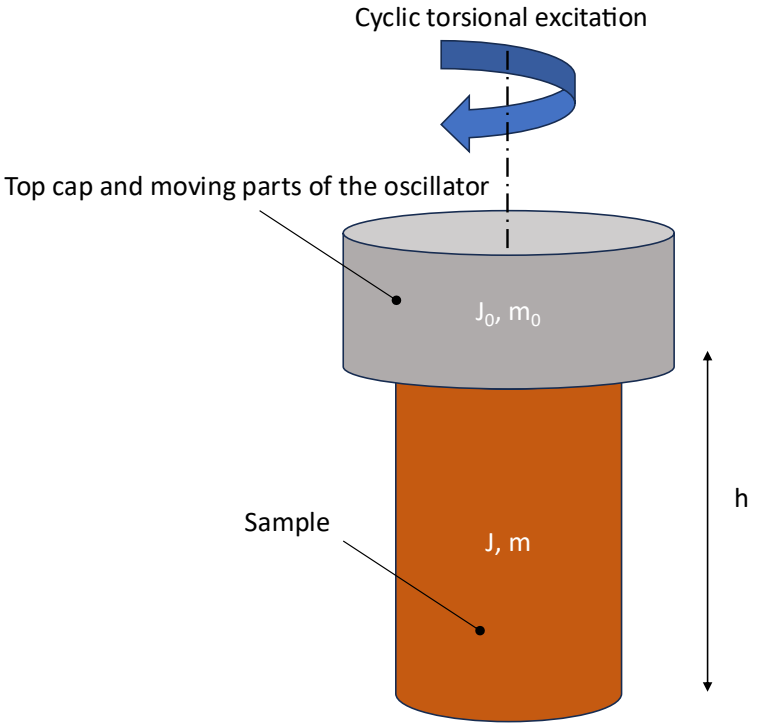


Figure 3-11 Schematic of resonant column test.

Once the resonant column specimen has been prepared and consolidated, cyclic loading is initiated. The excitation frequency begins at a low level and is gradually increased until the response of the specimen reaches a local maximum and the phase shift between the input signal and the measured acceleration signal attains a value of π. The lowest frequency at which a local maximum occurs in the response function is identified as the fundamental frequency of the specimen. This fundamental frequency is determined by the stiffness of the soil, the geometry of the specimen, and the properties of the testing apparatus. The analysis is based on the assumption of a single-degree-of-freedom system, as illustrated in Figure 3-11. The relevant formulas and for torsional and axial loading, taking into account the additional mass of the top cap and the moving parts of the driving unit, are given in Equations 3.1 and 3.2. They can be found for instance in Studer et al. (2008).

$$\frac{J}{J_0} = \frac{w_n\, h}{V_s} \tan \frac{w_n\, h}{V_s} \tag{3.1}$$

$$\frac{m}{m_0} = \frac{w_n\, h}{V_p} \tan \frac{w_n\, h}{V_p} \tag{3.2}$$

where
J , J_0 are the mass polar moments of inertia of respectively the sample and the top cap.
m, m_0 are the mass of respectively the sample and the top cap.
h is the sample height.
w_n is the circular frequency of the system at the resonance.

The initial shear modulus G_0 can be determined from the shear wave velocity V_s using Equation 2.36, while Young's modulus E can be obtained from the compressional wave velocity V_p through Equation 2.38. When the specimen is subjected to harmonic excitation, the response curve can be evaluated using either the half-power bandwidth method or the circle-fit method. Both techniques serve as system identification procedures for deriving the damping ratio, which may also be assessed through bender element measurements. Furthermore, if the dynamic loading applied to the specimen is precisely known through careful calibration of the testing apparatus, the amplification factor observed at resonance can provide an additional means of determining the damping ratio. The resonant column device employed in this study is of the Drnevich design as described in Mok et al. (1988), incorporating a Hardin oscillator to apply torque to the top of the specimen. This configuration does not allow for the application of dynamic axial loading. Nevertheless, both isotropic and anisotropic stress conditions can be applied within this system.

3.2.5 Free torsion pendulum test

The free torsion pendulum test, also known as the Zeevaert test, was first introduced by Zeevaert-Wiechers (2000) and subsequently applied to soil specimens obtained from sites in Waremmew and Sint-Katelijne-Waver in Belgium. A schematic representation of the apparatus used at the Soil Mechanics Laboratory of Ghent University is shown in Figure 3-12. This device has been widely employed in experimental studies for the evaluation of the dynamic properties of geomaterials, with several notable applications reported in the literature by Storrer et al. (1986), Van Impe (1977) and Karl (2005).

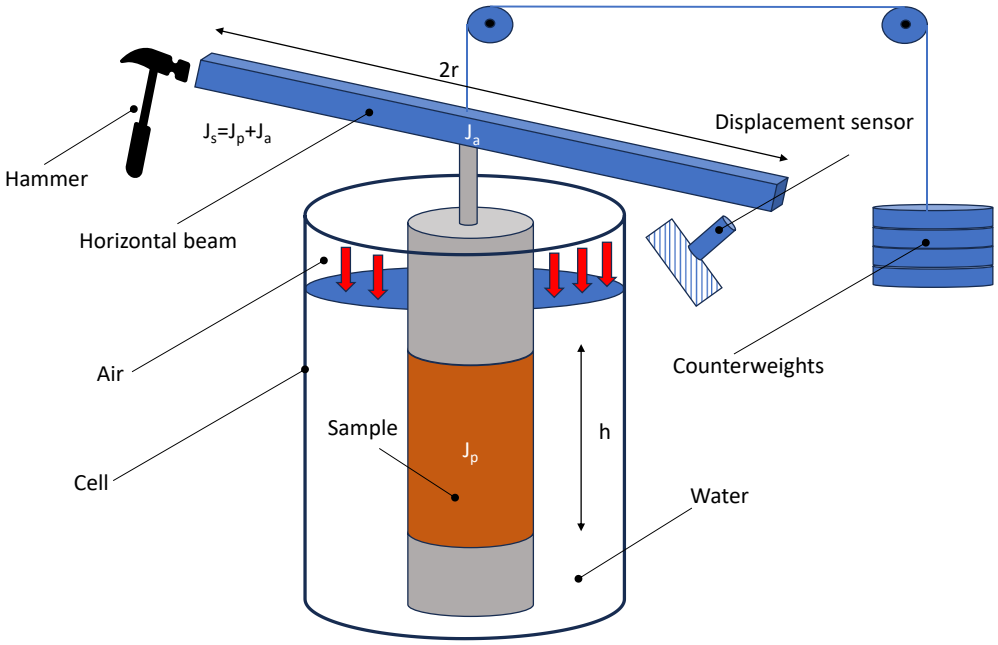


Figure 3-12 Schematic of the free torsion pendulum test after Karl (2005).

A cylindrical soil specimen with a diameter of 10 centimeters and a height of 20 centimeters is placed within the testing cell and enclosed in a rubber membrane under drained conditions, following the procedure of a conventional triaxial test. Inside the cell, the specimen is secured between an upper cap and a lower cap fitted with lamellas, and it is subjected to isotropic confining pressure. The soil is then allowed to fully consolidate under hydrostatic loading. The lamella caps ensure that no slippage occurs between the specimen and the caps. Once consolidation is complete, a torsional moment is applied to the specimen through the upper cap.

After consolidation, a horizontal beam is mounted directly along the axis of the soil specimen without slippage. To prevent initial distortion and to maintain balance, the beam is suspended with a thin steel wire so that no additional load is imparted on the specimen. For testing, the horizontal beam is struck with a hammer, producing an impulse that allows the system to vibrate freely. The resulting damped oscillations are measured using a non-contact displacement sensor, commonly referred to as a proximity transducer, positioned at one end of the beam. The amplitude of vibration is typically less than 2 millimeters. An example of a recorded time history is presented in Figure 3-13.

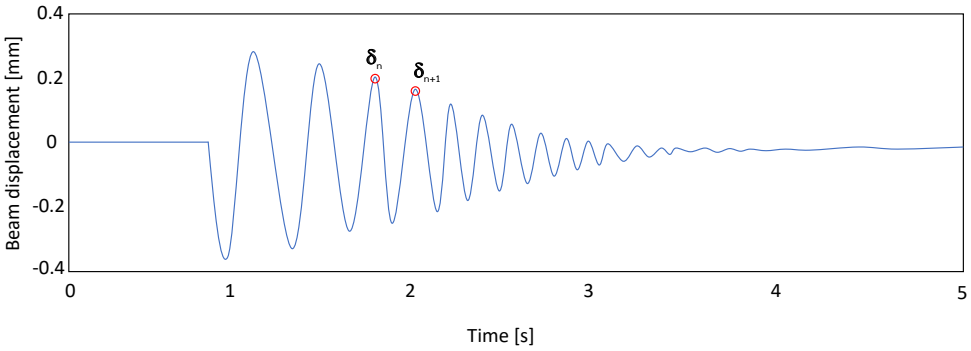


Figure 3-13 Displacement record of free torsion pendulum test.

Under the assumption of elastic deformation of the soil specimen during damped free oscillatory motion, the dynamic shear modulus G is determined using Equation 3.3, expressed as follows:

$$G = w_s^2 \cdot \frac{2h \cdot J_s}{\pi a^4} \tag{3.3}$$

In this formulation, w_s represents the undamped circular frequency of the system, which includes both the soil specimen and the testing apparatus. The parameter h denotes the specimen height, a is the specimen radius, and J_s is the polar moment of inertia consisting of two parts: J_a, corresponding to all oscillating components of the apparatus, and J_p, corresponding to the soil specimen. Karl (2005) reported a value of J_a equal to 3.26158 kg·m² for the apparatus at Ghent University. The undamped natural circular frequency w_s can be derived from the damped frequency w_D, which is obtained from the measured vibration period together with the critical damping ratio ξ, as expressed in Equation 3.4.

$$w_s = \frac{w_D}{\sqrt{1-\xi^2}} \tag{3.4}$$

ξ is calculated by Equation 3.5 as follows:

$$\xi = \frac{1}{2\pi} log \frac{\delta_n}{\delta_{n+1}} \tag{3.5}$$

Where δ_n and δ_{n+1} are amplitudes of the oscillation.

The parameter ξ of the viscous system must be correlated with the damping ratio D of the hysteretic system. The value of D is determined using Equation 3.6, given as follows:

$$D = \frac{\eta}{2} = \xi \qquad \text{for} \qquad \beta=1 \tag{3.6}$$

The magnitude of shear strain is estimated using Equation 3.7, expressed as follows:

$$\gamma = \frac{2}{3} \frac{\overline{\delta_{n,n+1}} \cdot a}{r \cdot h} \tag{3.7}$$

In this context, $\overline{\delta_{n,n+1}}$ denotes the average oscillation amplitude obtained from two successive amplitudes, δ_n and δ_{n+1}, which are used in the calculation of the damping ratio. The variable r represents the distance between the measurement point on the beam and the axis of rotation. The factor of two-thirds indicates that the strain is evaluated along a cylindrical surface corresponding to two-thirds of the specimen radius.

3.2.6 Stress path triaxial test



Figure 3-14 Stress path triaxial test at the KMUTNB campus.

For over five decades, a specialized apparatus known as the stress path cell has been developed and was first thoroughly described by Bishop & Wesley (1975). Figure 3-14 depicts the stress path triaxial test at the KMUTNB campus.

One of the key advantages of this stress path cell is its ability to decouple vertical and radial stress changes. This unique feature enables researchers to conduct anisotropic triaxial tests under both K_0 and K conditions, as well as to apply various stress paths in either stress-controlled or strain-controlled modes as seen in Figure 3-15. Piriyakul & Haegeman (2005) described K_0 and K conditions flowcharts as shown in Figures 3-16a and 3-16b respectively.

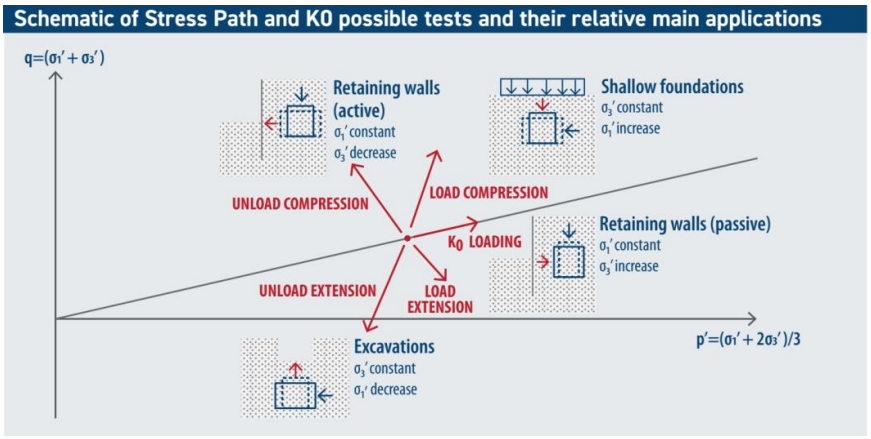
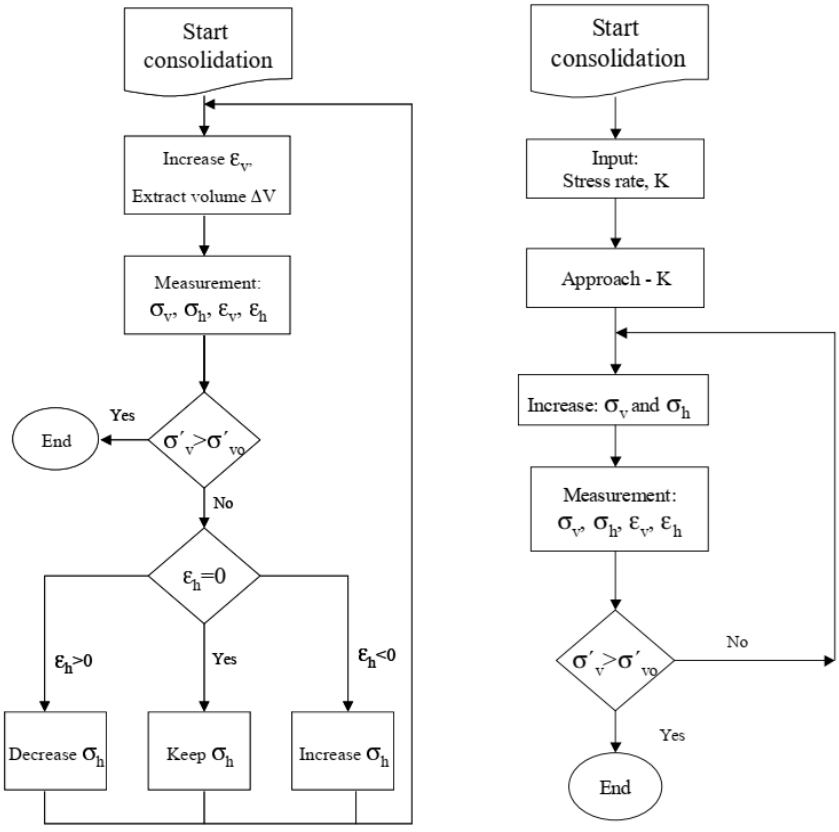


Figure 3-15 K_0 consolidation and shearing in stress path triaxial test after Controls Group (2025).



a) b)

Figure 3-16 a) K_0- and b) K-consolidation flow charts after Piriyakul & Haegeman (2005).



Figure 3-17 Part of the **s**tress path triaxial test after Controls Group (2025).

As illustrated in Figure 3-17, the upper portion of the cell resembles a conventional triaxial system. However, instead of applying the vertical load from the top, the load in compression tests is delivered by raising the sample pedestal from below, thereby pushing the top cap against a fixed rod. The pedestal is integrated into the top of a loading ram, which features a piston at its bottom end and is connected to a pressure chamber. To ensure fluid containment, Bellofram rolling seals are employed, while a linear motion bearing guides the vertical movement of the ram. The axial load exerted on the specimen is generated by increasing the pressure in the bottom chamber. A built-in internal load cell directly measures the axial force acting on the sample. The ram is equipped with a cross-arm that moves within wide vertical slots in a spacer, which links the bearing housing to the lower pressure chamber.

This cross-arm interacts with an LVDT (Linear Variable Differential Transformer) mounted on the cell's base, thereby measuring the vertical displacement of the ram. The Load Frame TRITECH load frame is used to perform high quality tests at high level of productivity on samples with diameters from 38 up to 150 mm. Soil testing laboratories can conduct triaxial UU, CU, CD and stress path (compression/extension) tests. Maximum compression capacity is 50 kN and shearing speed range from 0.00001 to 99.99999 mm/min. Hall effect on-sample transducers are used for measuring local deformation on soil samples in triaxial test as seen in Figure 3-18. The measured displacement is used to calculate the axial strain in the specimen. This design greatly facilitates specimen setup. The apparatus is self-contained, does not require an external loading frame, and is portable. It is equally suitable for conducting both axial compression and extension tests using a broad range of stress paths, under either stress-controlled or strain-controlled conditions.



Figure 3-18 Hall effect on sample transducers after Controls Group (2025).

3.3 Field-Based Methods of Shear Wave Measurement and Testing

3.3.1 Cross-, Up- and Down-hole Testing

The seismic cross-hole test is designed to measure P-wave and S-wave velocities between boreholes. A minimum of two boreholes is required—one to house the seismic source and the other (S) to contain the receiver (R). The seismic source can be either mechanical or explosive in nature. When the primary objective is to determine S-wave velocity, a mechanical source is generally preferred. This is because it allows for the generation of shear wave impulses with reversible polarity, which enhances the reliability and accuracy of S-wave detection. In a cross-hole test, a receiver is installed in a second borehole at the same depth as the seismic source located in the first borehole. The test is initiated by triggering the source, and the arrival times of the S-wave and P-wave are determined through visual interpretation of the signals recorded at the receiver. By repeating the test at different depths, a subsurface velocity profile can be developed. The overall test configuration is illustrated in Figure 3.19a. Due to the potential inaccuracies in trigger time measurements, it is often advantageous to use more than two boreholes, thereby enabling multiple receiver points. In such cases, wave velocities are calculated based on the differences in arrival times at the various receivers. This approach not only improves measurement accuracy but also allows for the application of cross-correlation techniques, which offer greater precision compared to simple visual interpretation. Typical spacing between boreholes ranges from 5 to 12 meters in layered soils and may extend up to 30 meters in nearly homogeneous ground conditions. Additionally, Mok et al. (1988) demonstrated the use of the attenuation coefficient method in cross-hole testing to determine the damping ratio of soils, providing further insight into their dynamic behavior.

In a down-hole test, the seismic source is positioned at the ground surface near a borehole, while the receiver is installed at a specified depth within the borehole. The generated seismic waves travel nearly vertically from the source (S) to the receiver (R). In contrast, the up-hole test involves placing the source within the borehole and recording the seismic waves at the surface. The configuration of both test setups is illustrated in Figures 3-19b and 3-19c. Among the two, the down-hole test is more widely employed due to the relative ease of positioning and adjusting the seismic source at the surface compared to within a borehole environment. The interpretation of wave arrival times in both tests follows a similar approach to that used in cross-hole testing. It typically involves visual analysis, though cross-correlation techniques may also be utilized when multiple receivers are positioned at varying distances from the seismic source.

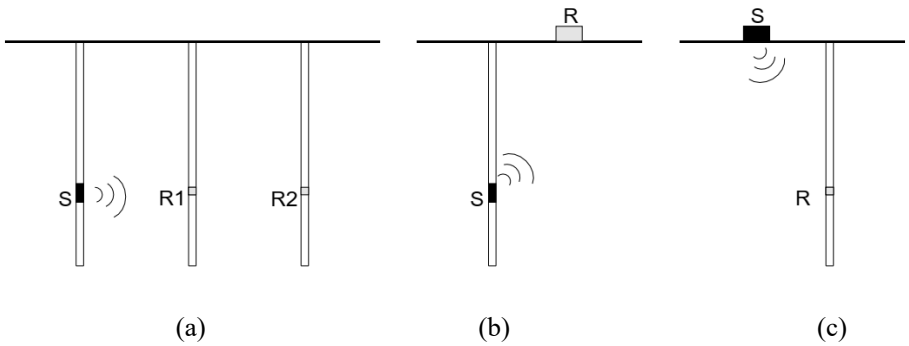


Figure 3-19 (a) Seismic cross-hole test, (b) seismic up-hole test and (c) seismic downhole test after Mok et al. (1988).

3.3.2 Seismic Refraction Methods

The seismic refraction test involves measuring the travel times of P-waves or S-waves generated by an impulse source to a linear array of surface-mounted receivers positioned at varying distances from the source. Compared to seismic reflection testing, the spacing between receivers in refraction surveys is significantly larger. Importantly, the seismic refraction method focuses solely on the arrival time of the first detected wave component, regardless of the specific travel path. As a result, complications arising from distinguishing between overlapping wave components are effectively avoided. The typical ray paths utilized in seismic refraction are illustrated in Figure 3-20.

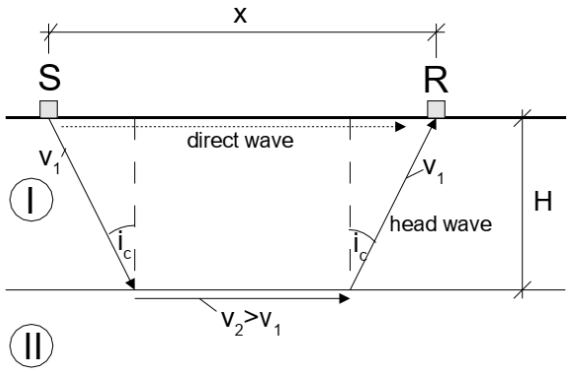


Figure 3-20 Ray paths for the seismic refraction test after Kramer (1996).

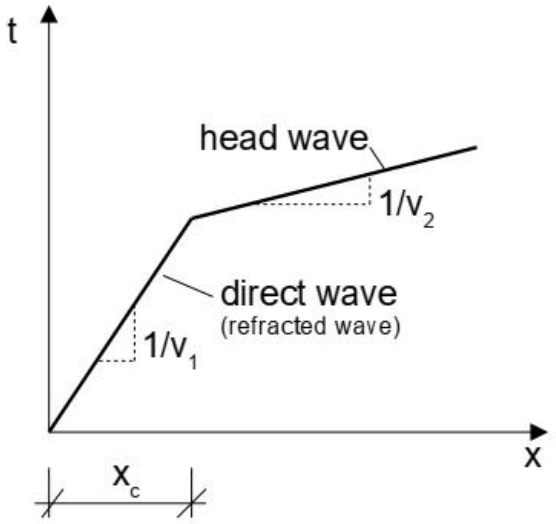


Figure 3-21 Time arrival diagram as result of a seismic refraction test after Kramer (1996).

Assuming the subsurface consists of a two-layered elastic half-space, part of the wave energy propagates directly from the source to the receivers. This direct arrival is used to compute the wave velocity in the upper (superficial) layer. Simultaneously, other wavefronts travel downward, encountering the boundary between Layer 1 and Layer 2, where they are subject to reflection and refraction. The path and behavior of the refracted waves are governed by Snell's Law, as expressed in Equation 3.8.

$$\frac{Sin\ i_1}{v_1} = \frac{Sin\ i_2}{v_2} \tag{3.8}$$

At the critical angle of incidence i_c—the angle just before total reflection—a portion of the wave energy becomes refracted and propagates horizontally along the boundary within Layer 2. This horizontal wave, known as the head wave, continuously radiates energy back into Layer 1. As it re-enters Layer 1, it refracts once more and travels upward to the surface. Notably, the refraction angle in Layer 1 equals the critical incidence angle, i_c.

Because the wave velocity in Layer 2 (v_2) is higher than that in Layer 1 (v_1), the head wave will eventually overtake the direct wave from a certain critical distance x_c onwards. Beyond this distance, the head wave arrives earlier than the direct wave despite the longer travel path. The velocity v_2 can be determined based on v_1 and the arrival times of the head wave at a minimum of two receiver distances from the source. Alternatively, it can be derived graphically from the slope of the travel-time curve, as depicted in Figure 3-21. Once both v_1 and v_2 are known, the geometry of the refracted wave path becomes fully defined, allowing for the calculation of the thickness H of the upper (superficial) layer.

3.3.3 Seismic Reflection Methods

The seismic reflection test is used to measure wave propagation velocities and to determine the thickness of superficial (near-surface) geological layers. This method operates on principles similar to echo-sounding and radar technology. During the test, an impulsive disturbance is generated at a source point (*S*), and the arrival time of the resulting wave is recorded at a receiver point (*R*), positioned at a known distance from the source (see Figure 3-22). Depending on the type of source used, the method can analyze both primary (P-waves) and secondary (S-waves). However, generating high-energy S-waves is often challenging, and as a result, distinguishing S-waves from the initial arrival of P-waves may not always be possible. The generated wave energy follows multiple paths: one part travels directly from the source to the receiver, while another portion propagates downward and reflects off the boundary of a deeper, underlying layer. The velocity of the superficial layer can be calculated based on the arrival time of the direct wave.

Since the angle of incidence equals the angle of reflection at the layer boundary, and the wave velocity of the upper layer is known, the thickness of the superficial layer can be computed. When multiple receivers are deployed, it becomes theoretically possible to estimate the inclination or dip of the layer boundary. In practice, however, achieving this is often unreliable.

Reflections from deeper interfaces can also be used to assess the properties of underlying layers. However, the method is only effective when the arrival times of direct and reflected waves are clearly distinguishable. This makes the technique especially suitable for investigating deeper layers, while its reliability decreases for shallower depths. Moreover, if reflections from multiple interfaces are to be interpreted, their arrival times must be sufficiently separated to allow for accurate identification. For further details on the seismic reflection test is clearly described by Kramer (1996).

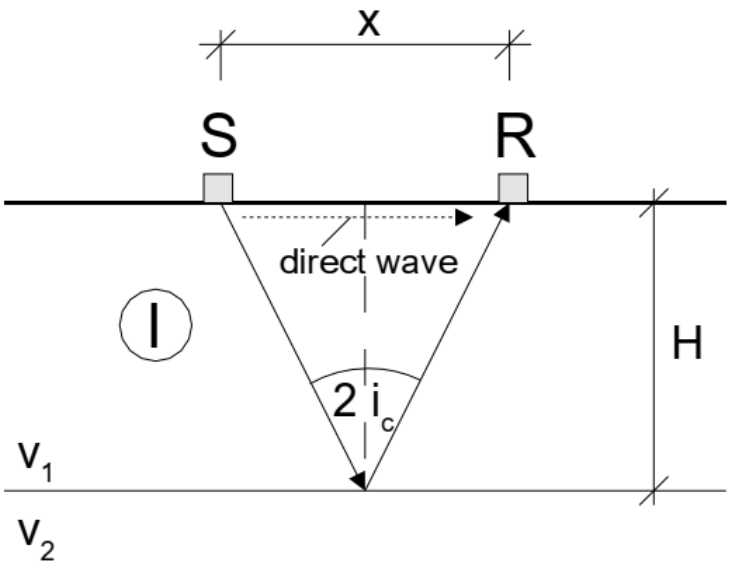


Figure 3-22 Ray paths for the seismic reflection test after Kramer (1996).

3.3.4 Spectral Analysis of Surface Waves (SASW)

The Spectral Analysis of Surface Waves (SASW) technique utilizes the propagation characteristics of Rayleigh waves to assess the stratification of subsurface materials. Rayleigh waves, which are a type of surface wave, travel near the soil-air interface and are particularly sensitive to the properties of the materials they pass through. A key feature of Rayleigh waves is that their penetration depth into the ground is approximately equal to their wavelength. As a result, the apparent wave velocity varies with wavelength (or frequency), since different wavelengths sample different depths. This variation of wave velocity with frequency is known as dispersion, a fundamental principle leveraged in the SASW method. Rayleigh waves are typically generated using impulsive sources such as a drop weight or hammer. In cases where a harmonic source is employed instead, the method is referred to as the Continuous Surface Wave (CSW) technique. Wave arrivals are recorded at a minimum of two receiver locations placed at varying distances from the source, using geophones or accelerometers. The basic measurement setup is illustrated in Figure 3-23.

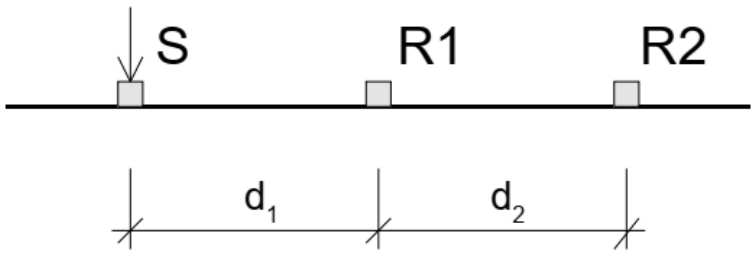


Figure 3-23 Typical configuration of source and receivers in a SASW test after Kramer (1996).

The determination of subsurface layer thicknesses and shear wave velocities is achieved through an iterative inversion process that matches a theoretical dispersion curve to the experimentally derived dispersion curve. The theoretical model is based on a system of uniform elastic layers with infinite horizontal extent, which is used to simulate the expected dispersion behavior. Initial estimates for both layer thicknesses and shear wave velocities are provided as input parameters. These estimates are then systematically refined through the inversion algorithm until an optimal match between the theoretical and measured dispersion curves is obtained, indicating the most accurate representation of the subsurface profile.

3.3.5 Cone Penetration Testing with Shear Wave Velocity (SCPT)

The Seismic Cone Penetration Test (SCPT) is a specialized variation of the down-hole test, in which the receivers—typically geophones or accelerometers—are integrated directly into the tip of a cone. This cone is advanced into the ground using standard cone penetration testing (CPT) equipment, such as a CPT truck (as shown in Figure 3-24). Because the SCPT does not require the drilling of a borehole, it offers a cost-effective alternative to traditional down-hole testing while still providing valuable seismic velocity data.

In an SCPT setup, P-wave and S-wave sources are positioned at the ground surface near the cone's penetration point. These sources typically consist of steel beams or plates, which are struck with a hammer—horizontally to generate S-waves and vertically to generate P-waves. The instrumented cone, equipped with receivers, is advanced into the ground in incremental steps, typically at intervals of 0.5 to 1.0 meters. At each depth increment, the source generates a seismic pulse, which is recorded by the cone's receivers.

The arrival times of P- and S-waves can be determined through visual inspection of the recorded signals. In cases where the cone is equipped with two receivers spaced apart within the same probe (known as a dual-cone configuration), the travel time between the two sensors can be calculated using cross-correlation techniques. This travel time enables a direct calculation of the wave velocity, assuming a direct wave path from the surface source to the cone.

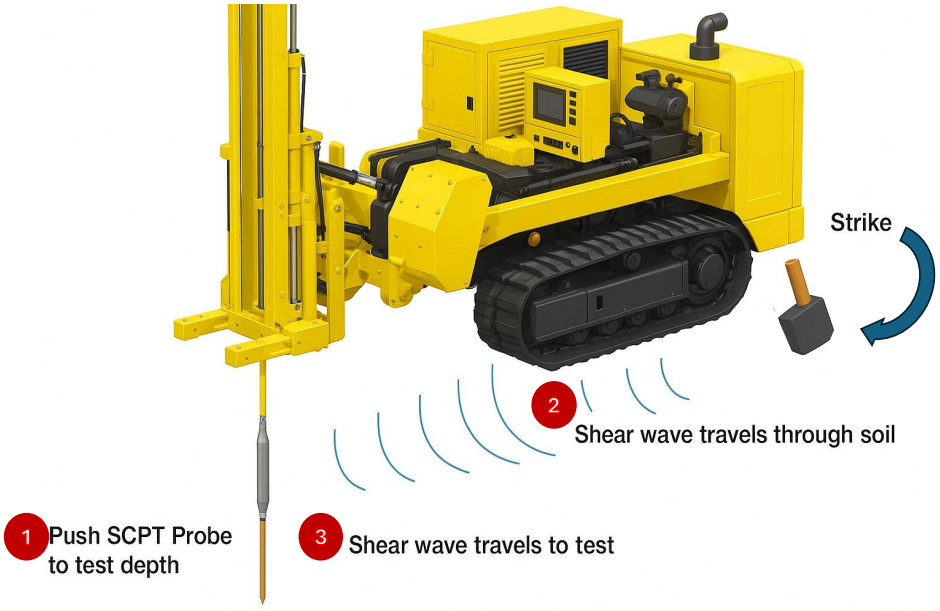


Figure 3-24 SCPT test.

3.4 Limitations and Challenges in Shear Wave Measurement and Testing

This section addresses the limitations associated with the application of shear wave velocity in geotechnical engineering. Three primary areas of concern are highlighted: (1) the influence of site-specific characteristics on shear wave testing techniques, (2) the technical constraints of the measurement equipment, and (3) the interpretational ambiguities involved in analyzing shear wave data.

While shear wave testing techniques—such as Downhole and Crosshole Seismic Tests and Surface Wave Methods—are valuable for characterizing subsurface stiffness, their accuracy and reliability under field conditions are often compromised by environmental and site-specific factors. These limitations affect both the quality of recorded data and the interpretation of key parameters such as shear wave velocity (V_s) and shear modulus (G_0). One major challenge is soil heterogeneity, which refers to the spatial variability in composition, stratification, density, grain size distribution, and moisture content. Such variability is typical in natural deposits due to complex depositional histories or anthropogenic influences like fill placement and compaction. Additionally, environmental conditions—including rainfall, runoff, temperature fluctuations, humidity, and wind—can significantly alter the physical state of the soil and the sensitivity of testing equipment. Furthermore, ambient noise and site vibrations may interfere with signal clarity, particularly in urban or industrial settings. Collectively, these environmental factors introduce uncertainty into shear wave measurements, which can compromise the accuracy of geotechnical models, especially in applications requiring high-resolution or real-time data. To mitigate these challenges, engineers and researchers must adopt robust data interpretation methods, implement redundant measurement protocols, and apply correction techniques to enhance the reliability of field results.

Accurate shear wave measurement is essential for assessing subsurface stiffness and the mechanical behavior of geomaterials. However, the quality and reliability of these measurements are heavily influenced by the performance and appropriateness of the equipment used. Factors such as instrument design, resolution, sensitivity, and adaptability to varying soil conditions must be carefully considered during both testing and interpretation. Limitations in these areas—such as low signal resolution, insufficient sensitivity, or unsuitable method selection—can introduce significant uncertainty into geotechnical analyses. To address these challenges, engineers and researchers must select testing methods and equipment that align with site-specific conditions and project requirements. Furthermore, strategies such as signal enhancement, routine calibration, and the integration of multiple measurement techniques are critical to improving data accuracy and ensuring the reliability of shear wave evaluations.

One of the most critical challenges in shear wave testing lies not in data acquisition, but in the accurate interpretation of that data. Even when high-quality signals are obtained under controlled conditions using reliable equipment, identifying the precise arrival time of the shear wave and converting it into meaningful soil parameters can be complex and subjective. These interpretation ambiguities—stemming from both the physical complexities of wave behavior and human judgment in waveform analysis—can introduce significant uncertainty and, if not properly addressed, lead to erroneous conclusions. In fact, such ambiguities often contribute more to measurement error than the testing process itself. To enhance interpretive accuracy, engineers and researchers should employ advanced signal processing techniques, adhere to standardized procedures, and validate results

through complementary testing methods. Recognizing and managing these limitations is essential for making confident, informed decisions in geotechnical engineering based on shear wave data.

3.5 Application of Shear Wave in Civil Engineering

3.5.1 Using of Shear Wave Velocity for Foundation Design

Poulos (2022) utilized in-situ shear wave velocity measurements as the basis for conducting preliminary design calculations and design verification for shallow and deep foundations. For clay soils, the correlations of Agaiby and Mayne (2015) and L'Heureux and Long (2017) appear to be reasonably consistent and provide intuitively reasonable values of S_u as shown in Figure 3-25.

Agaiby and Mayne (2015):

$$S_u = 0.152 \cdot V_s^{1.142} \tag{3.9}$$

L'Heureux and Long (2017):

$$S_u = 0.02 \cdot V_s^{1.45} \tag{3.10}$$

where V_s is in m/s and S_u is in kPa.

The settlement, S, can be calculated:

$$S = \sum\{(d\sigma_{zi} - 2\nu \cdot (d\sigma_{ri}) \times h_i)\}/\{E_{oi} \cdot (E/E_o)\} \tag{3.11}$$

Where $d\sigma_{zi}$, $d\sigma_{ri}$ = vertical and radial stress increments within a sublayer at average depth zi below the surface, h_i = thickness of sublayer, E_{oi} = small strain Young's modulus. E/E_o = the ratio of modulus to small-strain modulus as shown in Figure 3-26.

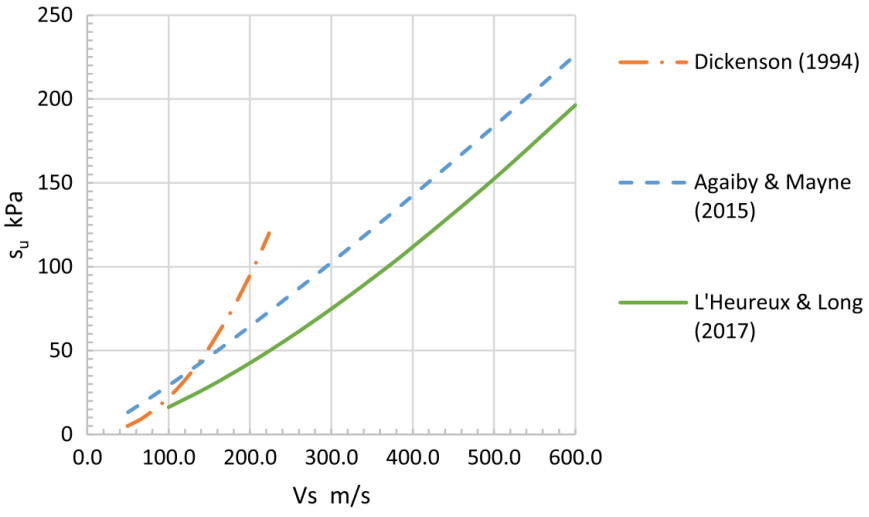


Figure 3-25 Correlations of S_u versus V_s after Poulos (2022).

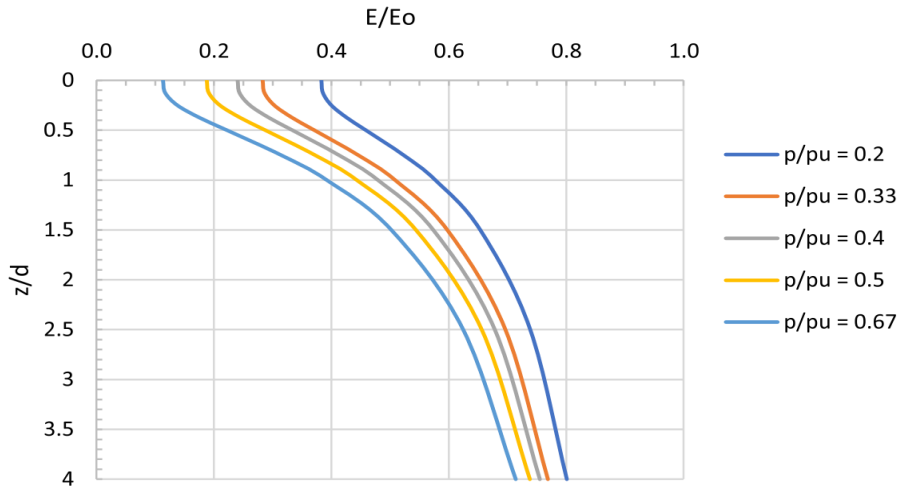


Figure 3-26 Young modulus reduction factors for a shallow circular footing after Poulos (2022).

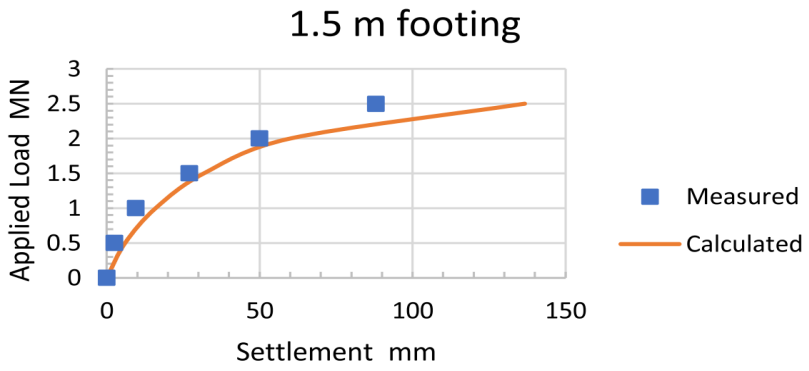


Figure 3-27 Measured and calculated load-settlement curves for 1.5 m diameter footing after Poulos (2022).

Figure 3-27 illustrates the consistency of load-settlement curves for a 1.5 m diameter footing. Although the calculated curves tend to overpredict settlement, the adopted approach provides an acceptably conservative design method for shallow footings on sand. Figures 3-28 to 3-29 show the ultimate shaft friction versus V_s for fine-grained and coarse-grained soils respectively. Figures 3-30 to 3-31 depicted the ultimate end bearing versus V_s for fine-grained and coarse-grained soils respectively.

For fine-grained soils:

$$\boldsymbol{N_e = \left(\frac{V_s}{100}\right)^{\frac{1}{0.33}}} \tag{3.12}$$

Where N_e = the equivalent SPT value.

For coarse-grained soils:

$$N_e = \left(\frac{V_s}{56}\right)^{\frac{1}{0.5}} \tag{3.13}$$

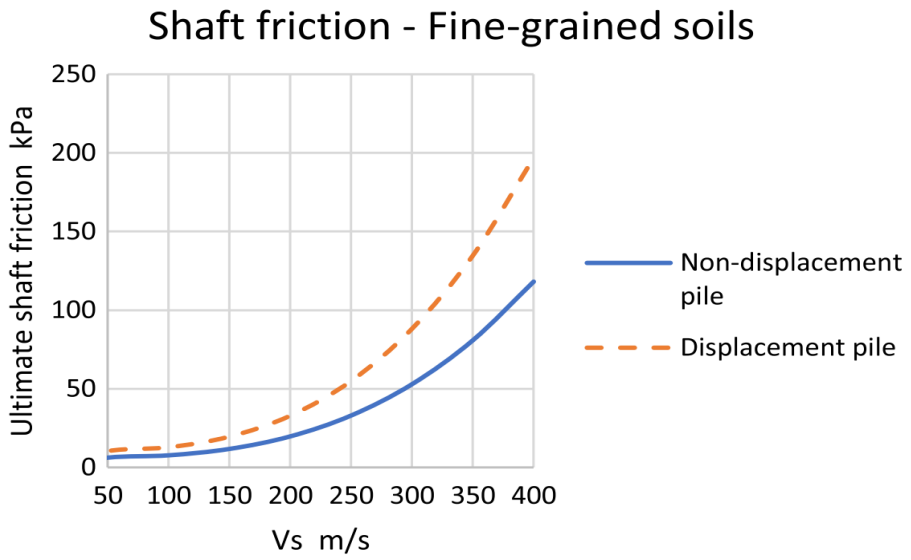


Figure 3-28 Ultimate shaft friction versus V_s for fine-grained soils after Poulos (2022).

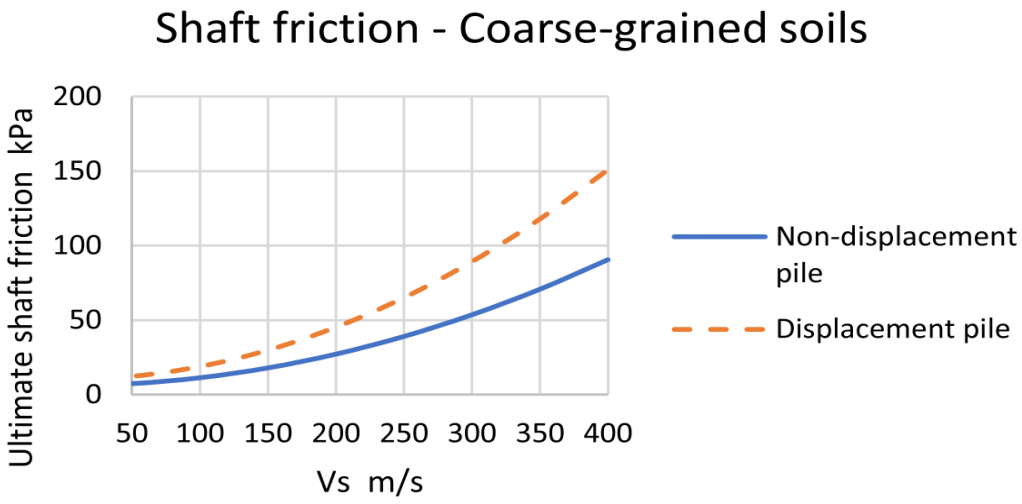


Figure 3-29 Ultimate shaft friction versus V_s for coarse-grained soils after Poulos (2022).

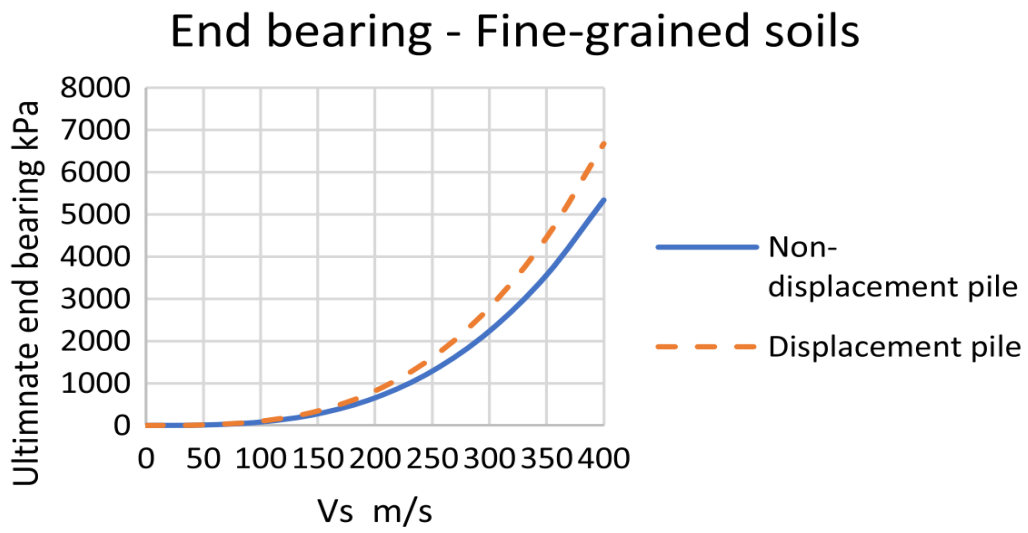


Figure 3-30 Ultimate end bearing versus V_s for fine-grained soils after Poulos (2022).

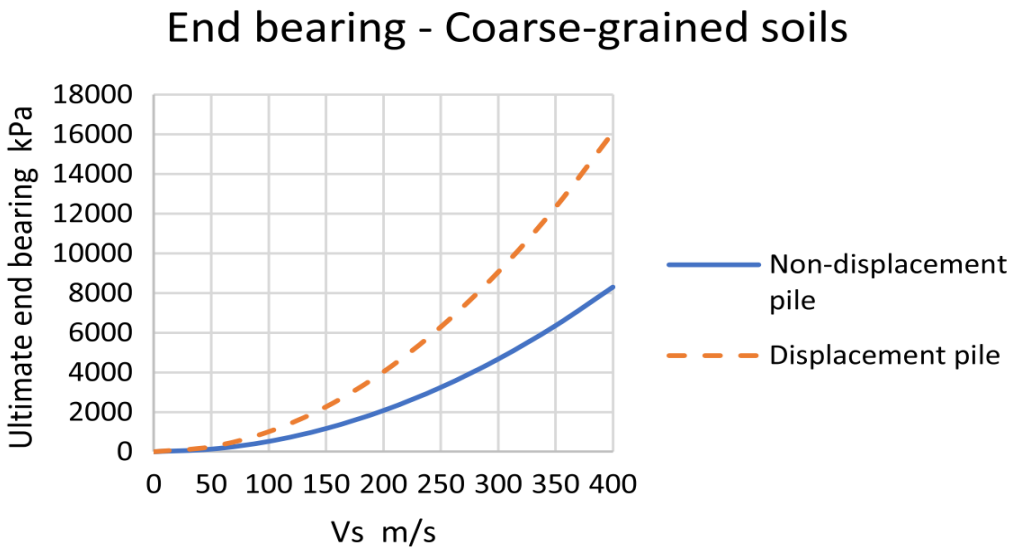


Figure 3-31 Ultimate end bearing versus V_s for coarse-grained soils after Poulos (2022).

3.5.2 Using of Shear Wave Velocity for the soil-structure interaction modelling on a tall building

Cruz et al. (2024) investigated the effects of soil-structure interaction (SSI) on the seismic response of a 50-story skyscraper with a basement and pile foundation system, as a function of soil shear wave velocity (V_s) ranging from 50 to 800 m/s. The tall building model is the Tongde Plaza Yue Center (TPYC) in Kunming, China as illustrated in Figure 3-27. A detailed three-dimensional finite element model of the structure and surrounding soil is shown in Figure 3-28 and excited by vertically incident plane SV-, SH-, and P-waves. Both translational and rotational components of the structural response — three in each direction — were examined. The analysis, conducted within the linear domain, evaluated SSI effects on apparent dynamic properties (natural frequencies and damping ratios), floor translations and rotations, effective input base motions, interstory drifts, and floor and base reaction forces and moments. The study concluded that SSI effects in tall buildings of this nature are non-negligible, and that neglecting them yields non-conservative estimates of structural response. The soil at the TPYC site consists predominantly of lacustrine sedimentary deposits, exhibiting a uniform distribution of material properties to a depth of at least 100 m, with an average shear wave velocity of approximately V_s = 220 m/s. The site is classified as stiff soil and it is modeled herein as a homogeneous viscoelastic half-space with V_s = 50, 100, 200, 400, and 800 m/s and a Poisson's ratio of ν = 0.4. Fourier spectra of acceleration recorded during 3 earthquakes the Yangbi, Dali earthquake, the Shuangbai, Chuxiong earthquake and the Kanding, Garze, Sichuan earthquake as seen in Figures 3-29 to 3-31.

It was noted that when the primary concern is the accurate specification of input ground motion for the fixed-base model and an error tolerance of 5% is adopted, the soil must possess a shear wave velocity of $V_s \geq 800$ m/s to yield acceptable estimates of linear structural response. When the quantities of interest are the dynamic properties of the structure, and the acceptable error tolerance approximates the variability of modal frequencies attributable to weather-related effects, the fixed-base model provides sufficiently accurate predictions of structural response for Vs ≥ 800 m/s, with an associated error of less than approximately 2%.

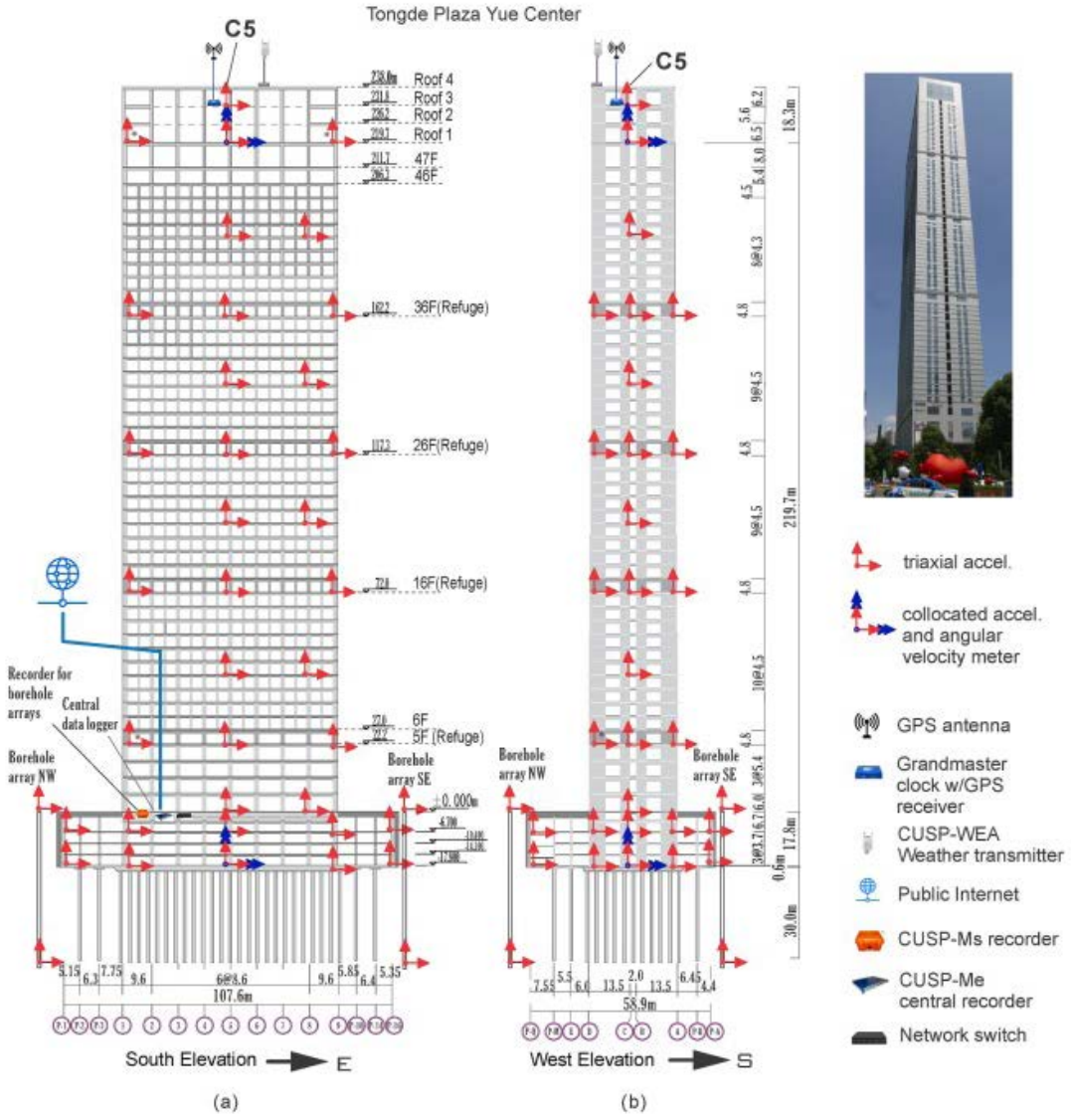


Figure 3-27 Vertical elevation a) South elevation and b) West elevation after Cruz et al. (2024).

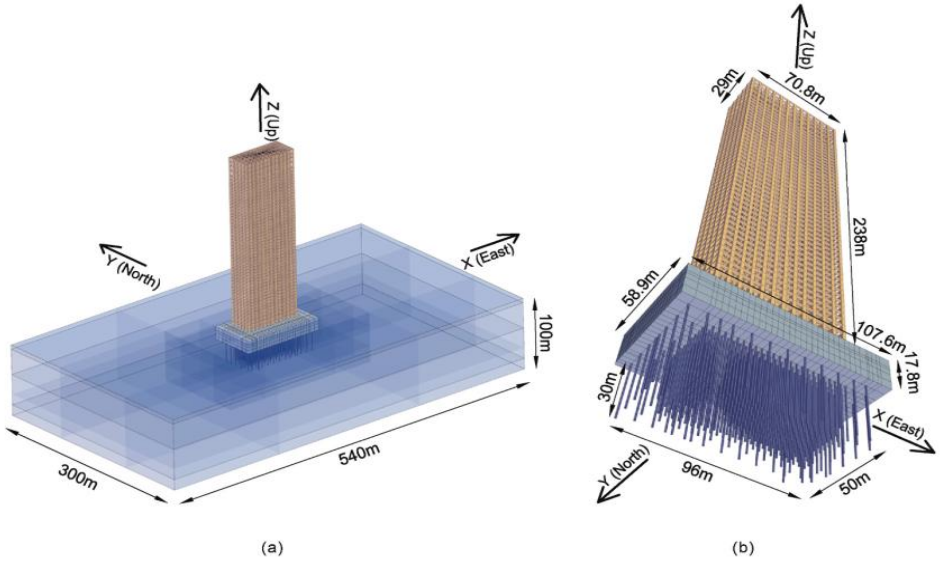


Figure 3-28 FEM model a) a complete model and b) foundation after Cruz et al. (2024).

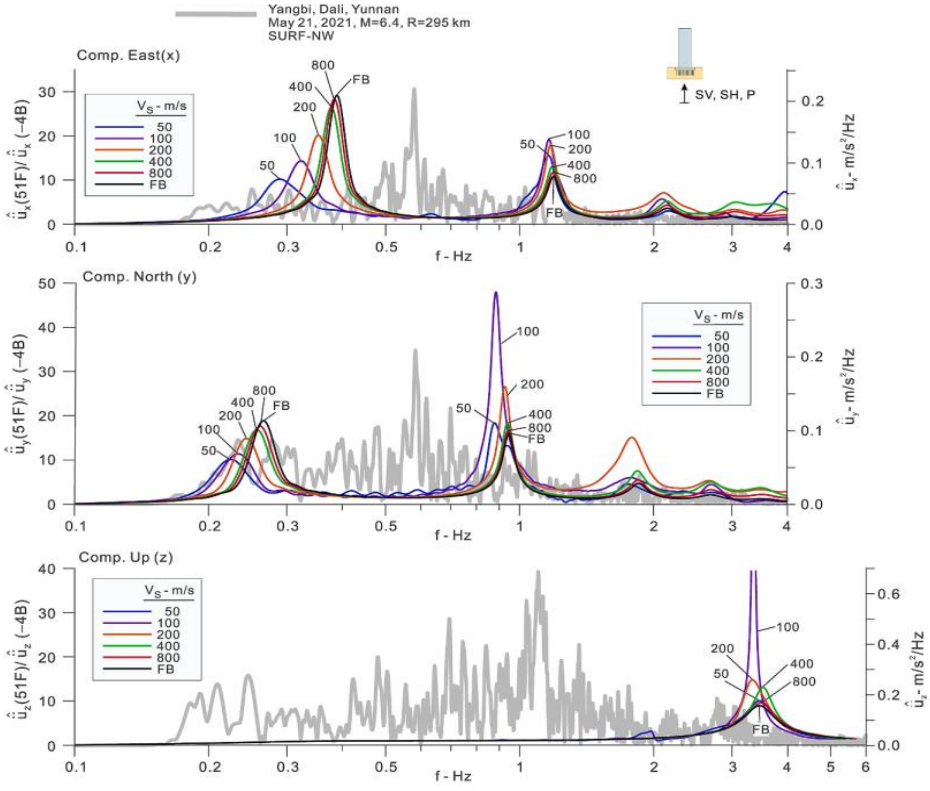


Figure 3-29 Transfer functions between the acceleration responses during Yangbi, Dali earthquake after Cruz et al. (2024).

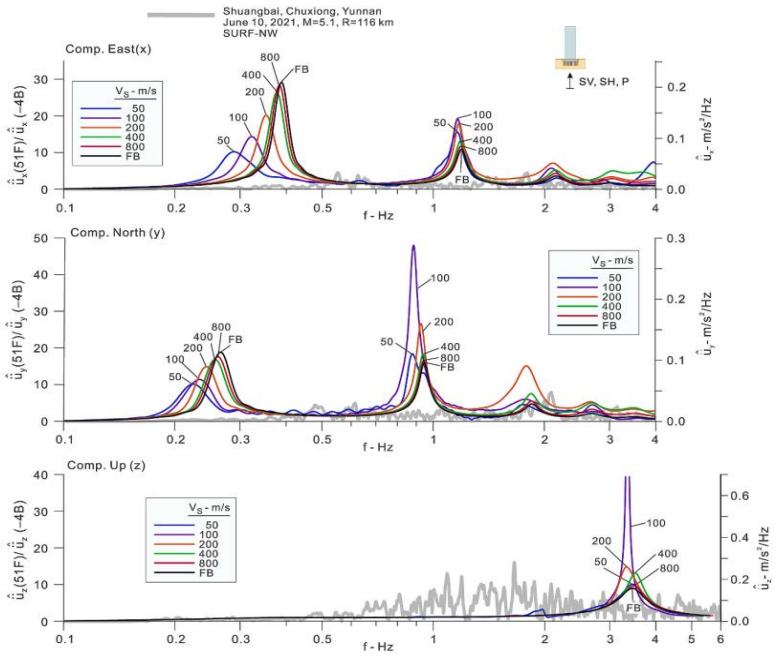


Figure 3-30 Transfer functions between the acceleration responses during Shuangbai, Chuxiong earthquake after Cruz et al. (2024).

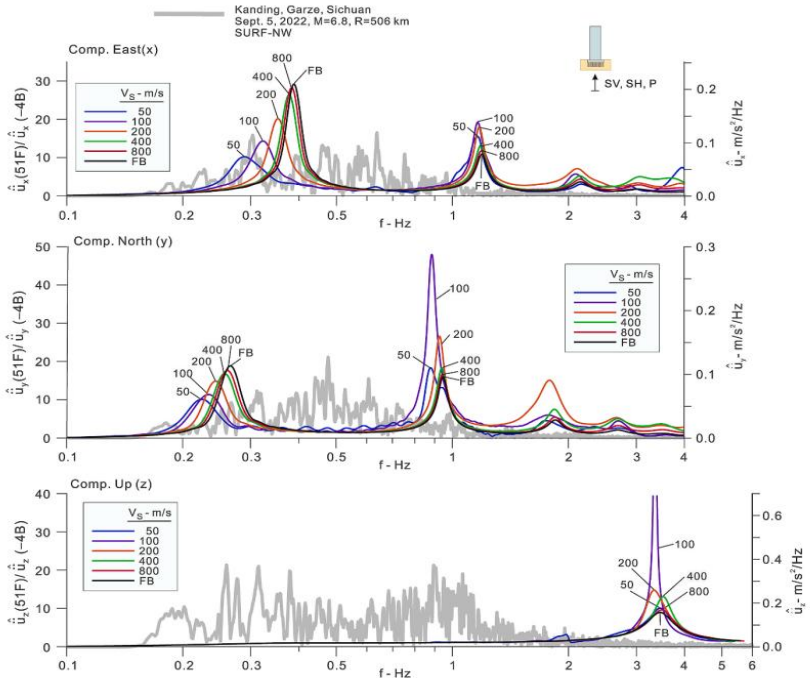


Figure 3-31 Transfer functions between the acceleration responses during Kanding, Garze, Sichuan earthquake after Cruz et al. (2024).

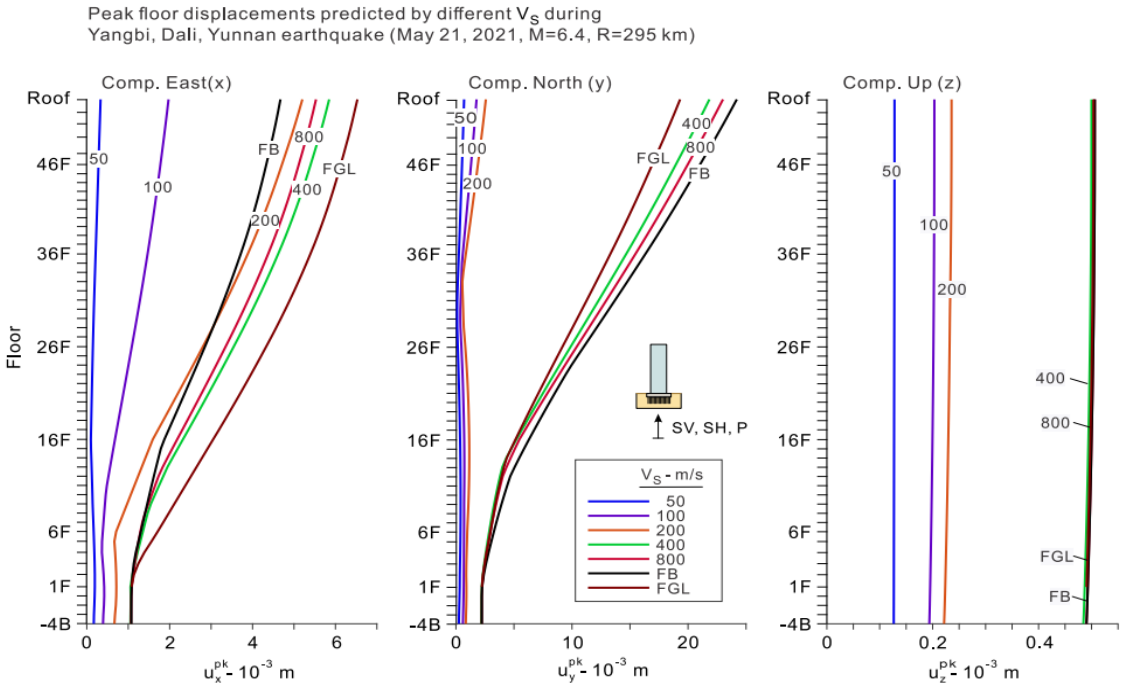


Figure 3-32 Peak floor displacements for different values of V_S during Yangbi, Dali earthquke after Cruz et al. (2024).

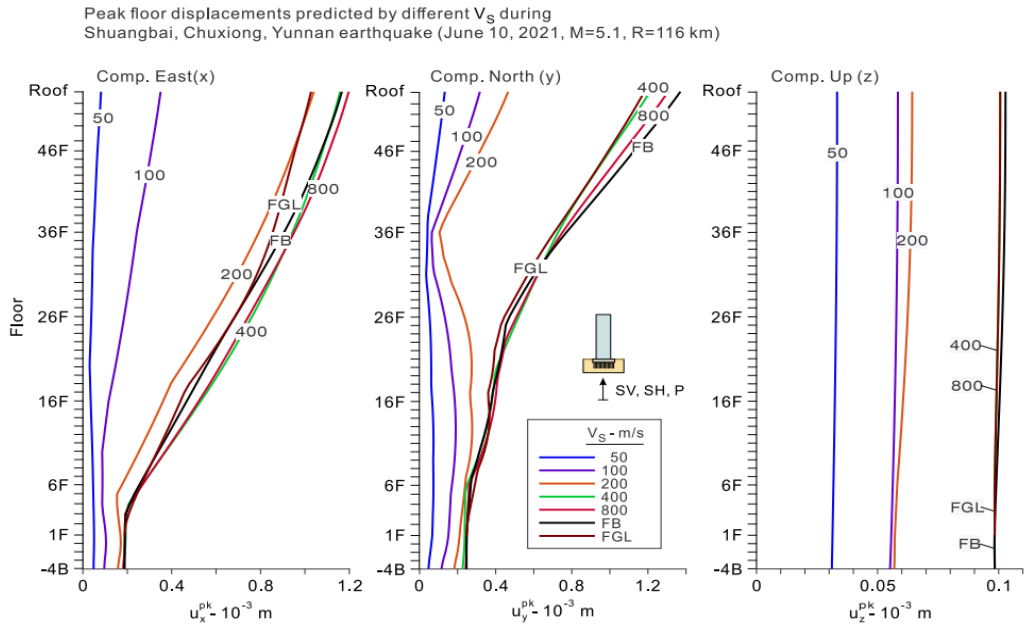


Figure 3-33 Peak floor displacements for different values of V_S during Shuangbai, Chuxiong earthquake after Cruz et al. (2024).

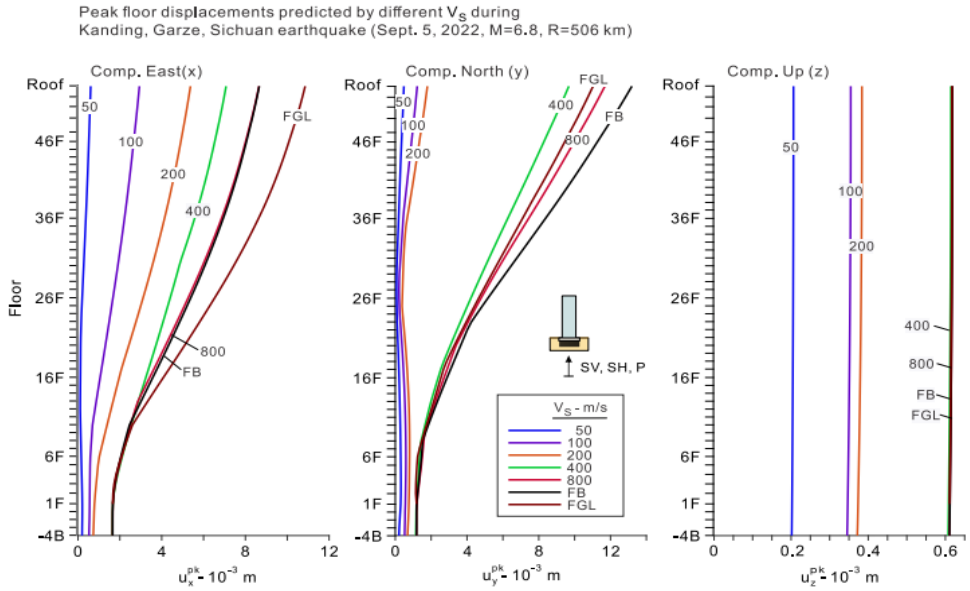


Figure 3-34 Peak floor displacements for different values of V_s during Kanding, Garze, Sichuan earthquake after Cruz et al. (2024).

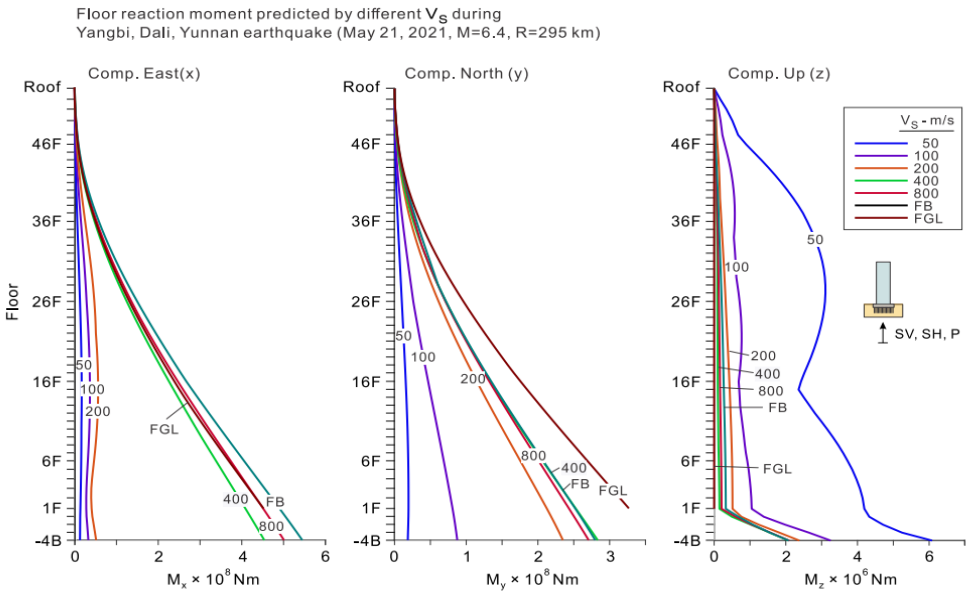


Figure 3-35 Floor moments for different values of V_s during Yangbi, Dali earthquke after Cruz et al. (2024).

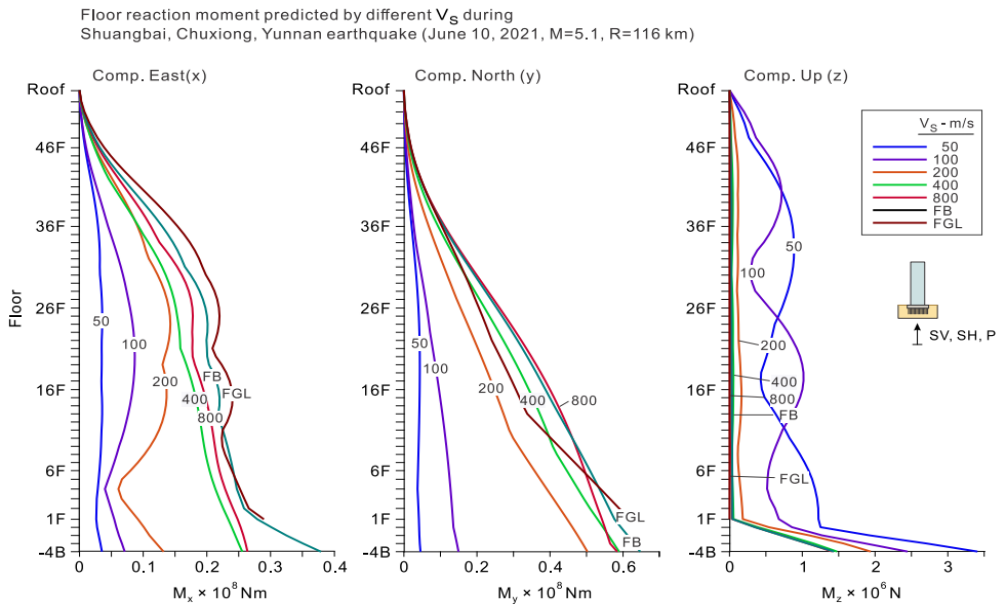


Figure 3-36 Floor moments for different values of V_s during Shuangbai, Chuxiong earthquake after Cruz et al. (2024).

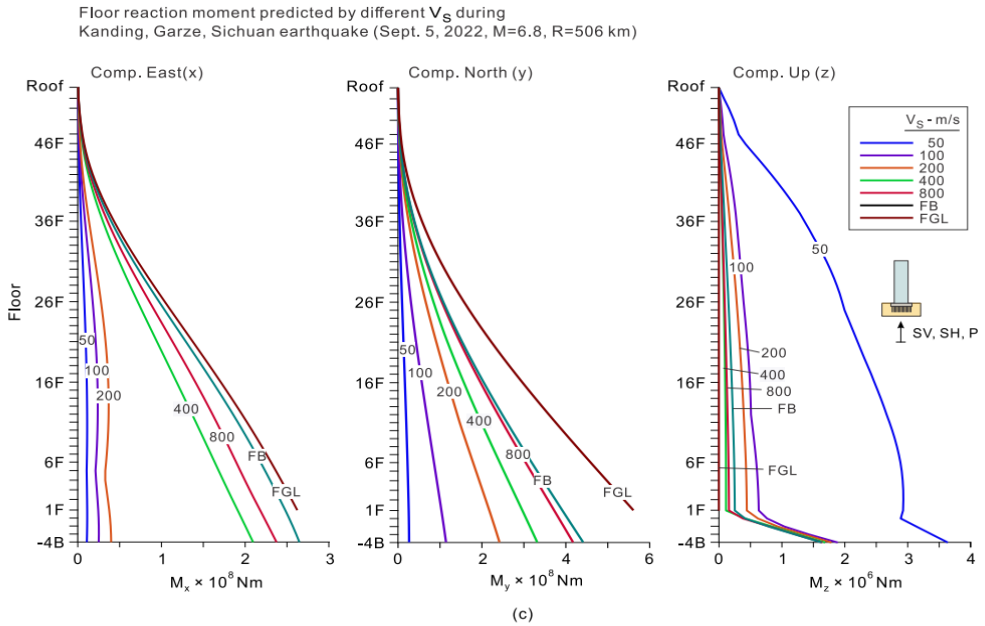


Figure 3-37 Floor moments for different values of V_s during Kanding, Garze, Sichuan earthquake after Cruz et al. (2024).

Summary

This section consolidates the key findings of the chapter, underscoring the critical importance of selecting appropriate shear wave measurement techniques based on specific project objectives, site conditions, and the desired level of precision. A diverse range of laboratory and field-based methods exists, each with unique operational characteristics, advantages, and limitations, requiring practitioners and researchers to develop a nuanced understanding of their applicability in various geotechnical and earthquake engineering contexts. Laboratory methods—such as bender element testing, cyclic triaxial and simple shear tests, resonant column tests, free torsion pendulum tests, and stress path triaxial tests—offer controlled environments for evaluating dynamic soil properties under repeatable conditions. These tests are particularly valuable for generating high-accuracy measurements of shear wave velocity and shear modulus at low to moderate strain levels. However, their representativeness can be compromised by sample disturbance during extraction, preparation, and confinement, as well as by boundary effects and scaling challenges that limit direct extrapolation to field conditions.

On the other hand, field testing methods—including cross-hole, up-hole, and down-hole techniques; seismic refraction and reflection methods; spectral analysis of surface waves (SASW); and cone penetration testing with shear wave velocity measurements (SCPT)—are essential for capturing in-situ soil behavior, accounting for natural stress conditions, soil layering, and heterogeneity. These methods are particularly effective in geotechnical site investigations, seismic hazard assessments, and foundation design, offering continuous profiles of subsurface stiffness and stratigraphy. Nevertheless, their practical application is often hindered by environmental noise, access constraints, equipment limitations, and the need for expert interpretation.

Questions and Problems

1. Explain the overview of laboratory and in-situ tests varied with shear strain amplitudes.
2. Explain the principle of the bender element test.
3. Explain the principle of the cyclic triaxial test.
4. Compare the working principle of the cyclic triaxial test with the cyclic simple shear test.
5. Explain the principle of the free torsional pendulum test.
6. Explain the principle of the stress path triaxial test.
7. What is the advantage of using the Halle effect transducers?
8. Compare the working principle of the cross hole and down hole methods.
9. Compare the working principle of the seismic refraction and the seismic reflection tests.
10. Explain the principle of SASW test.

Chapter 4: Analysis and Interpretation of Shear Wave Data

4.1 Introduction to Analysis and Interpretation of Shear Wave Data

At present, the Soil Mechanics Laboratory of the Department of Civil and Environmental Engineering Technology, College of Industrial Technology, King Mongkut's University of Technology North Bangkok, employs a bender element testing system to evaluate the shear wave velocity V_s and the initial shear modulus G_0 through the propagation of elastic shear waves in geomaterials. This testing approach is founded on the well-established principle that a direct relationship exists between shear wave velocity (V_s) and G_0, as documented in previous research of Dyvik & Madshus (1985). The initial shear modulus represents a fundamental parameter in soil dynamics and earthquake engineering, serving as a critical factor for predicting soil–structure interaction behavior and strength development.

The primary objective of this application is to enhance the bender element test apparatus for accurate measurement of V_s and G_0. To achieve this, bender element sensors are integrated into typical soil mechanical apparatus, designed similarly to the configuration detailed in Brignoli et al. (1996). Figure 4-1 shows the set-up of bender element test as clearly described by Petcherdchoo et al. (2023), allowing for precise measurement of shear wave velocity.

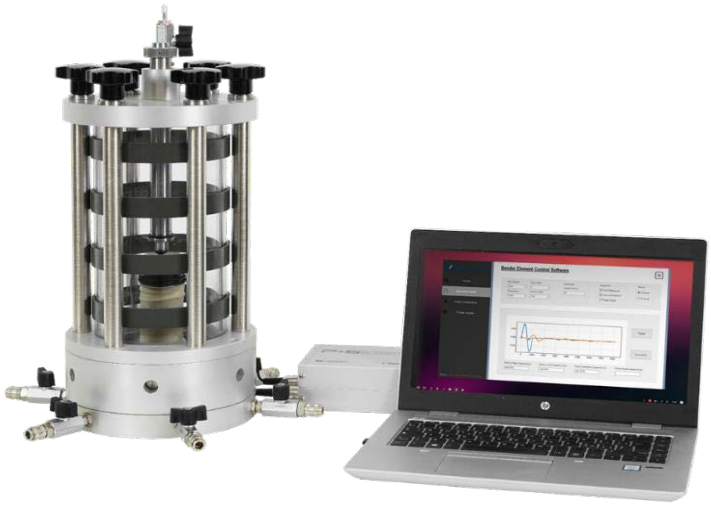


Figure 4-1 Set-up of bender elements after Petcherdchoo et al. (2023).

In the conventional arrangement, a shear wave is transmitted from one end of the soil specimen and detected at the opposite end by means of bender element transducers. The shear wave velocity V_s is calculated using Equation 4.1, which expresses the relationship between the tip-to-tip distance L separating the transducers and the corresponding travel time t of the shear wave.

$$V_s = \frac{L}{t} \tag{4.1}$$

The travel time (t) is calculated by subtracting the offset time (t_c) from the total recorded time (t_t), as expressed in Equation 4.2:

$$t = t_t - t_c \tag{4.2}$$

An alternative approach for determining shear wave velocity, as developed by Blewett et al. (1999), involves the use of a continue sinusoidal waveform applied to the transmitting transducer at low frequency. The receiving transducer records the output simultaneously. The frequency of the input signal is gradually increased until the output waveform aligns in phase with the input, indicating the formation of a standing wave pattern. When a full wavelength or multiple full wavelengths exist between the transducers, the shear wave velocity can be computed using Equation 4.3:

$$V_s = \left(\frac{L}{N}\right) \cdot f \tag{4.3}$$

where:

N is the number of full wavelengths between the transducers,

f is the frequency of the applied signal.

Once the shear wave velocity is determined, the initial shear modulus (G_0) is calculated using Equation 4.4, derived from the theory of elastic continuum mechanics:

$$G_0 = \rho \cdot V_s^2 \tag{4.4}$$

where ρ is the mass density of the soil specimen.

Boonyatee (2009) proposed a variable-path length method using bender elements and applied a continuous sinusoidal wave instead of a pulse signal within a triaxial test configuration. Their approach further highlights the versatility of waveform types in improving measurement accuracy for shear wave velocity.

4.2 Signal Processing of Shear Wave Data

The testing procedure involves applying a voltage pulse to the transmitting transducer, which in turn generates a shear wave that propagates through the soil specimen. Upon reaching the opposite end, the receiving transducer—distorted by the incoming wave—produces a voltage pulse. This receiver is connected directly to the signal analyzer, allowing for precise time-domain comparison between the transmitted and received signals, as shown in Figure 4-2.

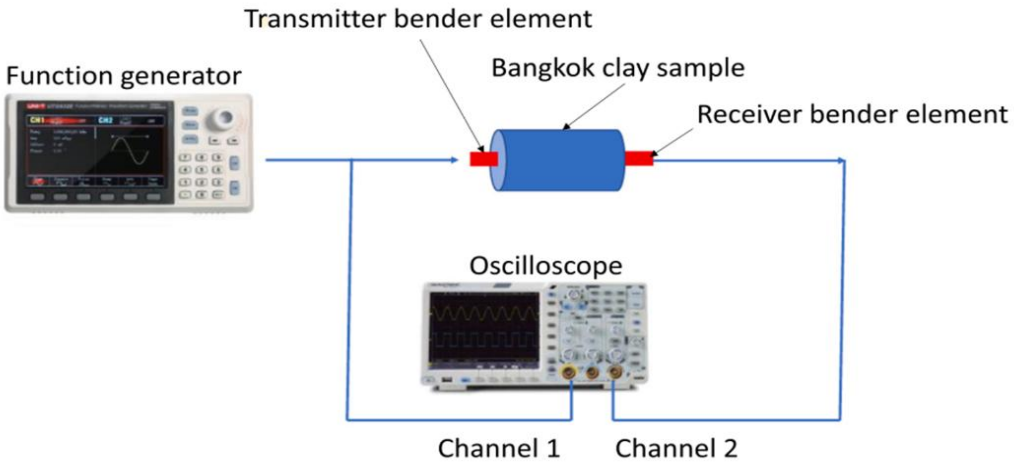


Figure 4-2 Schematic of piezoelectric bender element and associated electronics after Piriyakul (2010).

Shear wave velocity measurements are typically conducted using signal frequencies ranging from 2 to 10 kHz, under strain levels estimated to be less than 0.0001%, ensuring the test remains within the elastic, small-strain range. However, there are limitations to consider. At low frequencies, measurements may be affected by the near-field effect, which can distort the waveform and obscure arrival times—a topic further discussed in the following section.

Conversely, at high frequencies, the amplitude of the received signal often becomes weak, making it difficult to interpret. To enhance signal clarity and reduce noise, it is standard practice to average the waveform over 32 iterations, producing a more distinct and reliable output for analysis.

4.3 Near Field Effect on Shear Wave

At lower frequencies, the first deflection observed in the recorded signal often represents the arrival of a compression wave, also known as the near-field component, rather than the true arrival of the shear wave. This near-field effect can mask the identification of the shear wave onset, particularly when the spacing between the transmitter and the receiver ranges from approximately one quarter to four wavelengths. As shown in Figure 4-3, the impact of the near-field component decreases rapidly as the number of wavelengths separating the transducers increases, a trend consistent with earlier reported findings of Brignoli et al. (1996) and Piriyakul (2010).

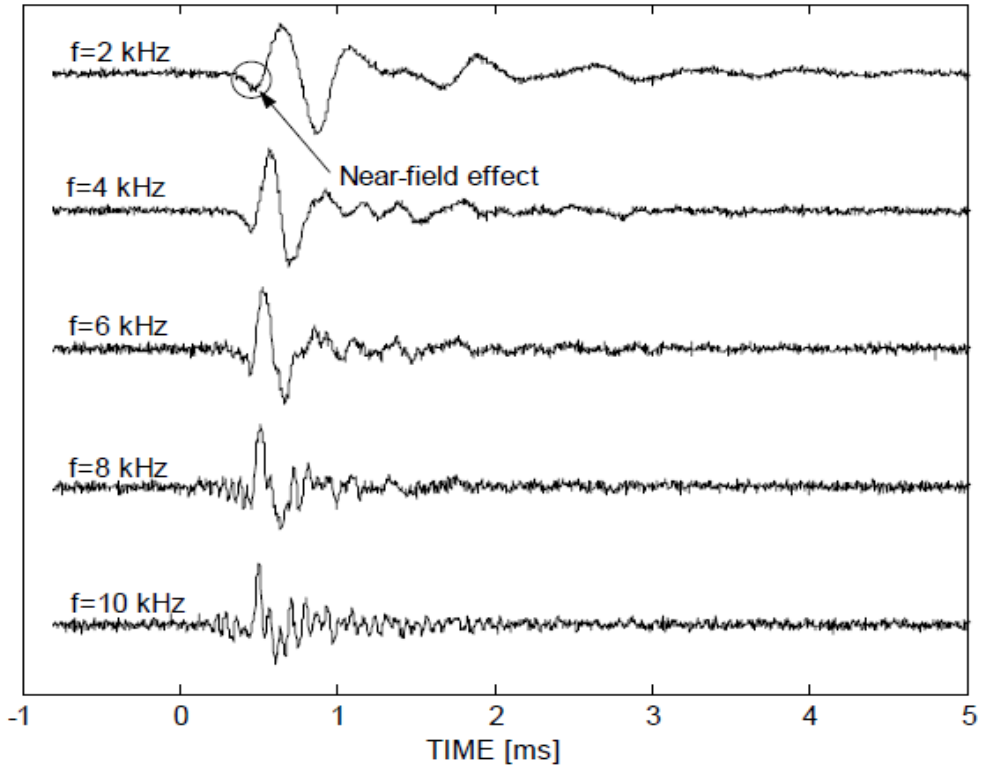


Figure 4-3 Near field effect on the shear wave arrival in a clay specimen with different frequencies after Piriyakul (2010).

It was found that optimal signal clarity was achieved at frequencies ranging from 2 to 10 kHz, where the near-field interference is minimal and the shear wave signal is distinct. It is important to note that the resonant frequency of the piezoelectric bender element used is 622 Hz. Consequently, frequencies below 1 kHz are avoided, as they fall near or below the resonance threshold and may produce distorted or unreliable waveforms.

4.4 Calibration of bender elements

Before conducting the bender element testing, it is essential to calibrate the entire system to ensure that no artificial delay is introduced by electronics, piezoelectric ceramics, or coating materials. The offset time (t_c) is determined by placing the transmitting and receiving bender elements directly in contact and measuring the time interval between the transmitted and received signals as seen in Figure 4-4. This approach isolates the delay introduced solely by the electronic and material components.

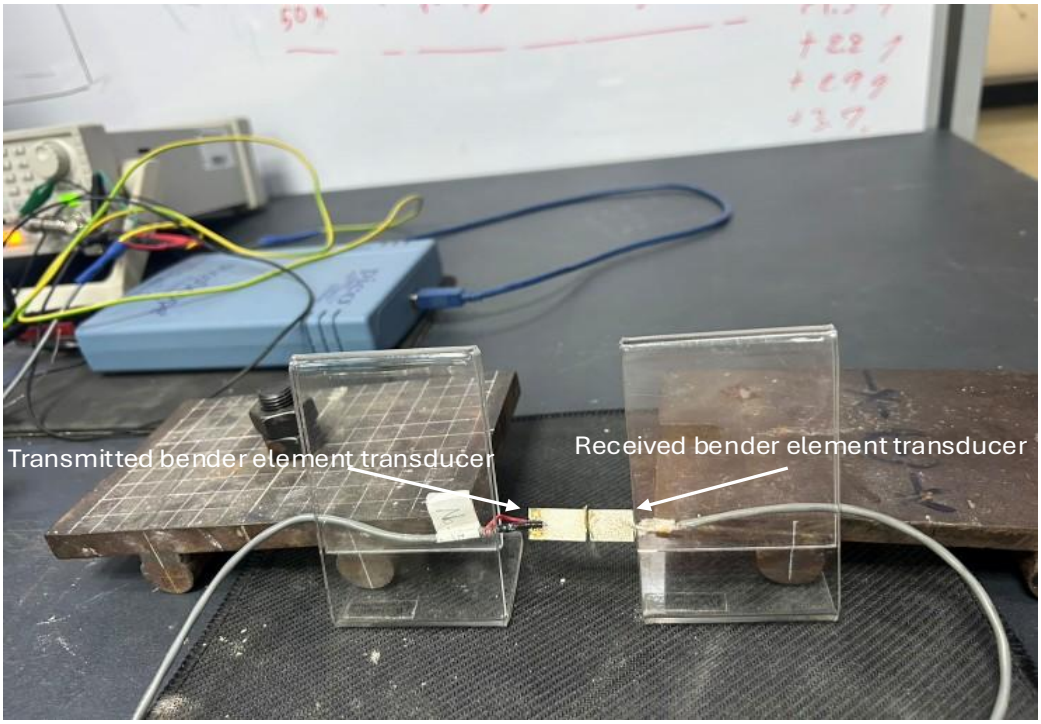


Figure 4-4 Calibration of bender element testing.

Table 4-1 Pattern of different wave forms.

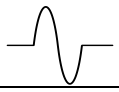
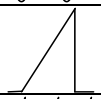
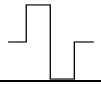
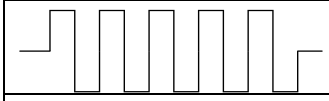
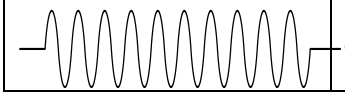
Waveform	Detail of waveform
	single period sinusoidal waveform
	5-period sinusoidal waveform
	single period triangle waveform
	5-period triangle waveform
	single period rectangle waveform
	5-period rectangle waveform
	continue sinusoidal waveform

Table 4-1 presents the pattern of different wave forms used for the bender element test such as a single period sinusoidal, 5 period sinusoidal, single period triangle, 5 period triangle, single period rectangle, 5 period rectangle and continue sinusoidal waveform. Figure 4-5 illustrates the measurement of offset time by attaching the transmitting transducer directly to the receiving transducer and transmitting a single-period sinusoidal waveform at a frequency of 10 kHz. The measured offset time (t_c) is 30.05 μs. Similarly, when a 5-period sinusoidal waveform at 10 kHz is transmitted, a delay of 30.73 μs is observed, as shown in Figure 4-6. In the same way, Figure 4-7 and Figure 4-8 show the t_c of a single and a 5-period triangle waveform as 29.13 μs and 30.24 μs respectively. Similarly, Figure 4-9 and Figure 4-10 depict the t_c of a single and a 5-period rectangle waveform as 29.54 μs and 31.07 μs respectively.

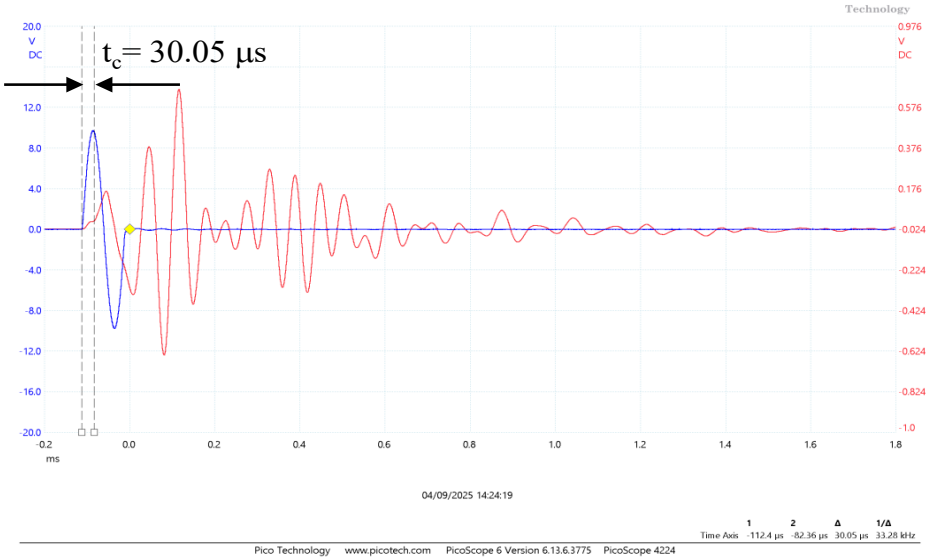


Figure 4-5 Calibration of bender element with a single period sinusoidal waveform.

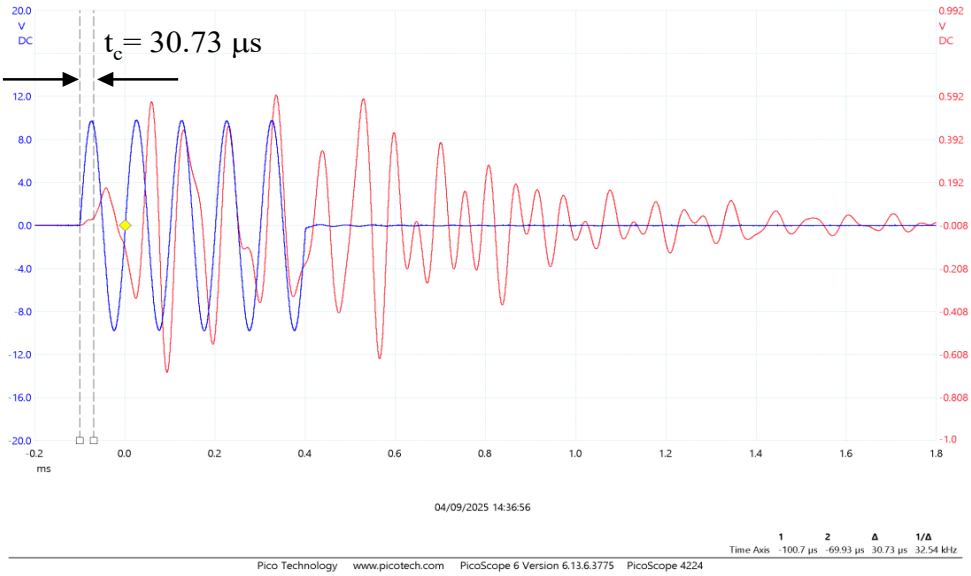


Figure 4-6 Calibration of bender element with a 5-period sinusoidal waveform.

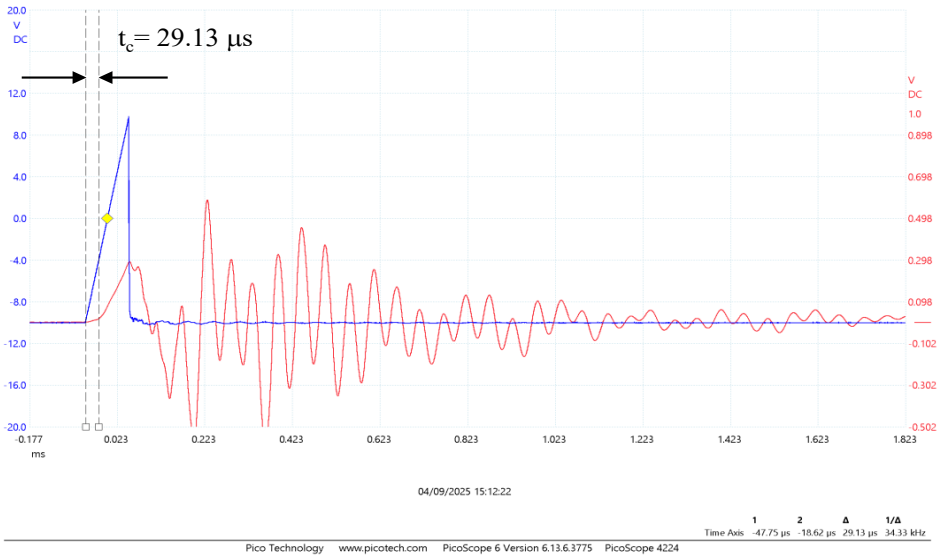


Figure 4-7 Calibration of bender element with a period triangle waveform.

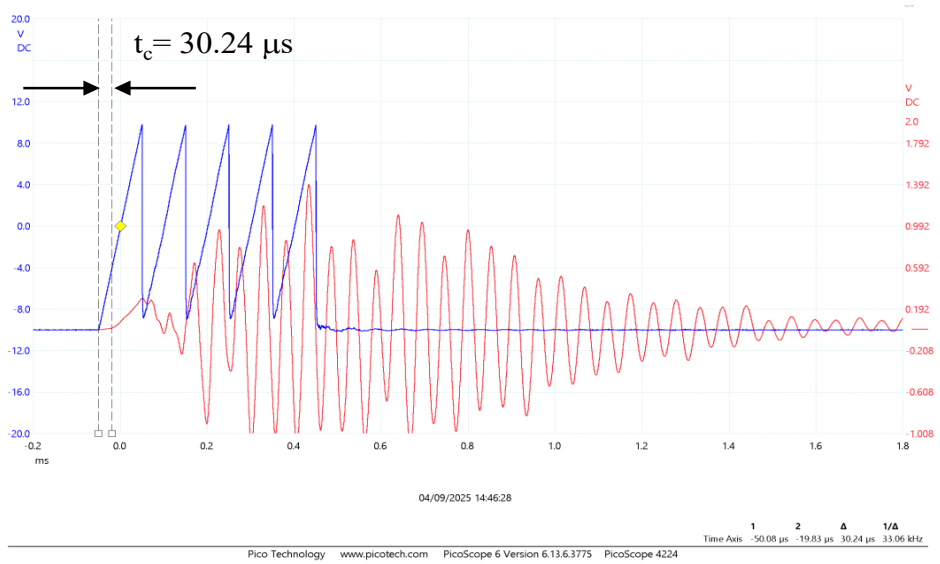


Figure 4-8 Calibration of bender element with a 5-period triangle waveform.

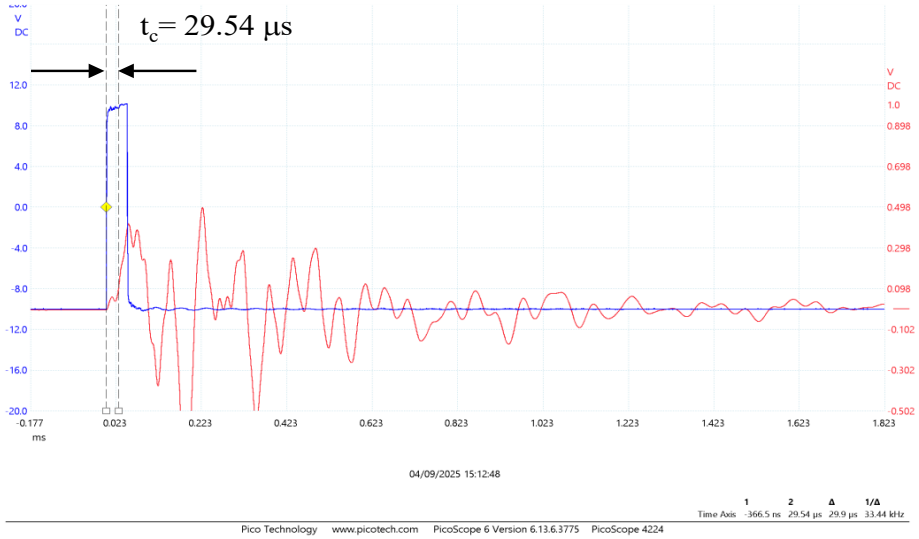


Figure 4-9 Calibration of bender element with a single period rectangle waveform.

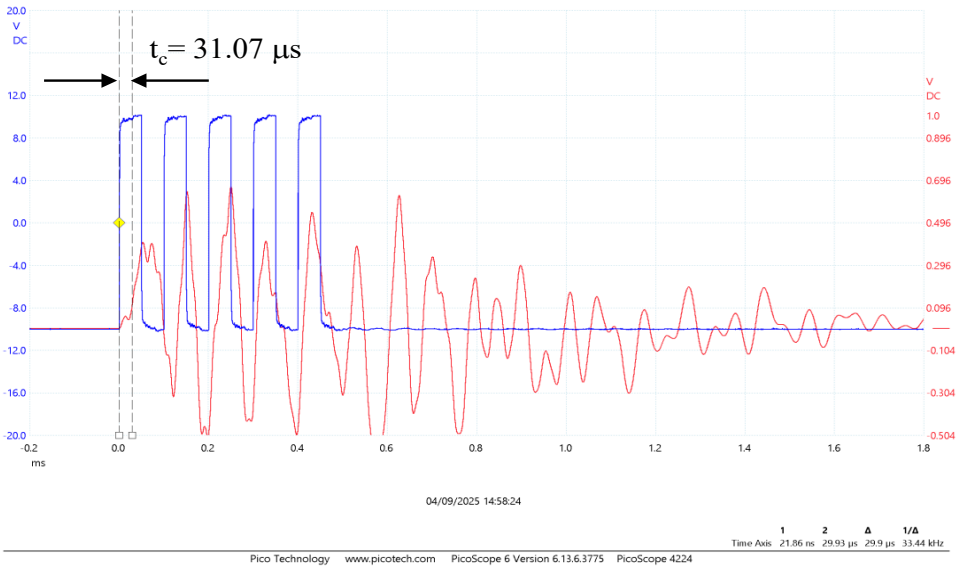


Figure 4-10 Calibration of bender element with a 5-period rectangle waveform.

4.5 Analysis of Shear Wave Data

The experimental arrangement of the bender element is illustrated in Figure 4-1. The specimen tested is a soil–cement mixture prepared from Bangkok clay at its liquid limit of 84 %, blended with 8% cement by weight. The material has a specific gravity of 2.68 and a bulk density of 1,470 kg/m^3. The specimen is molded into a cylindrical form with a diameter of 50.015 mm and a length of 99.196 mm. Figure 4-11 presents the measurement of the total travel time, denoted as t_t, for a single-period sinusoidal wave propagating through the soil–cement specimen, which was recorded as 381.5 µs. By applying Equation 4.2, the required travel time t is obtained after subtracting the offset time t_c, resulting in a corrected value of 351.45 µs. The distance between the transmitting and receiving transducers, measured tip-to-tip, is 99.196 mm. Using Equation 4.1, the shear wave velocity V_s is calculated to be 282.247 m/s. Subsequently, applying Equation 4.4, the initial shear modulus G_0 is determined as 117.11 MPa. A summary of the values of V_s and G_0 obtained from different waveforms is provided in Table 4-2.

Table 4-2 presents the measurement of the V_s and the G_0 out of different waveforms.

Waveforms	L **(mm)**	t_t **(µs)**	t_c **(µs)**	t **(µs)**	V_s **(m/s)**	G_0 **(MPa)**
single period sinusoidal	99.196	381.5	30.05	351.45	282.247	117.11
5-period sinusoidal	99.196	381.7	30.73	350.97	282.634	117.43
single period triangle	99.196	384.4	29.13	355.27	279.213	114.60
5-period triangle	99.196	381.3	30.24	351.06	282.561	117.37
single period rectangle	99.196	380.1	29.54	350.56	282.964	117.70
5-period rectangle	99.196	381.7	31.07	350.63	282.908	117.65

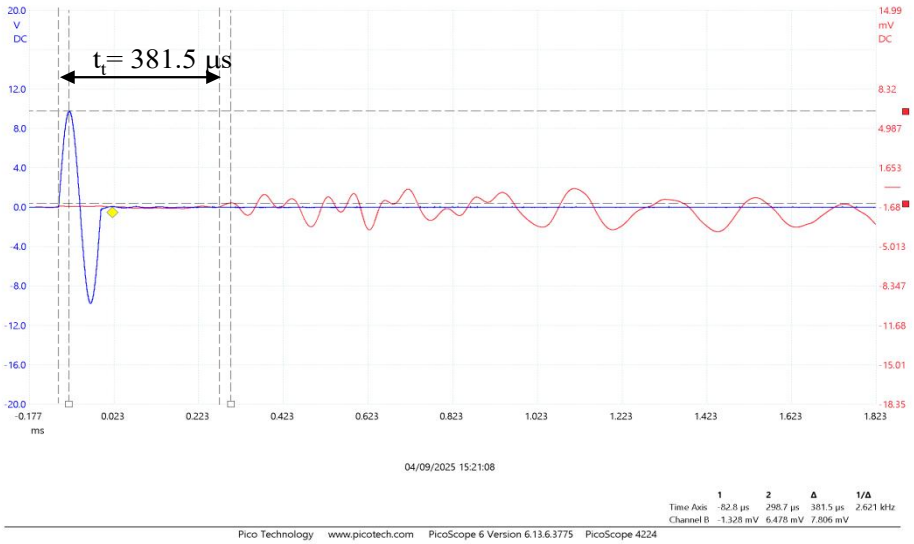


Figure 4-11 Measurement of shear velocity with a single period sinusoidal waveform.

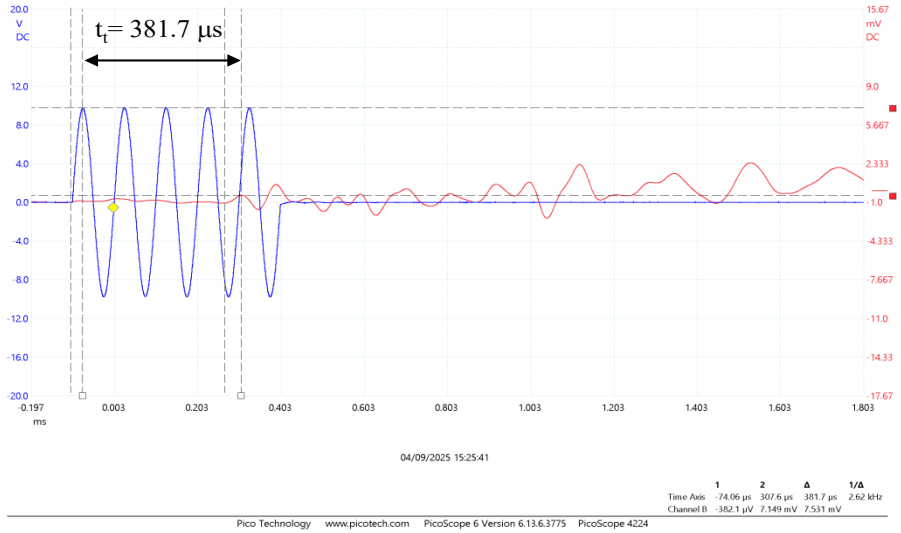


Figure 4-12 Measurement of shear velocity with a 5-period sinusoidal waveform.

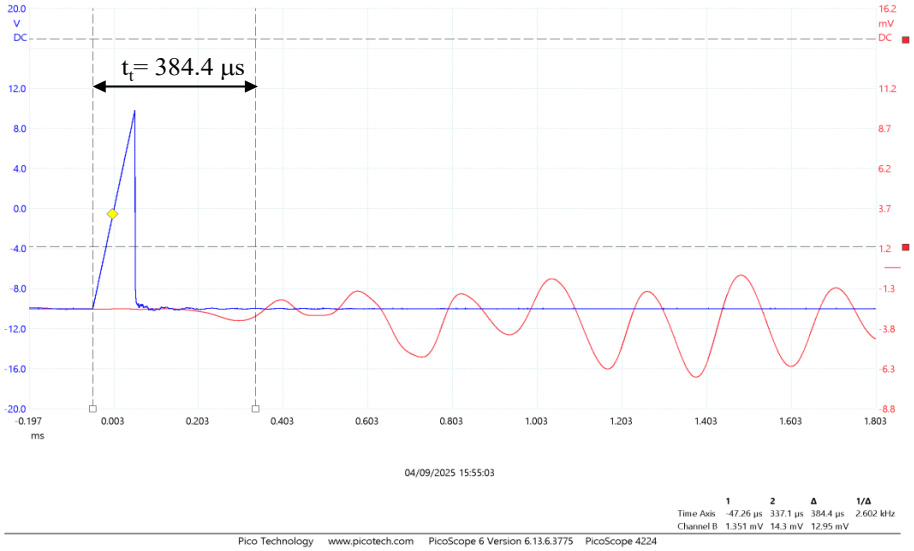


Figure 4-13 Measurement of shear velocity with a single period triangle waveform.

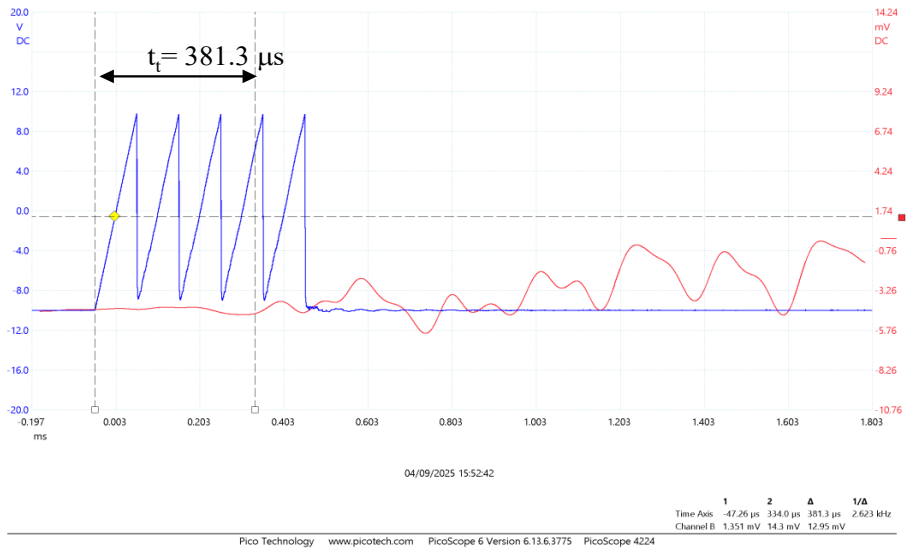


Figure 4-14 Measurement of shear velocity with a 5-period triangle waveform.

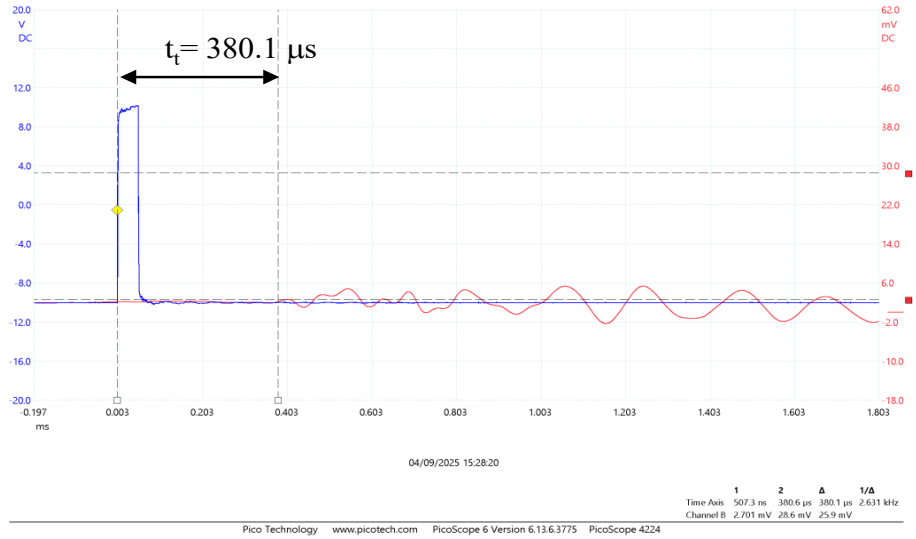


Figure 4-15 Measurement of shear velocity with a single period rectangle waveform.

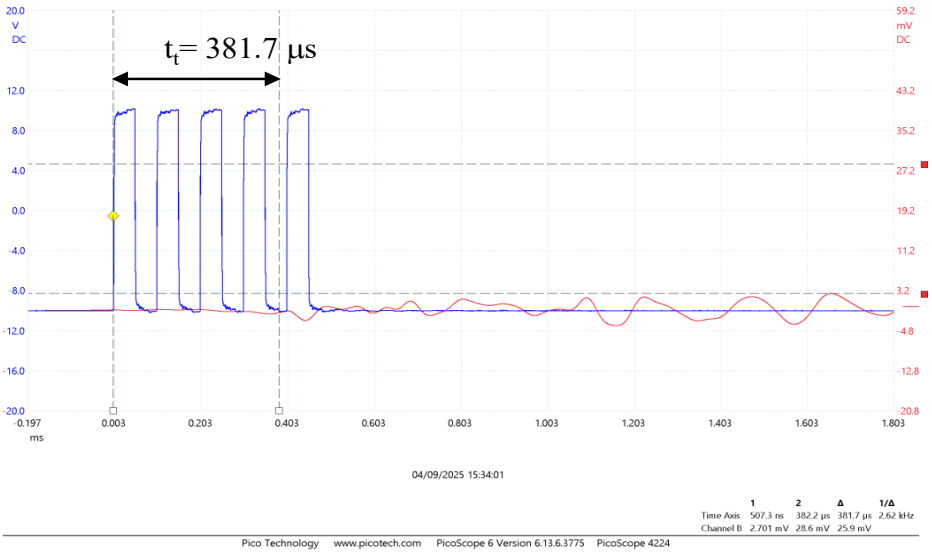


Figure 4-16 Measurement of shear velocity with a 5-period rectangle waveform.

In certain instances, the interpretation of either single- or 5-period waveforms can present ambiguities, particularly in identifying the precise arrival time of the shear wave. To mitigate this uncertainty, the use of a continuous sinusoidal waveform is recommended. This technique provides a more stable and consistent signal, offering a convenient and efficient means of improving the accuracy and reliability of shear wave velocity measurements.

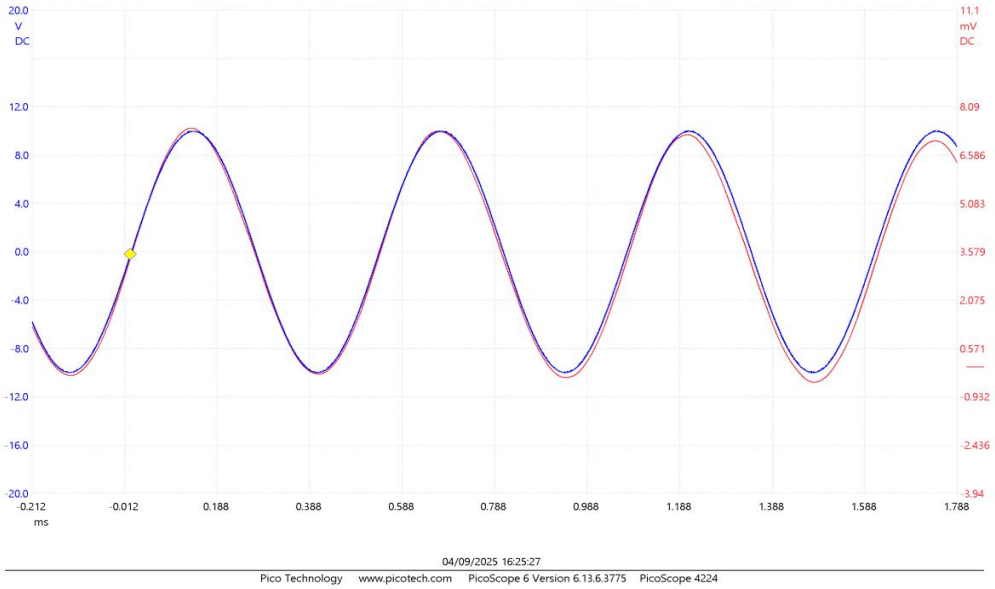


Figure 4-17 Example of measurement of a continue sinusoidal waveform of the soil-cement sample.

Figure 4-17 presents the cross-correlation analysis between the input and output signals, with a measured frequency of 622 Hz. Based on Equation 4.3, the shear wave velocity (V_s) is calculated to be 311.00 m/s, considering that the wavelengths (λ) is 0.5 m and the tip-to-tip distance between the transducers is 99.196 mm. The initial shear modulus (G_0) of 142.18 MPa is calculated by Equation 4.4. Table 4-3 expresses the V_s results and the G_0 data with different frequencies.

Table 4-3. Shear moduli of a clay specimen.

f (Hz)	λ (m)	V_s (m/s)	G_0 (MPa)
622	0.500	311.00	142.18
1282	0.250	320.50	151.00
1867	0.167	311.17	142.33
2583	0.125	322.88	153.24
3750	0.083	312.50	143.55

4.6 Measurement of shear wave velocity according to ASTM D8295–19

According to ASTM D8295–19 (Standard test method for determination of shear wave velocity and initial shear modulus in soils specimen using bender elements), the t_c and the t_t are measured at the first peak of the single sinusoidal waveform. Figure 4-18 shows the t_c of 30.44 µs and Figure 4-19 shows the t_t of 381.5 µs respectively. By using Equations 4.1 and 4.2, the V_s of 282.56 m/s and the G_0 of 117.37 MPa are calculated as good as the data in the last section.

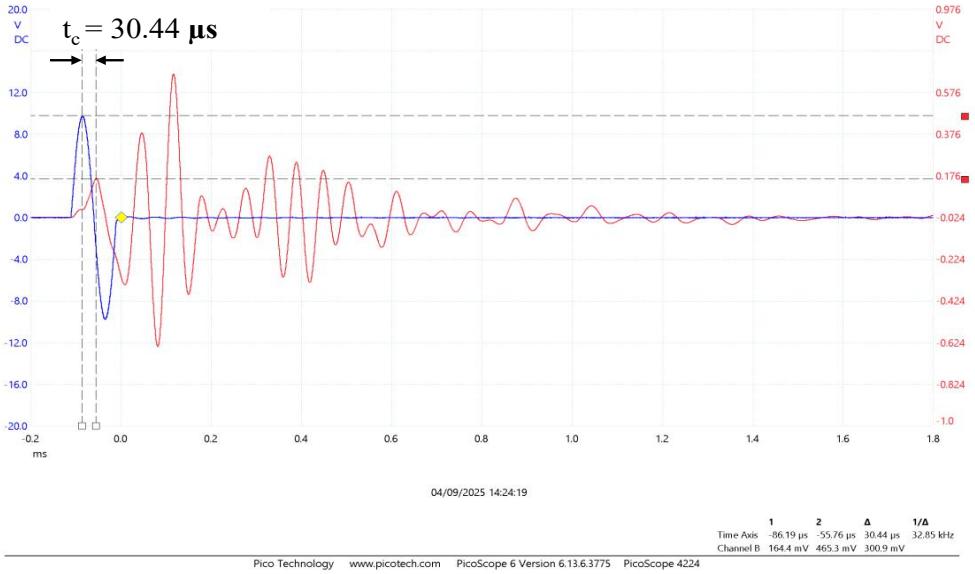


Figure 4-18 Calibration of bender element with a single period sinusoidal waveform ASTM D8295–19.

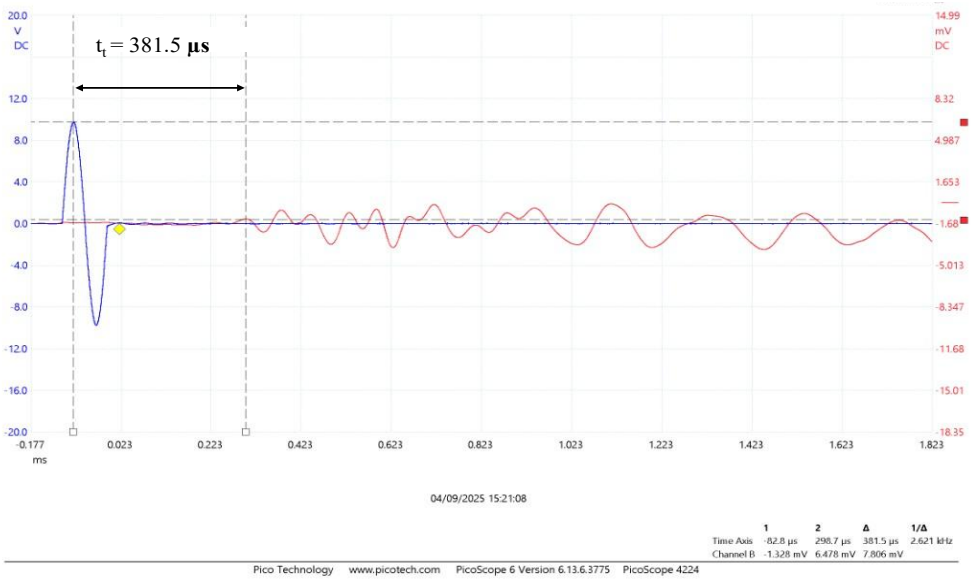


Figure 4-19 Measurement of shear velocity with a single period sinusoidal waveform according to ASTM D8295–19.

4.7 Site Characterization of Bangkok clay formation by Shear Wave Data

According to previous reports of Tuladhar et al. (2004), Bangkok is located on an extensive plain underlain by alluvial and deltaic deposits of the Chao Phraya basin. This plain, covering an area of approximately 13,800 square kilometers, is commonly referred to as the lower central plain. Geological evidence indicates that the area was submerged beneath a shallow sea between 3,000 and 5,000 years ago, with marine regression occurring around 2,700 years ago. This regression left behind thick accumulations of soft sediments that now constitute the lower central plain. The surficial deposit in this region consists of a distinctive clay layer, widely known as Bangkok clay, which has an average thickness ranging from 15 to 20 meters in the central city area. Bangkok clay is characterized by extremely low shear strength and high compressibility, conditions arising from the absence of prior mechanical consolidation. Undisturbed samples of this material were obtained at the campus of King Mongkut's University of Technology North Bangkok. Sampling extended from the ground surface to depths of approximately 25 meters. To preserve their natural condition, the undisturbed specimens were stored in glass containers under high-humidity conditions. The engineering properties of Bangkok clay are summarized in Table 4-3. A comprehensive study of soil characteristics conducted at nine sites across Bangkok yielded generalized soil profiles and shear wave velocity distributions, as documented in Warnitchai et al. (2000) and illustrated in Figure 4-20. Initial estimates of shear wave velocity were derived from both field and laboratory data using various published empirical correlations, and these values were subsequently verified by in-situ downhole shear wave measurements at an additional four sites. The collected data were later reanalysed by Teachavorasinskun & Lukkunaprasit (2004), who established that the shear wave velocity within the upper 30 meters of Bangkok subsoil could be expressed as a linear function of depth Z, measured in meters from the ground surface, as formulated in Equation 4.5.

$$V_s = 8.8Z + 45.4 \tag{4.5}$$

where Z is depth in meter.

Table 4-4 Engineering properties of Bangkok clay.

Depth (m)	ρ (kg/m^3)	G_s	LL (%)	PL (%)	w (%)	S_u (ksc)
4.0	1600	2.71	56.2	27.2	49.6	0.32
5.0	1470	2.72	74.8	32.1	90.1	0.21
13.0	2030	2.68	44.5	21.8	53.1	0.46
15.0	1992	2.54	41.4	12.0	26.1	1.22
18.0	2063	2.51	29.5	12.3	22.1	4.00
21.0	2105	2.56	32.8	12.1	25.0	2.75
22.5	2278	2.52	40.4	14.4	22.3	4.00
24.0	2123	2.50	26.4	11.1	17.2	3.74

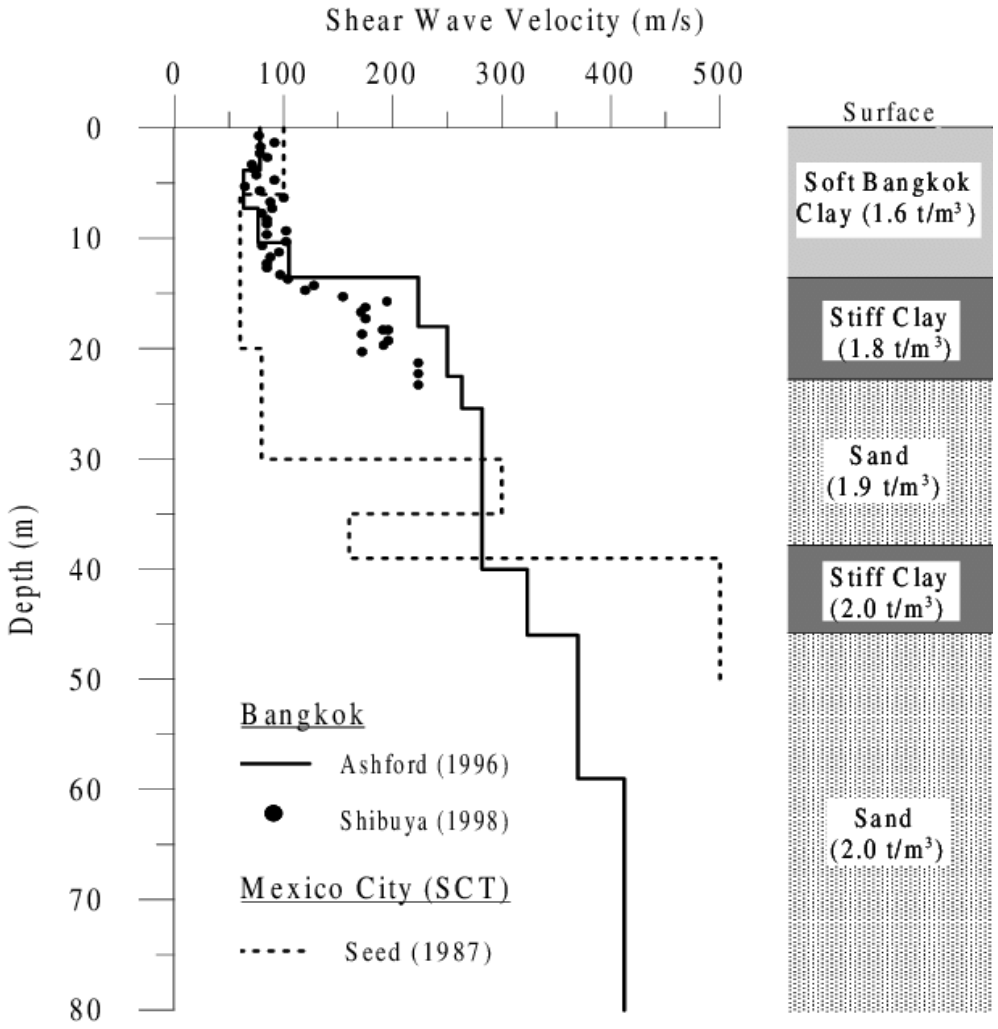


Figure 4-20 Generalized Bangkok soil and shear wave velocity profiles after Warnitchai et al. (2000).

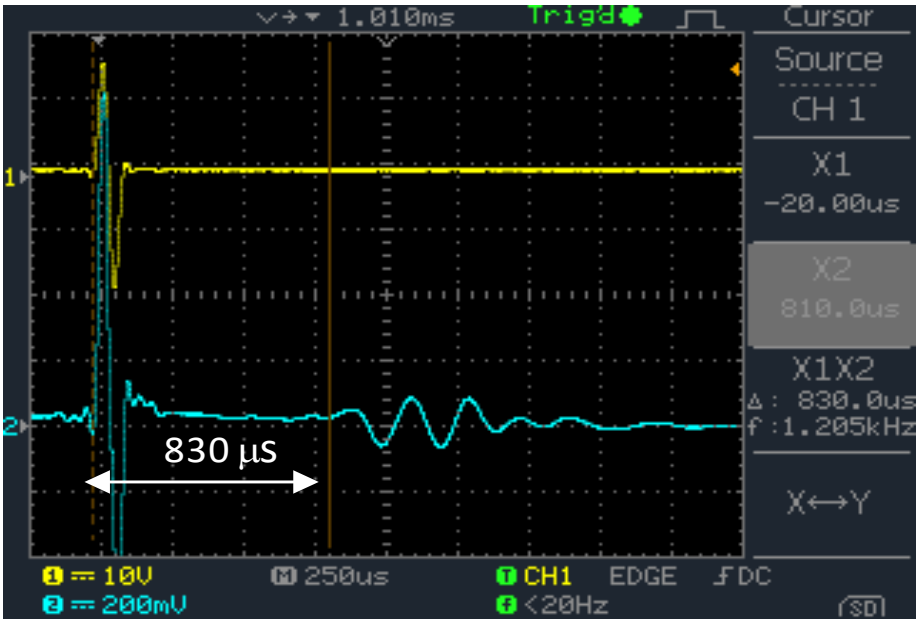


Figure 4-21 Measurement of shear wave velocity of Bangkok clay at 4.0 m depth (Frequency=12,000 Hz) after Piriyakul (2013a).

Figure 4-21 presents the shear wave velocity obtained from a Bangkok clay specimen sampled at a depth of 4.0 meters. The shear wave velocity, V_s, measured at the atmospheric pressure. Although some crosstalk was observed, the arrival of the shear wave signal could be clearly identified when a high excitation frequency of 12,000 Hz was applied. The total travel time, t_t, was measured as 830 microseconds, and after subtracting an offset time (t_c) of 4 microseconds, the corrected travel time t was determined as 826 microseconds, in accordance with Equation 4.2. The tip-to-tip distance between the transducers was 63 millimeters. Based on these values, the shear wave velocity V_s was calculated to be 76.3 meters per second using Equation 4.1. This measurement corresponds to the shear wave velocity profile of the Bangkok formation. At the depth of 4.0 meters, the soil is classified as soft Bangkok clay, with a shear wave velocity of approximately 70 meters per second, consistent with earlier findings of Warnitchai et al. (2000). The initial shear modulus G_0 was subsequently computed as 9.3 megapascals using Equation 4.4.

In a similar manner, the shear wave velocity of a Bangkok clay specimen at a depth of 5.0 meters was determined. As shown in Figure 4-22, the total travel time t_t was measured at 610 microseconds, and after subtracting the offset time, the corrected travel time t was obtained as 606 microseconds. With a tip-to-tip distance of 32 millimeters, the shear wave velocity V_s was calculated to be 52.8 meters per second. This value corresponds well with the field measurement of approximately 60 meters per second, as illustrated in Figure 4-20. The initial shear modulus, G_0, calculated using Equation 4.4, was found to be 4.1 megapascals. For the Bangkok clay specimen collected at a depth of 13.0 meters, the total travel time t_t was 456 microseconds, as illustrated in Figure 4-23, and the corrected travel time t was determined to be 452 microseconds. With a tip-to-tip distance of 60 millimeters, the calculated shear wave velocity V_s was 132.7 meters per second. The in-situ measurement at the same depth, shown in Figure 4-24, indicated a shear wave velocity of approximately 100 meters per second. From these results, the maximum shear modulus G_0 was calculated as 35.7 megapascals using Equation 4.4.

The overall results for shear wave velocity and shear modulus of Bangkok clay are summarized in Table 4-4. A comparison between laboratory bender element test results and field measurements is presented in Figure 4-24. The differences between laboratory and field values range from 5.3 percent to 62.3 percent, as reported in Table 4-5. In general, the shear wave velocities obtained from bender element tests were lower than those measured in situ. This discrepancy may be attributed to several factors. In field tests, shear waves propagate across soil layers that may include zones of higher stiffness, whereas laboratory specimens are smaller and may represent material of relatively lower stiffness. Additionally, the inversion analysis used to calculate shear wave velocity from field data assumes linear elastic isotropic behaviour, which may not be entirely appropriate for the Bangkok subsoil.

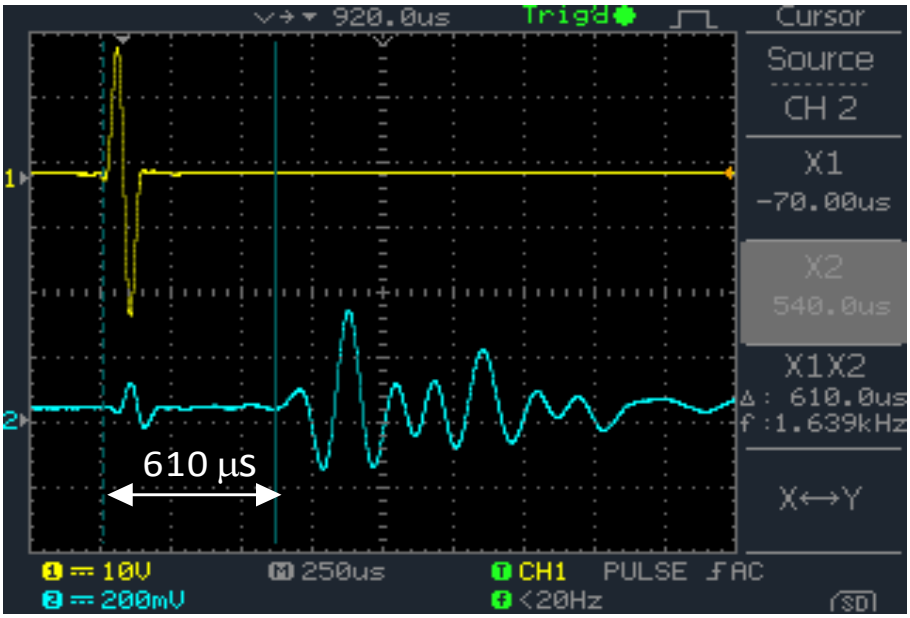


Figure 4-22 Measurement of shear wave velocity of Bangkok clay at 5.0 m depth (Frequency=12,000 Hz) after Piriyakul (2013a).

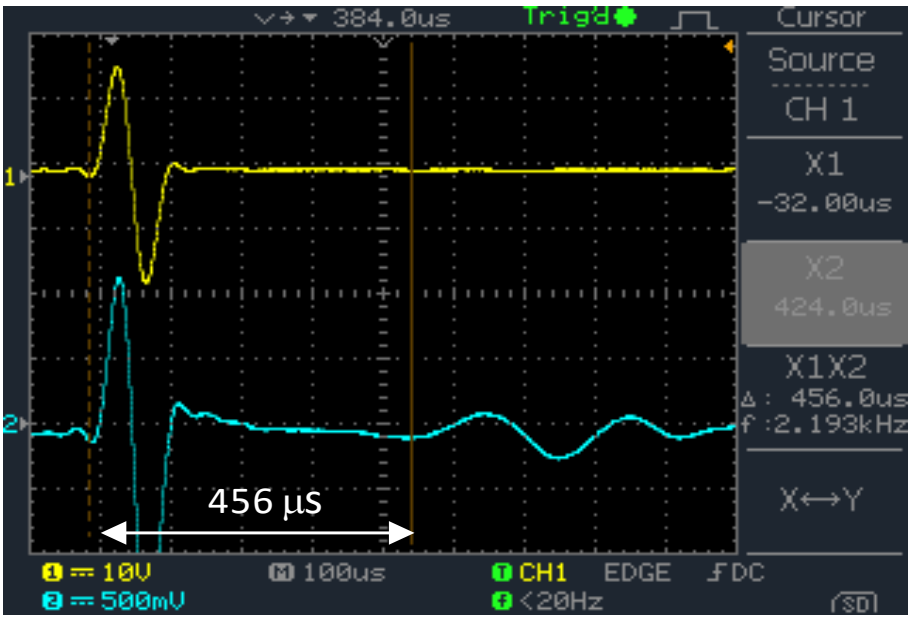


Figure 4-23 Measurement of shear wave velocity of Bangkok clay at 13.0 m depth (Frequency=12,000 Hz) after Piriyakul (2013a).

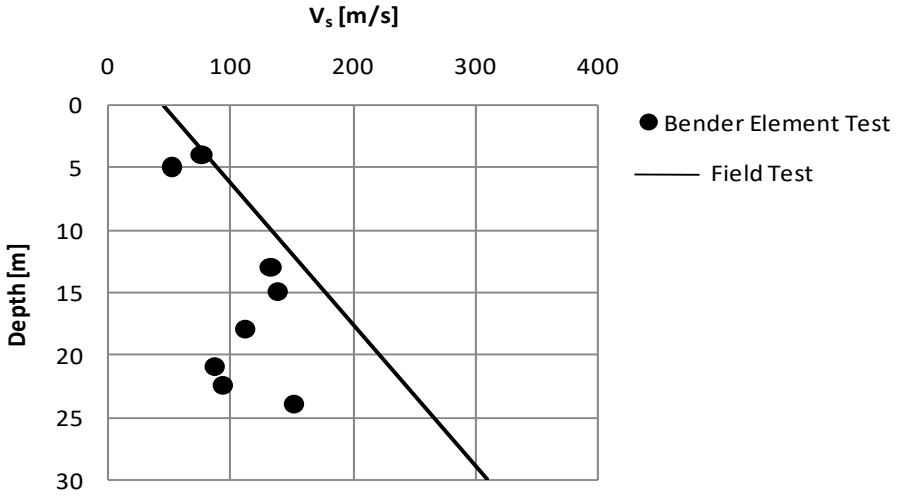


Figure 4-24 Results of shear wave velocity both laboratory and in-situ tests with depth of Bangkok clay formation after Piriyakul (2013a).

Table 4-5 Shear wave velocity and shear modulus results of Bangkok clay with depth after Piriyakul (2013a).

Depth (m)	V_s (m/s)	G_0 (MPa)
4.0	76.3	9.3
5.0	52.8	4.1
13.0	132.7	35.7
15.0	139.1	35.2
18.0	112.7	26.2
21.0	86.8	15.8
22.5	94.3	20.3
24.0	152.5	49.4

Table 4-6 Percent error of shear wave velocity after Piriyakul (2013a).

Depth (m)	V_s (m/s) Lab. Test	V_s (m/s) Field Test	% Error
4.0	76.3	80.6	5.3
5.0	52.8	89.4	40.9
13.0	132.7	159.8	17.0
15.0	139.1	177.4	21.6
18.0	112.7	203.8	44.7
21.0	86.8	230.2	62.3
22.5	94.3	243.4	61.3
24.0	152.5	256.6	40.6

The use of non-destructive testing methods to evaluate shear wave velocity and shear modulus with depth in the Bangkok clay formation provides a valuable approach. The Bangkok clay specimens were also utilized for complementary investigations, including unconfined compression testing. A comparison between laboratory bender element results and field measurements of shear wave velocity revealed discrepancies ranging from 5.3 to 62.3 percent. These differences can be explained in part by the fact that field measurements capture propagating waves that traverse soil layers with relatively higher stiffness, whereas laboratory tests are conducted on smaller specimens that may represent less stiff material. Furthermore, the inversion analysis used to derive shear wave velocity in field testing relies on the assumption of linear elastic isotropy, an assumption that is not entirely applicable to Bangkok subsoil conditions and may provide an additional explanation for the observed variations in shear wave velocity. Finally, the effective stress conditions of laboratory specimens do not replicate those encountered in situ.

4.8 Integration of Shear Wave Data with Other Geotechnical Data

Piriyakul (2013b) investigated the strength development of Bangkok soft clay stabilized with Portland cement. Bangkok clay samples were collected at a depth of 10 to 12 meters. The engineering properties of the material were determined, yielding a specific gravity of 2.72, a natural water content of 66.3 percent, a density of 1,470 kilograms per cubic meter, and a liquid limit of 88 percent. A total of twelve clay specimens were prepared at the liquid limit by mixing them with 20 percent Portland cement Type 1 by weight [8]. These samples were then cured for periods of 3, 7, 14, and 28 days prior to conducting both bender element tests and unconfined compression tests.

The relationship between the inverse of shear wave velocity and the inverse of curing time was found to be linear, as shown in Figure 4-25. This relationship is expressed by the saturation equation in Equation 4.6, where the maximum shear wave velocity V_s was recorded as 378.79 meters per second. A similar linear relationship was also observed between the inverse of the shear modulus and the inverse of curing time, as illustrated in Figure 4-26 and Equation 4.7, with the maximum shear modulus G_0 determined to be 224.72 megapascals. Likewise, Figure 4-27 and Equation 4.8 demonstrate the relationship between undrained shear strength S_u and curing time, where the maximum undrained shear strength reached 403.23 kilopascals. The correlation between V_s and S_u is expressed in Equation 4.9, while the relationship between G_0 and S_u is presented in Equation 4.10.

The observed strength development of soft Bangkok clay stabilized with 20 percent Portland cement Type 1 is attributed to cementation effects, and this improvement can be effectively evaluated using shear wave velocity testing. Overall, the experimental results demonstrated that both stiffness and strength increased with curing time, stabilizing after approximately 28 days. By applying the saturation equation, the relationships between V_s, G_0, S_u, and curing time were established, with the maximum values being 378.79 meters per second for V_s, 224.72 megapascals for G_0, and 403.23 kilopascals for S_u, as summarized in Table 4-6. Furthermore, the findings revealed that both V_s and G_0 are directly proportional to S_u.

$$V_s = \frac{378.79 \times t}{1.84 + t} \tag{4.6}$$

$$G_0 = \frac{224.72 \times t}{5.14 + t} \tag{4.7}$$

$$S_u = \frac{403.23 \times t}{3.51 + t} \tag{4.8}$$

$$V_s = (0.719 \times S_u) + 102 \tag{4.9}$$

$$G_0 = (0.643 \times S_u) - 40.39 \tag{4.10}$$

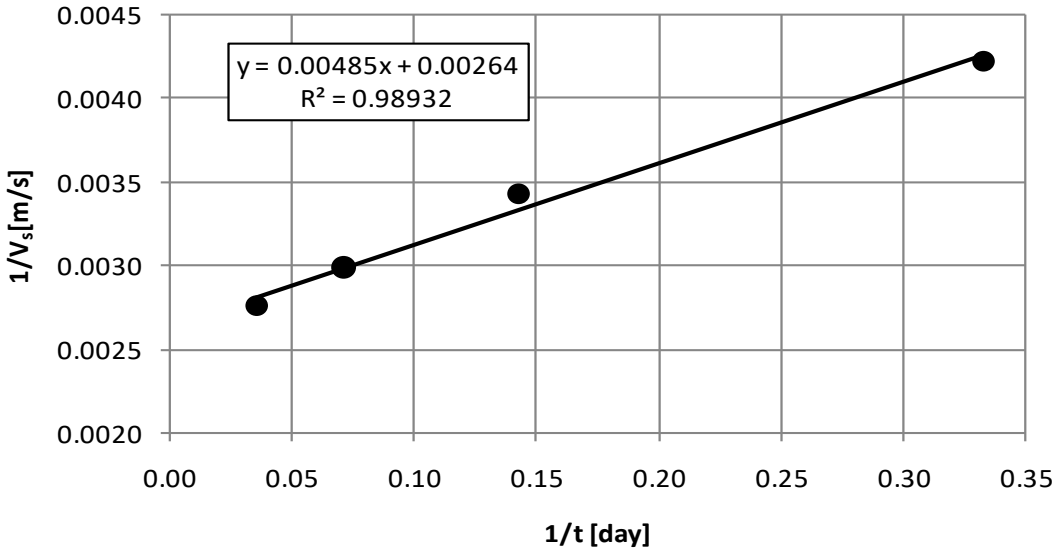


Figure 4-25 The relationship between $\frac{1}{V_s}$ and $\frac{1}{t}$ after Piriyakul (2013b).

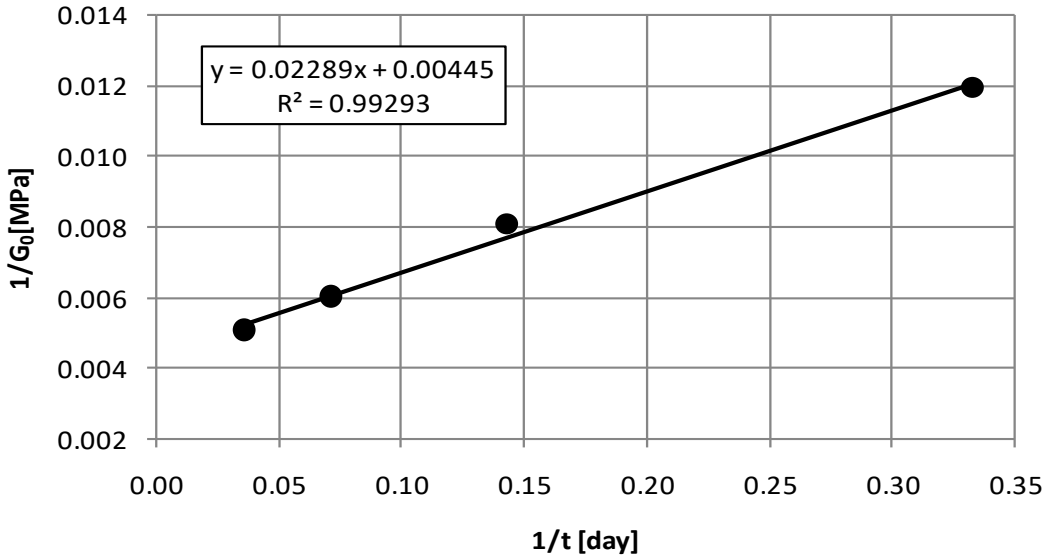


Figure 4-26 The relationship between $\frac{1}{G_0}$ and $\frac{1}{t}$ after Piriyakul (2013b).

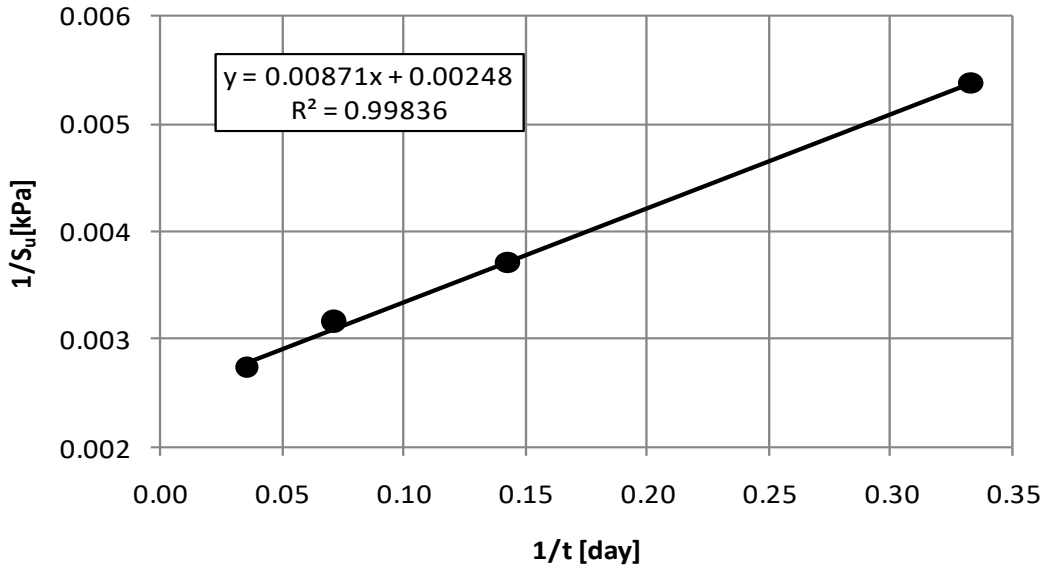


Figure 4-27 The relationship between $\frac{1}{S_u}$ and $\frac{1}{t}$ after Piriyakul (2013b).

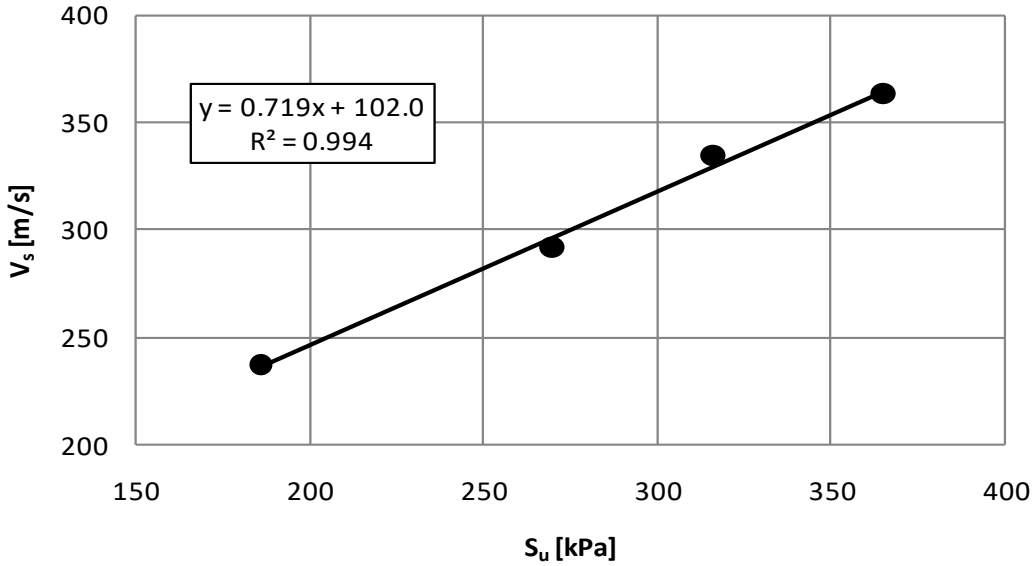


Figure 4-28 The relationship between V_s and S_u after Piriyakul (2013b).

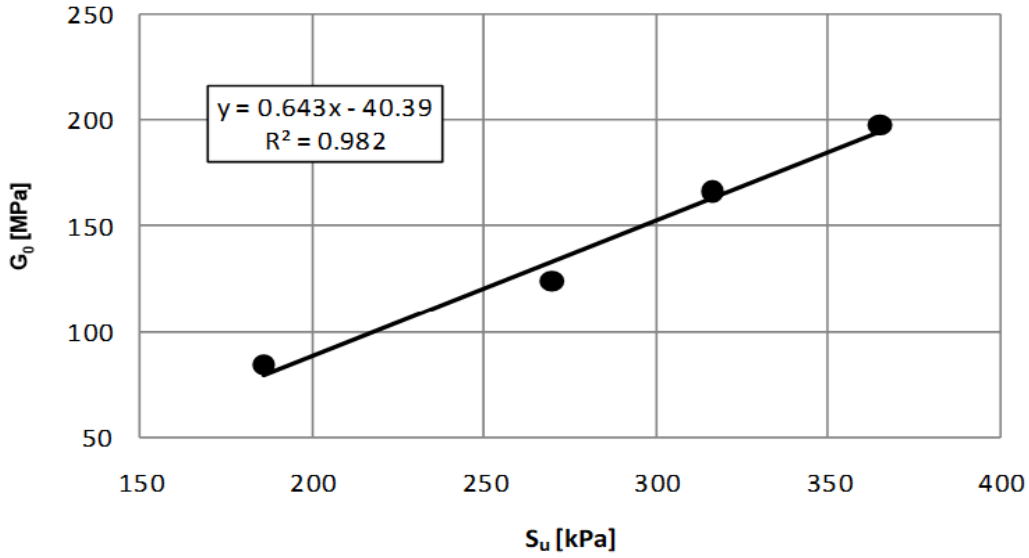


Figure 4-29 The relationship between G_0 and S_u after Piriyakul (2013b).

Table 4-7 Test results of Bangkok clay after Piriyakul (2013b).

Curing time [day]	V_s [m/s]	G_0 [MPa]	S_u [kPa]
3	237	84	186
7	292	124	270
14	335	166	316
28	363	197	365

4.9 Challenges and Limitations of Shear Wave Data Analysis and Interpretation

Despite the widespread use of shear wave velocity (V_s) and initial shear modulus (G_0) in modern geotechnical engineering, the analysis and interpretation of shear wave data remain subject to a number of significant challenges. One of the most fundamental limitations involves the identification of the first arrival time of the shear wave, which is critical for accurate V_s calculation. This task is often complicated by waveform distortions, low signal-to-noise ratios, and the superposition of compressional (P-wave) and shear wave components. In particular, in soft soils or saturated conditions, the low amplitude and clarity of the received signals may result in subjective or inconsistent interpretations across different analysts or test repetitions. The issue is further exacerbated in laboratory-scale tests, such as bender element testing, where near-field effects can dominate. When the source-receiver distance is on the order of one to five wavelengths, the recorded waveform can contain complex interactions, making it difficult to distinguish the true shear wave component from the near-field P-wave or other boundary-induced artifacts.

Additional complexity arises from the inherent nature of wave propagation in heterogeneous or layered soils. In such conditions, shear waves may undergo dispersion, where wave velocity varies with frequency, and mode conversion, where shear waves transform into surface or Rayleigh waves. These phenomena can lead to waveform distortions that complicate both time-domain and frequency-domain analyses, particularly in spectral methods such as the Multi-channel Analysis of Surface Waves (MASW). Moreover, equipment limitations—including insufficient sensor resolution, poor transducer-soil coupling, and interference from environmental noise—can further obscure signal clarity, especially in field applications.

Even under ideal conditions, the interpretation of V_s must be approached with caution, as the measured values reflect the soil's behavior under very small strain conditions (typically <0.001%). Most geotechnical design applications, however, require knowledge of soil behavior under large or nonlinear strain conditions, necessitating the use of modulus degradation curves or empirical correlations.

Another critical issue is the sensitivity of shear wave velocity to in-situ stress conditions and soil structure. Variations in confining pressure, overconsolidation ratio, and degree of saturation can significantly affect wave propagation characteristics. In the absence of correction or normalization for these variables, the use of raw V_s data may lead to erroneous interpretations. Compounding these difficulties is the lack of standardized procedures for waveform interpretation, signal processing, and equipment calibration, which introduces variability across laboratories and practitioners. In light of these limitations, a robust approach to shear wave data interpretation must incorporate cross-validation with complementary geotechnical tests, careful consideration of testing conditions, and adherence to consistent analytical frameworks.

Exercise 4.1 A soil specimen has a mass density of 1800 kg/m^3 and a length of 100 mm. The calibration time is depicted in Figure 4-30. A shear wave signal of a 1 sinusoidal signal is measured by the bender element test as shown in Figure 4-31. Calculate the shear wave velocity, V_s, and the initial shear modulus, G_0.

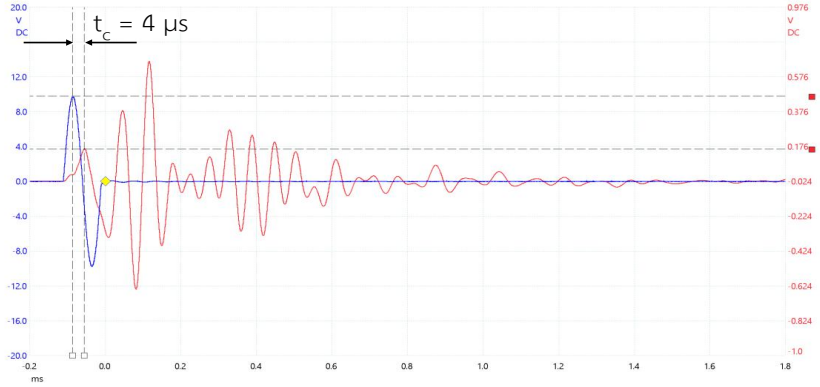


Figure 4-30 Measurement of calibration time for 1 sinusoidal signal.

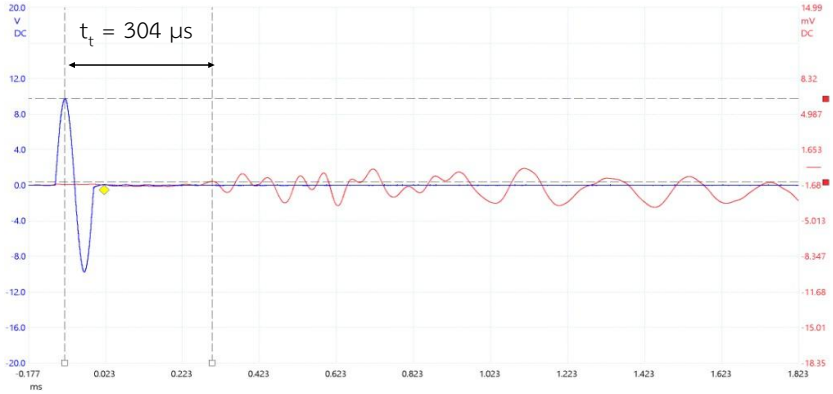


Figure 4-31 Measurement of shear velocity of 1 sinusoidal signal.

Solution

t_c = 4 µs
t_t = 304 µs
L = 100 mm
ρ = 1800 kg/m3

From Equation 4.2, $t = t_t - t_c$

t = 304 – 4 = 300 µs

From Equation 4.2, $V_s = \frac{L}{t} = \frac{100x10^{-3}}{300x10^{-6}}$

V_s = 333 m/s

From Equation 4.4, $G_0 = \rho \cdot V_s^2$

$G_0 = 1800 \times 333^2$

$G_0 = 199.6$ MPa

Ans.

Exercise 4.2 A soil specimen has a mass density of 1800 kg/m^3 and a length of 100 mm. The calibration time is depicted in Figure 4-32. A shear wave signal of a 5 sinusoidal signal is measured by the bender element test as shown in Figure 4-33. Calculate the shear wave velocity, V_s, and the initial shear modulus, G_0.

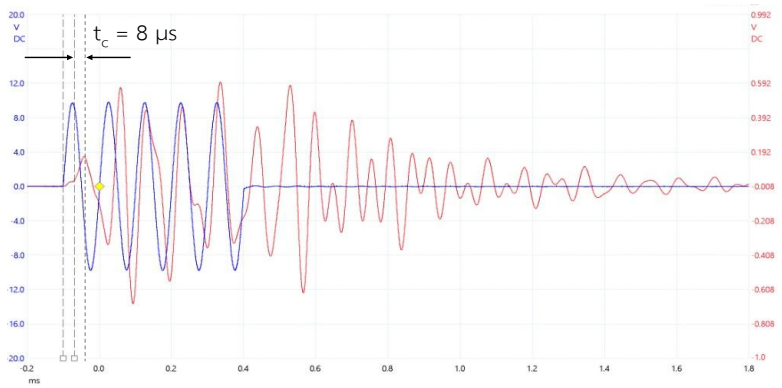


Figure 4-32 Measurement of calibration time for 5 sinusoidal signal.

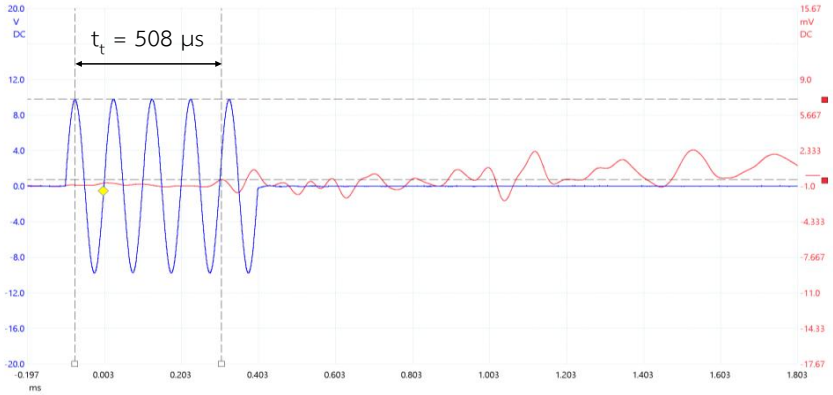


Figure 4-33 Measurement of shear velocity of 5 sinusoidal signal.

Solution

t_c = 8 µs
t_t = 508 µs
L = 100 mm
ρ = 1800 kg/m3

From Equation 4.2, $t = t_t - t_c$

t = 508 – 8 = 500 µs

From Equation 4.2, $V_s = \frac{L}{t} = \frac{100x10^{-3}}{500x10^{-6}}$

V_s = 200 m/s

From Equation 4.4, $G_0 = \rho \cdot V_s^2$

$G_0 = 1800 \times 200^2$

G_0 = 72 MPa

Ans.

Exercise 4.3 A soil specimen has a mass density of 1800 kg/m^3 and a length of 100 mm. The calibration time is depicted in Figure 4-34. A shear wave signal of a 1 triangle signal is measured by the bender element test as shown in Figure 4-35. Calculate the shear wave velocity, V_s, and the initial shear modulus, G_0.

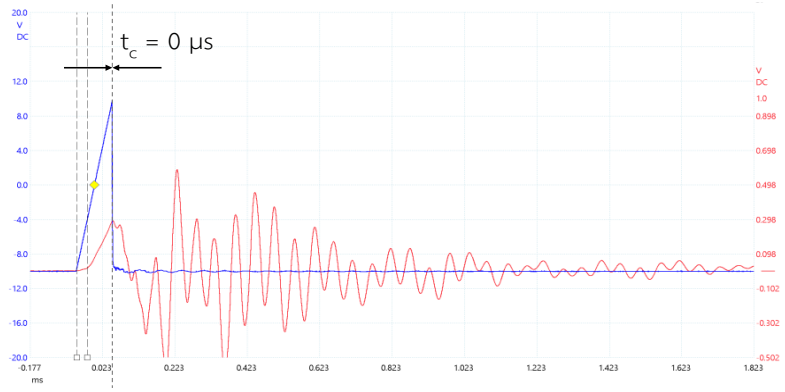


Figure 4-34 Measurement of calibration time for 1 triangle signal.

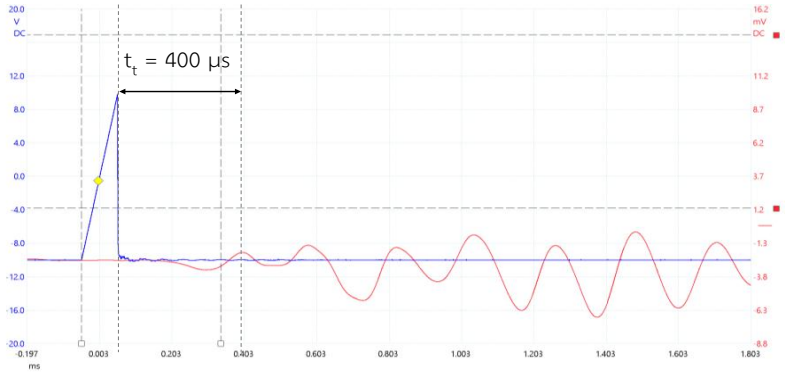


Figure 4-35 Measurement of shear velocity of 1 triangle signal.

Solution

t_c = 0 µs
t_t = 400 µs
L = 100 mm
ρ = 1800 kg/m3

From Equation 4.2, $t = t_t - t_c$
t = 400 – 0 = 400 µs

From Equation 4.2, $V_s = \frac{L}{t} = \frac{100x10^{-3}}{400x10^{-6}}$
V_s = 250 m/s

From Equation 4.4, $G_0 = \rho \cdot V_s^2$
$G_0 = 1800 \times 250^2$
G_0 = 112.5 MPa

Ans.

Exercise 4.4 A soil specimen has a mass density of 1800 kg/m^3 and a length of 100 mm. The calibration time is depicted in Figure 4-36. A shear wave signal of a 5 triangle signal is measured by the bender element test as shown in Figure 4-37. Calculate the shear wave velocity, V_s, and the initial shear modulus, G_0.

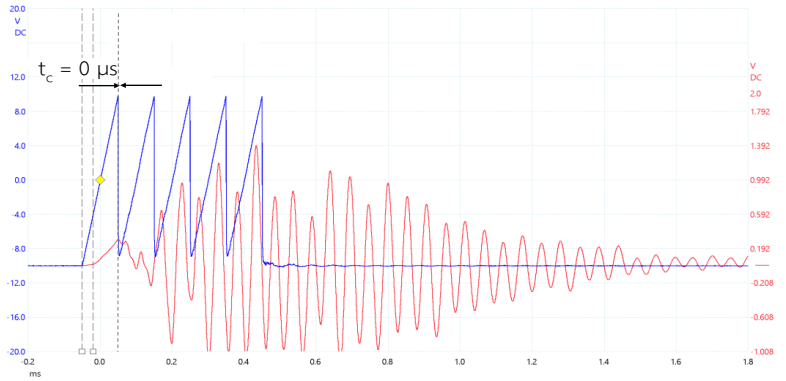


Figure 4-36 Measurement of calibration time for 5 triangle signal.

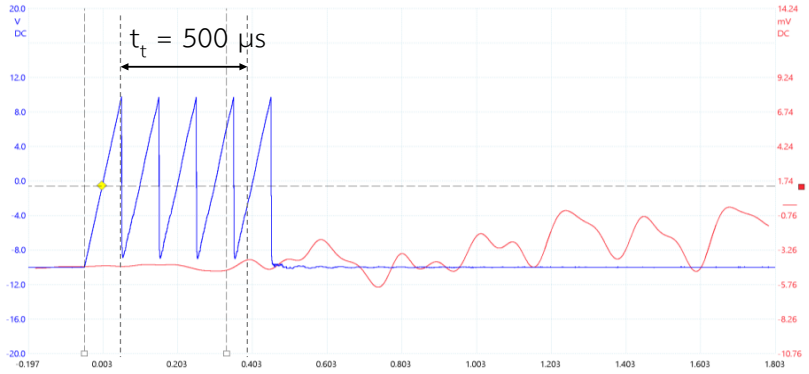


Figure 4-37 Measurement of shear velocity of 5 triangle signal.

Solution

t_c = 0 µs
t_t = 500 µs
L = 100 mm
ρ = 1800 kg/m3

From Equation 4.2, $t = t_t - t_c$

t = 500 – 0 = 500 µs

From Equation 4.2, $V_s = \frac{L}{t} = \frac{100x10^{-3}}{500x10^{-6}}$

V_s = 200 m/s

From Equation 4.4, $G_0 = \rho \cdot V_s^2$

$G_0 = 1800 \times 200^2$

G_0 = 72 MPa

Ans.

Exercise 4.5 A soil specimen has a mass density of 1800 kg/m^3 and a length of 100 mm. The calibration time is depicted in Figure 4-38. A shear wave signal of a 1 square signal is measured by the bender element test as shown in Figure 4-39. Calculate the shear wave velocity, V_s, and the initial shear modulus, G_0.

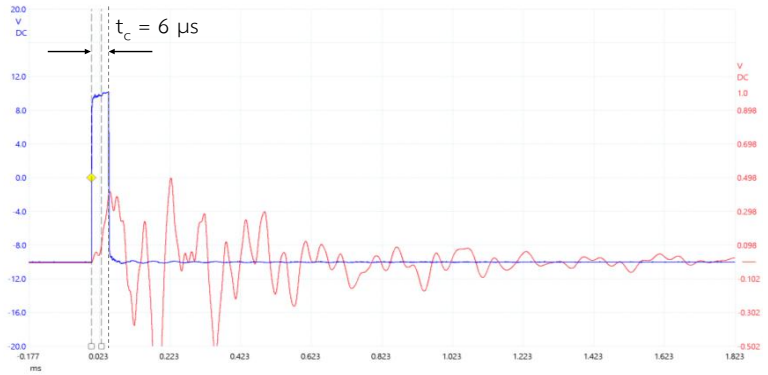


Figure 4-38 Measurement of calibration time for 1 square signal.

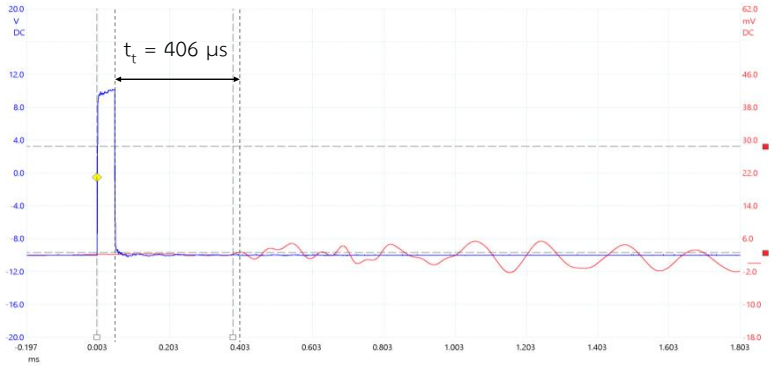


Figure 4-39 Measurement of shear velocity of 1 square signal.

Solution

t_c = 6 µs
t_t = 406 µs
L = 100 mm
ρ = 1800 kg/m3

From Equation 4.2, $t = t_t - t_c$

t = 406 – 6 = 400 µs

From Equation 4.2, $V_s = \frac{L}{t} = \frac{100x10^{-3}}{400x10^{-6}}$

V_s = 250 m/s

From Equation 4.4, $G_0 = \rho \cdot V_s^2$

$G_0 = 1800 \times 250^2$

G_0 = 112.5 MPa

Ans.

Exercise 4.6 A soil specimen has a mass density of 1800 kg/m^3 and a length of 100 mm. The calibration time is depicted in Figure 4-40. A shear wave signal of a 5 square signal is measured by the bender element test as shown in Figure 4-41. Calculate the shear wave velocity, V_s, and the initial shear modulus, G_0.

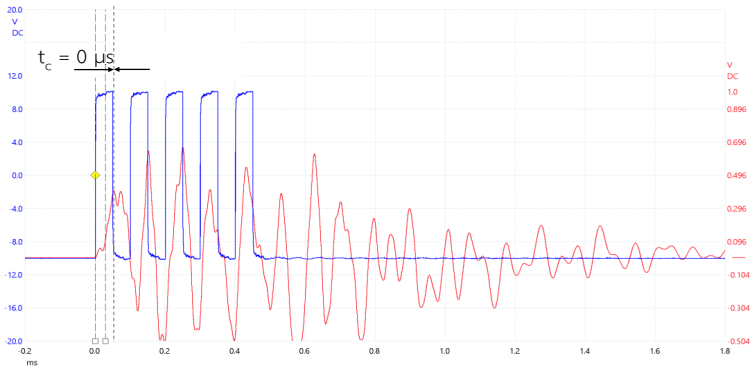


Figure 4-40 Measurement of calibration time for 5 square signal.

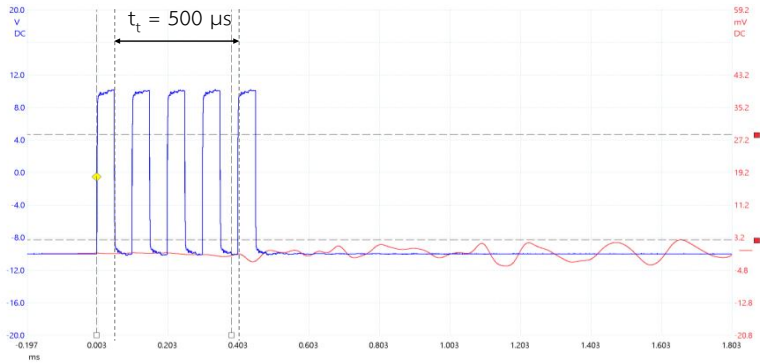


Figure 4-41 Measurement of shear velocity of 5 square signal.

Solution

t_c = 0 µs
t_t = 500 µs
L = 100 mm
ρ = 1800 kg/m3

From Equation 4.2, $t = t_t - t_c$
t = 500 – 0 = 500 µs

From Equation 4.2, $V_s = \frac{L}{t} = \frac{100x10^{-3}}{500x10^{-6}}$
V_s = 200 m/s

From Equation 4.4, $G_0 = \rho \cdot V_s^2$
$G_0 = 1800 \times 200^2$
$G_0 = 72$ MPa

Ans.

Exercise 4.7 A clay specimen has a mass density of 1949 kg/m^3 a tip to tip distance between the sensors is 83.96 mm. Figure 4-42 shows a continuously sinusoidal waveform and the Table 4-42 presents the frequency that comes into the same phase with different number of wavelengths. Calculate the shear wave velocity, V_s, and the initial shear modulus, G_0.

Table 4-8 Number of wavelengths and frequencies in phase of a clay specimen.

No. of wavelengths	f (Hz)
1	2050
2	3915
3	6150
4	9012
5	11050

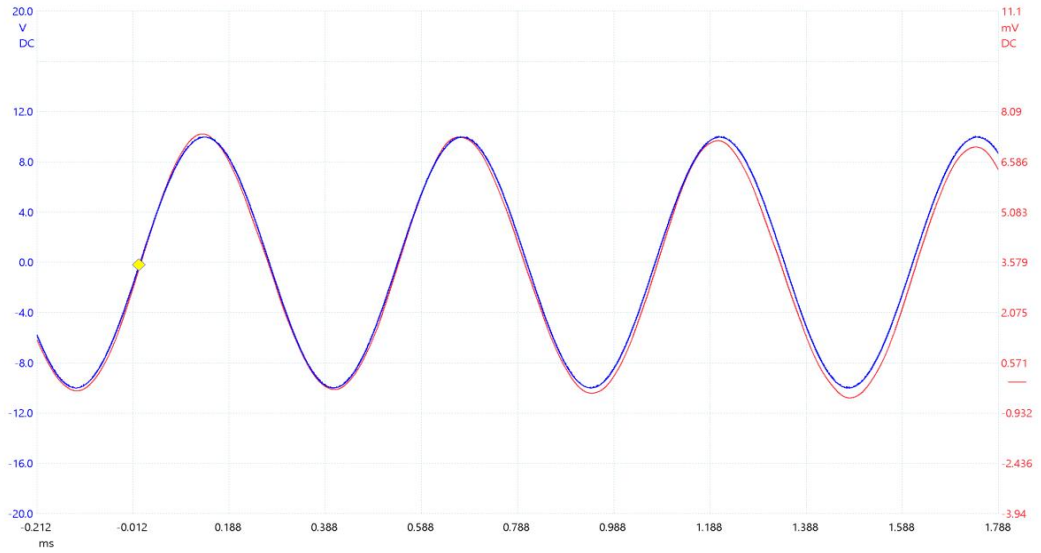


Figure 4-42 A continuously sinusoidal waveform.

Solution
L = 83.96 mm
N = 4
f = 9012 Hz

From Equation 4.3, $V_s = \left(\frac{L}{N}\right) \cdot f = \left(\frac{83.96 \times 10^{-3}}{4}\right) \times 9012$
V_s= 189.16 m/s

From Equation 4.4, $G_0 = \rho \cdot V_s^2 = 1949 \times 189.16^2$
G_0= 69.74 MPa

Like this calculation, Table 4-9 presents the shear wave velocity, V_s, and the initial shear modulus, G_0.

Table 4-9 Number of wavelengths, f, V_s, and G_0 of a clay specimen.

No. of wavelengths	f (Hz)	V_s (m/s)	G_0 (MPa)
1	2050	172.12	57.74
2	3915	164.22	52.56
3	6150	172.12	57.74
4	9012	189.16	69.74
5	11050	185.55	67.10

Ans.

Summary

Shear wave testing plays a pivotal role in modern geotechnical engineering, offering a non-destructive means of evaluating the small-strain stiffness of soils through the measurement of shear wave velocity (V_S) and the corresponding initial shear modulus (G_0). These parameters are fundamental in characterizing soil behavior under dynamic and static loading, particularly in applications such as seismic site response, ground improvement monitoring, and performance-based foundation design. However, the accuracy and applicability of shear wave data are contingent upon rigorous data interpretation and an in-depth understanding of the method's inherent limitations. The analysis in this study has highlighted several key challenges, including ambiguity in identifying the first arrival of the shear wave, distortions caused by near-field effects, limitations of signal quality and equipment sensitivity, and the influence of stress state, soil structure, and boundary conditions. These factors contribute to uncertainty in data interpretation and can compromise the reliability of engineering decisions if not properly addressed.

To improve the consistency and accuracy of shear wave data interpretation, several recommendations are proposed. First, the adoption of standardized procedures for waveform analysis—such as using defined arrival time criteria, signal cross-correlation, or frequency-domain methods—should be prioritized to reduce operator subjectivity and inter-laboratory variability. Where applicable, automated or semi-automated signal processing tools should be employed to enhance repeatability. Second, near-field effects, which are particularly problematic in short specimen lengths or bender element tests, must be accounted for through careful sensor placement and appropriate travel time correction techniques. In field applications, it is crucial to consider factors such as layering, saturation, and overconsolidation ratio, as these significantly influence shear wave propagation and V_s values.

Moreover, shear wave data should not be interpreted in isolation. Integration with conventional geotechnical data—such as unconfined compressive strength, cone penetration resistance, and consolidation parameters—provides a broader context for understanding the soil's mechanical behavior. This integrative approach allows for more robust correlations between small-strain stiffness and large-strain performance. Where applicable, modulus reduction curves should be employed to link G_0 to strain-dependent moduli for use in design. Future developments in machine learning and real-time signal analysis offer promising pathways to enhance interpretation accuracy and efficiency. Ultimately, the reliability and usefulness of shear wave data in engineering practice depend on careful measurement, standardized interpretation, and thoughtful integration with other geotechnical information. By adopting these practices, practitioners can maximize the benefits of shear wave testing for both research and applied engineering purposes.

Questions and Problems

1. Figure 4-43 shows the offset time (t_c) and Figure 4-44 presents the total recorded time (t_t), if the soil sample is 100 mm in length. What is the shear wave velocity (V_s)?

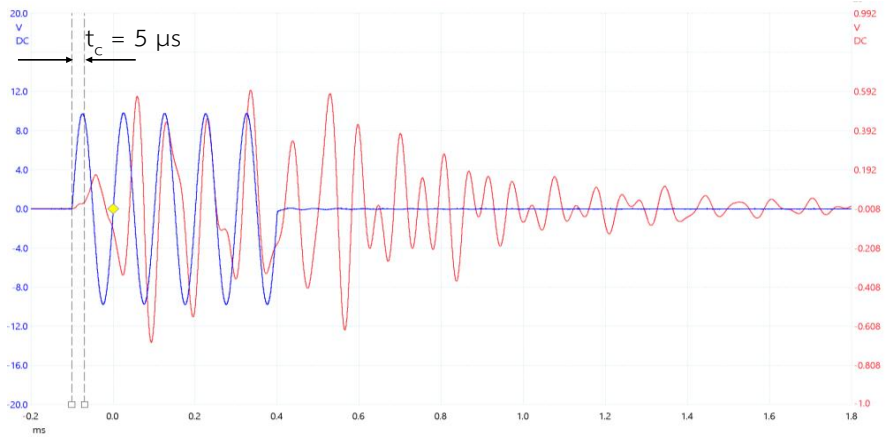


Figure 4-43 The offset time (t_c).

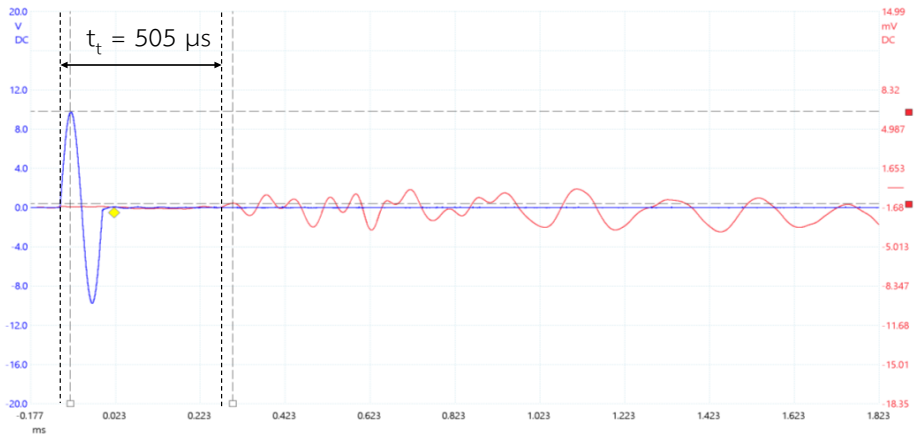


Figure 4-44 The total recorded time (t_t).

2. From exercise 1, if the soil density is 1,700 kg/m^3. What is the initial shear modulus (G_0)?
3. What is the near field effect?
4. Why should calibrate the sensors?
5. What is the advantage of using ASTM D8295–19?
6. What are the effects of waveforms?
7. What would happen if the shear wave propagated into the water?
8. How do you characterize the Bangkok formation by shear wave?
9. What is the advantage of integration of shear wave data with other geotechnical results?
10. What are limitations of shear wave data analysis and interpretation?

Chapter 5: Applications of Shear Wave Testing in Geopolymeric Materials

5.1 Introduction of Geopolymeric Materials

Ground improvement techniques have been extensively adopted in civil construction worldwide, with more than 40,000 infrastructure projects annually relying on such methods to enhance soil strength, reduce settlement, and control permeability as described in DeJong (2010). Traditionally, cement and chemical binders served as primary materials owing to their availability and cost-effectiveness. However, large-scale cement production imposes substantial energy demands and generates considerable environmental burdens, driving growing interest in sustainable alternatives. Among the most promising are geopolymer materials, which offer rapid strength development, high compressive strength, reduced carbon footprint, and favorable economics as shown in Alaskar (2020). Geopolymers can be synthesized from a wide range of aluminosilicate sources including fly ash, blast furnace slag, rice husk ash, silica fume, and metakaolin. Metakaolin in particular has attracted considerable research attention as a geopolymer precursor, produced by calcining kaolin clay at temperatures ranging from 450 to 800 °C, with approximately 700 °C identified as optimal as reported by Biel et al. (2020) and Elimbi et al. (2011). Its physicochemical characteristics have been extensively investigated through X-ray diffraction, chemical composition analysis, specific surface area measurement, nuclear magnetic resonance spectroscopy, and compressive strength testing as described in Takeda et al. (2013), Tataranni et al. (2018), Guzmán-Aponte et al. (2017), Sullivan et al. (2018) and Lopes et al. (2020).

The versatility of metakaolin-based materials has been demonstrated across a broad spectrum of applications. As a partial cement replacement in concrete, an optimal substitution level of approximately 20% was found to significantly enhance sorptivity, permeability, and long-term durability as noted by Nas & Kurbetci (2018). In alkali-activated mortars, the combination of metakaolin with fly ash and furnace slag yielded sustainable Portland cement-free binders with favorable workability and compressive strength as reported by Attanasio et al. (2018). In mass concrete, ternary mixtures incorporating metakaolin reduced internal temperatures and minimized the risk of delayed ettringite formation as shown by Hamid et al. (2018). Further applications include thermal insulating cores for sandwich panels as described in Natali Murri et al. (2017), cultural heritage restoration combined with epoxy resin as explained by Ricciotti et al. (2017), carbon dioxide adsorption binders as described in Vegere et al. (2019) and Pereira et al. (2018), and high-strength cold-bonded lightweight aggregates as shown by Vali & Murugan (2020). Systematic investigations revealed that compressive strengths approaching 90 MPa can be achieved when the silica-to-alumina ratio exceeds 2.3, the sodium oxide-to-alumina ratio falls between 0.6 and 1.2, and the water-to-sodium oxide ratio remains below 12 as noted by Abadel et al. (2021). Complementary studies developed microstructural models for carbonation in metakaolin-blended concrete as described in Wang & Lee (2019) and examined the combined effects of nano-CuO and polypropylene fibers on mechanical performance using ANFIS and support vector machine predictive models as established by Ghanei et al. (2017).

Non-destructive testing methods have played an indispensable role in characterizing both geomaterials and cementitious systems. Kang et al. (2021) employed microphones to detect cavities beneath plate structures and successfully estimated cavity dimensions based on sound wave responses, highlighting the potential of microphones as effective tools for cavity identification. Within soil mechanics, bender element testing has emerged as one of the most effective non-destructive techniques. In soil mechanics, bender element testing utilizing piezoelectric sensors has emerged as one of the most reliable approaches for measuring shear wave velocity and initial shear modulus as described in Shirley, & Hampton (1978), Brignoli et al. (1996) and Piriyakul (2010). This technique has been extended to evaluate thawing and stress restoration in frozen sandy soils as explained in Kim et al. (2021), capillarity-to-cementation transitions in fine sand as described in Park et al. (2021), shear wave propagation in compacted soils using piezoelectric ring benders as clearly explained by Kim et al. (2021), stress-dependent elastic wave behavior in modified oedometer configurations as outlined by Lee et al. (2020), crack propagation monitoring in rocks as shown by Ahn et al. (2020), transitional soil behavior under overburden pressure as reported by Kim, et al. (2021), and dynamic properties of recycled concrete aggregate blended with rubber chips as noted by of Gabryś et al. (2017). In parallel, investigations into alkali-activated slag concrete established that Na_2O content exceeding 6% combined with Na_2O-to-SiO_2 ratios greater than 1.0 reduced workability and accelerated setting, while maximum strengths of approximately 25 MPa were achieved within 24 hours as presented by Choi & Lee (2019).

Wave-based monitoring of setting and hardening in cementitious and geopolymer systems has been an equally active research domain. Derivative-based analytical methods applied to bender element data have enabled precise determination of initial and final setting times of cement mortars as noted by Zhu et al. (2018), with ultrasonic shear waves further confirming their superior reliability over compressional waves for this purpose as described in Liu et al. (2014). Continuous ultrasonic monitoring devices have been developed to track the full hardening cycle of cement, gypsum, lime, and novel binders as quality control tools as indicated by Reinhardt & Grosse (2004), while combining ultrasonic pulse velocity with Vicat needle testing demonstrated accurate prediction of initial setting times from velocity curve inflection points as established by Ylmén et al. (2009). Ultrasonic measurements have also been applied to assess concrete degradation from alkali–silica reaction as demonstrated by Ju et al. (2016). For geopolymer systems, fiber Bragg grating sensors enabled precise tracking of early-age shrinkage and temperature development in metakaolin geopolymers as noted by Palumbo et al. (2017), and ultrasonic devices revealed how reduced water-to-binder ratios, elevated curing temperatures, and silica fume incorporation collectively enhance early microstructure formation as reported by Liu et al. (2011). The present study builds upon this body of knowledge by employing piezoelectric bender element sensors to characterize metakaolin geopolymer pastes produced from kaolin calcined at 0, 200, 800, 1000, and 1200 °C, mixed at powder-to-solution ratios of 0.8:1.0 to 1.5:1.0 and across seven sodium hydroxide-to-sodium silicate ratio configurations, with initial and final setting times validated against standard Vicat needle tests.

5.2 Geopolymeric Materials and Methods

Metakaolin geopolymer was synthesized through the thermal treatment of kaolin powder at calcination temperatures of 200, 800, 1000, and 1200 °C, as illustrated in Figure 1. A control sample at 0 °C, which was not subjected to thermal treatment, was also included for comparison. The prepared metakaolin was blended with geopolymer solution at different mixing ratios of 0.8:1.0, 1.0:1.0, 1.2:1.0, and 1.5:1.0, where the first value corresponds to the proportion of metakaolin and the second to the geopolymer solution. The geopolymer solution was formulated by combining sodium hydroxide at a concentration of 10 N with sodium silicate. The ratio between sodium hydroxide and sodium silicate was varied systematically as 1.0:1.0, 1.0:1.2, 1.0:1.5, 1.0:2.0, 1.2:1.0, 1.5:1.0, and 2.0:1.0. The chemical composition of the kaolin used in this study is presented in Table 1, while its basic engineering properties are summarized in Table 2. The kaolin was found to consist of very fine particles, all of which were able to pass through ASTM mesh number 400.

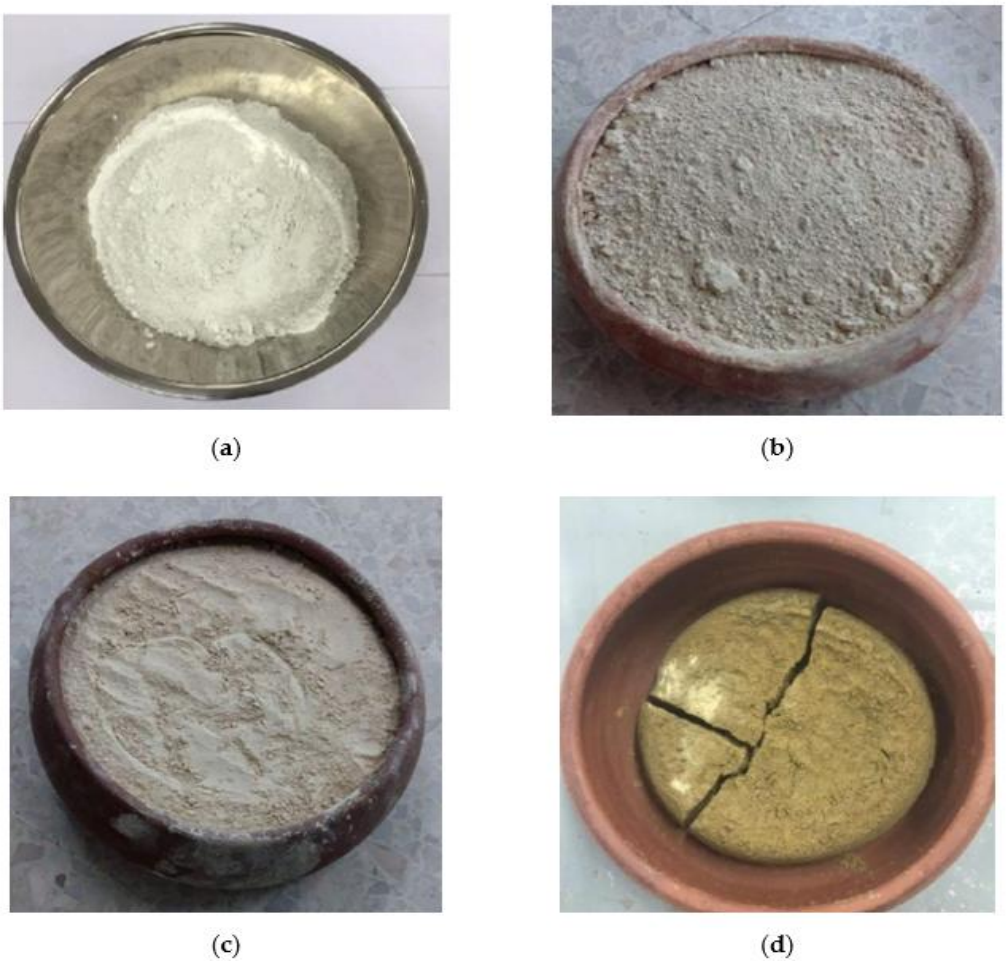


Figure 5-1 Thermal treatment of kaolin at the calcined temperatures:
(a) 200°C; (b) 800°C; (c) 1000°C; (d) 1200°C after Iamchaturapatr et al. (2022b).

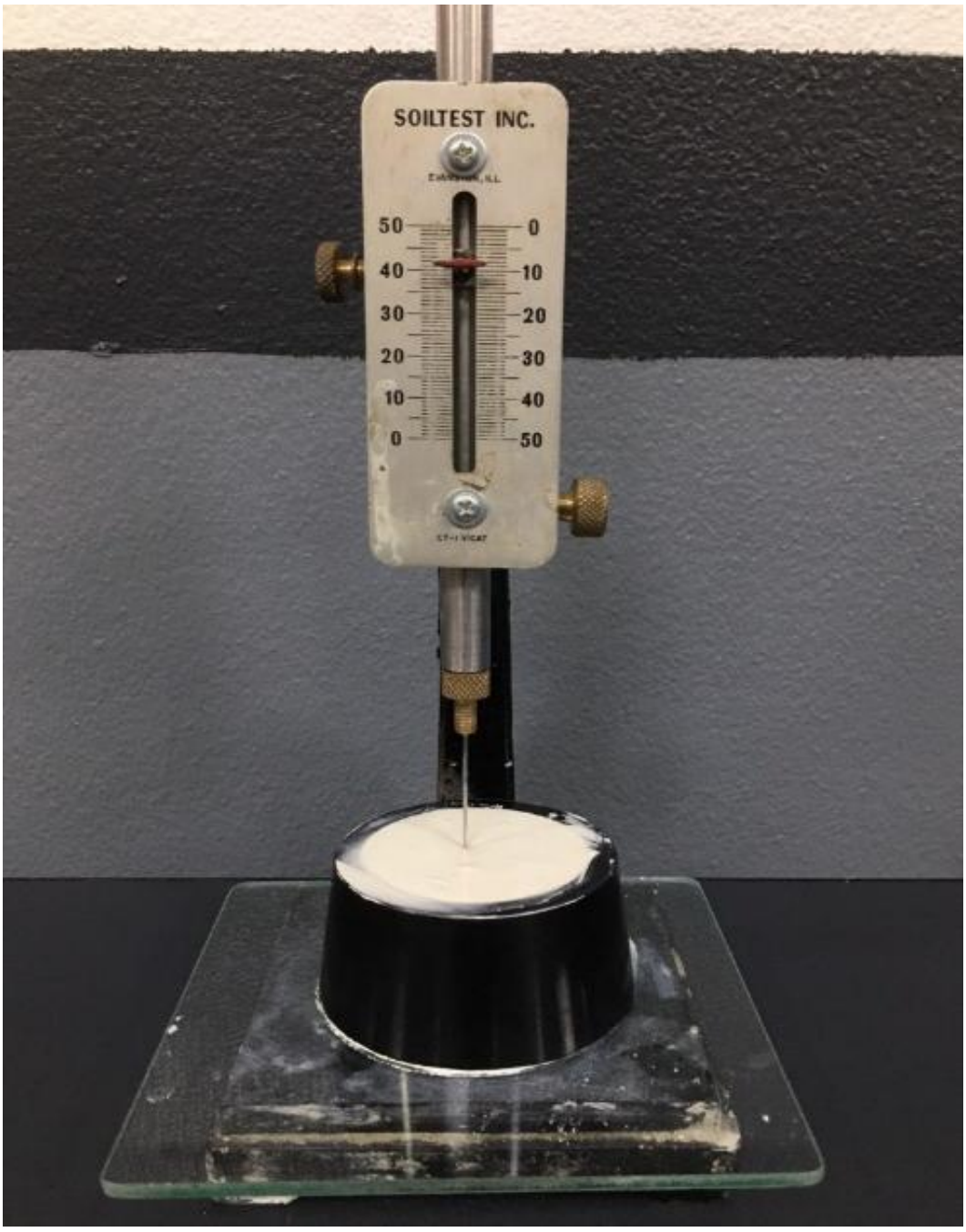


Figure 5-2 The Vicat needle apparatus after Iamchaturapatr et al. (2022b).

Table 5-1. Chemical composition of kaolin.

Chemical composition	%
SiO_2	65-70
Al_2O_3	17-20
K_2O	4.20
Na_2O	3.30
MgO	1.66
Fe_2O_3	< 1.60
TiO_2	0.10
CaO	0.07

Table 5-2. Basic engineering properties of kaolin.

Properties	Unit
Moisture	1.0% max.
Particle size pass through mesh No. 400	100%
Finer than 2 microns	30-40%
pH	6.5±1
Oil absorption	37±2 gm/100 gm
Brightness	80±2%
Liquid limit	46.84%
Plastic limit	34.19%
Plastic index	12.65%
Total unit weight	2.36 T/m^3

In accordance with ASTM C191-08, which specifies the standard test method for determining the setting time of hydraulic cement using the Vicat needle, tests were performed on metakaolin geopolymer paste to evaluate both the initial and final setting times. The Vicat needle apparatus is illustrated in Figure 6. The initial setting time was identified at the point where the penetration reached 25 millimeters, whereas the final setting time was defined as the stage at which no further penetration of the needle was observed.

5.3. Results and discussions

5.3.1. Effect of Thermal Treatment on Metakaolin

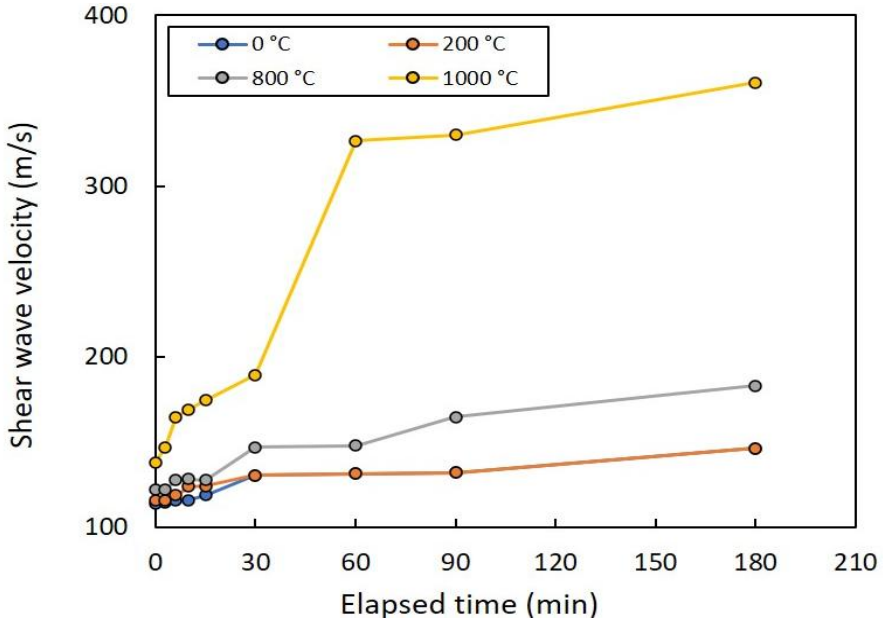


Figure 5-3. The shear wave velocity varied with elapsed time for thermal treatment after Iamchaturapatr et al. (2022b).

The effect of thermal treatment on metakaolin geopolymer was shown in Figure 5-3. The metakaolin geopolymer control sample was no treatment and showed as 0°C. The other metakaolin geopolymer samples were treated with calcined temperatures of 200, 800, 1000 and 1200°C. In order to investigate the effect of thermal treatment, the mixing ratio between the metakaolin powder and the geopolymer solution was also controlled at 1.0:1.0. The geopolymer solution mixing ratio between sodium hydroxide (NaOH) and sodium silicate (Na_2SiO_3) was fixed at 2.0:1.0. In general, it was found that the shear wave velocity data of all metakaolin geopolymer pastes samples were increased when the elapsed time increased. The measurement of shear wave velocity for geopolymer material is clearly described in Piriyakul & Iamchaturapatr, (2014).

For the metakaolin geopolymer paste specimens subjected to thermal treatments of 0 and 200 °C, the shear wave velocity increased only slightly, from approximately 115 meters per second to 146 meters per second over a testing period of 180 minutes. This indicated that no significant improvement in shear wave velocity occurred as a result of geopolymerization under these conditions. In contrast, the specimen treated at 800 °C demonstrated a moderate enhancement, with shear wave velocity rising from about 122 meters per second to 183 meters per second during the same elapsed time. The bender element test data further revealed that the sample treated at 1000 °C exhibited the highest shear wave velocity across all measured intervals, increasing from 138 meters per second to 361 meters per second. These results confirm that 1000 °C represents the optimum calcination temperature for metakaolin preparation. The initial and final setting times of the metakaolin geopolymer paste specimens were also determined using the Vicat needle apparatus. As shown in Figure 5-4, the initial setting time was defined at a penetration depth

of 25 millimeters. Overall, it was observed that higher calcination temperatures corresponded to shorter setting times. For the untreated control sample at 0 °C, the initial setting time was approximately 123 minutes. In comparison, the samples treated at 200, 800, and 1000 °C displayed significantly shorter initial setting times of 71, 48, and 12 minutes, respectively. For the kaolin treated at 1200°C, this metakaolin was changed into the ceramic. So, it could not be able to mix with any geopolymer solutions. In the same way, the final setting time results were measured and found that only the metakaolin geopolymer pasted sample treated at 1000°C has the final setting time of 30 minutes while other metakaolin geopolymer paste samples were about 180 minutes or more. Therefore, it was confirmed the finding for the shear wave velocity test that the metakaolin with the thermal treatment at 1000°C was the optimum temperature.

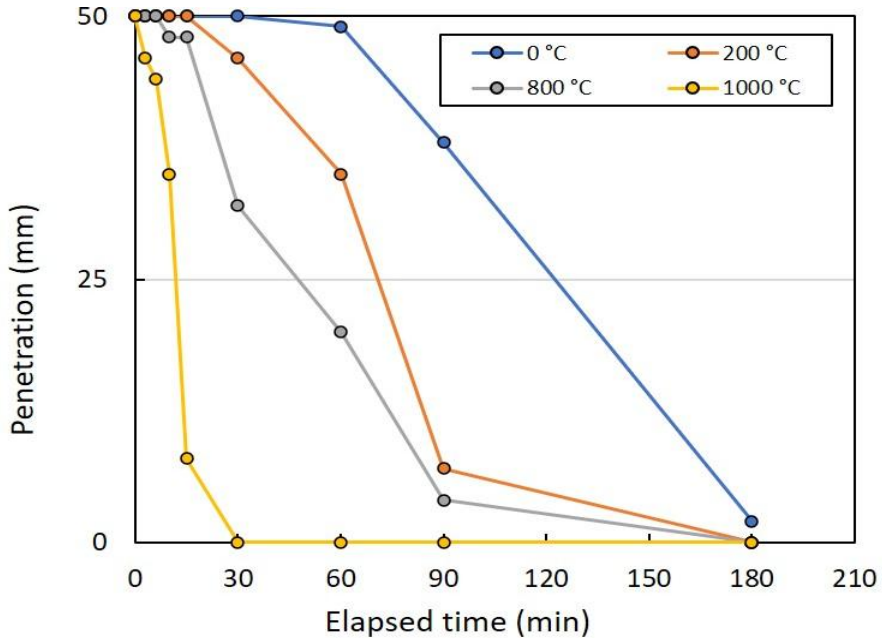


Figure 5-4 The penetration varied with elapsed time for the thermal treatment after Iamchaturapatr et al. (2022b)..

5.3.2. Effect of Mixing on Geopolymer Solution

The effect on the variation for the mixing of geopolymer solution between the sodium hydroxide (NaOH) and the sodium silicate (Na_2SiO_3) was investigated. From the previous section, it was found that the thermal treatment for metakaolin at 1000° was the optimum temperature. Therefore, all metakaolin geopolymer paste samples were prepared with the thermal treatment of 1000°C. Also, the mixing ratio between the metakaolin powder and the geopolymer solution was fixed at 1.0:1.0. The mixing proportion between NaOH and Na_2SiO_3 were 1.0:1.0, 1.0:1.2, 1.0:1.5, 1.0:2.0, 1.2:1.0, 1.5:1.0 and 2.0:1.0. Figure 5-5 showed the strength development with elapsed time of the metakaolin geopolymer paste by shear wave velocity. It was observed that there were no geopolymerization occurred for the mixing proportion between NaOH and Na_2SiO_3 of 1.0:1.0, 1.0:1.2, 1.0:1.5 and 1.0:2.0, since the shear wave velocity data were remained constant. The geopolymerization occurred only with the mixing proportion between NaOH and Na_2SiO_3 of 1.2:1.0, 1.5:1.0

and 2.0:1.0. It was found that the shear wave velocity results were increased from 131 m/s to149 m/s for the mixing proportion between NaOH and Na_2SiO_3 of 1.2:1.0. For the mixing proportion between NaOH and Na_2SiO_3 of 1.5:1.0, the shear wave velocity data changed from 136 m/s to 193 m/s. It was noted that the shear wave velocity results were the maximum with the mixing proportion between NaOH and Na_2SiO_3 of 2.0:1.0 and varied from 138 m/s to 361 m/s. So, the optimum mixing ratio between NaOH and Na_2SiO_3 of 2.0:1.0 was recommended. In the similar way, Figure 5-6 presented the Vicat needle test results of metakaolin geopolymer paste with different mixing ratio between the sodium hydroxide (NaOH) and the sodium silicate (Na_2SiO_3) with the variation of 1.0:1.0, 1.0:1.2, 1.0:1.5, 1.0:2.0, 1.2:1.0, 1.5:1.0 and 2.0:1.0.

From the Vicat needle test results, it was observed that the mixing ratio between the NaOH and Na_2SiO_3 of 1.0:1.0, 1.0:1.2, 1.0:1.5 and 1.0:2.0 have no occurrence of geopolymerization reaction. During 180 minutes, the penetration data were 50 mm showing no any setting of these metakaolin geopolymer paste specimens. The geopolymerization reaction occurred with the only the mixing ratio between the sodium hydroxide (NaOH) and the sodium silicate (Na_2SiO_3) of 1.2:1.0, 1.5:1.0 and 2.0:1.0 since there were the initial setting time results of 8, 8 and 12 minutes respectively while the final setting time data were 15, 15 and 30 minutes respectively.

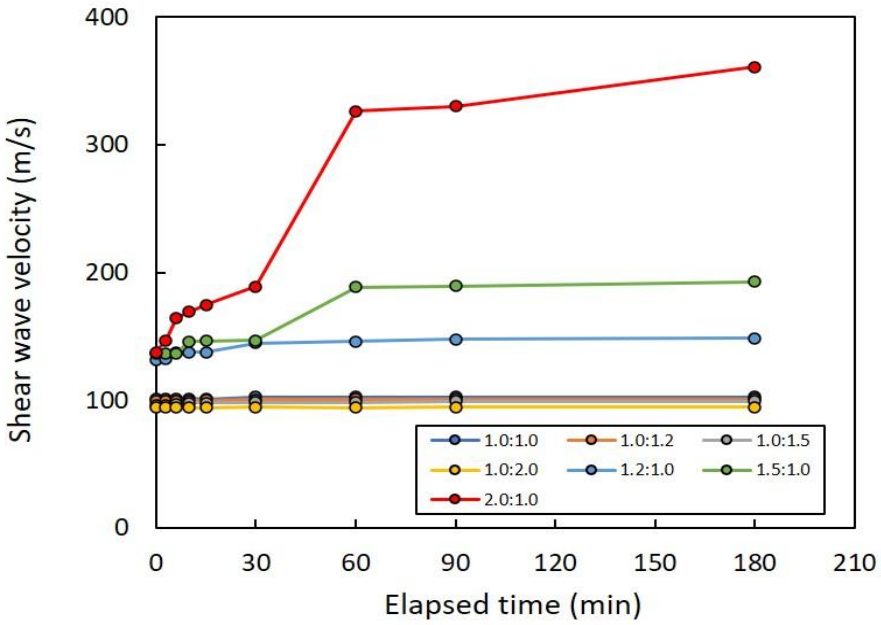


Figure 5-5 The shear wave velocity varied with elapsed time for the mixing of geopolymer solution after Iamchaturapatr et al. (2022b).

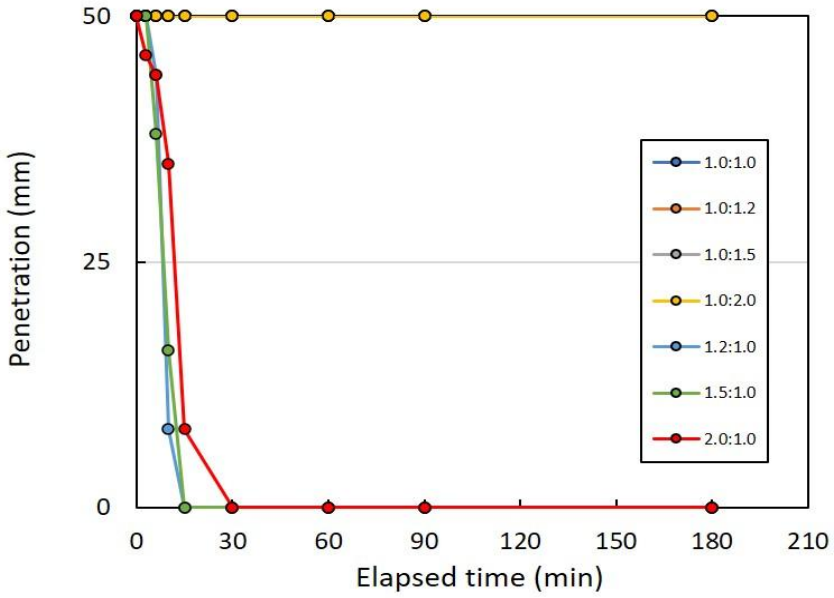


Figure 5-6 The penetration varied with elapsed time for the mixing of geopolymer solution after Iamchaturapatr et al. (2022b).

5.3.3 Effect of Mixed Proportion between the Metakaolin and the Geopolymer Solution

The optimal proportion between metakaolin powder and geopolymer solution was examined using the bender element test. Metakaolin samples thermally treated at 800 °C and 1000 °C were combined with geopolymer solution while maintaining a fixed NaOH-to-Na_2SiO_3 ratio of 2.0:1.0. As shown in Figure 5-7, the shear wave velocity of the specimens treated at 800 °C increased progressively with elapsed time. For example, after 180 minutes the measured shear wave velocities were 165, 183, 189, and 235 meters per second for mixing ratios of 0.8:1.0, 1.0:1.0, 1.2:1.0, and 1.5:1.0, respectively. Among these, the ratio of 1.5:1.0 produced the highest velocity values, indicating it to be the optimum mixing proportion.

A similar trend was observed in the specimens treated at 1000 °C, as illustrated in Figure 5-8. In this case, only two proportions of metakaolin to geopolymer solution could be successfully prepared, namely 0.8:1.0 and 1.0:1.0. The data revealed that the 1.0:1.0 ratio consistently produced higher shear wave velocities compared to the 0.8:1.0 ratio. For instance, after 180 minutes the shear wave velocity of the 1.0:1.0 mixture reached 361 meters per second, whereas the 0.8:1.0 mixture recorded 317 meters per second. These results confirm that a metakaolin-to-geopolymer solution ratio of 1.0:1.0 represents the optimum mixing proportion, producing the maximum shear wave velocity.

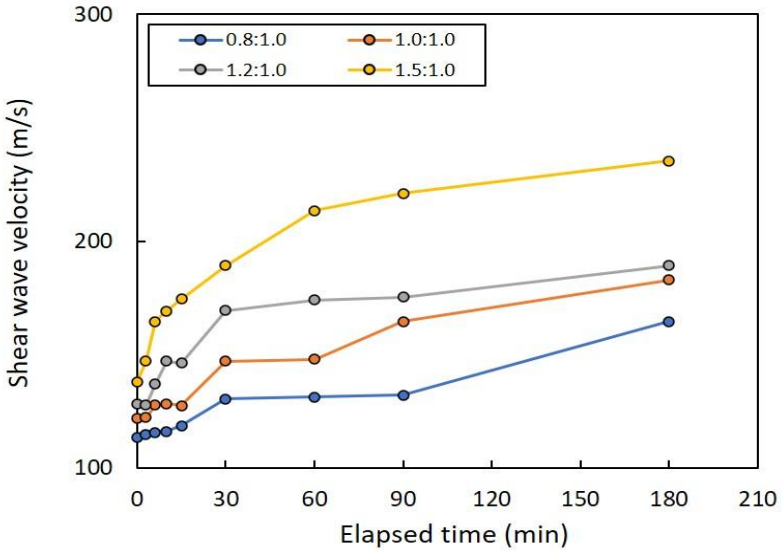


Figure 5-7. The shear wave velocity varied with elapsed time for the mixing proportion between the metakaolin treated at 800°C and the geopolymer solution after Iamchaturapatr et al. (2022b).

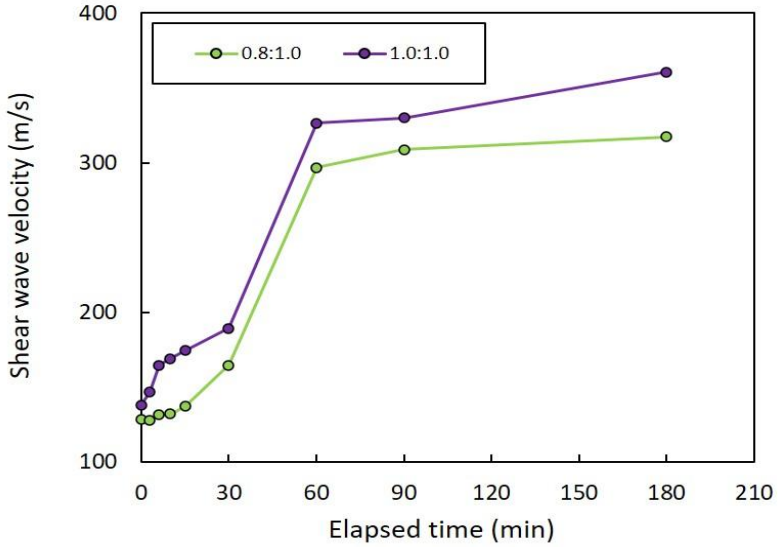


Figure 5-8. The shear wave velocity varied with elapsed time for the mixing proportion between the metakaolin treated at 1000°C and the geopolymer solution after Iamchaturapatr et al. (2022b).

Figure 5-9 presents the Vicat needle test results for metakaolin treated at 800 °C combined with geopolymer solution at different mixing proportions. The initial setting times, defined by a penetration depth of 25 millimeters, were recorded as 123, 48, 23, and 12 minutes for mixing ratios of 0.8:1.0, 1.0:1.0, 1.2:1.0, and 1.5:1.0, respectively. Correspondingly, the final setting times, defined by zero penetration, were 185, 180, 90, and 30 minutes for the same mixing ratios.

Similarly, Figure 5-10 illustrates the Vicat needle test data for specimens prepared with metakaolin treated at 1000 °C. In this case, the initial setting time was 12 minutes for both mixing ratios tested. The final setting times were 60 minutes for the 0.8:1.0 mixture and 30 minutes for the 1.0:1.0 mixture. These findings confirm that the 1.0:1.0 ratio of metakaolin to geopolymer solution represents the optimum proportion, as it yielded the maximum shear wave velocity values.

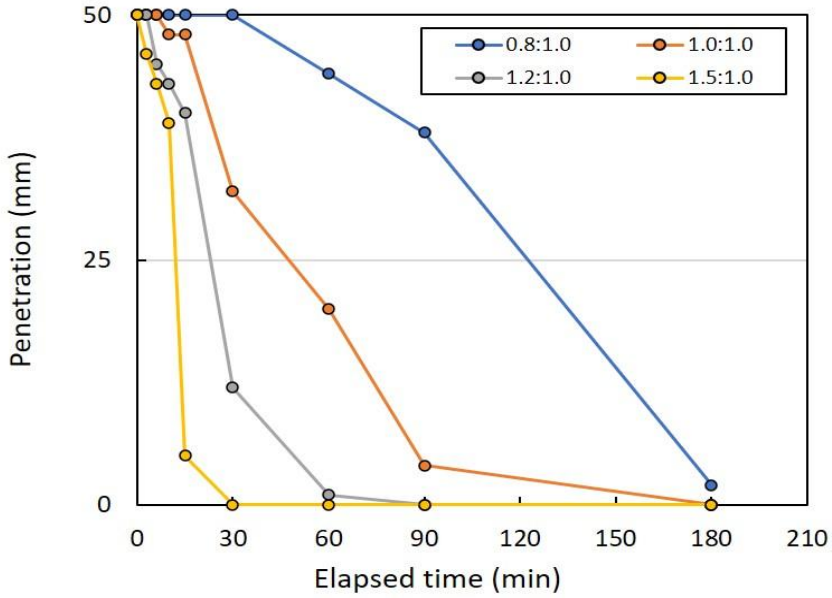


Figure 5-9. The penetration varied with elapsed time for the mixing proportion between the metakaolin treated at 800°C and the geopolymer solution after Iamchaturapatr et al. (2022b).

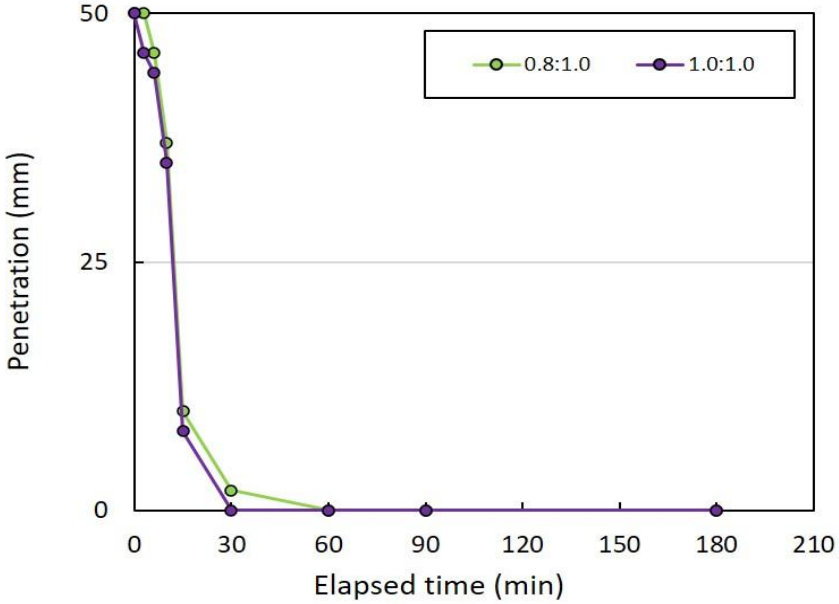


Figure 5-10 The penetration varied with elapsed time for the mixing proportion between the metakaolin treated at 1000°C and the geopolymer solution after Iamchaturapatr et al. (2022b).

5.3.4 Relationship between the S-wave Velocity and Setting Times

The relationship between shear wave velocity and penetration results for metakaolin geopolymer paste is illustrated in Figure 5-11. As described in the preceding sections, the specimens were prepared using metakaolin thermally treated at 1000 °C, with a fixed mixing ratio of 1.0:1.0 between metakaolin powder and geopolymer solution. The geopolymer solution itself was formulated with NaOH-to-Na_2SiO_3 ratios of 1.2:1.0, 1.5:1.0, and 2.0:1.0. The results demonstrated that all mixtures exhibited a linear relationship between shear wave velocity and penetration resistance.

The initial setting times, corresponding to a penetration depth of 25 millimeters, were associated with shear wave velocities of 136, 142, and 168 meters per second for the NaOH-to- Na_2SiO_3 ratios of 1.2:1.0, 1.5:1.0, and 2.0:1.0, respectively. Likewise, the final setting times, defined by the absence of penetration, corresponded to shear wave velocities of 138, 148, and 187 meters per second for the same proportions. Among these, the mixture with a NaOH-to- Na_2SiO_3 ratio of 2.0:1.0 exhibited significantly higher strength development compared with the others. These findings confirm that a ratio of 2.0:1.0 represents the optimum geopolymer solution proportion, producing the maximum shear wave velocity.

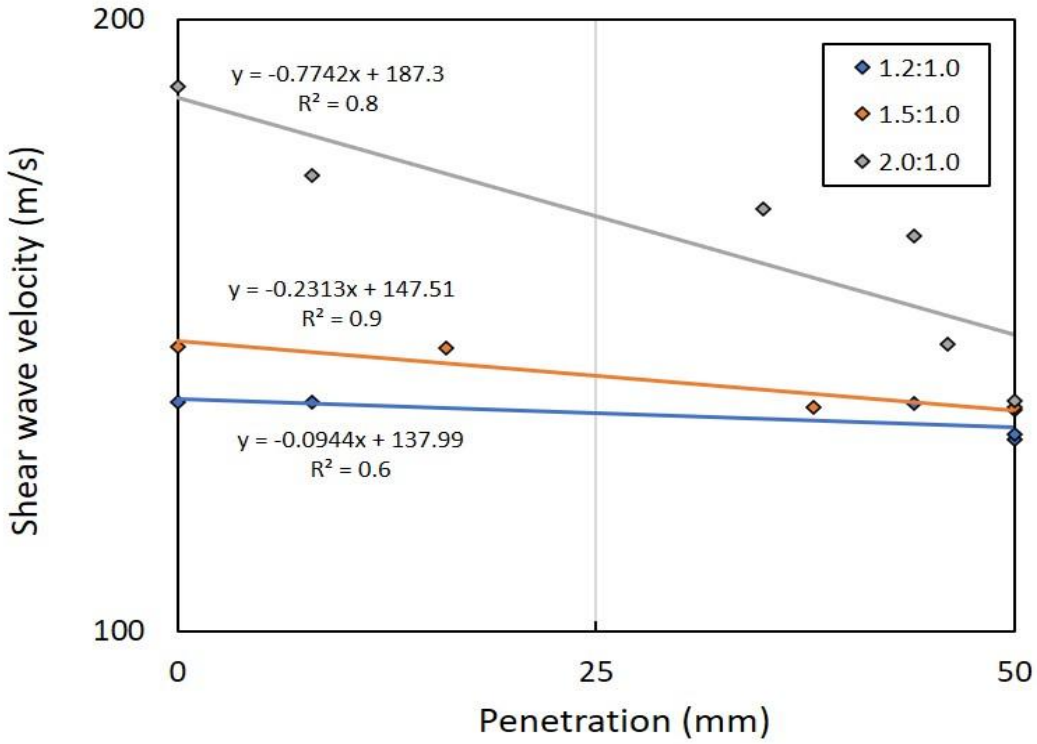


Figure 5-11 Relationship between the shear wave velocity and the penetration after Iamchaturapatr et al. (2022b).

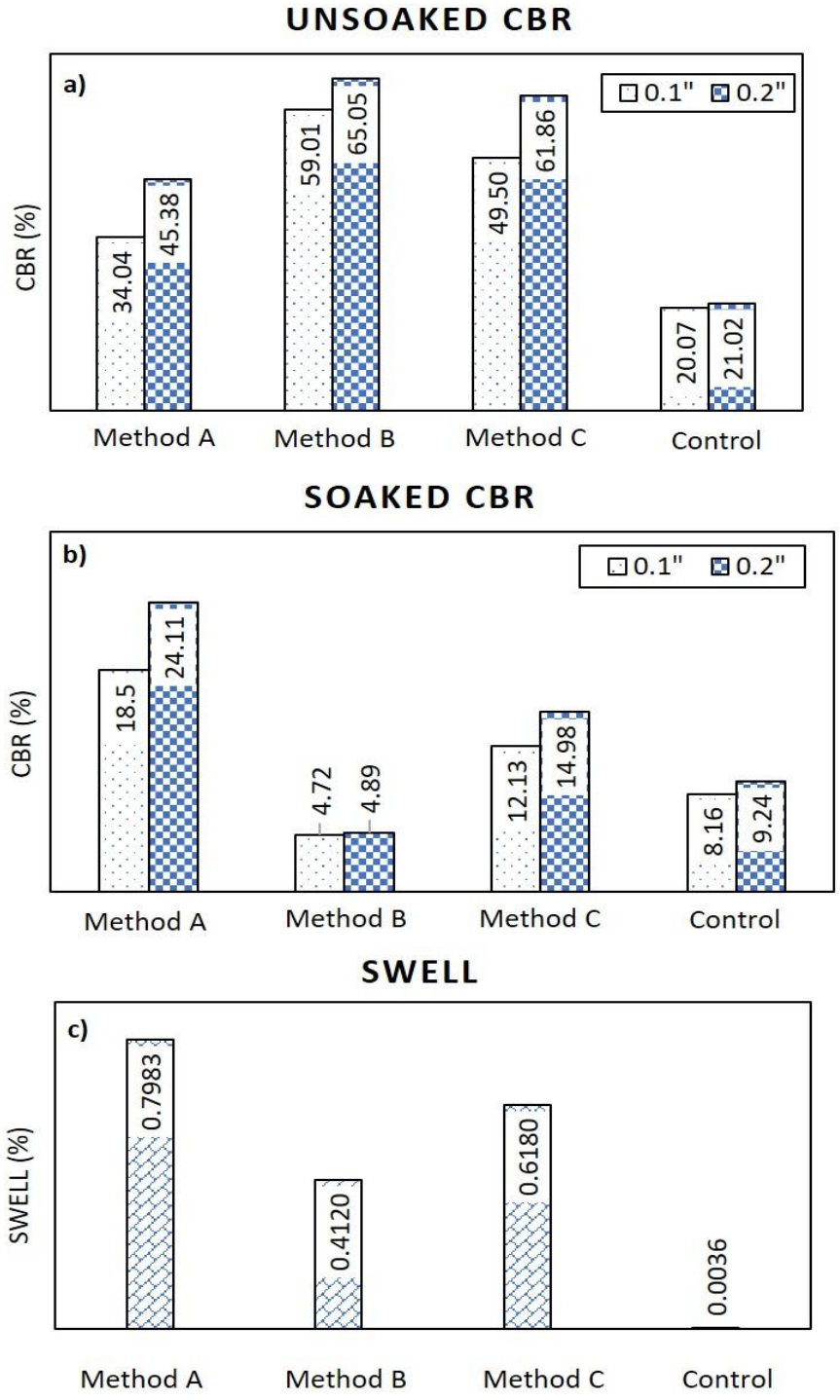


Figure 5-12 CBR test results for different mixing methods and conditions: (a) unsoaked (b) soaked (c) swelling after Iamchaturapatr et al. (2022b).

5.3.5 Effect of CBR on Mixing Methods for Laterite

Figure 5-12 presents the California Bearing Ratio (CBR) test results for lateritic soils stabilized with metakaolin geopolymer. For consistency, the NaOH-to- Na_2SiO_3 ratio was fixed at 2.0:1.0, while the mixing ratio between metakaolin calcined at 1000 °C and geopolymer solution was maintained at 1.0:1.0.

Figure 5-12a shows the unsoaked CBR test results. The untreated lateritic soil compacted at an optimum moisture content of 10.17 percent yielded unsoaked CBR values of 20.07 percent at 0.1 inches penetration and 21.02 percent at 0.2 inches penetration. With stabilization, mixing Method A produced unsoaked CBR values of 34.04 percent at 0.1 inches and 45.38 percent at 0.2 inches. Mixing Method B achieved the highest values, recording 59.01 percent at 0.1 inches and 65.05 percent at 0.2 inches. Mixing Method C provided intermediate values of 49.50 percent at 0.1 inches and 61.86 percent at 0.2 inches. These results indicate that mixing Method B delivered the best performance under unsoaked conditions, with CBR values approximately three times greater than those of the untreated sample. Figure 5-12b illustrates the soaked CBR test results. The control sample compacted at 10.17 percent moisture content showed soaked CBR values of 8.16 percent at 0.1 inches and 9.24 percent at 0.2 inches. Among the treated samples, mixing Method A produced the highest soaked CBR values of 18.50 percent at 0.1 inches and 24.11 percent at 0.2 inches, which were roughly three times higher than those of the control specimen.

Finally, Figure 5-12c depicts the swelling CBR results. The untreated lateritic soil compacted at the optimum moisture content exhibited a swelling value of 0.0036 percent. In contrast, mixing Method B produced the most pronounced swelling response, with a value of 0.41 percent.

Summary

This chapter summarizes as follows:

1. The application of piezoelectric sensors for determining the initial and final setting times of metakaolin geopolymer paste proved to be highly effective. This non-destructive method utilized shear wave velocity to monitor the strength development of the material and provided a reliable means of detecting the progression of geopolymerization over time.

2. The influence of thermal treatment on metakaolin geopolymer was assessed through both shear wave velocity measurements obtained from piezoelectric sensors and conventional Vicat needle tests. With the mixing ratio of metakaolin powder to geopolymer solution maintained at 1.0:1.0 and the solution composition fixed at a sodium hydroxide-to-sodium silicate ratio of 2.0:1.0, the results confirmed that calcination at 1000 °C represented the optimum treatment condition.

3. The effect of varying the proportions of sodium hydroxide and sodium silicate in the geopolymer solution was also examined. Under the same conditions of metakaolin thermal treatment at 1000 °C and a fixed powder-to-solution ratio of 1.0:1.0, solution ratios of 1.0:1.0, 1.0:1.2, 1.0:1.5, 1.0:2.0, 1.2:1.0, 1.5:1.0, and 2.0:1.0 were tested using both bender element shear wave velocity analysis and Vicat needle penetration. The findings indicated that the sodium hydroxide-to-sodium silicate ratio of 2.0:1.0 produced the most favorable results, confirming it as the optimum proportion.The application of piezoelectric sensors for determining the initial and final setting times of metakaolin geopolymer paste proved to be highly effective. This non-destructive method utilized shear wave velocity to monitor the strength development of the material and provided a reliable means of detecting the progression of geopolymerization over time.

4. The influence of the mixing ratio between metakaolin powder and geopolymer solution was evaluated through bender element testing with piezoelectric sensors and confirmed by Vicat needle measurements. Specimens prepared from metakaolin calcined at 800 °C and 1000 °C were tested under a fixed sodium hydroxide-to-sodium silicate ratio of 2.0:1.0. The results demonstrated that for metakaolin treated at 1000 °C, the optimum powder-to-solution ratio was 1.0:1.0, yielding the highest shear wave velocity. In contrast, for metakaolin treated at 800 °C, the most effective proportion was identified as 1.5:1.0, which also produced maximum shear wave velocity values.

5. The relationship between shear wave velocity and penetration resistance was further investigated for geopolymer pastes prepared from metakaolin treated at 1000 °C with a fixed powder-to-solution ratio of 1.0:1.0. The results confirmed a linear correlation for all sodium hydroxide-to-sodium silicate solution ratios tested. Specifically, at ratios of 1.2:1.0, 1.5:1.0, and 2.0:1.0, the corresponding shear wave velocities at initial setting (25 mm penetration) were 136, 142, and 168 meters per second, while the values at final setting (zero penetration) were 138, 148, and 187 meters per second, respectively. These findings indicate that the NaOH-to-Na_2SiO_3ratio of 2.0:1.0 represented the optimum solution proportion, as it provided the highest shear wave velocity and the greatest strength development.

Questions and Problems

1. What are geopolymer materials?
2. How the geopolymer reaction occur?
3. What is the metakaolin?
4. What calcined temperature is recommended for preparation of the metakaolin geopolymer?
5. Describe the initial and the final setting times are determined by the shear wave velocity?
6. What is recommended for the mixing proportion between the metakaolin powder and the geopolymer solution?
7. What is recommended for the mixing ratio between the sodium hydroxide (NaOH) and the sodium silicate (Na_2SiO_3)?
8. What is the relationship between the shear wave velocity and the penetration?
9. Which mixing method is recommended for CBR test?
10. What are the limitations for application of metakaolin geopolymer to improve ground strength?

Chapter 6: Applications of Shear Wave Testing in Biocemented Sand

6.1 Introduction of Biocement

Ground improvement techniques represent a major global industry, with annual project costs exceeding USD 6 billion across approximately 40,000 projects worldwide as reported by DeJong (2010). Growing environmental awareness and the construction sector's shift toward sustainable practices have driven the development of bio-mediated soil improvement methods as promising alternatives to conventional chemical-based approaches as described in Umar (2016), Petcherdchoo (2018a), Petcherdchoo (2018b) and Petcherdchoo et al. (2020). Among these, Microbially Induced Calcite Precipitation (MICP) has emerged as a particularly attractive technique, requiring attention to three key components: a fundamental understanding of microbiological, geochemical, and fluid flow processes; the ability to link environmental benefits such as carbon footprint reduction with improved engineering performance; and a commitment to ecological compatibility and energy efficiency as shown by Jiang et al. (2020). Comprehensive system modeling and real-time monitoring tools at field scale have been further identified as essential for ensuring the spatial uniformity and effectiveness of MICP treatment as reviewed by Piriyakul & Iamchaturapatr (2013).

Numerous studies have investigated the mechanisms and optimization of MICP for geotechnical applications. MICP operates through two fundamental pathways — bioclogging, which reduces porosity and hydraulic conductivity, and biocementation, which bonds soil particles through in-situ calcium carbonate precipitation as presented by Ivanov and Chu (2008). Large-scale bio-grouting experiments demonstrated that soil stiffness increased significantly within one day of treatment, with improvements quantitatively linked to injected solution volume and radial distance from the injection point as shown by van Paassen et al. (2010). Investigations using various bacterial species, including Bacillus megaterium and Sporosarcina pasteurii, confirmed that MICP effectively enhances shear strength and reduces hydraulic conductivity in both sandy and residual soils as described in Le & Lee (2014) and Ezzat (2023), with soil cohesion gains closely associated with bio-treatment-induced strength increases as noted by Li (2015). Further studies examined the influence of $CaCO_3$ content on compressibility and particle breakage as outlined by Xiao et al. (2020), the isolation of halotolerant and alkaliphilic urease-producing bacteria for demanding field environments as demonstrated by Stabnikov et al. (2013), and the effect of urease concentration on peak pH and maximum shear strength in biocemented sand as observed by Iamchaturapatr and Piriyakul (2014). Modified treatment approaches exploiting naturally available seawater calcium achieved unconfined compressive strengths of up to 300 kPa as exhibited by Cheng et al. (2014), while optimization of urea-to-calcium chloride ratios as shown by Carmona et al. (2016), injection versus mixing techniques as explained by Yu & Gao (2018), simplified one-phase low-pH injection as described in Cui et al. (2021), and careful balancing of treatment frequency as noted by Mohamed et al. (2021) collectively advanced the practical efficiency of MICP-based stabilization.

Microstructural characterization and novel treatment strategies have further enriched the understanding of MICP behavior. Bender element monitoring of bio-cemented sandy soil demonstrated higher strength and stiffness compared to gypsum-treated specimens even at less than 4% calcite content, with mixing techniques producing more homogeneous cementation than conventional injection methods as reported by Duraisamy and Airey (2019). Bentonite-enhanced MICP grouting improved bonding matrices at lower bentonite concentrations, though excessive concentrations impeded microbial activity and reduced mechanical performance as noted by Ma et al. (2021). SEM and XRD analyses revealed that naturally derived soluble calcium produces aragonite crystals of acicular morphology, distinct from the rhombohedral calcite crystals formed using conventional calcium chloride sources as shown by Liu et al. (2018). Comparative evaluation of six $CaCO_3$ quantification methods identified acid washing as yielding the highest measured content as presented by Choi et al. (2017), while in-situ sealing using microbially produced Ca^{2+}-alginate gels enhanced impermeability as described in Cheng et al. (2019a). Discrete element modeling incorporating meso-parameter calibration identified three bonding interaction types in microbial cemented sand as established by Tang et al (2018), and multiple treatment cycles were shown to substantially increase unconfined compressive strength up to 4 MPa through extensive $CaCO_3$ crystal bonding as noted by Wang et al. (2018). Additional findings confirmed that MICP-treated sands exhibit higher thermal conductivity facilitated by $CaCO_3$ thermal bridges as reported by Wang et al. (2019), and that coarser sand particle sizes promote improved mechanical properties and more uniform $CaCO_3$ distribution as described in Yang et al. (2020). Surface percolation methods have also been explored for ground stabilization as explained by Pan et al. (2020), Piriyakul & Iamchaturapatr (2017) and Yan et al. (2022), though bioclogging limits effective treatment depth to less than one meter in fine sands as noted by Cheng & Cord-Ruwisch (2014). To overcome surface clogging, a one-phase low-pH injection method combining calcium chloride, urea, and mixed bacterial culture into a single solution was developed, yielding UCS values as high as 2.5 MPa through deeper and more uniform treatment distribution as reported by Cheng et al. (2019b).

Bender element testing has been widely established as an effective non-destructive technique for evaluating shear wave velocity and small-strain stiffness parameters, with its utility in monitoring MICP-treated soils well documented in the literature as described in Piriyakul & Pochalard (2013), Iamchaturapatr et al. (2021), Iamchaturapatr et al. (2022a), Iamchaturapatr et al. (2022b), Petcherdchoo et al. (2023). Nevertheless, two critical challenges remain: optimizing treatment techniques that minimize bioclogging while promoting uniform biocement distribution and developing real-time monitoring systems capable of capturing the dynamic response of treated soils under saturated conditions. The present study addresses these gaps by proposing the use of urease enzymes to accelerate the MICP process with strategic adjustment of calcium ion concentration to complete biocementation within one week. The integrated approach employs custom-designed bender element testing for continuous real-time shear wave velocity monitoring, optimized biocementation protocols to enhance mechanical performance, and XRD and SEM analyses to verify the formation and mineralogical characteristics of $CaCO_3$ precipitates, collectively aiming to enhance the efficiency, uniformity, and monitoring capability of MICP for sustainable ground improvement.

6.2 Principle of MICP process

The two principal approaches for Microbially Induced Calcite Precipitation (MICP) in soil biocementation are bioaugmentation and biostimulation. In bioaugmentation, specialized bacterial strains—typically *Sporosarcina pasteurii*—are introduced to initiate and complete the biogeochemical reactions necessary for calcite precipitation. While effective under controlled conditions, this method poses practical limitations related to environmental compatibility, microbial viability, and economic feasibility. In contrast, biostimulation relies on the enrichment and activation of native microbial communities by modifying environmental conditions, such as the availability of substrates, nutrients, and electron acceptors, to support ureolytic activity. Gomez et al. (2017a) and Gomez et al. (2017b) compared bioaugmentation and biostimulation in a large-scale experiment by assessing shear wave velocity, biogeochemical changes, and cone penetration resistance. The results indicated that, at the meter scale, both treatment methods achieved comparable improvements in soil strength and stiffness. In a related field investigation, Zeng et al. (2021) assessed the feasibility of applying MICP through urea hydrolysis using regionally enriched bacterial communities. The study adopted a bioaugmentation protocol followed by sequential injections of urea and calcium chloride, with treatment performance evaluated through in-situ monitoring and two-dimensional reactive transport modeling. The outcomes revealed that biocementation was confined to roughly 5 percent of the treated soil volume. This limitation was attributed to the heterogeneous nature of the soil, which contained a high proportion of fines. The fines promoted preferential flow paths through more permeable layers and may have triggered hydraulic fracturing, leading to uneven substrate distribution and reduced calcite conversion efficiency.

Further work by Fang and Achal (2019a) and Fang and Achal (2019b) explored the application of biostimulation in Cement-Stabilized Rammed Earth (CSRE) as a sustainable construction material. Their findings demonstrated that biostimulation enhanced compressive strength while decreasing water absorption. The biocementation process was characterized using Fourier Transform Infrared Spectroscopy (FTIR), X-ray Diffraction (XRD), and Scanning Electron Microscopy coupled with Energy Dispersive Spectroscopy (SEM-EDS). In addition, microbial community profiling using Illumina MiSeq sequencing revealed that ureolytic activity was dominated by members of the Firmicutes phylum, particularly the Sporosarcina genus. These results highlight the potential of naturally occurring, environmentally benign bacteria to induce calcite precipitation in a self-propagating manner, without imposing significant disturbance to soil structure or requiring substantial energy inputs. The biocementation process via MICP begins with the microbial hydrolysis of urea ($CO(NH_2)_2$), facilitated by the enzyme urease, which is secreted by microorganisms such as *Bacillus* and *Sporosarcina* spp. The enzymatic breakdown of one mole of urea initially yields one mole each of ammonia (NH_3) and carbamate (NH_2COOH). The carbamate then spontaneously hydrolyzes to produce an additional mole of NH_3 and carbonic acid (H_2CO_3). In aqueous conditions, NH_3 is protonated to form ammonium ions (NH_4^+) and hydroxide ions (OH^-), resulting in an increase in pH. Concurrently, carbonic acid dissociates to form carbonate ions (CO_3^{2-}). The elevated pH and presence of carbonate and calcium ions (Ca^{2+}) in solution lead to the precipitation of calcium carbonate ($CaCO_3$), as described in Equation 6.6. This precipitation occurs within soil pores, effectively binding soil particles together and enhancing soil strength and stiffness. The role of urease is particularly critical, as it accelerates the overall reaction kinetics and ensures rapid calcite formation under controlled treatment conditions. Figure 6-1 illustrates the precipitation of calcium carbonate ($CaCO_3$) as described in Equation (1). This biocementation process has been shown to significantly improve the mechanical properties of porous materials by

enhancing their strength and stiffness through the formation of calcium carbonate bonds between particles. The biocementation process, primarily driven by microbial activity, is a promising technique for soil stabilization and strength enhancement. It begins with the enzymatic hydrolysis of urea ($CO(NH_2)_2$ or $NH_2–CO–NH_2$), which initiates a sequence of biochemical reactions. As shown in Equation 6.1, one mole of urea is hydrolyzed by the bacterial enzyme urease to produce ammonia (NH_3) and carbamate (NH_2COOH). The carbamate intermediate then spontaneously decomposes, as described in Equation 6.2, yielding an additional mole of NH_3 and one mole of carbonic acid (H_2CO_3). The ammonia produced subsequently reacts with water, establishing an equilibrium in Equations 6.3 and 6.4 that results in the formation of ammonium ions (NH_4^+) and hydroxide ions (OH^-). Simultaneously, the carbonic acid dissociates to form carbonate ions (CO_3^{2-}). At this stage, the aqueous solution contains elevated concentrations of NH_4^+, CO_3^{2-}, and OH^-, as shown in Equation 6.5. The urease enzyme plays a critical role in accelerating the overall reaction kinetics, enabling efficient ion generation under mild environmental conditions. The increase in OH^- concentration contributes to a rise in pH, which is favorable for carbonate precipitation. When sufficient quantities of calcium ions (Ca^{2+}) are present, typically introduced via calcium chloride or naturally occurring sources, they combine with CO_3^{2-} ions to precipitate calcium carbonate ($CaCO_3$), as represented in Equation 6.6. This precipitate forms within the pore spaces of soil, bonding particles together and significantly enhancing the mechanical integrity and durability of the treated soil mass. As noted by De Muynck et al. (2010), ureolysis-based biocementation offers several advantages over other carbonate-generating methods. In particular, the ureolytic pathway exhibits a high potential for producing substantial quantities of carbonate ions (CO_3^{2-}) within a relatively short time frame, thereby making it an efficient and promising technique for soil stabilization and structural enhancement.

Urea hydrolysis:

$$CO(NH_2)_2 + H_2O \rightarrow NH_2COOH + NH_3 \quad (6.1)$$

Carbamate hydrolysis:

$$NH_2COOH + H_2O \rightarrow H_3 + H_2CO_3 \quad (6.2)$$

Ammonia reaction with water:

$$2NH_3 + 2H_2O \rightarrow 2NH_4^+ + 2OH^- \quad (6.3)$$

Carbonic acid dissociation:

$$2OH^- + H_2CO_3 \rightarrow CO_3^{2-} + 2H_2O \quad (6.4)$$

Overall urea hydrolysis reaction:

$$CO(NH_2)_2 + 2H_2O \xrightarrow{\text{Urease}} 2NH_4^+ + CO_3^{2-} \quad (6.5)$$

Calcium carbonate precipitation:

$$Ca^{2+} + CO_3^{2-} \xrightarrow{\text{Urease}} CaCO_3 \quad (6.6)$$

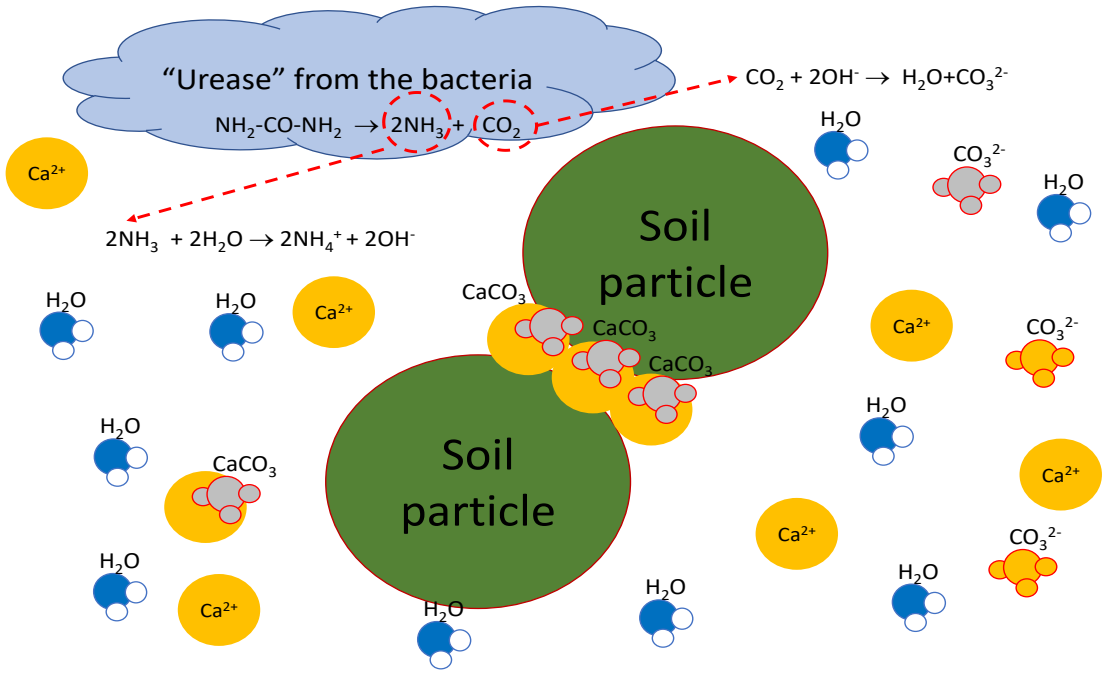


Figure 6-1 Biocementation process via MICP after Petcherdchoo et al. (2026).

6.3 Biocemented Materials and methods

6.3.1 Sandy Soil Preparation

The sandy soil employed in this investigation was obtained from the northern bank of the Chao Phraya River in Suphanburi Province, situated approximately 100 kilometers west of Bangkok, Thailand. The raw sand was first washed with deionized water to eliminate fine particles and other impurities. After cleaning, the material was oven-dried at a temperature of 110 ± 5 °C for a duration of 72 hours, then cooled to room temperature within a desiccator. To ensure a consistent particle size distribution, the dried sand was passed through ASTM sieve No. 100 (0.149 mm aperture) and retained on ASTM sieve No. 200 (0.074 mm aperture), thereby producing a fine sand fraction. This sieved fraction underwent an additional drying cycle at 110 ± 5 °C for 24 hours and was subsequently stored in moisture-controlled polyethylene bags until use, as illustrated in Figure 6-2.

The physical characteristics of the sand were determined as follows: specific gravity (G_s) of 2.64, dry unit weight of 1,470 kilograms per cubic meter, relative density (D_r) of 25.8 percent, maximum dry density of 1,547 kilograms per cubic meter, and minimum dry density of 1,445 kilograms per cubic meter. The soil was classified as cohesionless, exhibiting an internal friction angle (ϕ) of 32.85° and cohesion (c) equal to 0 kilopascals.

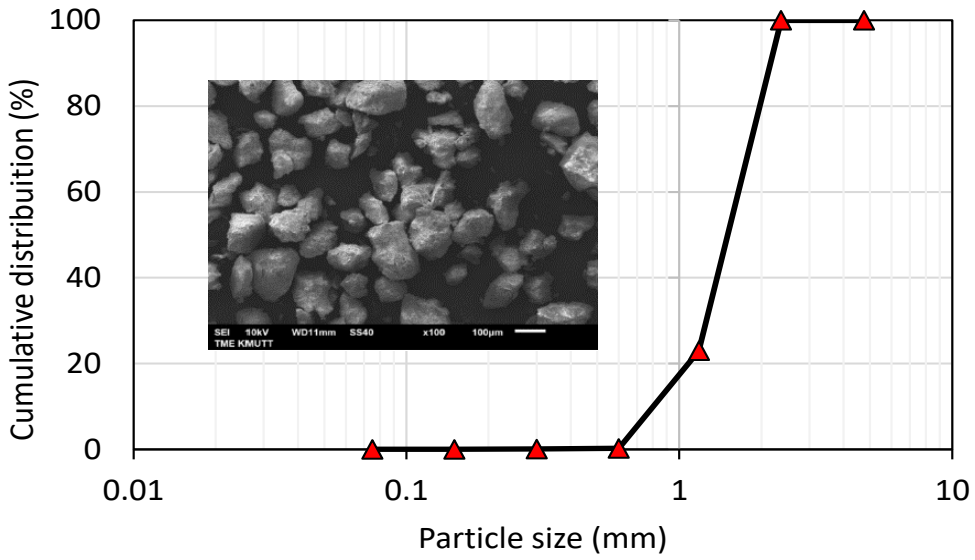


Figure 6-2 Particle size distribution of sandy soils after Petcherdchoo et al. (2026).

6.3.2 Biocement Solution Composition

The biocement solution, also referred to as the Biocemented Initiative Solution (BIS), was prepared to induce calcium carbonate ($CaCO_3$) precipitation via an enzyme-catalyzed urea hydrolysis reaction. The BIS formulation consisted of 1. 250 mM urea ($CO(NH_2)_2$), 2. 250 mM calcium chloride ($CaCl_2$), 3. 1.5 mM glucose ($C_6H_{12}O_6$), and 4. 20% v/v soybean-derived urease enzyme. The urease was extracted from natural soybeans and developed in-house. Unlike live microbial cultures, this enzyme-based solution eliminates the need for microbial cultivation while providing a stable and efficient catalyst for the hydrolysis of urea. The water used for preparing all solutions was deionized.

6.3.3 Biocement Sand Reactor (BSR) Configuration

To conduct the MICP treatment experiments under controlled laboratory conditions, a Biocement Sand Reactor (BSR) was designed and constructed. The BSR served as a test chamber to simulate biocementation in a one-dimensional column system. The reactor was fabricated from rigid plastic and had internal dimensions of 15 cm in width, 15 cm in length, and 25 cm in height, as shown in Figure 6-3. Sand specimens were prepared in accordance with the procedure outlined in Section 3.1 and placed into the reactor using a free-fall deposition method to achieve natural compaction. The target height of the sand column was 16 cm, which allowed sufficient space for solution injection or percolation while minimizing the risk of overflow. The BSR was sealed with a transparent plastic film during the treatment period to prevent moisture loss due to evaporation and to maintain consistent environmental conditions. All experiments were carried out at a room temperature of 25 ± 2 °C. The reactor design enabled both surface percolation and subsurface injection approaches to be tested under identical geometric and environmental conditions. Additionally, the rectangular plan view and open access to sidewalls facilitated the horizontal installation of bender element (BE) sensors for shear wave velocity monitoring, as described in Section 6.4.

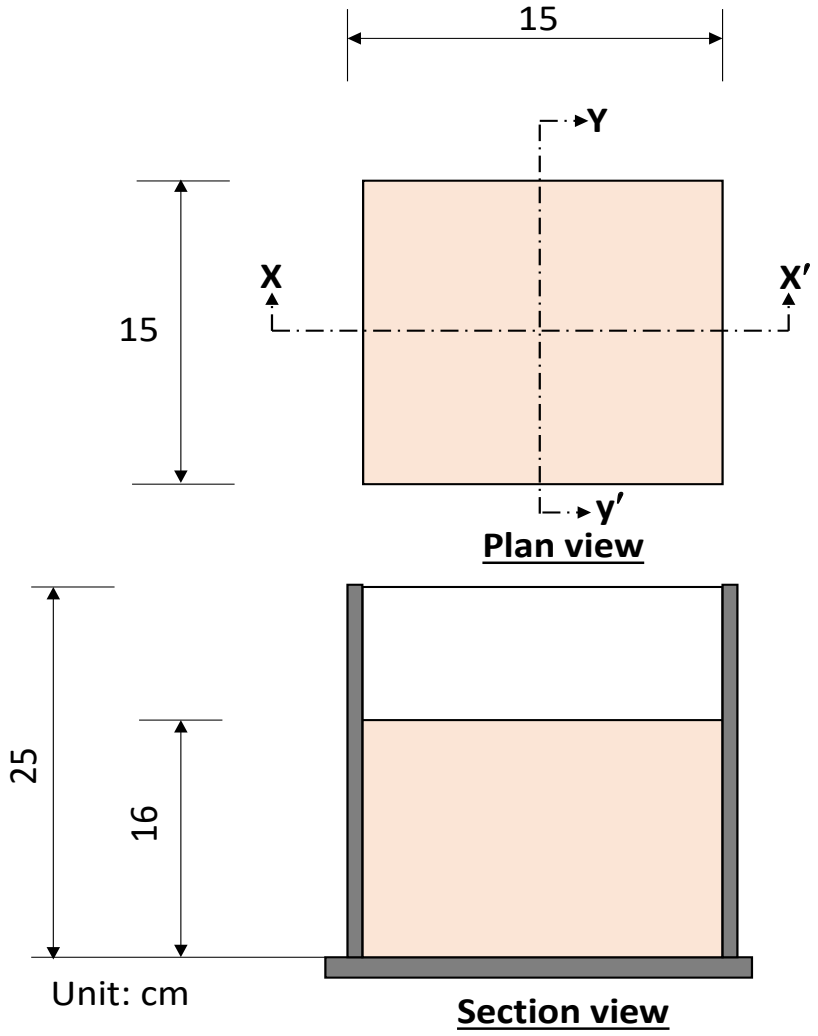


Figure 6-3 Biocement Sand Reactor (BSR) after Petcherdchoo et al. (2026).

6.3.4 Bender Element Testing and Data Analysis

The bender element test (BET) is principally associated with the determination of shear wave velocity (V_s) and the initial shear modulus (G_0), both of which are fundamental indicators of soil stiffness. The method offers several advantages, including its non-destructive nature, the capability to monitor variations in soil stiffness under dynamic conditions, and the relatively short testing time required. In this study, the BET was employed to evaluate changes in shear wave velocity during enzyme kinetics and to track the strength development of sand specimens.

As illustrated in Figure 6-4, the BE system, consisting of a transmitter and a receiver in accordance with ASTM D8295-19, was mounted on opposite sides of the BSR apparatus. The transmitter generated shear waves (S-waves) in the form of sinusoidal signals with an amplitude of 10 volts and frequencies ranging from 3 to 12 kHz, which were supplied by a function generator. These waves propagated through the sand specimens under examination before being detected by the receiver. The oscilloscope then recorded the travel time of the waves across the sample. Shear wave velocity was subsequently calculated using the equation provided in Piriyakul (2010). The method to mount horizontally bender element sensors for measuring shear wave velocity for sandy soil in soaking condition was proposed by Piriyakul & Iamchaturapatr (2014). Application of shear wave velocity measurement on green road materials is described by [46]. Application of shear wave velocity measurement on green road materials is described by Pochalard et al. (2025a). The ground improvement technique for sandy or clayey soils is clearly described in Pochalard et al. (2025b), Wungsumpow et al. (2025) and Pochalard et al. (2025c).

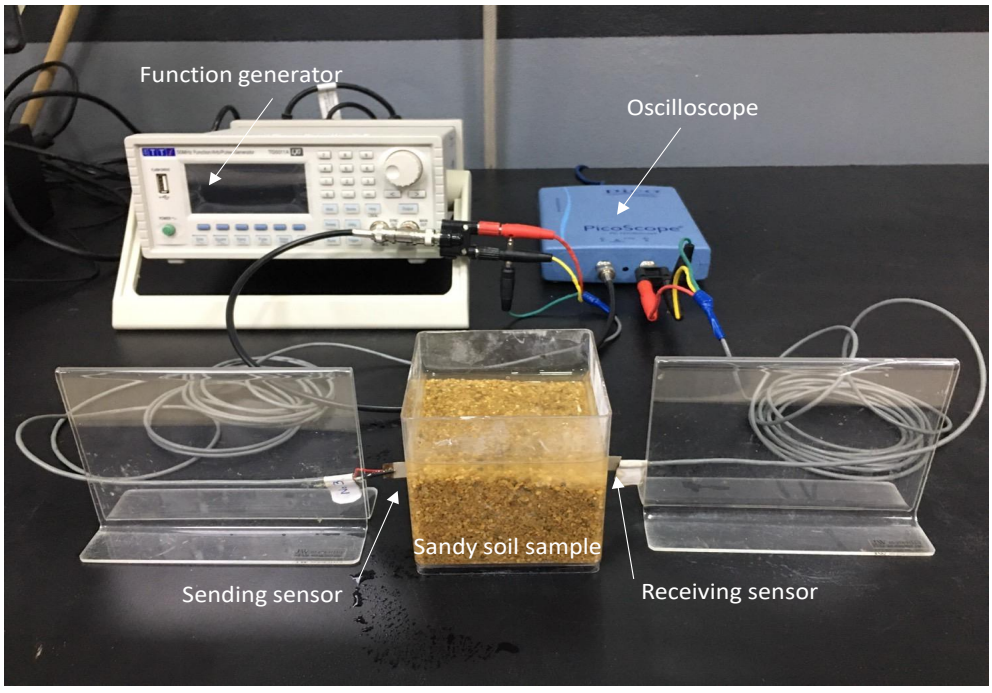


Figure 6-4 Setting-up of bender element testing for BSR after Petcherdchoo et al. (2026).

Figure 6-5 presents the biocementation process, showing the pH and G_0 increase with the time being. After 4 days, the biocementation is overed resulting the pH is about 8 and the G_0 is around 140 MPa.

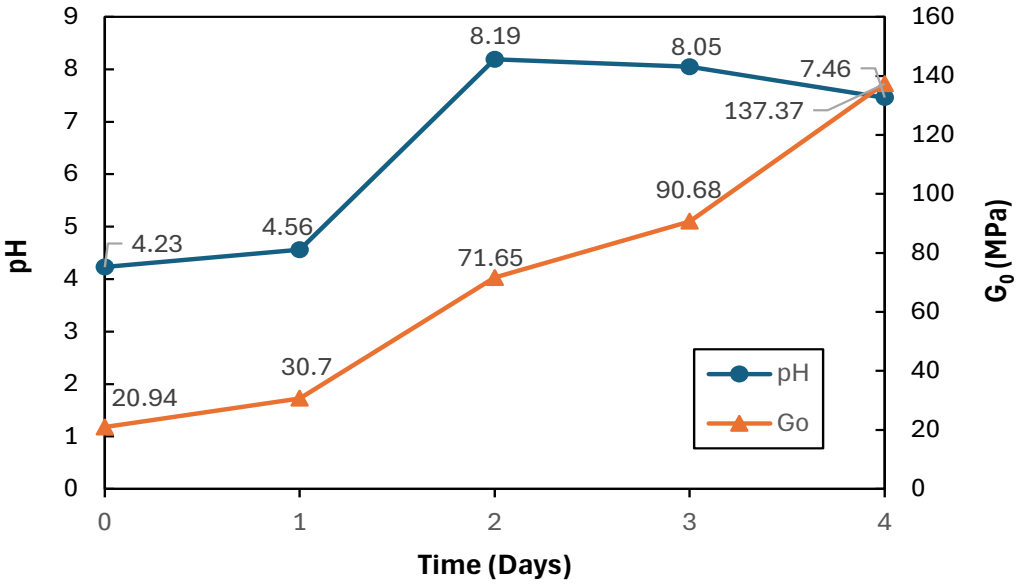


Figure 6-5 Relationship between pH and G_0 varied with Time after Petcherdchoo et al. (2026).

6.3.5 Surface percolation technique

Three surface percolation strategies were examined to evaluate their impact on biocementation performance: firstly, method (a): Single Pour – 315 mL of BIS was poured at a rate of 157.5 mL/h in a single application. Secondly, method (b): Continuous Drip – BIS was applied continuously using a drip system at a flow rate of 3.3 mL/h and lastly, method (c): Periodic Drip – 79 mL of BIS was applied per day at 13.5 mL/h, repeated over four consecutive days. Each application was carefully measured to ensure that the same total volume of BIS (315 mL) was distributed across all test specimens. These methods were designed to assess the effects of different flow regimes on $CaCO_3$ precipitation and the homogeneity of biocementation as described in Zeng et al. (2021). Figure 6-6 illustrated the MICP treatment with the surface percolation methods for sandy soil samples. Each 315 mL of BIS has contained 250 mM of $CO(NH_2)_2$, 250 mM of Ca^{2+} and 20% (v/v) urease to distribute completely the BSR. Figure 6-6a shows the sample no.1 treated with the method (a) by pouring all the biocemented initiative solution (BIS) at one time with the rate of 157.5 mL/h. Figure 6-6b illustrates the sample no.2 was treated with the method (b) by continue dropping the biocemented initiative solution (BIS) with the rate of 3.3 mL/h. Last, the sample no.3 was tested with the method (c) by periodically drops the biocemented initiative solution (BIS) of 79 mL/day with the rate of 13.5 mL/h for 4 days as seen in Figure 6-6c.

6.3.6 Injection technique

A fourth treatment, referred to as method (d), involved a subsurface injection technique as shown in Figure 6-7. The BIS was delivered via a porous pipe installed horizontally at mid-depth in the BSR. A total of 315 mL of BIS was injected over four days at a flow rate of 13.5 mL/h Also, the BIS of 315 mL has contained 250 mM of $CO(NH_2)_2$, 250 mM of Ca^{2+} and 20% (v/v) urease. This method aimed to overcome limitations associated with surface clogging and to promote more uniform distribution of $CaCO_3$ throughout the soil matrix. Then, Scanning Electron Microscope (SEM) and X-ray Diffractometer (XRD) tests were performed on all samples of biocemented sand to determine the $CaCO_3$ precipitation.

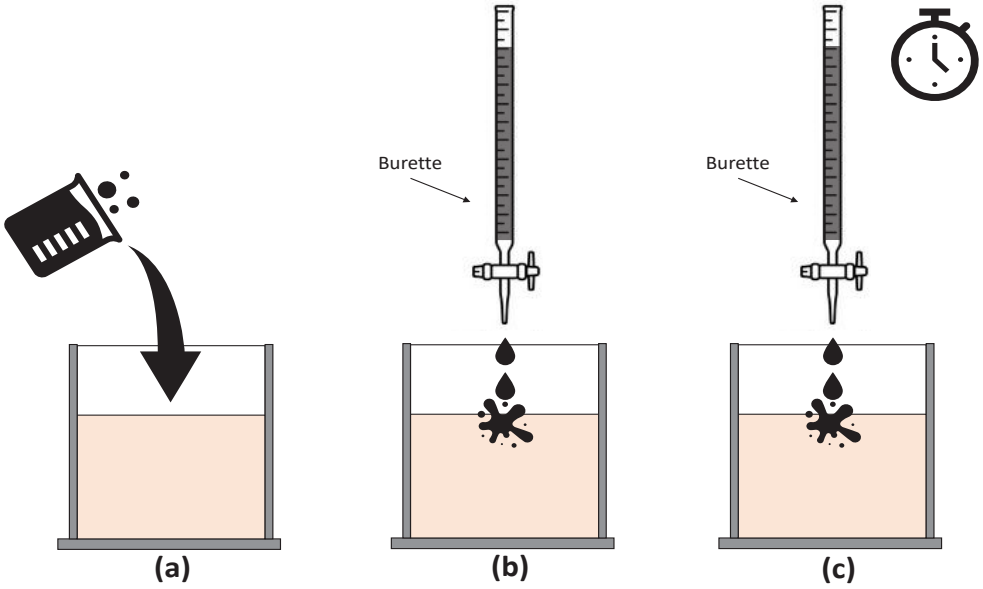


Figure 6-6 MICP treatment with the surface percolation methods for sandy soil samples (a) pour all the biocement solution at one time with the rate of 157.5 mL/h (b) continue drop the biocement solution with the rate of 3.3 mL/h, and (c) periodically drop the biocement solution of 79 mL/day with the rate of 13.5 mL/h for 4 days after Petcherdchoo et al. (2026).

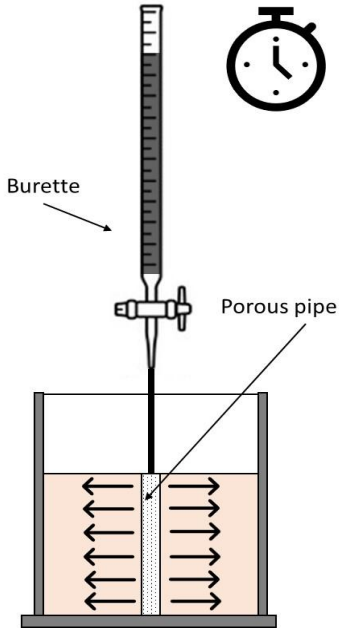


Figure 6-7 MICP treatment with the injection method for a sandy soil by periodically injection after Petcherdchoo et al. (2026).

6.4 Results and Discussions

6.4.1 Shear wave velocity on sandy soils using the surface percolation method

The shear wave velocity (V_s) profiles were measured across the test specimens treated using three different surface percolation techniques to evaluate the uniformity and effectiveness of biocementation. These profiles provide critical insight into the spatial distribution of stiffness within the treated sand columns. Method (a) involved pouring the entire volume of the biocement solution (BIS) at once at a flow rate of 157.5 mL/h. The shear wave velocity contour for this method is shown in Figure 6-8 (X–X′ cross section) and Figure 6-9 (Y–Y′ cross section). After one week of treatment, V_s values ranged from approximately 120 m/s at the top to 225 m/s at the bottom of the specimen, indicating a gradient in stiffness likely caused by bioclogging near the base, where excess $CaCO_3$ accumulated due to gravity-driven flow. In contrast, Method (b) used a continuous drip application of BIS at a low rate of 3.3 mL/h. This method exhibited the opposite trend, as shown in Figure 6-10 (X–X′) and Figure 6-11 (Y–Y′). V_s values were higher near the top surface (172–176 m/s) and decreased toward the bottom layers (around 128 m/s). This non-uniform profile is attributed to early clogging at the top surface, which hindered further penetration of the solution. Method (c), involving periodic application of BIS at a rate of 13.5 mL/h (79 mL/day for four days), demonstrated the most uniform Vs distribution. As depicted in Figure 6-12 (X–X′) and Figure 6-13 (Y–Y′), V_s values ranged narrowly from approximately 162 to 186 m/s throughout the depth of the specimen. This consistency indicates even biocementation and improved treatment homogeneity, suggesting that periodic dosing effectively prevented both top-surface clogging and bottom-heavy accumulation. Among the three surface percolation methods, periodic application (Method c) was identified as the most effective in achieving homogeneous shear stiffness.

The results emphasize the importance of optimizing flow rates and application timing to mitigate bioclogging and enhance uniform $CaCO_3$ distribution during MICP treatment.

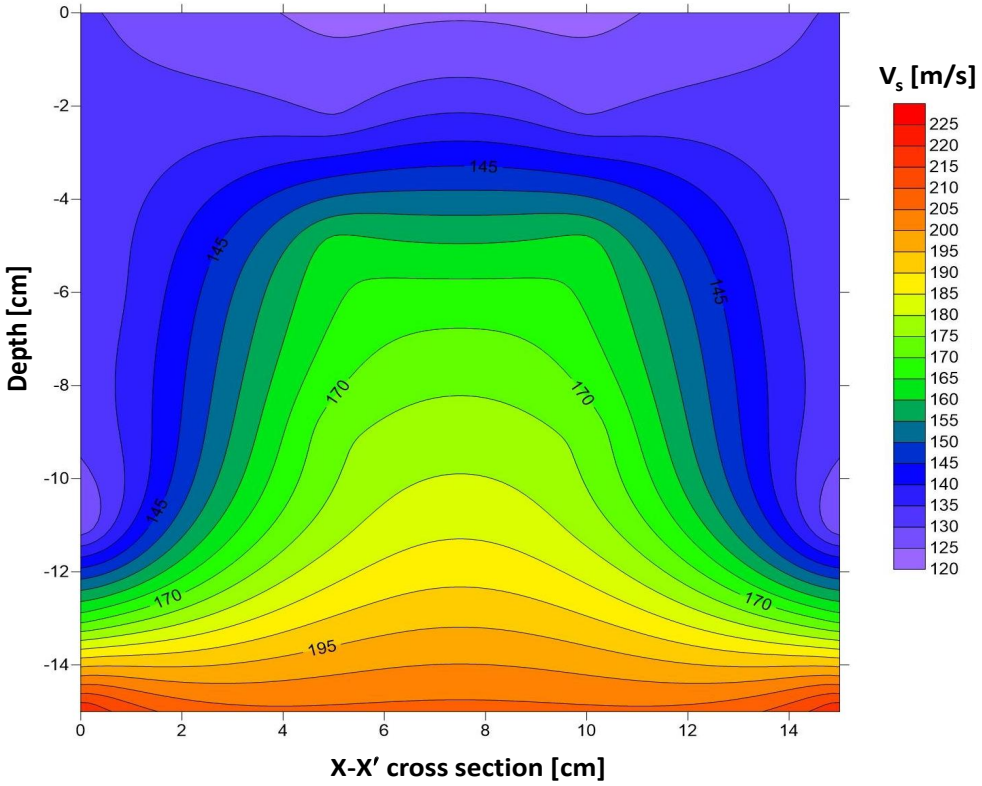


Figure 6-8 Contour of shear wave velocity for sample no.1 at cross section X-X′ after Petcherdchoo et al. (2026).

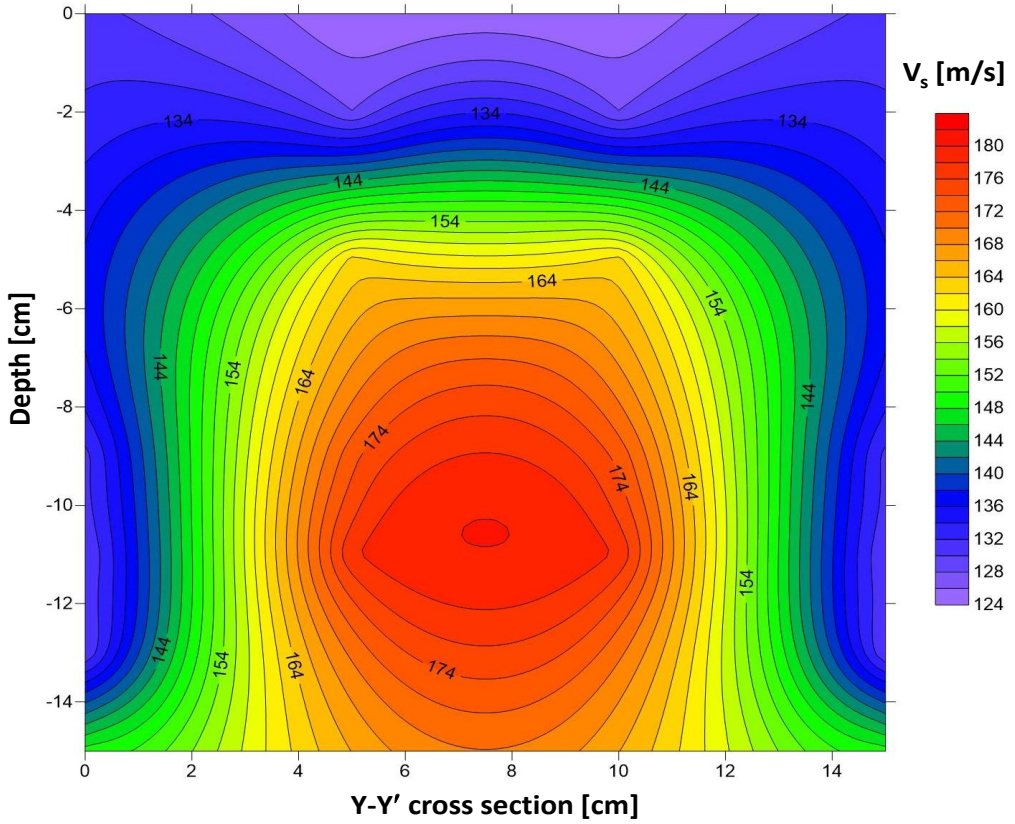


Figure 6-9 Contour of shear wave velocity for sample no.1 at cross section Y-Y′ after Petcherdchoo et al. (2026).

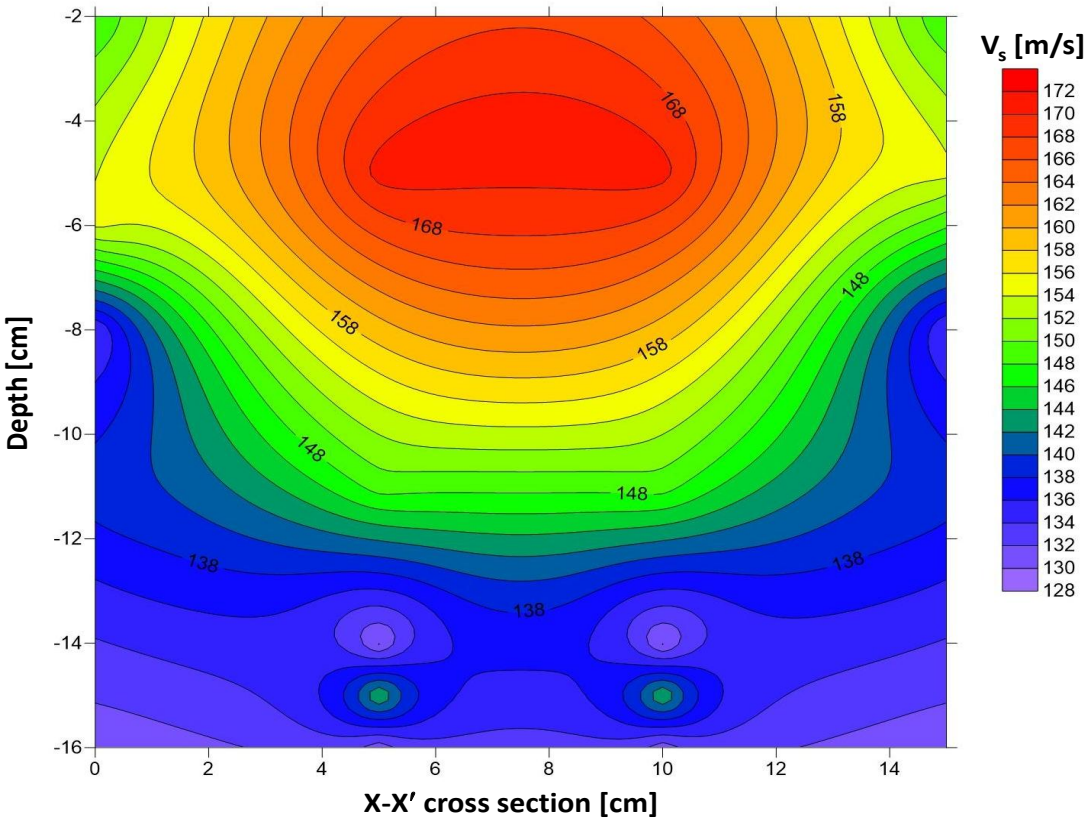


Figure 6-10 Contour of shear wave velocity for sample no.2 at cross section X-X′ after Petcherdchoo et al. (2026).

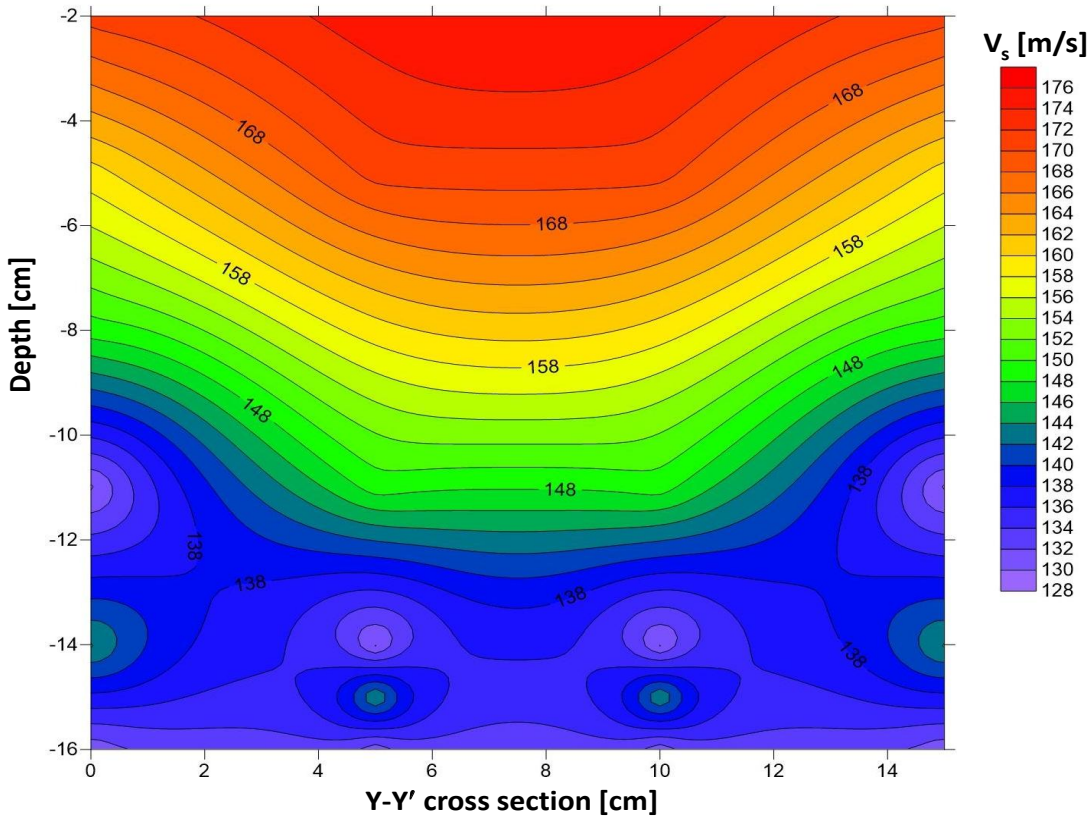


Figure 6-11 Contour of shear wave velocity for sample no.2 at cross section Y-Y′ after Petcherdchoo et al. (2026).

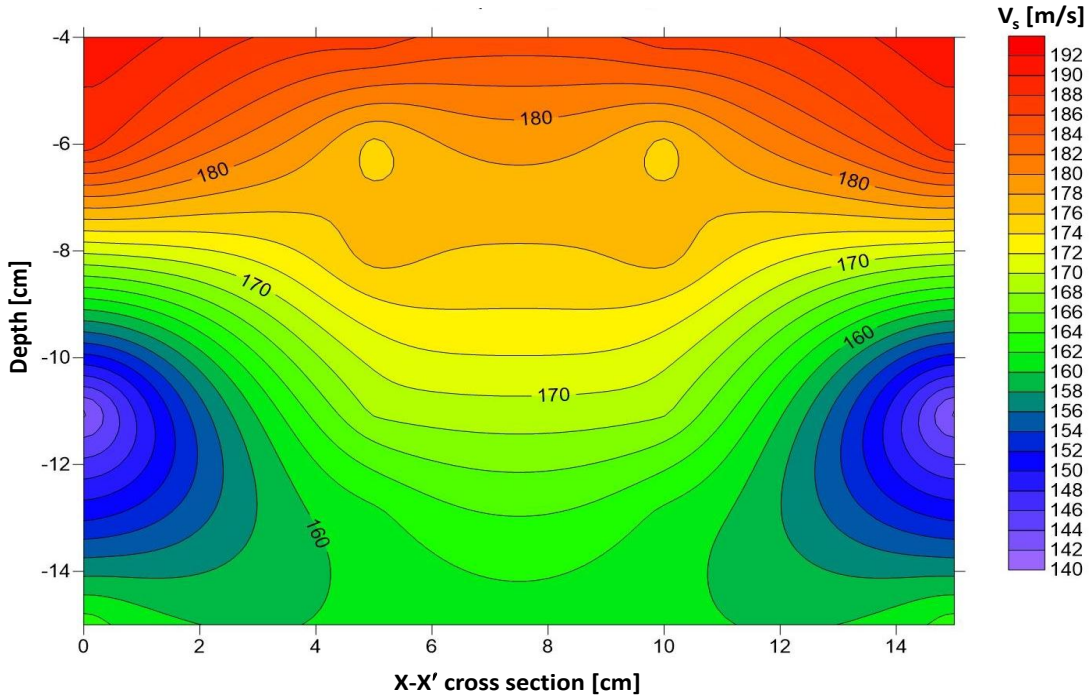


Figure 6-12 Contour of shear wave velocity for sample no.3 at cross section X-X′ after Petcherdchoo et al. (2026).

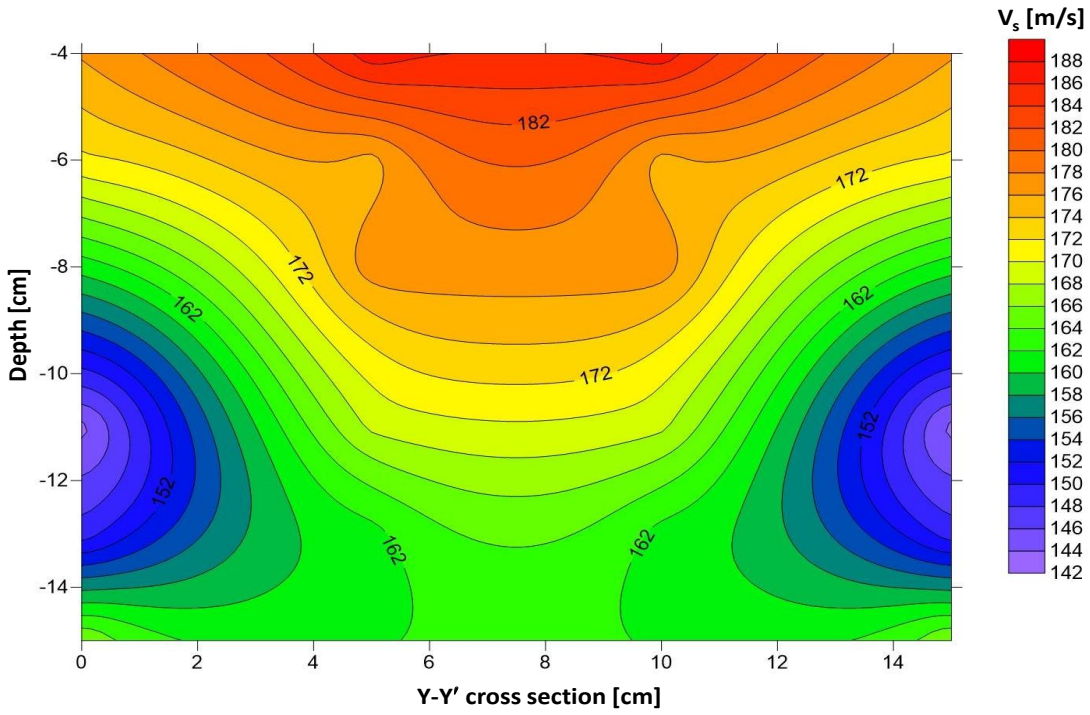


Figure 6-13 Contour of shear wave velocity for sample no.3 at cross section Y-Y′ after Petcherdchoo et al. (2026).

6.4.2 Shear wave velocity on sandy soil using the injection method

Figure 6-14 presents the shear wave velocity contour of sample no. 4 along the X–X′ cross-section. In this case, the sandy soil specimen was stabilized using method (d), which involved periodic injection of the BIS solution through a porous pipe at a controlled rate of 13.5 milliliters per hour over a four-day period. After one week, the measurements indicated that the shear wave velocity reached approximately 185 meters per second at the upper level of the sample and about 170 meters per second at the lower level.

Similarly, Figure 6-15 illustrates the shear wave velocity contour of sample no. 4 along the Y–Y′ cross-section. The results showed that the velocity was approximately 186 meters per second at the top surface and around 168 meters per second at the bottom, demonstrating a relatively uniform distribution. These findings suggest that this MICP treatment method provides effective and homogeneous stabilization for dry sandy soils.

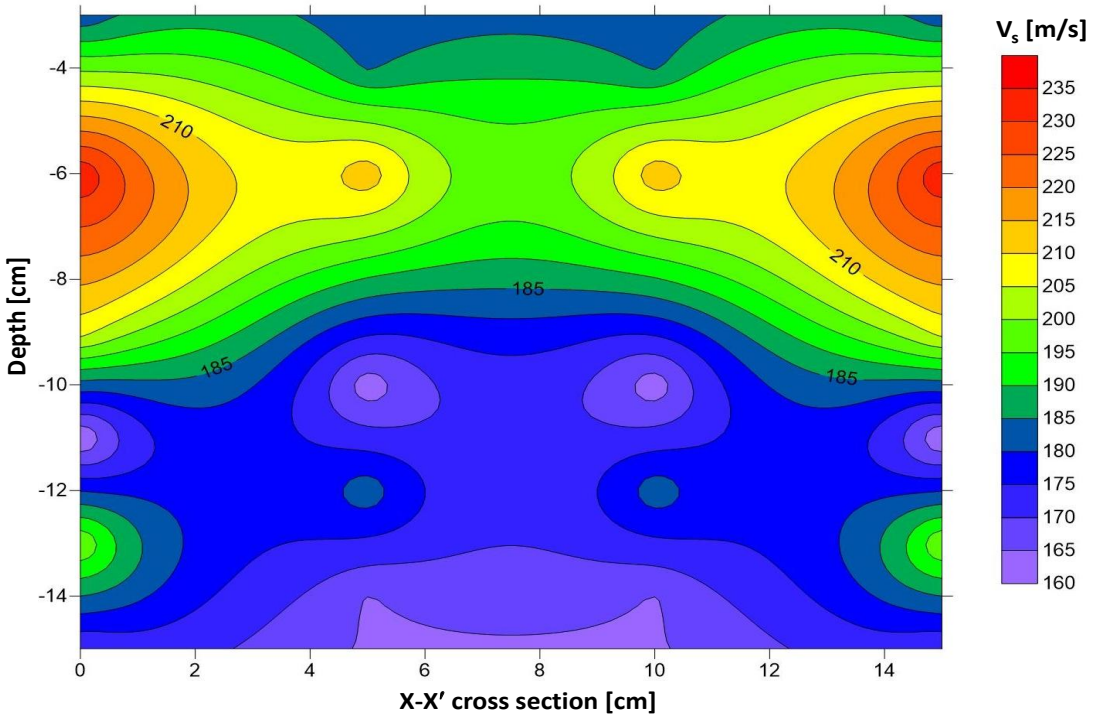


Figure 6-14 Contour of shear wave velocity for sample no.4 at cross section X-X′ after Petcherdchoo et al. (2026).

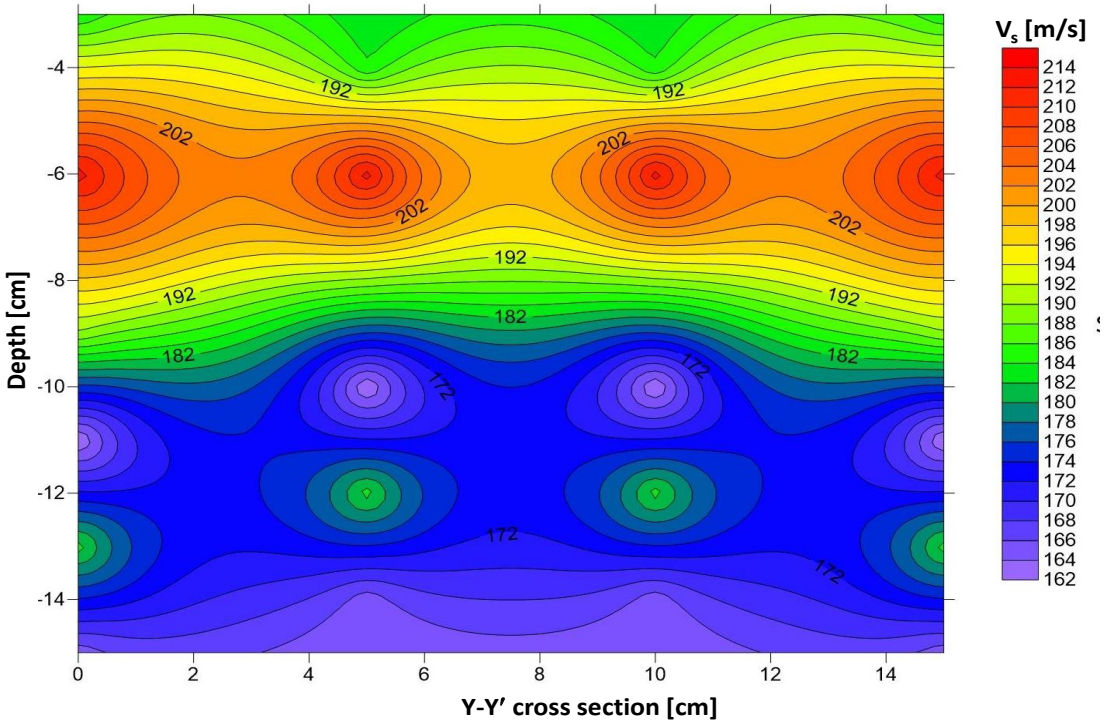


Figure 6-15 Contour of shear wave velocity for sample no.4 at cross section Y-Y′ after Petcherdchoo et al. (2026).

6.4.3 Initial Shear modulus of biocemented sandy soil

Figure 6-16 illustrates the initial shear modulus, G_0, of BIS untreated and treated sandy soils. Results of G_0 for untreated dry sandy soil were 26.1 MPa both on X-X′ and Y-Y′ cross sections. For surface percolation treatment technique, the method (a) has G_0 of 74.42 MPa on the X-X′ cross section or was 185% higher than untreated dry sandy soil data and 47.63 MPa on Y-Y′ cross section or was increased 82.5%. In a similar way, the method (b) showed the G_0 of 43.49 MPa or increased 66.6% and 45.53 MPa or increased 74.4% on X-X′ and Y-Y′ cross sections, respectively. Last, the method (c) presented the G_0 data of 54.19 MPa or increased 107.6% and 51.96 MPa or increased 99.1% on X-X′ and Y-Y′ cross sections. Since the method (c) has high G_0 values and less fluctuation on both cross sections. It was a recommended technique.

For the BIS injection treatment techniques, the G_0 results were 81.18 MPa on the X-X′ cross section or increment of 211.0% and 67.32 MPa on the Y-Y′ cross section or increased 157.9%. Therefore, the BIS injection technique is a preferred method.

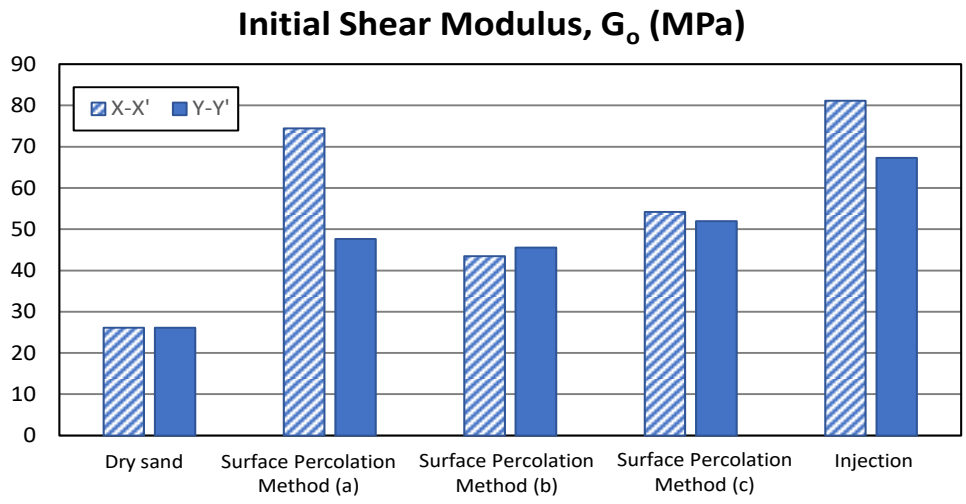


Figure 6-16 Initial shear modulus (G_0) of untreated and treated sandy soils with surface percolation and injection techniques after Petcherdchoo et al. (2026).

6.4.4 Morphology of biocemented sandy soil

The microstructure of the biocemented sandy soil was investigated using Scanning Electron Microscopy (SEM) to evaluate the morphology and distribution of calcium carbonate ($CaCO_3$) precipitates. The SEM images confirm the occurrence of successful biocementation resulting from the enzymatically induced MICP process. As shown in Figure 6-17, the SEM image at 250× magnification reveals the widespread deposition of $CaCO_3$ crystals across the surfaces of the sand particles. These precipitates form inter-particle bridges that promote bonding between adjacent grains, effectively increasing the mechanical integrity of the sand matrix. A higher magnification image (1000×), presented in Figure 6-18, further illustrates the detailed surface morphology. The $CaCO_3$ precipitates appear as clusters and coatings adhered to the sand grain surfaces and within interstitial voids. This indicates not only surface coverage but also partial pore-filling behavior, both of which are characteristic of efficient MICP treatment. The presence of such agglomerations suggests improved particle interlocking and increased cohesion within the soil structure. The formation of $CaCO_3$ is attributed to the ureolytic reaction facilitated by the soybean-derived urease, which increases the alkalinity of the solution, thus promoting carbonate ion availability. These findings confirm that the MICP process achieved through enzyme induction effectively altered the microstructure of the treated sand and enhanced its mechanical behavior.

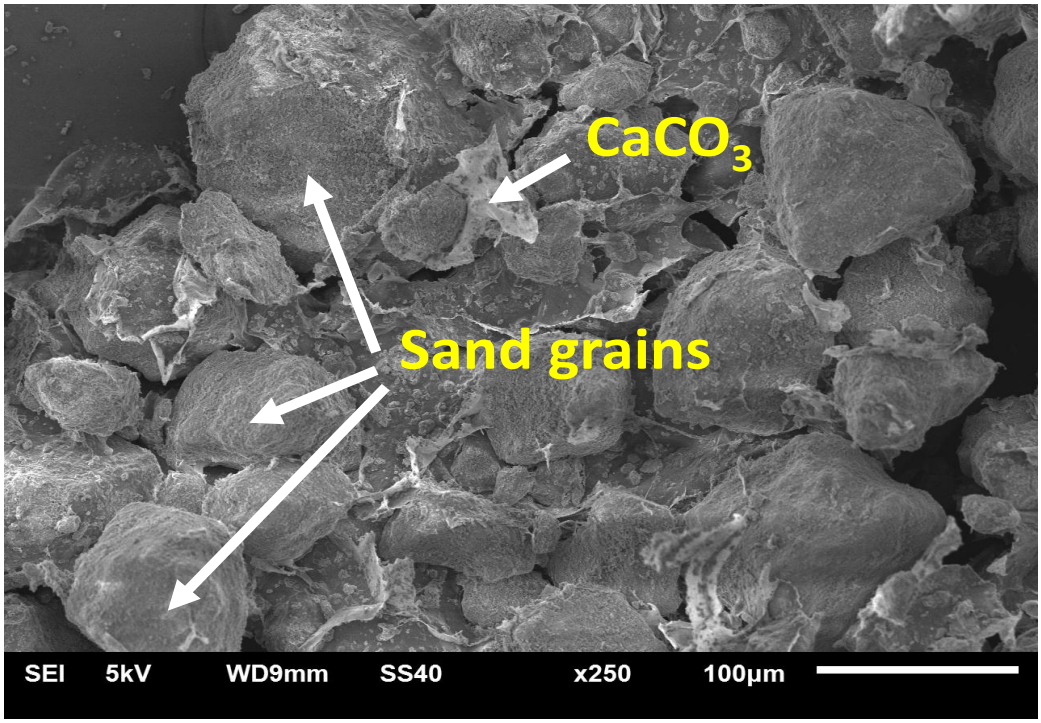


Figure 6-17 SEM image of the biocemented sandy soil at 250x after Petcherdchoo et al. (2026).

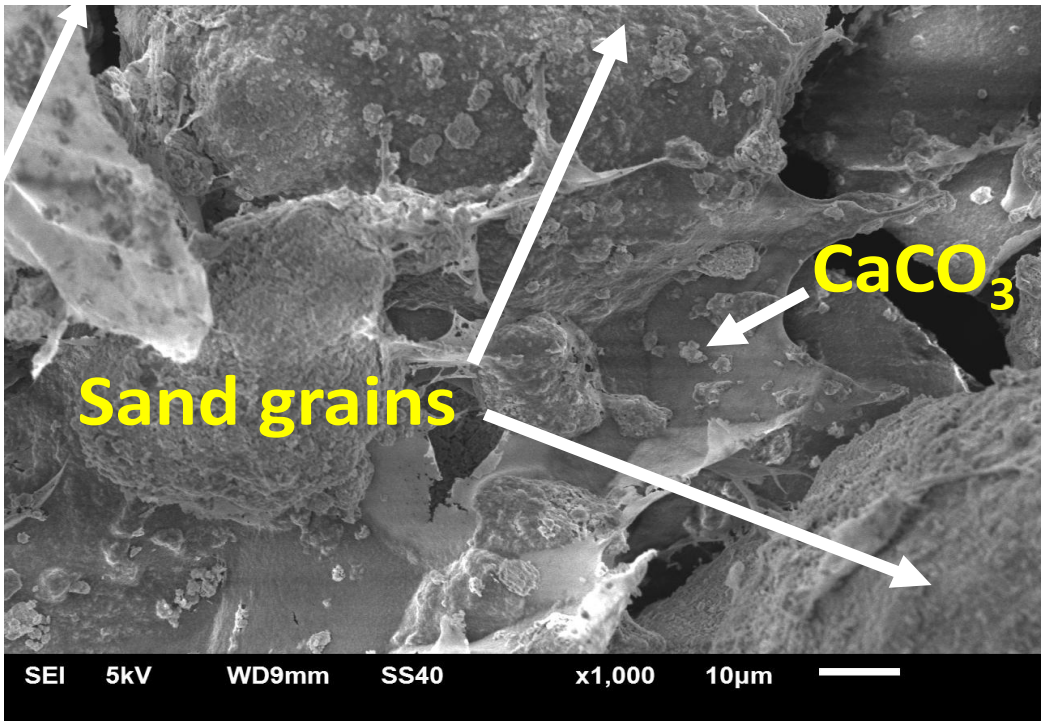


Figure 6-18 SEM image of the biocemented sandy soil at 1000x after Petcherdchoo et al. (2026).

6.4.5 X-ray Diffractometer (XRD) of biocemented sandy soils

To further validate the mineralogical composition of the biocemented sand, X-ray Diffraction (XRD) analysis was conducted. The primary objective was to confirm the presence and crystalline nature of calcium carbonate precipitates formed during the MICP treatment. As illustrated in Figure 6-19, the XRD pattern of the biocemented sample displays distinct diffraction peaks consistent with the calcite phase of $CaCO_3$, as compared to the untreated sand. The emergence of these peaks confirms successful mineral transformation and the precipitation of carbonate minerals within the treated soil matrix. While the overall chemical composition of the sand remained relatively unchanged, the observed shift in peak intensities suggests the incorporation of crystalline $CaCO_3$ into the soil structure. The intensity and sharpness of the peaks further indicate a well-developed and stable mineral phase. This agrees with the SEM results, where $CaCO_3$ was visually confirmed to have formed coatings and bridges between sand grains. The formation of $CaCO_3$ is primarily governed by the availability of carbonate and calcium ions in the solution and is enhanced by the elevated pH resulting from enzymatic urea hydrolysis. This alkaline environment supports the nucleation and growth of calcite crystals. The XRD results, therefore, corroborate the morphological observations and confirm the effectiveness of the enzymatic MICP approach for soil stabilization.

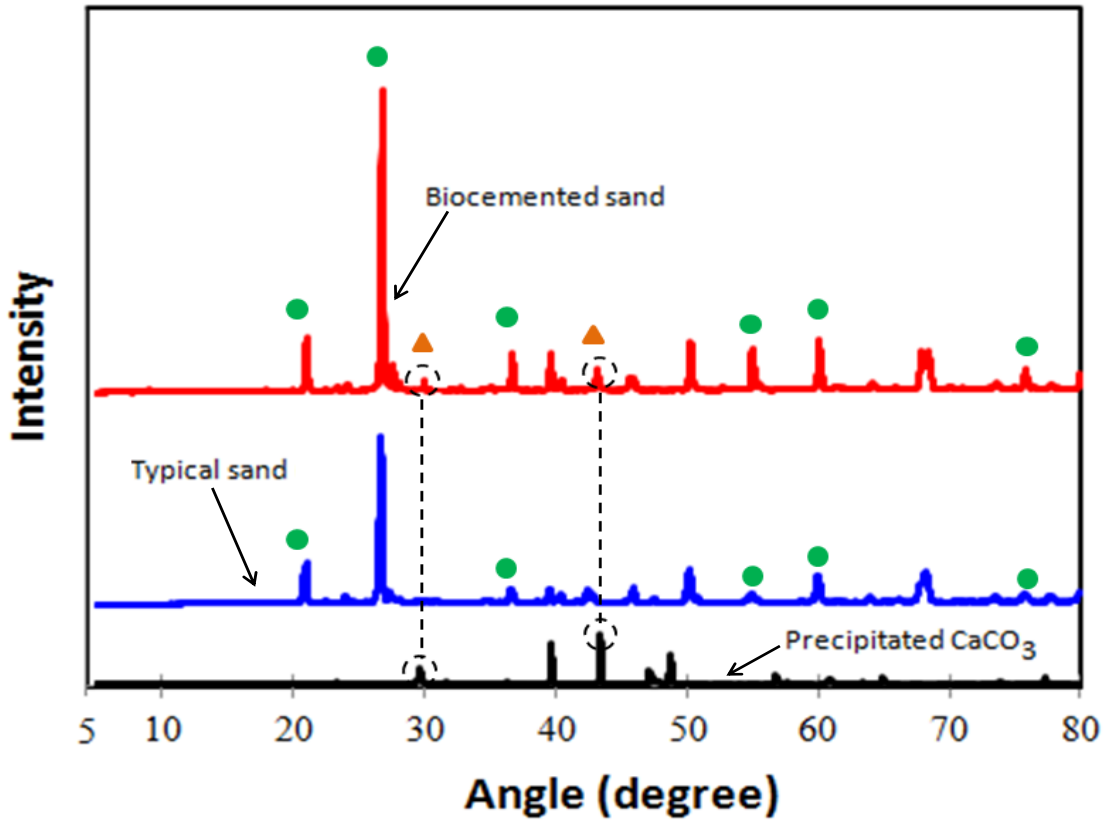


Figure 6-19 X-ray Diffractometer (XRD) result after Petcherdchoo et al. (2026).

Summary

This chapter sheds light on the following:

1. The real-time bender element monitoring system is capable to measure the shear wave velocity during biocementation process of MICP with the advantage of using the self-developed urease enzymes in the acceleration method.

2. For the surface percolation treatment technique, the research purposed the method (c) with periodically drops the biocemented initiative solution (BIS) of 79 mL/day with the rate of 13.5 mL/h for 4 days as it has the homogeneity in stabilizing dry sand.

3. For the injection treatment technique, the study purposed the new injection technique for stabilizing the dry sand by injecting the BIS on a periodic basis via the porous pipe at a rate of 13.5 mL/h for 4 days, showing its homogeneity.

4. The precipitation of $CaCO_3$ crystal is readily visible in the scanning electron microscope (SEM) pictures. Additionally, $CaCO_3$ coatings the surface of the sand in addition to filling up spaces within it. These result in sand agglomeration and occurrence of $CaCO_3$ after biocementation process.

5. The biocementation method has a little effect on the chemical compositions of the biocemented sand, but dramatically influences their physical strength, according to a slight variation in the XRD pattern. Additionally, it is likely that the variation in peaks in the biocemented sand is caused by $CaCO_3$ precipitation, which depends on the production of CO_3^{2-} and OH^- as produced by urease enzymes.

6. It is advised that the bacterial genome be identified for further research so that its urease activity may be compared to other studies.

Questions and Problems

1. What is the MICP?
2. Describe the biocementation process.
3. Describe the Injection technique.
4. Describe the surface percolation technique.
5. What is the advantage of using the bender element testing to monitor the biocementation process?
6. What results are found by SEM images?
7. How do the XRD results confirm the biocementation process?
8. Which technique is recommended for the Injection technique?
9. Which technique is recommended for the surface percolation technique?
10. What would be the limitations for MICP treatment?

Chapter 7: Applications of Shear Wave Testing in Bangkok Clay mixed with Cement and Industrial Waste

7.1 Introduction of Bangkok Clay mixed with Cement and Industrial Waste

Clayey soils stabilized with cement, commonly referred to as soil–cement, are widely utilized in geotechnical applications to improve strength characteristics and reduce compressibility through deep mixing methods as reported by Madhyannapu et al. (2010) and Szymkiewicz et al. (2015). Numerous studies have examined the effectiveness of cement stabilization in clayey soils, consistently identifying the clay-to-water/additive ratio as a critical factor governing strength development, particularly when the liquidity index ranges between 1 and 2 as noted by Naveena et al. (2013). Phase diagram analysis of clay–cement mixtures demonstrated that reductions in the plasticity index serve as effective indicators of stabilization effectiveness as explained by Saadeldin & Siddiqua (2013), while investigations of soils treated with various additives confirmed that stabilized soil functions as a composite material whose properties can be optimized through careful selection and combination of stabilizing agents, though cement treatment is less effective in clays with high plasticity index as described in Firoozi et al. (2017). Specialized stabilizing agents such as GX07 — comprising gypsum, quicklime, water glass, sodium hydroxide, superplasticizer, and triethanolamine — were shown to improve cemented soil strength economically as reported by Li et al. (2012). Studies on soft clays stabilized with cement, metakaolin, and slag under varying clay fraction, water content, and curing duration demonstrated that newly developed stabilized materials achieved strength comparable to conventional cement-treated soils as documented in Liu et al. (2019). The incorporation of granite powder into cement-stabilized clay increased unconfined compressive strength (UCS) through enhanced surface area and pozzolanic activity while reducing cement consumption by 28.6 percent as noted by Nakayenga et al. (2021), and the use of fly ash as a recycled additive in soil–cement was shown to achieve optimum UCS at replacement levels between 20 and 25 percent as found in Chindaprasirt et al. (2021).

Predictive modeling of strength development in stabilized soils has been an active area of research. The gel–space ratio theory was applied to estimate compressive strength of cement-treated marine clays with varying initial water contents, yielding a validated predictive equation applicable across six Japanese marine clay types as described in Tsuchida and Tang (2015). Empirical prediction equations incorporating initial water content and specific volume ratio normalized by liquid limit were proposed for cement-treated dredged clays, revealing that strength mobilization occurs in two distinct stages before and after three days of curing as explained by Kang et al. (2015). A generalized hyperbolic model demonstrated applicability across different soil types, cement types, and curing times for evaluating both strength and stiffness of cement-stabilized clays as shown by Yao et al. (2019). UCS of chemically stabilized soft soils was shown to be predictable independently of binder type and content from a single unconfined compression test as presented by Correia et al. (2013), while SEM-supported investigations confirmed that supplementary cementing agents facilitated pozzolanic reactions and enhanced UCS in cement-stabilized soft clay as demonstrated by Cong et al. (2014). Bangkok soft clay, characterized by high natural water content close to its liquid limit, exhibits high settlement potential and low shear strength, necessitating targeted soil improvement strategies as described in Horpibulsuk et al. (2007). Studies on Bangkok clay stabilization identified the

clay-water/cement ratio as the primary factor controlling strength development in both laboratory and field conditions, recommending a water-to-cement ratio of 1.0 for wet mixing applications as indicated by Miura et al. (2001) and Horpibulsuk et al. (2011). The inclusion of cement was further shown to significantly reduce areal shrinkage strain and vertical free swelling strain while improving strength and stiffness of expansive clay as explained by Por et al. (2017).

To promote sustainability, studies have investigated Bangkok soil–cement mixtures incorporating industrial by-products such as fly ash from the Mae Moh Power Plant in Thailand. Incorporation of fly ash into cement-stabilized silty clay was found to disperse larger cement–clay clusters into smaller aggregates, increasing the surface area available for hydration and producing additional cementitious compounds, with maximum strength achieved at a water content of 1.2 times the optimum moisture content with 10 percent fly ash replacement as noted by Horpibulsuk et al. (2009) and Horpibulsuk et al. (2010). Strength development in cement-stabilized clay with fly ash was shown to follow three distinct stages — active, inert, and deterioration zones — governed by pore structure evolution and availability of water for hydration as shown by Horpibulsuk (2012). Alternative stabilizing agents including calcium carbide residue and biomass ash were found to achieve higher strength than cement-stabilized clay through pozzolanic reactions under high pH conditions after 28 days of curing as described in Vichan & Rachan (2013), while bagasse ash replacement at 20 percent was identified as the optimum proportion for enhancing Bangkok soft clay strength as indicated in Jamsawang et al. (2017). Deep soil mixing investigations using ordinary Portland cement with 15 percent fly ash replacement at a binder-to-water ratio of 0.4 proposed preliminary design guidelines based on UCS, elastic modulus, and shrinkage cracking resistance evaluated at 7 and 28 days as reported by Chompoorat et al. (2022). Scanning electron microscopy and X-ray diffraction analyses confirmed increased particle cluster formation and the presence of hydration and pozzolanic products in cement- and lime-stabilized expansive clays as presented in Chompoorat et al. (2021a). These findings have been extended to related applications including improvement of sediments using Portland cement and fly ash as described in Chompoorat et al. (2019), Chompoorat et al. (2021b) and Chompoorat et al. (2021c), evaluation of heavy metal leaching from fly ash in soil stabilization as demonstrated by Leelarungroj et al. (2018), treatment of municipal solid waste incineration fly ash by cement-based solidification as presented by Dontriros et al. (2020), and stabilization of dredged sediments for geotechnical and environmental purposes as reported by Yoobanpot et al. (2020a), Yoobanpot et al. (2020b), Chompoorat et al. (2021d) and Jamsawang et al. (2021).

While UCS testing has been extensively applied in soil stabilization research as a standard evaluation method, its destructive nature renders it unsuitable for cyclic or continuous monitoring of the same specimen throughout curing cycles. Non-destructive methods are therefore preferable for tracking strength gain over time, and bender element testing has been introduced as an effective alternative providing rapid, real-time evaluation of shear modulus development within the small-strain domain as described by Piriyakul & Pochalard (2013), Iamchaturapatr et al. (2021), Iamchaturapatr et al. (2022a) and Iamchaturapatr et al. (2022b). The preceding review underscores the critical role of cement in stabilizing soft clay, and the partial replacement of cement with fly ash is emphasized as a sustainable approach that offers both environmental and engineering benefits. In the present study, the stabilization of Bangkok soft clay with ordinary Portland cement and fly ash replacement is investigated using a self-developed bender element system to determine initial shear modulus from shear wave velocity measurements after curing periods of 7, 14, 28, and 90 days. Results are compared against UCS measurements obtained from destructive testing, enabling direct correlation between shear modulus and UCS.

Establishing this relationship is of practical significance as it allows prediction of UCS — a conventional destructive test parameter — from non-destructive bender element measurements, thereby providing an efficient means of deriving design parameters while minimizing reliance on destructive testing.

7.2 Materials

7.2.1 Bangkok clay

Soft clay samples are taken from the northern area of Bangkok to the experimental site, which is located in the King Mongkut's University of Technology North Bangkok (KMUTNB), Bangkok campus. All of samples are taken at the depth of 10 to 12 m due to its homogeneity. By various measurements, the fundamental properties of those samples are evaluated as follows. As an example, its main chemical compositions are shown in Tables 1 and 2 after Piriyakul (2010). It is noted that their natural water content is in the range of 81%, whereas their liquidity index of the clay near the ground surface is about 1.0, but decreases with depth.

7.2.2 Portland cement and Fly ash

In this study, Ordinary Portland Cement (OPC) was employed as a stabilizing agent for the Bangkok clay samples described earlier. The principal chemical compositions of OPC are presented in Table 1, and its specific gravity was determined to be approximately 3.14. Fly ash (FA), obtained as a by-product from the Mae Moh Power Plant in Lampang Province, northern Thailand, was also incorporated as a supplementary material. According to ASTM C618 (2019), this fly ash is classified as Class F. Its major chemical constituents are also summarized in Table 1, while its specific gravity was measured to be around 2.3. The average particle sizes (D_{50}) of OPC and FA were found to be 0.6 mm and 0.08 mm, respectively.

Table 7-1 Chemical compositions of Bangkok clay, Portland cement and Fly ash (class F).

Comp.	Bangkok clay in this study	Ordinary Portland cement	Fly ash (class F)
$\%SiO_2$	62.5	20.90	37.34
$\%Al_2O_3$	18.4	4.76	18.63
$\%Fe_2O_3$	8.49	3.41	13.17
%CaO	1.07	65.41	17.85
%MgO	2.35	1.25	3.92
$\%SO_3$	1.86	2.71	3.51

Table 7-2 Properties of Bangkok soft clay in this study.

Liquid limit	Plastic limit	Undrained shear strength	Specific gravity	Natural water content	Total unit weight
88%	34%	14.5 kPa	2.68	81%	1,470 kg/m^3

7.2.3 Soil cement preparation

For the preparation of all Bangkok clay specimens, Ordinary Portland Cement (OPC) was incorporated at 20 percent by dry weight of soil, with water added at the liquid limit of 88 percent as described in the Department of Highways of Thailand (DOH), & Japan International Cooperation Agency (JICA) (1998). The mixtures were further modified by partially replacing OPC with fly ash (FA) at varying replacement levels of 0, 10, 15, 20, 25, and 30 percent, followed by curing for 7, 14, 28, and 90 days, as summarized in Table 3. Each testing condition consisted of three replicate specimens. For example, the mixture containing 0 percent FA included a total of 12 specimens, corresponding to four curing periods (7, 14, 28, and 90 days). In total, 72 specimens were prepared for this study. The test results obtained from each set of three replicates were averaged to produce a representative value for subsequent analysis. It should be noted that if any of the three specimens exhibited a deviation greater than ±10 percent from the mean, that result was excluded from the dataset.

Table 7-3 Mixing proportions of Bangkok clay samples.

Dry clay [g]	Curing time [days]	Cement [g]	Fly ash [g]	Water content [%]	Unit Weight [kg/m^3]
101.36	7, 14, 28, 90	25.34	0	88	1479.9
101.36	7, 14, 28, 90	25.34	2.534	88	1573.2
101.36	7, 14, 28, 90	25.34	3.801	88	1499.9
101.36	7, 14, 28, 90	25.34	5.068	88	1476.5
101.36	7, 14, 28, 90	25.34	6.335	88	1498.4
101.36	7, 14, 28, 90	25.34	7.602	88	1574.9

7.3 Methods

In accordance with ASTM D8295-19 (2019), the bender element test (BET) was employed to measure the shear wave velocity (V_s), which was subsequently used to determine the stiffness of clay specimens in terms of the initial shear modulus (G_0). The BET test was further applied to monitor variations in V_s of the cement–fly ash admixed Bangkok soft clay during the progression of pozzolanic reactions, thereby providing insight into changes in shear modulus. For comparison, unconfined compressive strength (UCS) testing was also performed. Although UCS is a destructive method, it remains advantageous in terms of simplicity and time efficiency.

In the experimental program, Bangkok clay specimens were prepared in cylindrical form with a diameter of 38 mm and a height of 76 mm. To prevent moisture loss, the specimens were sealed with plastic membranes and cured for 7, 14, 28, and 90 days. At the completion of each curing period, UCS tests were conducted in accordance with ASTM D1633-17 (2017). The overall experimental procedure and testing framework are summarized in the flow chart presented in Figure 7-1.

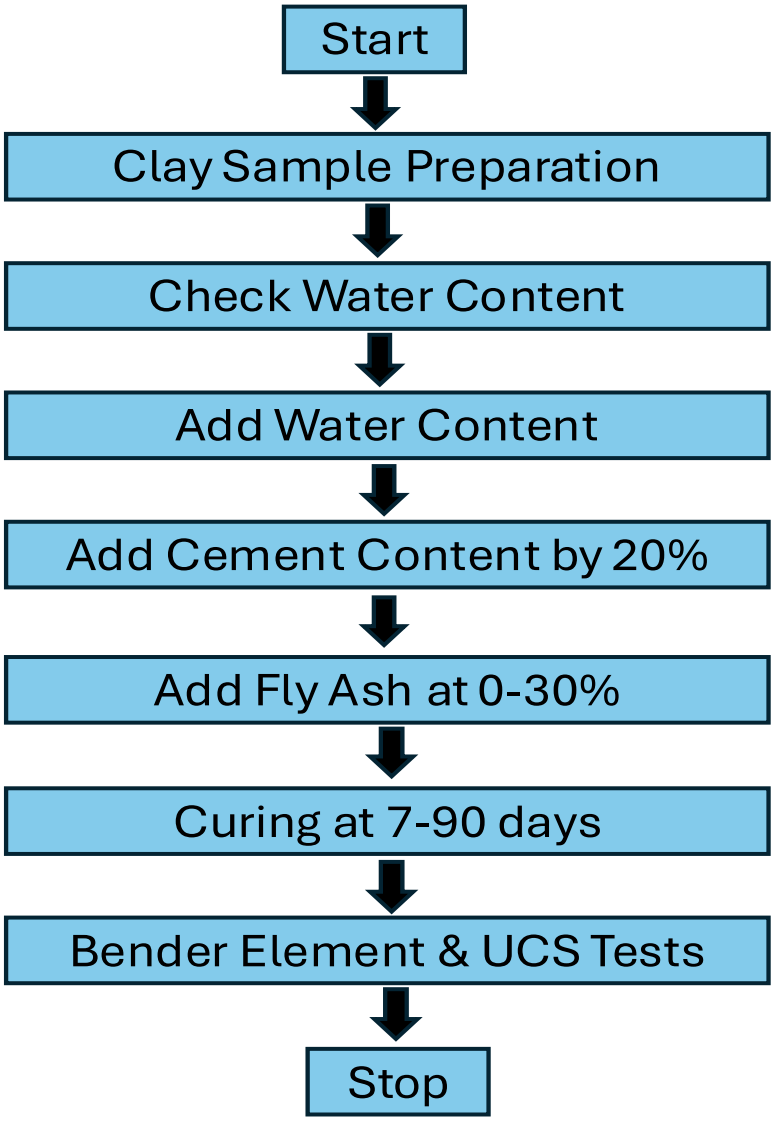


Figure 7-1 Flow chart for sample preparation and tests after Petcherdchoo et al. (2023).

7.4 Results and Discussions

7.4.1 Effect of curing time

For the Bangkok clay specimens stabilized with cement and fly ash (FA), Figures 3 and 4 illustrate the influence of curing time on shear wave velocity (V_s) and initial shear modulus (G_0), respectively. Regression analysis of the experimental data, as presented in Figure 7-2, shows that V_s increases progressively with curing duration. The regression slope for the control specimen (0% FA) was 32.786, which is comparable to the slopes obtained for mixtures containing 10%, 25%, and 30% FA replacement. However, significantly higher slopes of 82.424 and 103.04 were recorded for the mixtures with 15% and 20% FA replacement, respectively, indicating that these two replacement levels provide optimal improvement in V_s.

A similar trend was observed for G_0, as shown in Figure 7-3. While the regression slopes for mixtures with 0%, 10%, 25%, and 30% FA replacement ranged between 27 and 40, much higher values of 89.105 and 128.95 were obtained for the 15% and 20% FA replacement mixtures, confirming that these proportions are optimal for enhancing G_0. Furthermore, the mixture containing 10% FA replacement after 14 days of curing, G_0 and unconfined compressive strength (q_u) were measured as 145.97 MPa and 303.33 kPa, respectively. Compared with the findings of Madhyannapu et al. (2010), the G_0 values in this study are slightly higher, whereas the q_u values are lower, which may be attributed to the lower cement content used in the present investigation.

Figure 7-4 presents the regression analysis of experimental results to establish the relationship between q_u and curing time. The analysis indicates that q_u increases consistently with longer curing durations. The regression slope for the control specimen (0% FA) was 298.36, which was comparable to the slope for the mixture with 15% FA replacement (316.16). These results suggest that the optimum FA replacement level for achieving the highest q_u is approximately 15%.

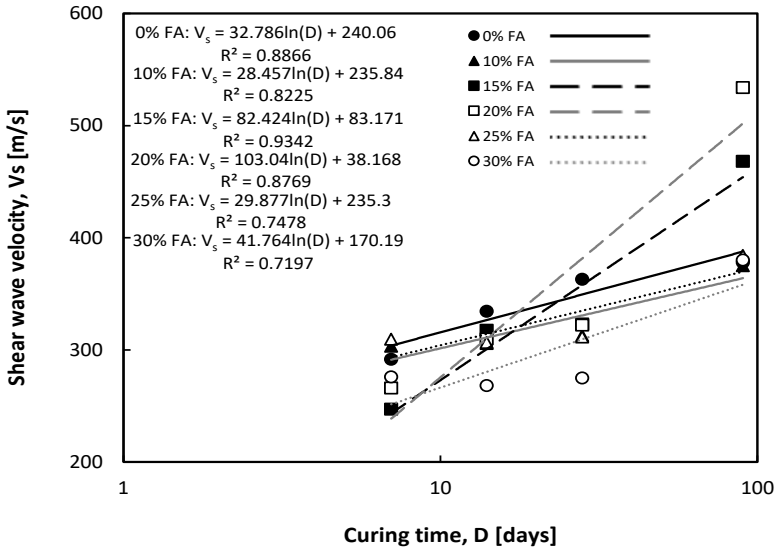


Figure 7-2 Development of V_s with curing time of FA stabilized Bangkok soft clay after Petcherdchoo et al. (2023).

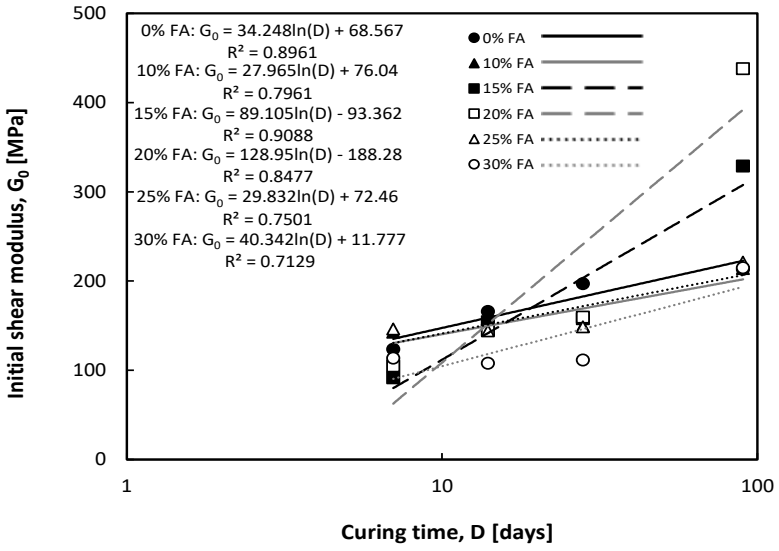


Figure 7-3 Development of G_0 with curing time of FA stabilized Bangkok soft clay after Petcherdchoo et al. (2023).

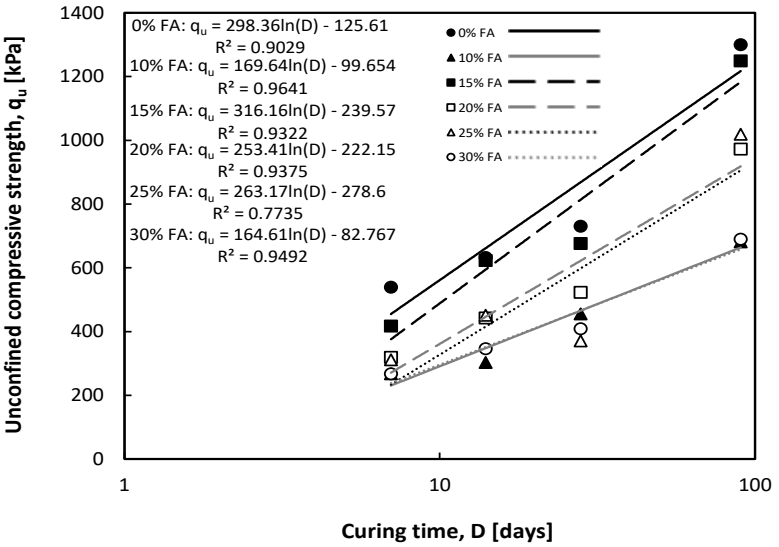


Figure 7-4 Development of q_u with curing time of FA stabilized Bangkok soft clay after Petcherdchoo et al. (2023).

7.4.2 Effect of FA content

Figures 7-5 and 7-6 illustrate the variation of shear wave velocity (V_s) and initial shear modulus (G_0) as functions of fly ash (FA) content. The maximum recorded values were 534 m/s for V_s at 20% FA after 90 days of curing and 438 MPa for G_0 under the same conditions. These peak values at 20% FA replacement are consistent with findings reported in earlier studies by Horpibulsuk et al. (2010). It was further observed that prior to 90 days of curing, both V_s and G_0 exhibited a slight tendency to decrease with increasing FA content.

Similarly, Figure 7-7 presents the variation of unconfined compressive strength (q_u) with FA replacement. The results indicate that mixtures with 15% FA consistently produced the highest q_u across all curing periods, identifying 15% FA as the optimum replacement level. This conclusion aligns with findings from previous literature of Petcherdchoo et al. (2023). It is also noteworthy that before 90 days of curing, q_u showed a tendency to decrease with increasing FA content.

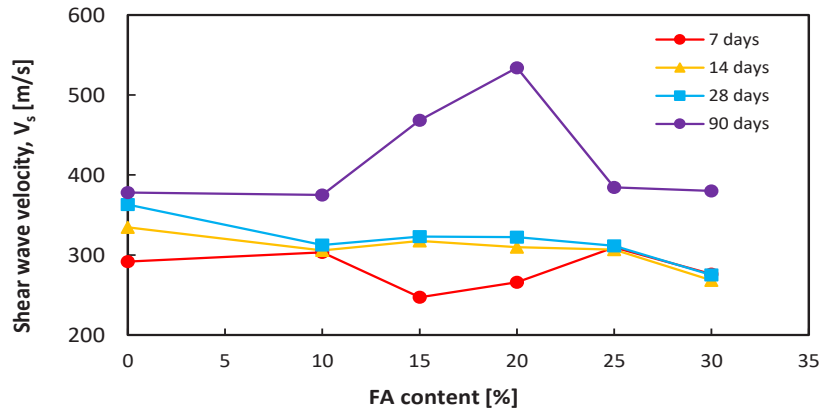


Figure 7-5 Variation of V_s and FA contents of stabilized Bangkok soft clay after Petcherdchoo et al. (2023).

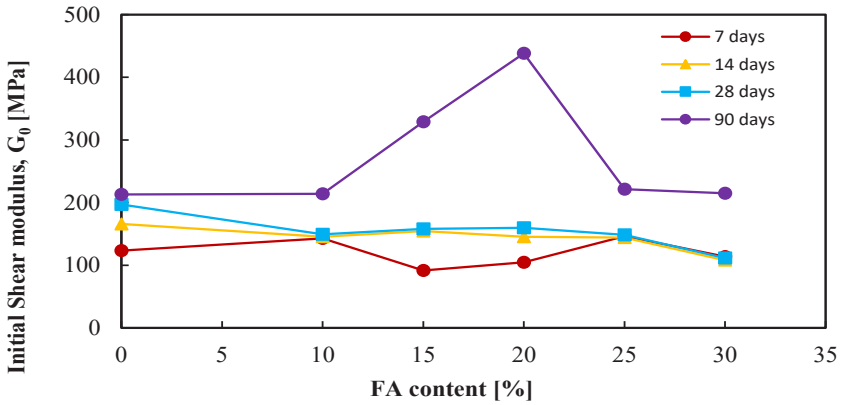


Figure 7-6 Variation of G_0 and FA contents of stabilized Bangkok soft clay after Petcherdchoo et al. (2023).

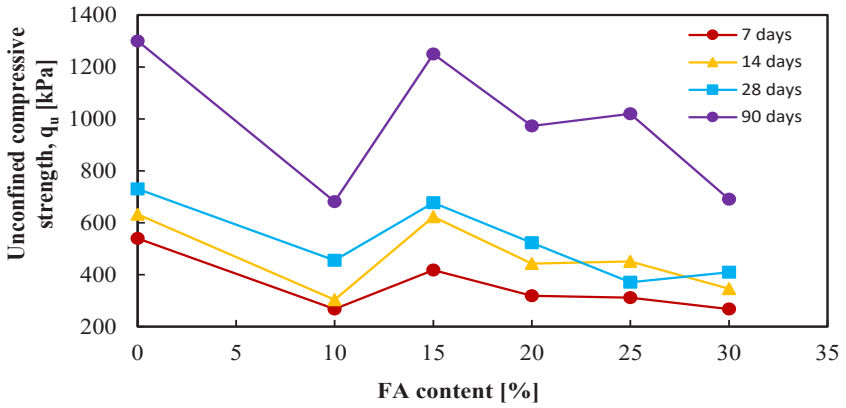


Figure 7-7 Variation of q_u and FA contents of stabilized Bangkok soft clay after Petcherdchoo et al. (2023).

7.4.3 Relationships of normalized q_u and curing time

While the primary objective of this research is to employ the bender element test for evaluating the properties of soft clay, it is also valuable to demonstrate the consistency of the present findings with those reported in previous studies. Such consistency not only reinforces the reliability of the bender element method but also validates its applicability for soft clay characterization. To achieve this comparison, the normalized unconfined compressive strength was utilized.

Several researchers have examined the relationship between normalized unconfined compressive strength (q_u/q_{28}) and curing time in soft clay stabilized with OPC and FA. Their results indicated that q_u/q_{28} increases with curing duration. In particular, Horpibulsuk et al. (2010) highlighted that normalization of q_u is necessary to account for variations in clay type, water content, and cement content among different studies. They subsequently presented the normalized strength development of stabilized Bangkok clay treated with OPC, fly ash (FA), and biomass ash (BA) admixtures as a means of achieving meaningful comparisons across diverse experimental conditions as shown in Equation 7.1.

$$\frac{q_u}{q_{28}} = 0.293\ln(D) + 0.026 \tag{7.1}$$

In addition, Yoobanpot et al. (2020a) and Chompoorat et al. (2022) presented the development of normalized unconfined compressive strength for dredged sediment stabilized with OPC and FA, as well as for Bangkok soft clay treated with OPC–FA admixtures, respectively, expressed as seen in Equations 7.2 and 7.3, respectively.

$$\frac{q_u}{q_{28}} = 0.313\ln(D) + 0.075 \tag{7.2}$$

$$\frac{q_u}{q_{28}} = 0.31\ln(D) + 0.003 \tag{7.3}$$

Furthermore, the unconfined compressive strength of recycled clay soil obtained from Nakhon Ratchasima Province in northeastern Thailand, stabilized with Ordinary Portland Cement (OPC) and fly ash (FA) after a curing period of 28 days as described in Chindaprasirt et al. (2021), was reported as expressed in Equation 7.4.

$$\frac{q_u}{q_{28}} = 0.649 \log(D) + 0.0355 \tag{7.4}$$

where D denotes the curing period in days. Equation 7.4 can subsequently be reformulated as shown in Equation 7.5.

$$\frac{q_u}{q_{28}} = 0.2819 \ln(D) + 0.0355 \tag{7.5}$$

Based on regression analysis of the experimental data obtained in this study, Figure 7-8 illustrates that the relationship between normalized unconfined compressive strength (q_u/q_{28}) and curing time for cement-admixed Bangkok soft clay with fly ash (FA) addition can be represented as expressed Equation 7.6.

$$\frac{q_u}{q_{28}} = 0.3642 \ln(D) + 0.019 \tag{7.6}$$

This linearized natural logarithmic equation is consistent with Equations 7.1 to 7.6 reported in previous studies as shown for comparison in Figure 7-8. Two key observations can be drawn from this comparison. First, the normalized unconfined compressive strength (q_u) values obtained in all referenced studies exhibit a similar trend. Both Yoobanpot et al. (2020a) and Chompoorat et al. (2022) attributed this similarity to the comparable mechanisms of strength development arising from cement hydration and pozzolanic reactions. Specifically, cement hydration, which represents the primary reaction, involves the interaction of calcium oxide (CaO) from cement with water in the soil. The secondary process, namely the pozzolanic reaction, occurs when calcium hydroxide [$Ca(OH)_2$], a product of cement hydration, reacts with silica (SiO_2) from fly ash to form additional cementitious compounds. For the second observation, Figure 7-8 indicates that while the slope of the normalized unconfined compressive strength (q_u) obtained in this study is generally consistent with those reported in other investigations, discrepancies arise in terms of the early-age normalized q_u, represented by the y-intercept. In the reviewed studies, early-age normalized q_u values ranged between 0.003 and 0.075, whereas in the present study it was measured at 0.09. This difference can be attributed to variations in soil type, initial water content, and cement dosage. Specifically, the present research employed Bangkok soft clay, while Yoobanpot et al. (2020) examined dredged sediment from Chiang Mai Province, and Chindaprasirt et al. (2021) utilized recycled clay from Nakhon Ratchasima Province. Although the Bangkok clay used here is similar in origin to that tested in Horpibulsuk et al. (2011) and Chompoorat et al. (2022), differences in sampling locations contribute to distinct material properties, such as particle size distribution and related characteristics. These differences likely account for the variation in early-age normalized q_u values. Consequently, the comparison across studies should be interpreted as reflecting general trends rather than exact parameter values for the normalized q_u equation.

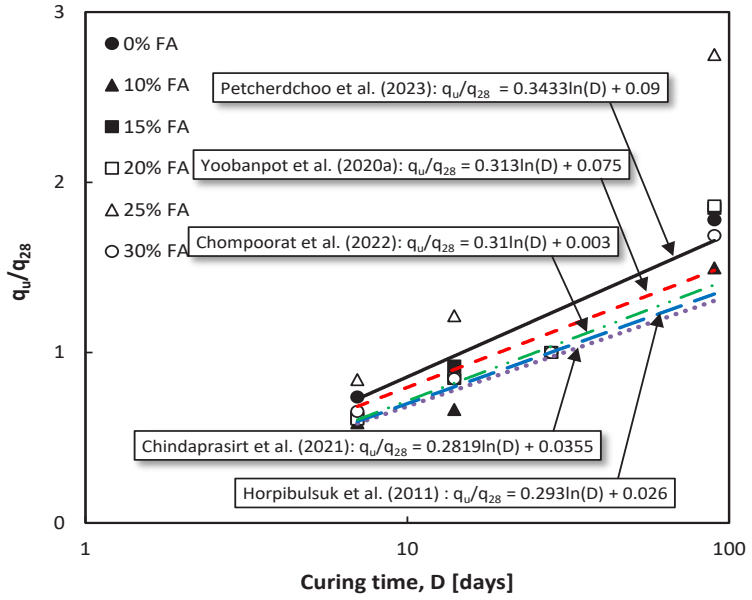


Figure 7-8 Relationships between q_u/q_{28} and curing time after Petcherdchoo et al. (2023).

7.4.4 Other comparisons

Figure 7-9 illustrates the relationship between normalized shear modulus ($G_0/G_{0(28)}$) and normalized unconfined compressive strength (q_u/q_{28}), comparing the results of Kim et al. [44] with those obtained in the present study. In their investigation, the relationship was expressed in the form of a natural logarithmic function as follows:

$$\frac{G_0}{G_{0(28)}} = 0.287ln\left(\frac{q_u}{q_{28}}\right) + 1 \tag{7.7}$$

Based on regression analysis of the experimental data obtained in this study, two functional relationships are proposed: a natural logarithmic function and a linear function, as illustrated in Figure 7-9. These relationships can be expressed as follows:

$$\frac{G_0}{G_{0(28)}} = 0.8972ln\left(\frac{q_u}{q_{28}}\right) + 1 \tag{7.8}$$

$$\frac{G_0}{G_{0(28)}} = 0.9526\left(\frac{q_u}{q_{28}}\right) \tag{7.9}$$

In comparison, both Equations 7.8 and 7.9 adopt the form of a linearized natural logarithmic function, with slopes of 0.287 for the study by Kim et al. (2018) and 0.8972 for the present study. However, when considering Figure 7-9, it is evident that the fit of the linearized logarithmic function to the experimental data in this study is inadequate, as reflected by an R^2 value of 0.5436. To address this limitation, Equation 7-9 is alternatively

proposed in the form of a linear function, which clearly yields an improved R^2 value, as shown in the figure.

Two key observations may be drawn from this analysis. First, the experimental results were validated only within a specific range, namely when the normalized q_u/q_{28} was less than 1.5, as illustrated in Figure 7-9. When applying this same range to the present study, as shown in Figure 7-10, it can be observed that both the natural logarithmic and linear functions provide nearly identical relationships between normalized $G_0/G_{0(28)}$ and q_u/q_{28}.

When the relationship extends beyond the range of normalized $q_u/q_{28} > 1.5$, the linear function appears to provide a more appropriate fit than the natural logarithmic function. Although the overall consistency of the three relationships is of a comparable order, certain discrepancies are evident, largely attributable to differences in soil types, material compositions, and mix designs adopted in the two studies. Specifically, Kim et al. (2018) conducted their experiments using marine clays obtained from Busan and Ulsan Newport in

Korea, whereas the present study employed Bangkok clay from Thailand. In terms of stabilizing agents, Kim et al. (2018) utilized Ordinary Portland Cement (OPC) combined with blast furnace slag (BFS), while this research incorporated OPC with fly ash (FA). Furthermore, the cement contents varied 10–16% cement for Busan clay and 16–22% cement for Ulsan clay, while this study adopted a cement content of 22% for Bangkok clay.

From these observations, it is recommended that future studies should explore the potential of incorporating other sustainable stabilizing agents, particularly waste-derived and recycled materials as described in Petcherdchoo (2018a), Petcherdchoo et al. (2020), Petcherdchoo (2015) and Petcherdchoo (2018b), to broaden the comparative framework and further enhance the sustainability of soil stabilization practices.

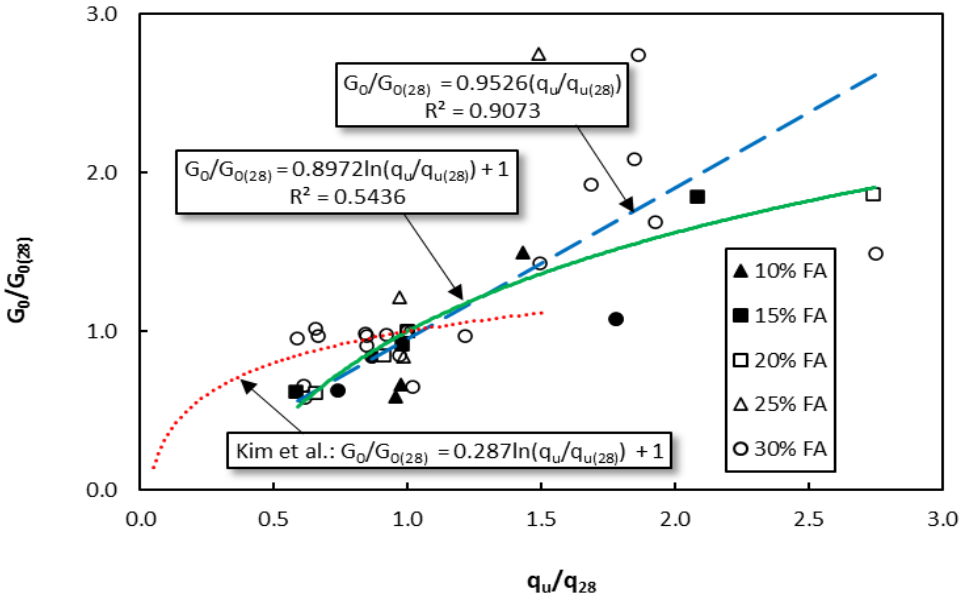


Figure 7-9 Relationships between $G_0/G_{0(28)}$ and q_u/q_{28} after Petcherdchoo et al. (2023).

7.4.5 Limitation of bender element tests

Chindaprasirt et al. (2021) established a correlation between the deformation modulus (E_{50}, in MPa) and the unconfined compressive strength (q_u, in MPa) of recycled clay soil obtained from Nakhon Ratchasima Province, Thailand. The soil was stabilized with Ordinary Portland Cement (OPC) and fly ash (FA) and tested after 28 days of curing. The relationship was expressed as presented in Equation 7.10.

$$E_{50} = 50q_u \tag{7.10}$$

In the bender element tests conducted in this study, shear wave velocity was first measured and subsequently converted to the initial shear modulus (G_0) using Equation 7.11. Complementarily, destructive unconfined compressive strength (q_u) tests were also performed to obtain strength parameters for comparison.

$$G_0 = 275.7q_u \tag{7.11}$$

Figure 7-10 presents the regression analysis of the experimental results, illustrating the relationship between G_0 (MPa) and q_u (MPa). The data were found to be well represented by a linear function, which can be expressed as follows:

$$\frac{E}{2(1+\nu)} = G_0 = 275.7q_u \tag{7.12}$$

By further incorporating the relationship between the elastic modulus (E) and the initial shear modulus (G_0), Equation 7.12 can be reformulated as shown in Equation 7.13. Where ν is denoted as a Poisson ratio which is equal to 0.3 to 0.5.

$$E = (71.68\ to\ 82.71)q_u \tag{7.13}$$

In comparison, E_{50} in Equation 7-12 was measured at large strain state in combination with considering the history of the compressive stress-axial strain relationship obtained from a destructive test. However, E in Equation 7-15 is determined based on G_0 in Equation 7-13, which is measured at small strain state based on the non-destructive bender element tests. This implies that the bender element test can be used to determine only the small strain quantity in terms of G_0 or E obtained from non-destructive tests, but not the large strain quantity in terms of E_{50} obtained from destructive tests. However, such small strain quantity is beneficial for constitutive modelling in various computations, such as the finite element method (FEM), dynamic analysis of soil property, etc.

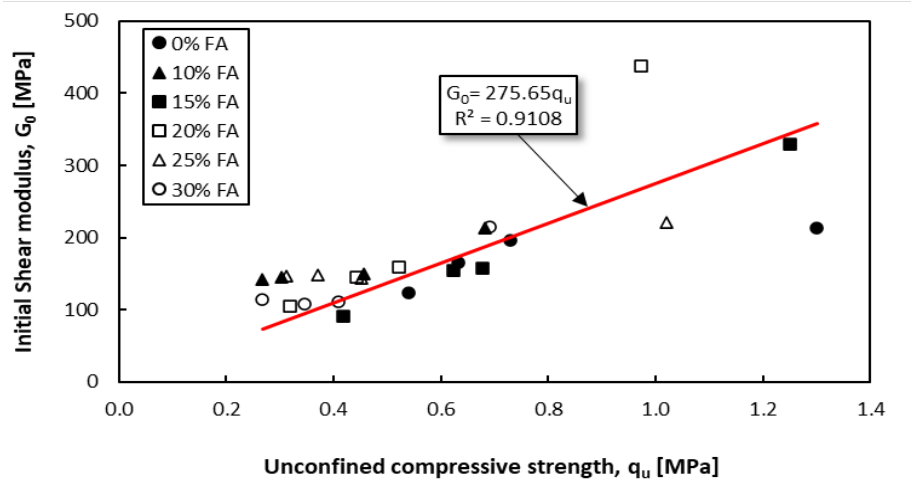


Figure 7-10 Relationships between G_0 and q_u after Petcherdchoo et al. (2023).

7.4.6 SEM analysis

Figure 7-11 presents the SEM micrograph of the specimen containing 20% fly ash (FA). The spherical FA particles, approximately 5–10 microns in diameter, participate in pozzolanic reactions, producing cementitious compounds. This observation corroborates the findings of Horpibulsuk et al. (2009), who emphasized that strength development in blended cement–stabilized clay is governed by cementitious products resulting from the combined effects of hydration and particle dispersion. Both the microstructural analyses and strength test results from this study indicate that the pozzolanic activity of FA in this system is relatively limited compared with its more pronounced role in conventional concrete. This reduced reactivity is attributed primarily to the limited availability of calcium hydroxide [$Ca(OH)_2$], which is critical for initiating and sustaining pozzolanic reactions.

Within this context, the principal contribution of FA appears to be physical rather than chemical, as it facilitates the breakdown of large clay–cement agglomerates into finer, more uniformly distributed clusters, thereby enhancing the efficiency of cementitious bonding. FA, being a pozzolanic material, reacts with $Ca(OH)_2$ (a by-product of cement hydration) and water to form calcium silicate hydrate (C–S–H). These C–S–H products, together with other secondary reaction products such as ettringite and calcite, further improve the mechanical behaviour of stabilized soils, including q_u, V_s and G_0. Since pozzolanic reactions occur as a secondary process, they progress more slowly than initial cement hydration, with strength gains continuing beyond 28 days and often showing significant enhancement after 90 days.

In addition, the extremely fine particle size of FA allows it to fill voids between cement grains, improving packing density and long-term strength. However, due to its high water absorption capacity, higher FA contents can reduce the availability of free water for cement hydration, leading to reduced strength. These behavioural characteristics will be further validated in future work using advanced techniques such as XRD, XRF, and EDX analysis.

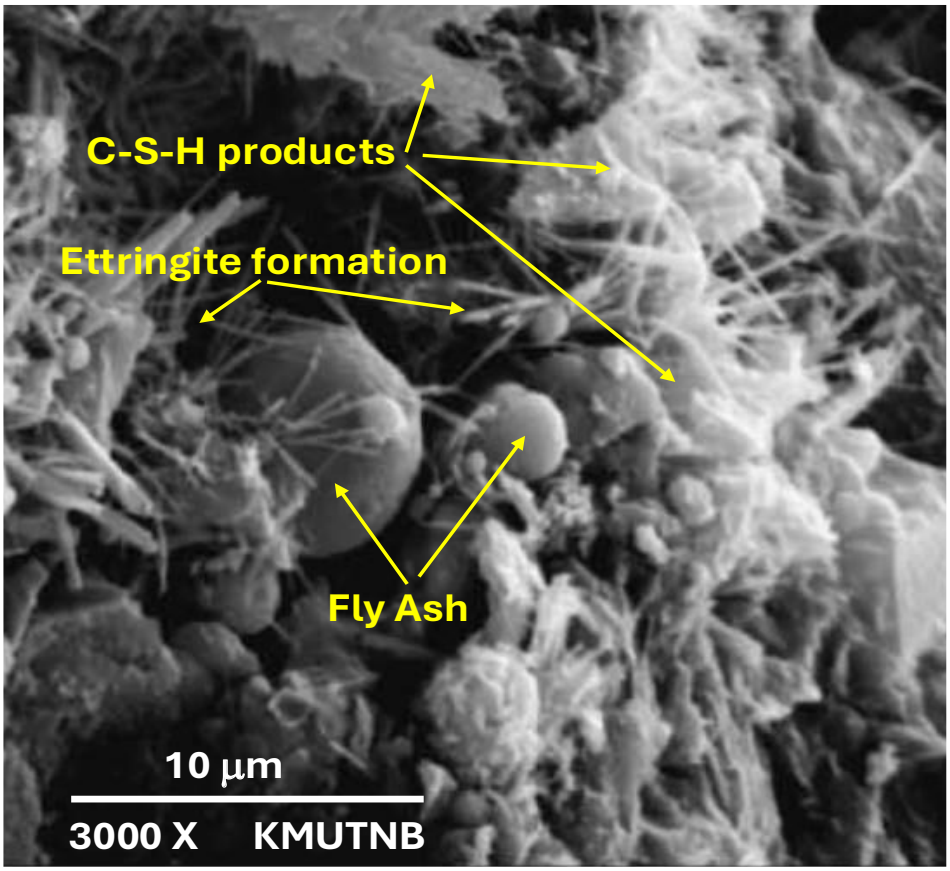


Figure 7-11 SEM image of 20% FA sample at 28 days after Petcherdchoo et al. (2023).

Summary

In this investigation, Bangkok soft clay was stabilized through the addition of 20% Type I Portland cement by weight and water at its liquid limit of 88%. Fly ash (FA) was subsequently incorporated at replacement levels of 0%, 10%, 15%, 20%, 25%, and 30%, with curing periods of 7, 14, 28, and 90 days. Following each curing stage, both destructive unconfined compressive strength (UCS) tests and non-destructive bender element tests (BET) were conducted to evaluate the improvement in soil behavior. The main findings can be summarized as follows:

1. First, based on shear wave velocity (V_s) and the initial shear modulus (G_0), FA replacement levels of 15% and 20% were identified as optimal. In contrast, when evaluated using UCS results, the optimum replacement level was found to be 15%.

2. Second, all key parameters—V_s, G_0, and UCS—exhibited increases with curing time. At 90 days, V_s and G_0 suggested an optimum FA content of 20%, while UCS indicated an optimum value of 15%. These findings are in line with trends reported in other studies, confirming the consistency of the results.

3. Third, the relationship between normalized UCS (q_u/q_{28}) and curing time followed a natural logarithmic function, with a rate of increase of 0.3433. The early-age normalized UCS was found to be 0.09. Although the material compositions used in this study were similar to those reported by Chindaprasirt et al. (2021), discrepancies were observed, likely due to variations in clay types and cement contents. Nevertheless, the relationship identified in this study remains broadly compatible with those reported in previous investigations, despite some differences arising from compositional variations.

4. The normalized shear modulus in relation to the normalized unconfined compressive strength was observed to increase following a natural logarithmic trend, with coefficients of 0.8972 in the present study and 0.287 in the work of Kim et al. (2018). However, due to inconsistencies in curve fitting with the experimental data, a linear function was proposed as an alternative to represent the relationship. While the overall relationships are generally consistent, discrepancies remain, which may be attributed to differences in clay origin (Bangkok versus Busan/Ulsan), cement content (20% in this study compared with 10–22% in Kim et al. (2018)), and the type of stabilizers used (OPC with fly ash in this study versus OPC with blast furnace slag in Kim et al. (2018).

5. It is emphasized that the bender element test is limited to the evaluation of small-strain soil parameters, such as G_0 or the elastic modulus (E) derived from non-destructive testing and cannot be applied to large-strain parameters such as E_{50}, which require destructive testing.

6. For future work, it is recommended that the findings of this study be further applied in practical construction contexts. Additionally, comparative investigations with other sustainable stabilizers, particularly waste-derived or recycled materials, are suggested to broaden the understanding and enhance the environmental sustainability of soil stabilization practices.

Question and Problems

1. Explain the soil-cement and its importances.
2. Why is Bangkok clay needed to enhance its strength?
3. What would be the potential to use industrial waste to enhance the engineering properties of soft Bangkok clay?
4. What is the advantage of the relationships between G_0 and q_u?
5. What is the optimum proportion of fly ash to be used in soil-cement as a cement replacement?
6. What is the effect of aging in soil-cement when adding fly ash?
7. Why does fly ash show the long term increasement of strength?
8. What is the advantage of applying the bender element test to monitor strength development?
9. What is the relationship between the Young's modulus and the q_u?
10. If you were a project engineer who built the road in Bangkok area, how you are going to use fly ash in your project?

Chapter 8: Applications of Shear Wave Testing in Bangkok Clay mixed with Cement and Fibers

8.1 Introduction of Bangkok Clay mixed with Cement and Fibers

Thailand's textile sector has grown substantially over the past five decades, positioning the country among the world's leading producers of synthetic fibers, including ranking ninth in polyester and fifth in acrylic production globally, with notable year-over-year growth in both domestic consumption and production of man-made fibers recorded in 2016 as reported by Thailand Board of Investment (2017). Sustainable waste management guidelines for the fast fashion industry have encouraged the adoption of recycled materials, including recycled polyester fabric promoted by major international clothing businesses as described in Wongchittaphok (2018) and Thai Polyester Co., Ltd. (2024). In parallel, ground improvement technologies such as Deep Mixing Columns and Shallow Soil Mixing have been essential for developing subsurface structures on soft ground as outlined by Piriyakul & Iamchaturapatr (2017) and Piriyakul (2013). Ordinary Portland Cement has been widely employed to stabilize soft clay with the objectives of increasing UCS, decreasing permeability, and reducing ground settlement. Studies on Bangkok soft clay stabilized with cement and fly ash geopolymer demonstrated that increasing cement content enhanced UCS while reducing the sodium silicate-to-sodium hydroxide ratio led to strength reductions as noted by Suksiripattanapong et al. (2022). Investigations integrating environmental geotechnics with chemical ground improvement confirmed that OPC combined with up to 10% fly ash replacement substantially improved strength, with long-term strength continuing to increase in mixtures containing more than 20% fly ash as shown in Nontananandh et al. (2004). Comprehensive reviews of soil stabilization principles established that enhanced geotechnical performance can be achieved through cementitious binders or industrial by-products such as fly ash and slag as presented by Firoozi et al. (2017). Further studies highlighted the pozzolanic benefits of nano-silica in improving interfacial bonding and accelerating hydration as described in Patro & Sahoo (2021) and Vichan et al. (2013), while nano-zeolite reinforcement was confirmed through SEM and XRD analyses to generate cementitious products responsible for strength enhancement as noted by Ali et al. (2023). Investigations of Bangkok clay contaminated with zinc sludge and stabilized with high-calcium fly ash geopolymer demonstrated acceptable UCS and leaching properties meeting international landfill disposal standards despite the retarding effect of heavy metals as explained by Phojan et al. (2023). Strength development in clay–fly ash geopolymer systems was found to increase with higher alkaline activator quantities up to a threshold, beyond which excess activator caused premature precipitation and microcracking as demonstrated by Sukmak et al. (2013).

Fiber-reinforced soils are composite materials formed by incorporating synthetic or natural fibers into soil matrices, enhancing tensile strength, ductility, and durability, and are widely applied for slope stabilization, embankment construction, and erosion control as described in Iamchaturapatr et al. (2022a), Ma et al. (2018) and Bawadi et al. (2020). The optimum fiber content in reinforced clay soils subjected to large shear displacements was found to depend primarily on initial void ratio, irrespective of stress history or applied effective normal stress as presented by Mirzababaei et al. (2017). Studies on polyethylene terephthalate fiber-reinforced silty soil confirmed that increasing fiber content enhanced shear strength and deformability, reducing the likelihood of crack formation under loading or environmental conditions as shown in Botero et al. (2015).

Investigations of basalt fiber-reinforced loess identified two primary reinforcement mechanisms — spatial mesh effect and individual tensile effect — yielding reliable predictive models for shear strength applicable to slope stabilization and subgrade engineering as reported by Chen et al. (2023). The incorporation of sisal and coconut fibers into lightweight expanded clay fiber concrete demonstrated improvements in compressive and flexural strength, with sisal fibers providing superior reinforcement over coconut fibers as demonstrated by. Özkılıç et al. (2023). Recycled garnet residues and tire-derived aggregates were shown to enhance the mechanical behavior of soft clay subgrades, with optimal mixture proportions of SC:GR = 90:10, 2% cement content, and 2% TDA content identified for sustainable subgrade development as noted by Sukmak et al. (2021). Microstructural investigations of Bangkok clay stabilized with cement and bottom ash revealed significant strength improvements when base cement content was maintained at no less than 20% with more than 15% bottom ash addition as shown by Phutthananon et al. (2023). Multi-stage drained reverse direct shear tests on polypropylene fiber-reinforced soft clay demonstrated that fiber reinforcement markedly improved effective cohesion — by factors of up to 8.5 at 0.50% fiber dosage — while exerting little influence on the effective internal friction angle as observed by Mirzababaei et al. (2018).

Road engineering applications of glass fiber-reinforced clayey soils demonstrated substantial increases in UCS, California Bearing Ratio, and shear strength at an optimum fiber content of 0.75%, with reinforcement transforming soil behavior from brittle to ductile failure and identifying significant potential for flexible pavement subgrade applications as reported by Patel (2022). Studies on polypropylene fiber-reinforced cement-stabilized Shanghai soft clay highlighted an innovative approach for recycling waste polymer textile bags as reinforcement material in soil mixing applications as presented by Chen (2015). Polyester fibers applied in deep mixing of sandy soils achieved strengths at three-hour curing comparable to cement- or lime-stabilized soils cured for 28 days, demonstrating considerable potential as a rapid-acting binder as described in Arasan et al. (2015). Comparative investigations of glass fiber-reinforced sandy and clayey soils confirmed that strength improvement in sandy soils is primarily attributed to induced cohesion, whereas in clayey soils it results from both increased friction angle and induced cohesion, while fiber inclusion also reduced bulging and shear failure zones as shown in Patel & Singh (2022). Combined use of polypropylene fibers and liquid polymers in cement-stabilized soft clay revealed that 0.5% fiber content increased remolded cemented soft clay strength by up to 240%, with the two additives operating through substantially different reinforcement mechanisms as noted by Ayeldeen & Kitazume (2017). Further investigations confirmed that fiber reinforcement below optimum moisture content increased ductility, compressive and shear strength, and cohesion, while reinforcement above optimum moisture content produced more brittle behavior alongside continued improvements in compressive and shear strength as reported by Arabani & Haghsheno (2020).

Bender element testing has been widely applied in soil mechanics to evaluate shear wave velocity and small-strain shear modulus of soil specimens, providing a reliable non-destructive alternative to conventional destructive testing methods as described in Piriyakul (2013b), Iamchaturapatr et al. (2022b) and Iamchaturapatr et al. (2021). Investigations of fiber-reinforced clays using bender element testing highlighted the importance of fiber–clay contact area within the soil matrix, proposing a novel regression model relating UCS to small-strain shear modulus G_0 that successfully predicted strength across different fiber types, densities, and contents as shown in Ekinci et al. (2022) [33]. Bender element testing applied to Bangkok clay stabilized with fly ash and cement demonstrated broad consistency with established UCS correlations, though

noticeable variations were observed due to differences in soil type, material composition, cement content, and stabilizer combinations, prompting recommendations for further research to refine predictive correlations as described in Petcherdchoo et al. (2023). The present study builds upon these findings by investigating Bangkok soft clay stabilized with ordinary Portland cement and recycled polyester fibers derived from the textile industry waste stream, integrating bender element testing for non-destructive shear modulus evaluation alongside UCS testing across curing periods of 7, 14, 28, and 90 days. This integrated approach aims to establish reliable correlations between small-strain stiffness parameters and compressive strength, while simultaneously promoting sustainable use of industrial textile waste as a soil reinforcement material in geotechnical engineering applications.

According to the aforementioned literature reviews, there are two concerns that require more attention. The quantity of polyester fiber must first be put to the Bangkok soft clay mixture. Second, the soil-cement mixture must also include the required amount of cement. So, the purpose of this research is to determine the ideal ratio of polyester fiber to soil-cement by examining the impacts of polyester fiber on soil-cement. The bending element test and the unconfined compression test were used in the study to verify the polyester fiber content of 0, 1, 2, 5, 10, and 20% by volume and the cement content of 1, 2, 5, 10, and 20% by weight in soil-cement samples combined at the liquid limit. The samples were then studied for 3, 7, 14, and 28 days.

8.2 Fiber Materials and Methods

8.2.1 Materials

The soft marine clay in this research was Bangkok soft clay and was collected from a depth between -8.0 and -10.0 m at the Bang Kruai Hospital in the Northern area of Bangkok nearby the KMUTNB campus. At these depths the soft Bangkok clay samples are homogeneous and have no impurities, which is suitable to characterize its properties in geotechnical engineering. All soft Bangkok clay samples were wrapped in plastic bags to preserve their humidity.

Tables 8-1 and 8-2 show the chemical compositions of Bangkok clay and the ordinary Portland cement (OPC). The Plastic Limit (PL) is 27.7%, the Liquid Limit (LL) is 82.6%, the natural water content (w_n) is 70.8%, the wet total unit weight (γ_t) is 1.65 T/m^3 and the dry unit weight (γ_d) is 0.97 T/m^3. The Liquidity Index (LI) of near-surface clay is about 1.0, but it decreases down by depth.

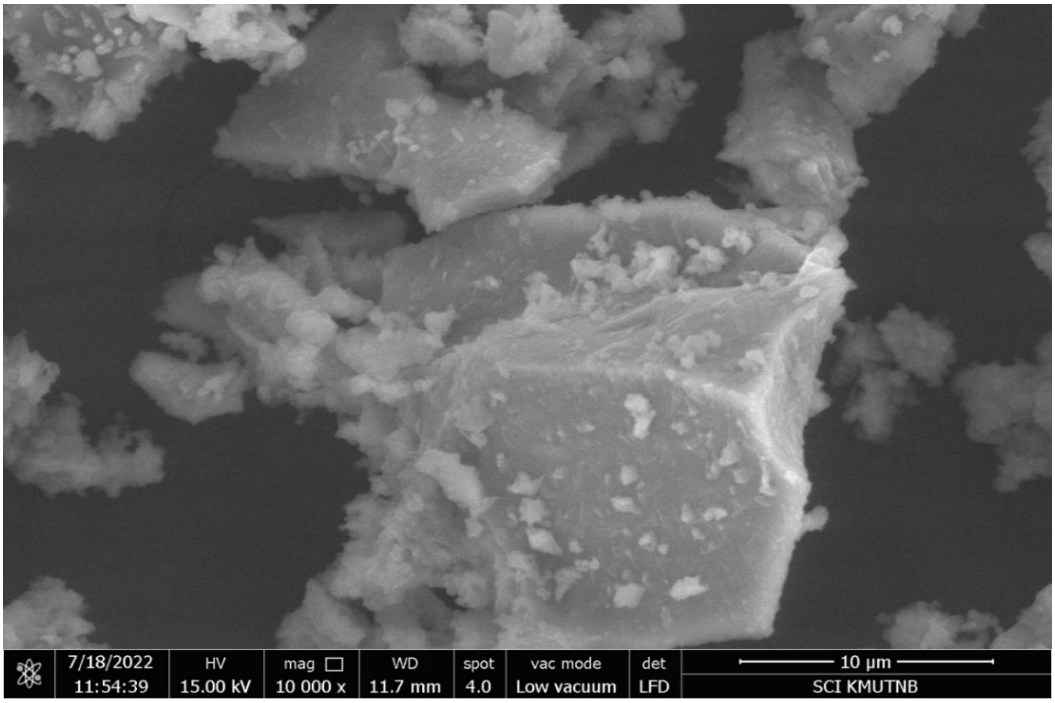


Figure 8-1 SEM image of OPC after Piriyakul et al. (2026).

Table 8-1 Chemical compositions of Bangkok clay and Ordinary Portland Cement (OPC).

Comp. (%)	Bangkok clay	Ordinary Portland Cement
CaO	1.07	65.41
SiO_2	62.50	20.90
Al_2O_3	18.40	4.76
Fe_2O_3	8.49	3.41
MgO	2.35	1.25
SO_3	1.86	2.71

Ordinary Portland Cement Type I (OPC) was employed as the primary cementing agent to enhance the unconfined compressive strength (UCS) of soft Bangkok clay. The OPC used in this study was obtained from CPAC, Bangkok, and exhibited a specific gravity of 3.14. In accordance with ASTM C150 (2007), it was classified as Type I Portland cement, appropriate for general construction applications. The chemical composition of OPC is summarized in Table 8-1, with calcium oxide (CaO) and silicon dioxide (SiO_2) representing the major constituents, accounting for 65.41% and 20.90%, respectively.

A Scanning Electron Microscope (SEM) analysis at a magnification of 10,000×, presented in Figure 8-1, illustrates the microstructural features of the OPC particles. Complementary Energy Dispersive X-ray (EDX) analysis, shown in Figure 8-2, confirms that calcium (Ca), oxygen (O), and silicon (Si) are the predominant elemental components of the cement. The engineering and physical properties of the Bangkok soft clay utilized in this research are provided in Table 8-2.

Table 8-2 Properties of Bangkok soft clay.

Parameters	Values
Liquid limit	82.4 %
Plastic limit	27.7 %
Undrained shear strength	15.5 kPa
Specific gravity	2.68
Natural water content	70.8 %
Total unit weight	1,650 kg/m^3

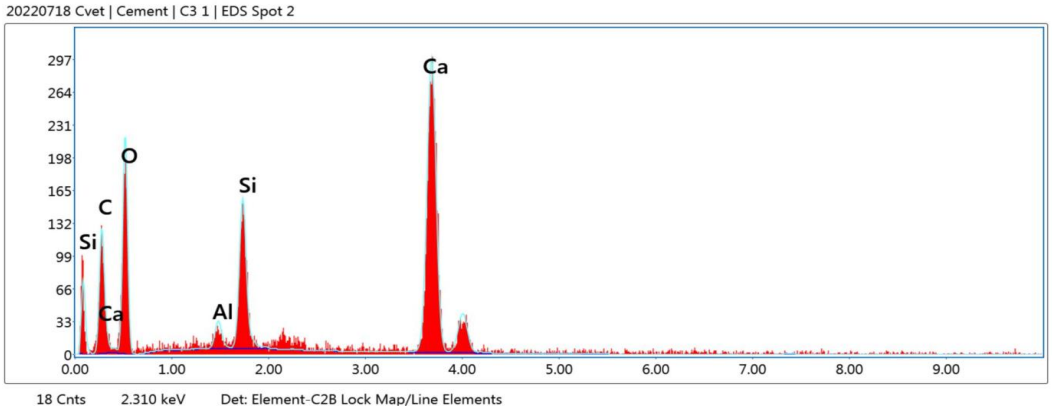


Figure 8-2 EDx result of OPC after Piriyakul et al. (2026).

Polyester fiber, often known as polyester, is a polymer created by combining alcohol and acidic aromatic compounds together. This polyester fiber was taken from the waste of textile industry and was used to strengthen the cemented soft Bangkok clay (see Figure 8-3). For the physical properties, its color is white and has medium strength. The ability to absorb moisture is quite low. This polyester fiber was cut to a length of 10 mm and a diameter of 0.035 mm. The specific gravity is 0.56 g/cm^3. This fiber's chemical characteristics include resistance to practically all acids and organic solutions.

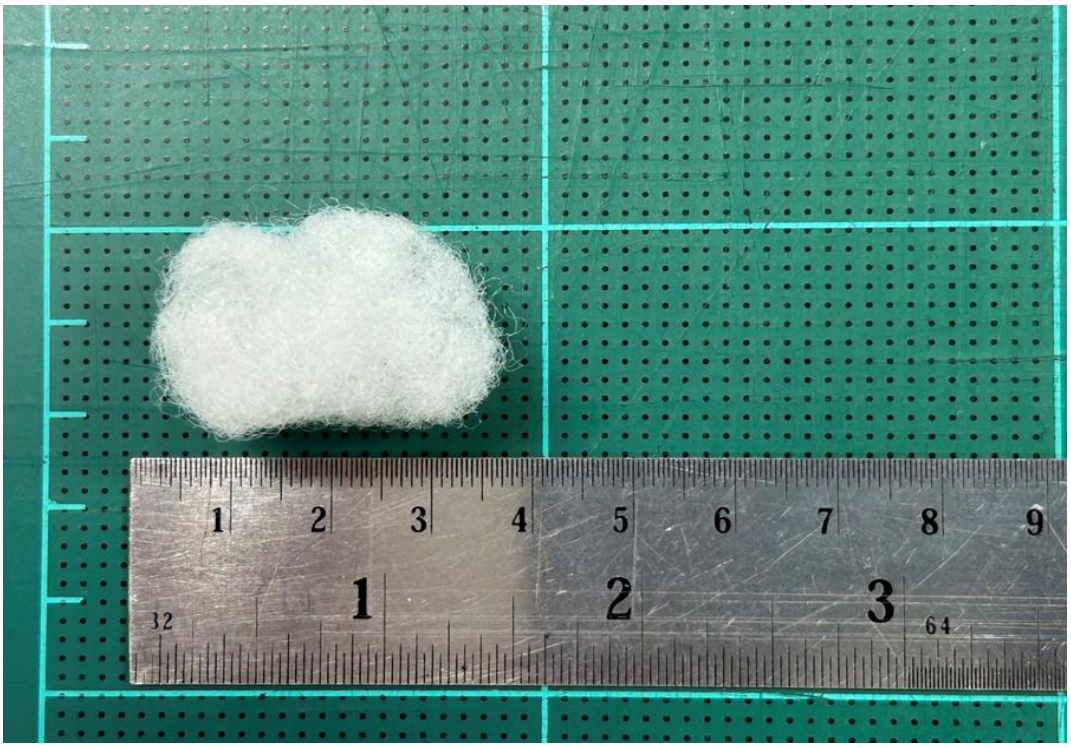


Figure 8-3 Polyester fiber after Piriyakul et al. (2026).

8.2.2 Sample preparation

The specimens were prepared by mixing soft Bangkok clay with Ordinary Portland Cement (OPC), polyester fibers, and distilled water, as detailed in Table 8-3. The natural water content of the clay was 70.8%, and additional distilled water was introduced to reach the liquid limit of 82.6%. Following preparation, the samples were sealed with plastic membranes to prevent moisture loss and subsequently cured for periods of 7, 14, and 28 days.

All mixtures of Bangkok clay with OPC and polyester fibers were molded into cylindrical specimens with dimensions of 38 mm in diameter and 76 mm in height. Mechanical testing included unconfined compressive strength (UCS) tests, conducted in accordance with ASTM D1633–17 (2017) and bender element tests (BET), carried out following ASTM D8295–19 (2019). A series of preliminary trials were performed to determine the most effective mixing ratios, thereby eliminating combinations that contributed minimally to strength improvement and reducing the number of unnecessary tests.

8.2.3 Methods

The unconfined compression strength (UCS) was selected as the main indicator in this study to examine how well cement and fibers stabilize soft Bangkok clay. Further research was done on the several variables that affected the enhanced soil's mechanical behavior. Bangkok clay samples for the experiment are cut into a cylindrical shape that measures 38 mm in diameter and 76 mm in height. After that, they are cured for 3, 7, 14, and 28 days while being covered with plastic barrier to stop moisture loss. The unconfined compressive strength of them is measured following each curing period. For the unconfined compression testing, an automatic strain-controlled unconfined compression apparatus with a maximum capacity of 50 kN was utilized, with an applied shearing rate of 2.0 mm/min. Following the curing period, loading was maintained until the strain reached 15% or the load values reached their maximum and then started to decline. Every test conducted during the loading process complied with ASTM D2166-06 (2006). The unconfined compression strength of the three specimens at the same ratio must not differ from the mean value by more than 15% in order to meet the acceptance criteria.

Table 8-3 Parameters of specimens with polyester fibers.

Serial number	Cement content	Fiber content	Curing time (days)
A	1	0, 1, 2, 5, 10, 20	3, 7, 14, 28
B	2	0, 1, 2, 5, 10, 20	3, 7, 14, 28
C	5	0, 1, 2, 5, 10, 20	3, 7, 14, 28
D	10	0, 1, 2, 5, 10, 20	3, 7, 14, 28
E	20	0, 1, 2, 5, 10, 20	3, 7, 14, 28

In soil mechanics, the Bender Element Test (BET) is a lab method used to measure soil sample shear wave velocity (V_s). This test is essential for determining the dynamic properties of soils, such as an initial shear modulus (G_0) and stiffness, which are essential for comprehending how soils react to dynamic stresses like traffic, industrial vibrations, and earthquakes. In this research, the BET test is used to monitor the shear development of the fiber-reinforced cement Bangkok clay. As per the ASTM D8295–19 (2019) standard test method, which measures the initial shear modulus and shear wave velocity in soil specimens using bender elements as described in Piriyakul (2010), the function generator produces a sinusoidal waveform with an amplitude of 10 $V_{p\text{-}p}$ and a frequency of 2–15 kHz, which is how the shear wave is generated in the current case. Following generation, the shear wave is transmitted to the bender element's transmitter along with a measurement of the sending shear wave via oscilloscope channel 1. The shear wave passes through the soil sample after exiting the sending transmitter and is picked up by channel 2 at the other end of the sample.

The shear modulus of fiber (G_f) is obtained by using the rule of mixtures theory in Equations 8.1 to 8.3.

$$\frac{1}{G_0} = \frac{V_f}{G_f} + \frac{(1+V_f)}{G_m} \tag{8.1}$$

where

G_f= Shear modulus of fiber
G_m = Shear modulus of matrix
V_f= Fiber volume fraction
V_m= Matrix volume fraction

$$G_0 = \frac{G_f \cdot G_m}{V_f \cdot G_m + V_m \cdot G_f} \tag{8.2}$$

$$G_f = \left(G_0 \cdot V_f\right) - \frac{(G_m \cdot V_f)}{(1-V_f)} \tag{8.3}$$

8.2.4 Michaelis & Menten Kinetics

Michaelis & Menten (1913) proposed the new saturation equation in biochemistry. This saturation equation can be used to predict the enzyme kinetics and the reaction rate. Based on the Michaelis – Menten kinetics equation, the UCS and the G_0 data are predicted as expressed in Equations 8.4 and 8.5. Figure 8-4a shows the UCS or G_0 curve versus the curing time (D). The $UCS_{(max)}$ or $G_{0\,(max)}$ data are saturated and constant with the curing time being. Then, the reaction rate at the half of the $UCS_{(max)}$ or $G_{0\,(max)}$ data can be found at the K_{m1} or K_{m2}. Figure 8-4b depicts the plot with the invert of the UCS or G_0 data (1/UCS or $1/G_0$) and the invert of the curing time ($1/D$). The slope of this plot will present the maximum UCS or G_0 values. The intersection of the x-axis will be the haft rate as K_{m1} or K_{m2}.

$$UCS = \frac{UCS_{(max)} \cdot D}{K_{m1}+D} \tag{8.4}$$

where

D = Curing time (day)
K_{m1} = Michaelis constant for UCS

$$G_0 = \frac{G_{0\,(max)} \cdot D}{K_{m2}+D} \tag{8.5}$$

where

K_{m2} = Michaelis constant for G_0

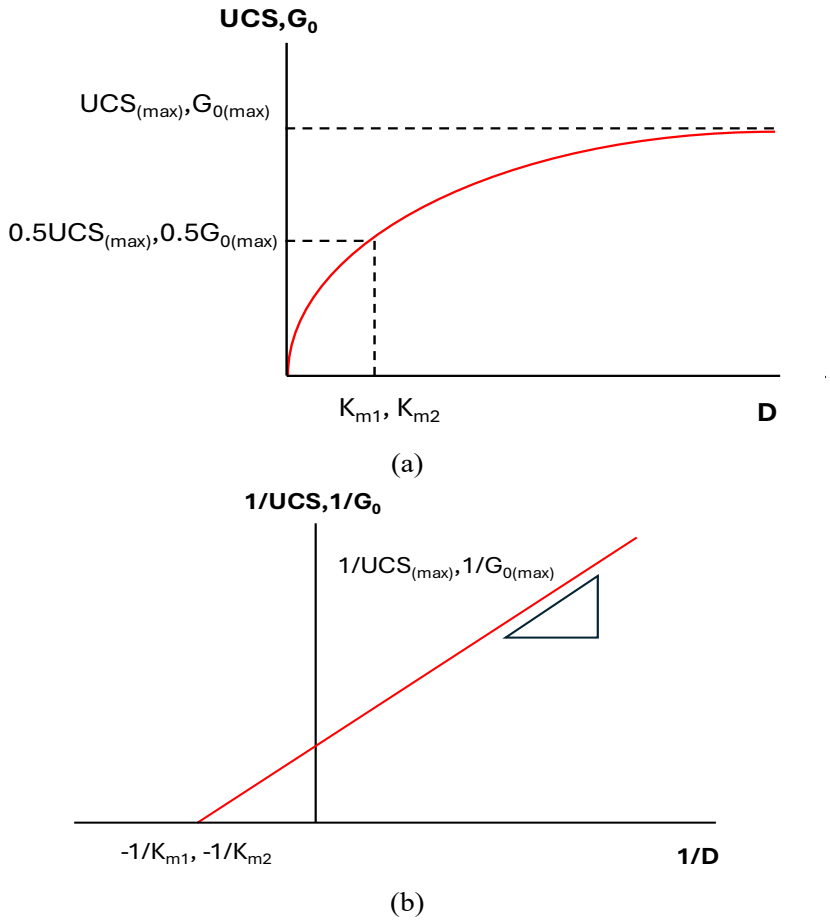
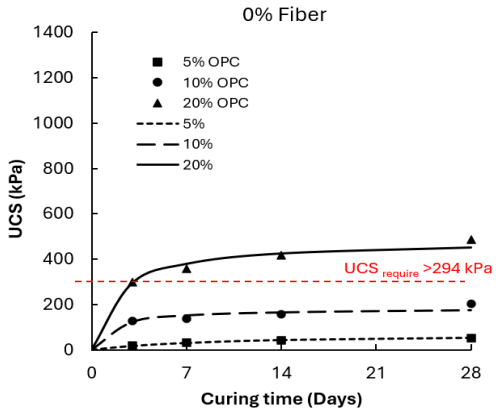


Figure 8-4 Michaelis-Menten Kinetics (a) curve (b) invert of curve after Piriyakul et al. (2026).

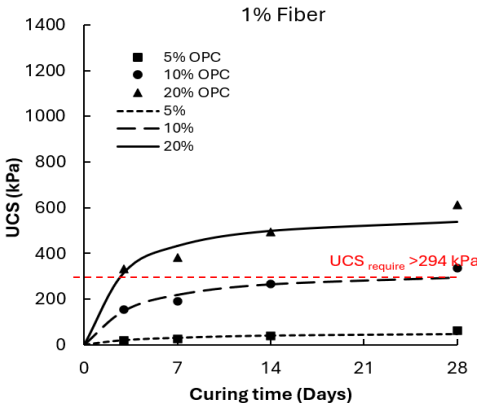
8.3 Results and Discussions

8.3.1 UCS test results

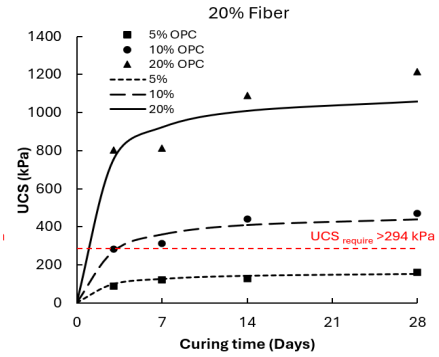
The UCS tested results versus the curing time are displayed in Figure 8-5, which also exhibits the effect of OPC cement on fiber-reinforced cement Bangkok clay, without the addition of polyester fibers as control samples (see Figure 8-5a). Bangkok soft clay was stabilized with OPC at different concentration from 1%, 2%, 5%, 10% and 20%. The UCS test could not be performed with adding of 1% and 2% OPC content to Bangkok soft clay. Thailand Department of Highways established the standard for highway construction (DH-S201/2532) (1989). Based on this standard, the requirement of UCS for the subgrade material is required at least 294 kPa. From the UCS test results, only 20% OPC content mixed into Bangkok soft clay was qualified at the beginning of 3 day curing time and the results were above the standard for all curing times. The UCS results for 1% polyester fiber are shown in Figure 8-5b. It was discovered that after 28 days, the 10% OPC UCS had surpassed the Thai highway standard. Similarly, the UCS test results of 20% polyester fiber were presented in Figure 8-5c. It was noted that after just 3 days, the UCS results of 10% OPC had surpassed the Thai highway standard.



(a)



(b)



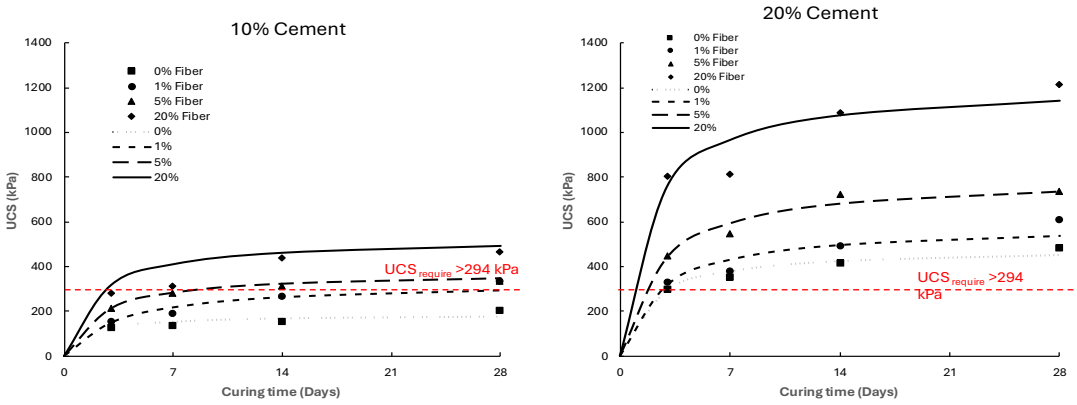
(c)

Figure 8-5 UCS *vs* Curing time (a) 0% polyester fiber (b) 1% polyester fiber and (c) 20% polyester fiber after Piriyakul et al. (2026).

The UCS results of Bangkok soft clay samples adding with 10% OPC content are depicted in Figure 8-6a. It was observed that all UCS tested results of Bangkok soft clay samples mixing with 1%–20% polyester fiber content had the results above the Thailand highway standard (> 294 kPa) at the curing time of 28 days. In the same way, Figure 8-6b illustrates the UCS data for samples with a 20% OPC content. The results revealed that samples with 1%–20% polyester fiber content had the largest UCS values, which were beyond the Thailand highway standard of 294 kPa from 3 days and were approximately 1000 kPa at 28 days. Therefore, it was recommended to add at least 1% of the polyester fiber content in the mixing. Figure 8-7 presents the correlation between the normalized UCS ($\frac{q_u}{q_{28}}$) with the curing time (D) by using Equation 8.6 as follows:

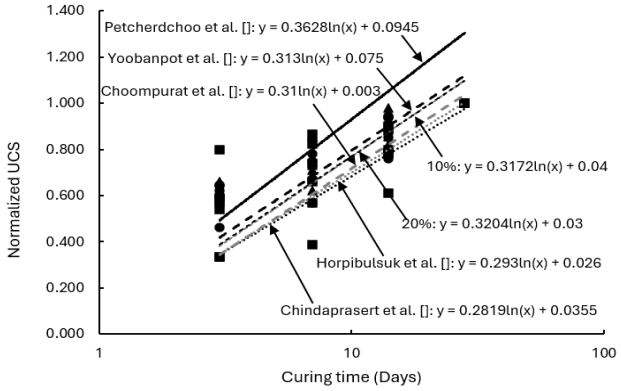
$$\frac{q_u}{q_{28}} = E \cdot \ln(D) + F \tag{8.6}$$

where the fitting parameters are E and F.

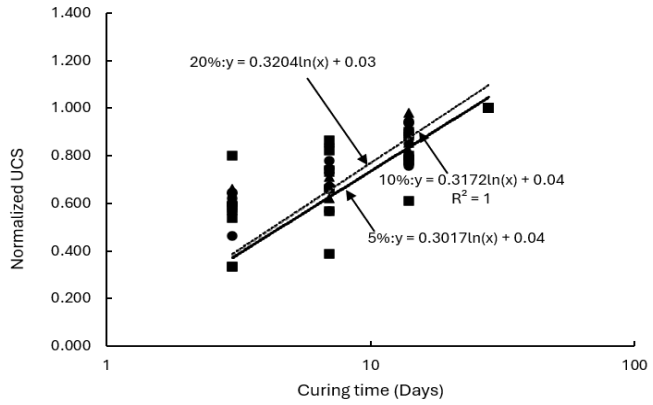


(a) (b)

Figure 8-6 UCS *vs* Curing time (a) 10% cement and (b) 20% cement after Piriyakul et al. (2026).



(a)



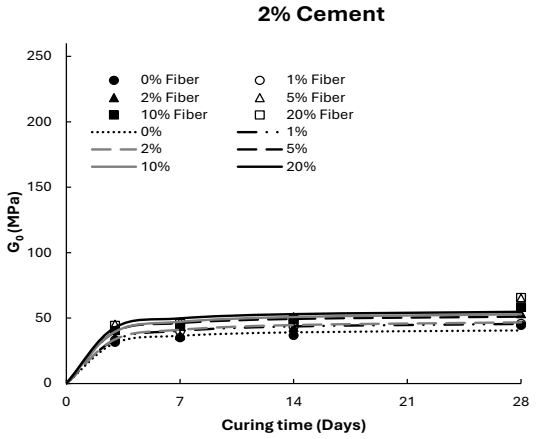
(b)

Figure 8-7 Normalized UCS *vs* Curing time (a) 10% cement and (b) 20% cement after Piriyakul et al. (2026).

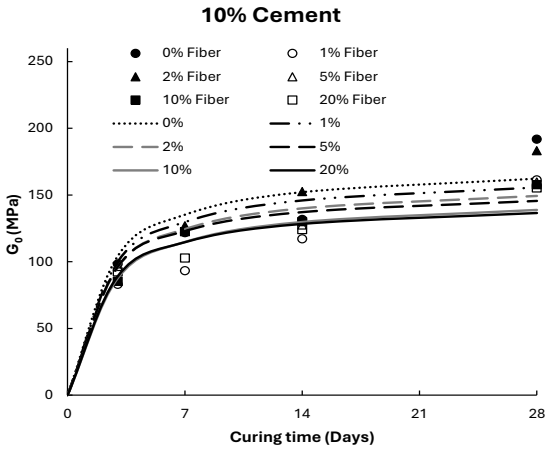
According to the results, the E and F parameters are 0.3017 and 0.04, respectively, at an OPC concentration of 5% (see Figure 8-7b). Similarly, for an OPC contents of 10% and 20%, the E parameters are 0.3172 and 0.3204and the F parameters are 0.04 and 0.03, respectively. The E parameters and the F parameters are in good agreement with the previous works which the values of E parameter are in between 0.28 and 0.36 and the values of F parameter are in between 0.02 and 0.09 as reported by Petcherdchoo et al. (2023), Horpibulsuk et al. (2011), Chompoorat et al. (2022), Chindaprasirt et al. (2021) and Yoobanpot et al. (2020a).

8.3.2 Bender element test results

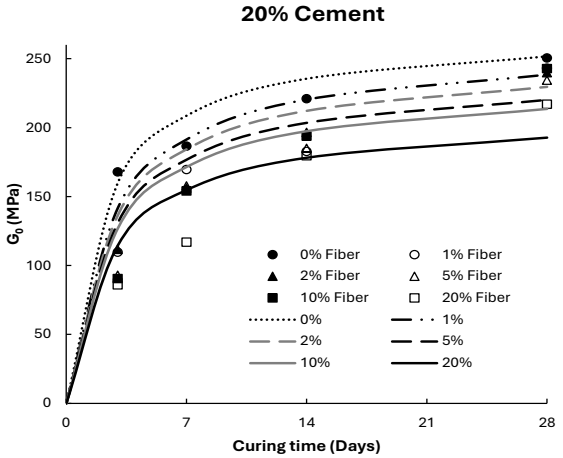
The relationship between G_0 and the curing time is shown in Figure 8-8. It was discovered that the G_0 normally rises as the OPC cement content does. 2% OPC data's G_0 results are displayed in Figure 8-9a. The lowest G_0 was found to be the 0% polyester fiber, while the highest G_0 was found to be the 20% polyester fiber. The propagation of the shear wave through the polyester fiber, which was stiffer than the soft Bangkok clay matrix at 2% OPC, could be the cause. However, as can be seen in Figures 8-9b and 8-9c, the G_0 findings were lowest at 20% polyester fiber and highest at 0% polyester fiber at 10% and 20% OPC contents, respectively.



(a)

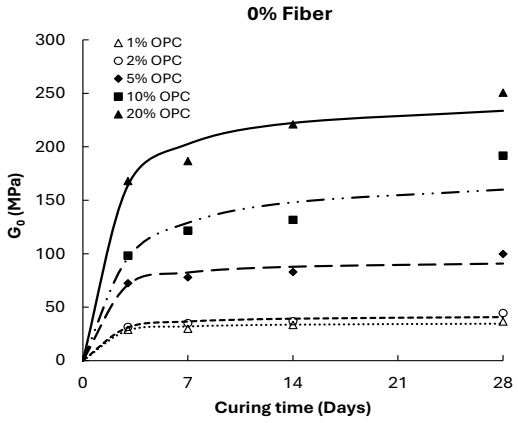


(b)

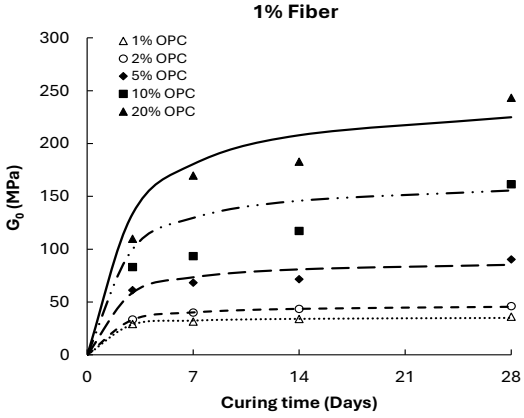


(c)

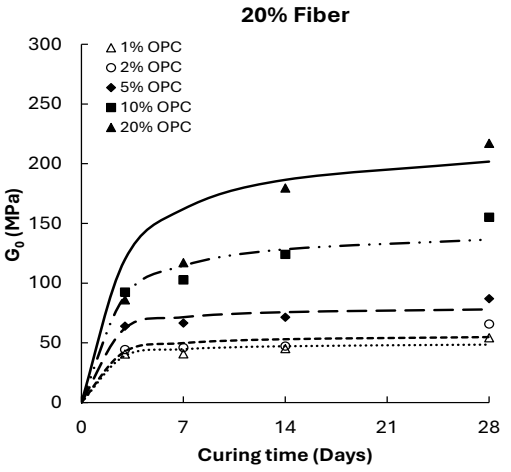
Figure 8-8 G_0 *vs* Curing time (a) 2% cement (b) 10% cement and (c) 20% cement after Piriyakul et al. (2026).



(a)



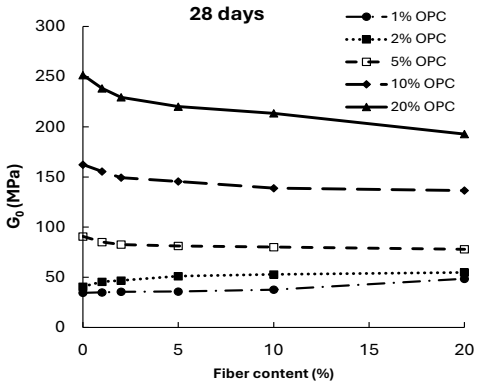
(b)



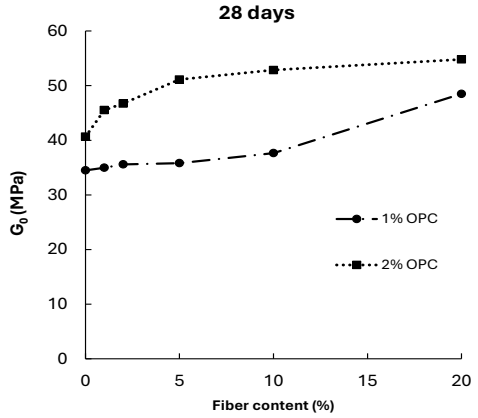
(c)

Figure 8-9 G_0 *vs* Curing time (a) 0% fiber (b) 1% fiber and (c) 20% fiber after Piriyakul et al. (2026).

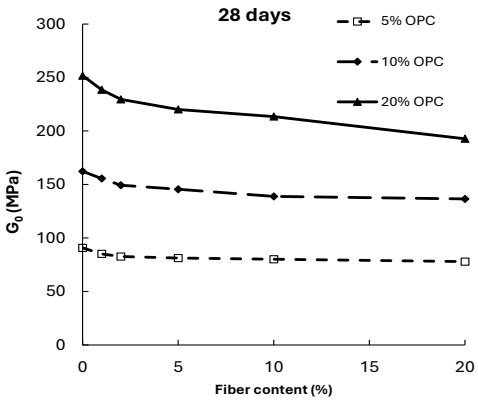
Similarly, the behaviour between G_0 and the curing time is presented in Figure 8-9. It was noted that the G_0 normally decreases with increasing the polyester fiber content. Figure 8-9a expresses the control sample with 0% polyester fiber content. The research found the directed relationship that the G_0 increases with increasing the OPC content. By adding 1% polyester content into the mixing, the G_0 values tend to decrease with increasing the OPC content as seen in Figure 8-9b. Figure 8-9c displays the G_0 data of 20 % polyester content in the mixing. The results showed that the G_0 values of 5-20% OPC content tend to again decrease in comparing with the controlled data. It is because the polyester fiber has less stiffness than the soil matrix. However, it confirmed the finding before that the G_0 results of 1-2% OPC contents were increased with increasing the polyester fiber content since the polyester fiber was stiffer than the soft Bangkok clay matrix.



(a)



(b)

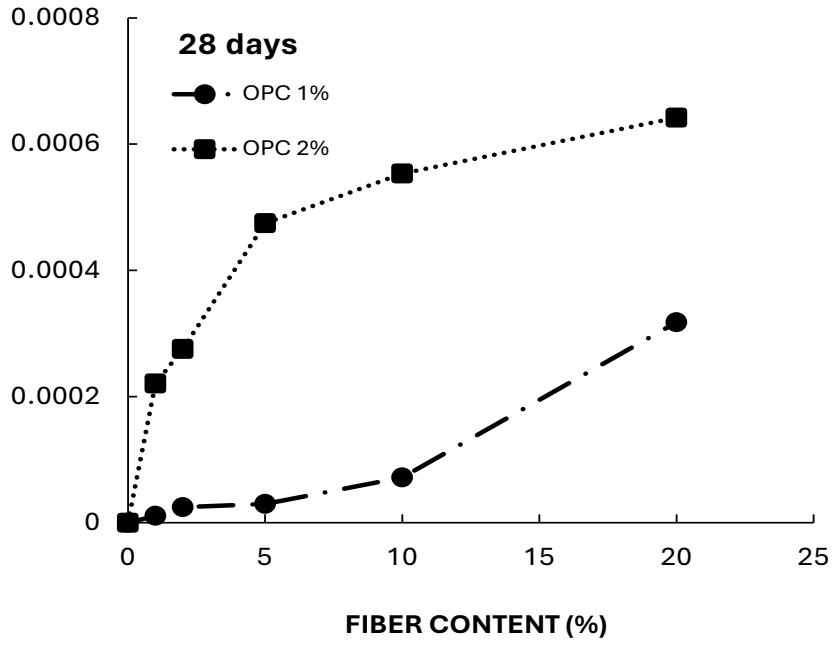


(c)

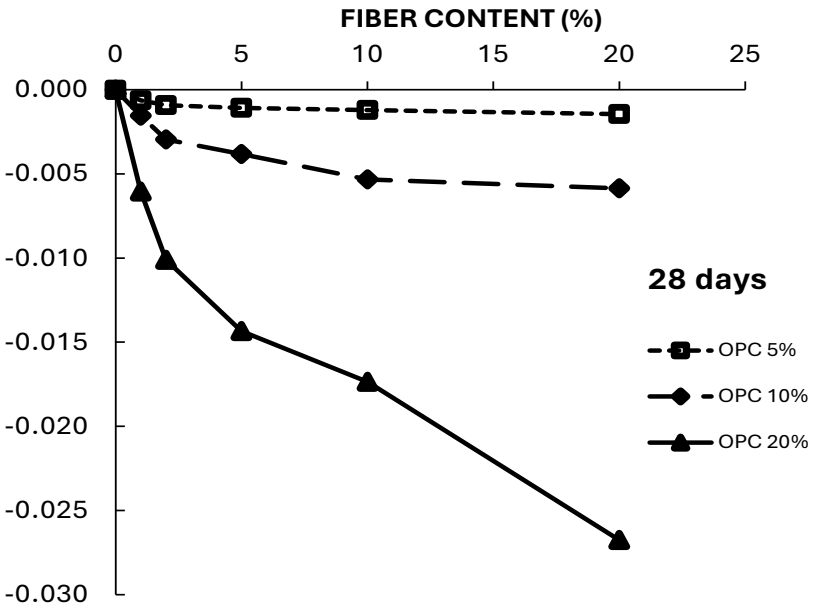
Figure 8-10 G_0 *vs* Fiber content (a) 1-20% cement (b) 1-2% cement and (c) 5-20% cement after Piriyakul et al. (2026).

Figure 8-10a depicts the relationship between the G_0 data and the polyester fiber content at 28 days. Again for 1-2% OPC contents, the G_0data were increased with increasing the polyester fiber content as seen in Figure 8-10b. Figure 8-10c displays the G_0 results of 5-20% OPC contents were decreased with increasing the polyester fiber content. It was noted that the bender element test can be used to investigate the effect of polyester fiber content even if there was very low OPC content as 1-2% in the soft Bangkok clay matrix. The relationship between the fiber content and polyester fiber's shear modulus is depicted in Figure 8-11. The G_f values of 1-2% polyester fiber, which were positive and increased with increasing fiber content, are expressed in Figure 8-11a. On the other hand, the G_f data for 5-20% polyester fiber content is shown in Figure 8-11b. As the fiber content increased, those unfavorable outcomes diminished. It was shown that increasing the G_f does not benefit from the addition of more polyester fiber.

Figure 8-12 displays the relationship between the G_f and the OPC content. It was observed that the optimum amount of OPC content should be around 3% which showed the G_f value around zero.



(a)



(b)

Figure 8-11 G_f *vs* Fiber content (a) 1-20% cement and (b) 5-20% cement after Piriyakul et al. (2026).

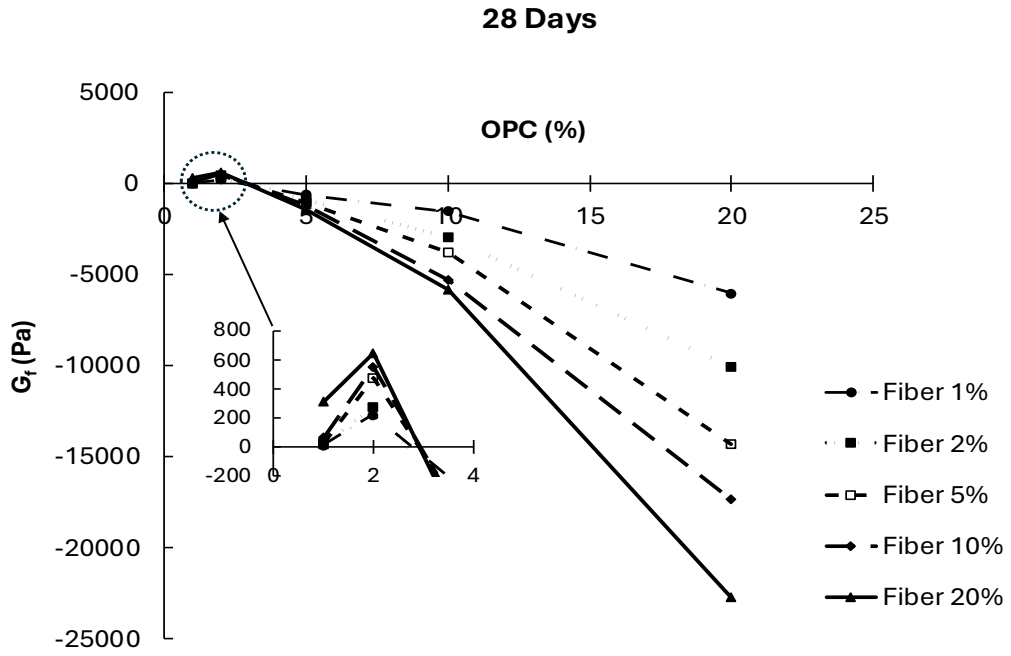


Figure 8-12 G_f *vs* OPC content after Piriyakul et al. (2026).

8.3.3 The effect of water to cement ratio (W/C)

In engineering practice, pre-mixed cement slurry is often added to the wet soil. The mass of water used to determine the mixing water content consists of both the mass of water in the wet soil and the mass of water in the cement slurry. Figure 8-13 depicts the relationship between the G_0 and W/C based on Abram's Law as expressed in Equation 8.7. It was noted that the use of bender element test is able to determine the relationship between G_0 and W/C. Table 4 summarizes the fitting equations, A, B and R^2 values. A is observed to rise with curing time, while B exhibits a minor variation between 0.616 and 0.701.

$$G_0 = A \cdot (\frac{W}{C})^{-B} \tag{8.7}$$

where the fitting parameters are A and B.

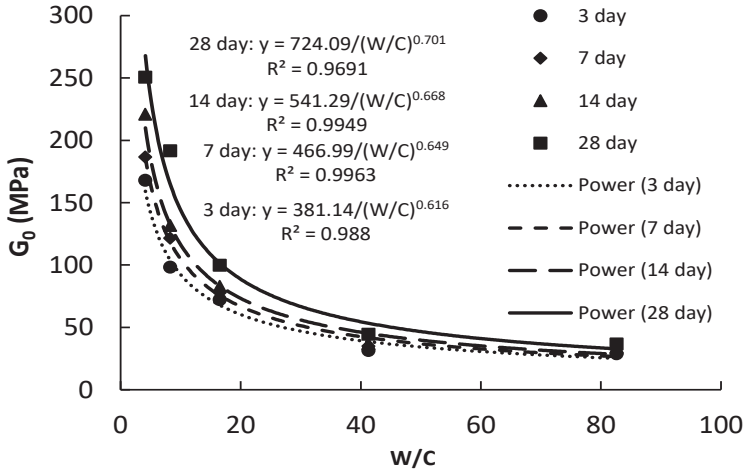


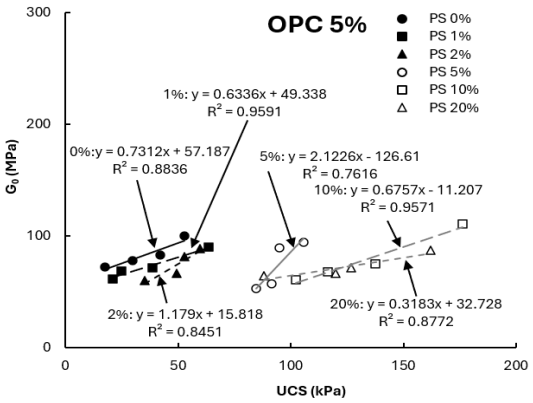
Figure 8-13 G_0 *vs* W/C after Piriyakul et al. (2026).

Table 8-4 Calibrated fitting functions of G_0-W/C relationships of cemented Bangkok clay.

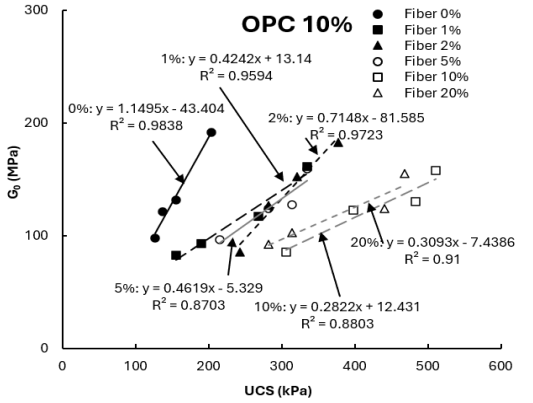
Curing Time (Day)	Fitting Equation	A	B	R^2
3	$G_0=381.14/(W/C)^{0.616}$	381.14	0.616	0.9569
7	$G_0=466.99/(W/C)^{0.649}$	466.99	0.649	0.9872
14	$G_0=541.29/(W/C)^{0.668}$	541.29	0.668	0.9958
28	$G_0=724.09/(W/C)^{0.701}$	724.09	0.701	0.9877

8.3.4 Relationship between G_0 and UCS

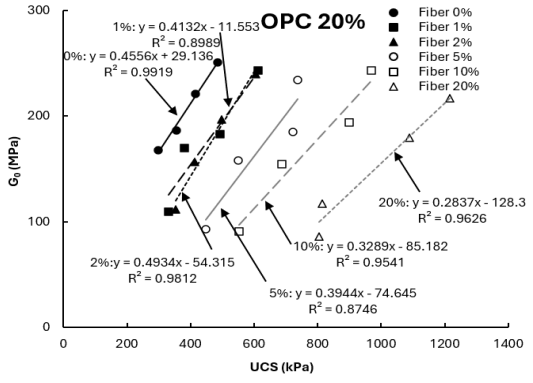
The relationship between G_0 and UCS for Bangkok soft clay stabilized with polyester fiber and OPC is depicted in Figure 8-14. The data for Bangkok soft clay admixed with 5% OPC is shown in Figure 8-14a. There are two sets of results: the first set includes polyester fiber in concentrations of 0%, 1%, and 2%. The second set consists of 5%, 10%, and 20% polyester fiber. Adding 10% OPC into Bangkok soft clay as seen in Figure 8-14b, the results showed that the G_0 and UCS were increased and clearer. Figure 8-14c expresses the tested data of 20% OPC mixed into the Bangkok soft clay. The controlled data at 0% Fiber showed the tendency of G_0 is increased with increasing the UCS. The slope is 0.4556 with R^2 of 0.9919. The relationship of all the data shifts to the right as the polyester fiber content is increased, indicating that an increase in polyester fiber content tends to improve G_0 at the same G_0. While the polyester fiber content increases, the G_0 tends to drop at the same UCS.



(a)



(b)



(c)

Figure 8-14 G_0 *vs* UCS (a) 5% cement (b) 10% cement and (c) 20% cement after Piriyakul et al. (2026).

Summary

This research aims at investigation of the optimum ratio of polyester fiber to Bangkok soft clay admixed with cement by examining the impacts of polyester fiber on this soil-cement. The bender element test and the unconfined compression test were used in this study to verify the polyester fiber content of 0, 1, 2, 5, 10, and 20% by volume and the cement content of 1, 2, 5, 10, and 20% by weight in soil-cement samples combined at the liquid limit. The samples were then studied for 3, 7, 14, and 28 days. This chapter sheds light on the following:

1. The use of polyester fiber for stabilizing Bangkok soft clay-cement mixtures appears promising. According to the Thailand highway standard (UCS > 294 kPa), the Bangkok soft clay admixed with OPC of 10% and at least 1% of the polyester fiber content in the mixing. This mixture meets the Thailand Highway Standard, which requires a curing time of 28 days and a UCS of greater than 294 kPa. For the Bangkok soft clay mixed with 20% OPC and 1%–20% polyester fiber content, all UCS test data were larger than the Thailand highway standard of 294 kPa from 3 days and were approximately 1000 kPa at 28 days.

2. The research found the relationship between the normalized UCS and the curing time. With the variation of OPC between 5%, 10% and 20%, the E and F parameters are 0.3017 and 0.04, respectively, at an OPC concentration of 5%. Similarly, for an OPC contents of 10% and 20%, the E parameters are 0.3172 and 0.3204 and the F parameters are 0.04 and 0.03, respectively. The E parameters and the F parameters are in good agreement with the previous works which the values of E parameter are in between 0.28 and 0.36 and the values of F parameter are in between 0.02 and 0.09.

3. The bender element monitoring system is capable to measure the shear wave velocity and the initial shear modulus during the hydration process. In general, as the curing period and OPC concentration grow, so does the initial shear modulus (G_0). It was found that the mixture of 20% OPC cement and Bangkok soft clay had the greatest G_0 value. It was discovered that the G_0 normally decreases with increasing the polyester fiber content. Also, the bender element has an advantage to measure the strength development of the low OPC contents at 1% and 2%, while the UCS test could not be performed. The propagation of the shear wave through the polyester fiber, which was stiffer than the soft Bangkok clay matrix at 2% OPC, could be the cause.

4. It was observed that the optimum amount of OPC content should be around 3% which showed the G_f value around zero. It was shown that increasing the G_0 does not benefit from the addition of more polyester fiber.

5. Based on Abram's Law, the research proposed the relationship between G_0 and W/C for soft Bangkok clay admixed with OPC at 28 days as G_0=724.09/(W/C)$^{0.701}$.

6. The unconfined compressive strength (UCS) and the initial shear modulus (G_0) are shown to be related, and the results indicate that G_0 tends to rise as UCS increases. As the polyester fiber content is raised, it was observed that the relationship between all the data shifts to the right, suggesting that an increase in polyester fiber content tends to improve G_0 at the same G_0. The G_0 tends to decrease at the same UCS as the polyester fiber content rises.

Questions and Problems

1. Discuss the effect of fiber in the soi-cement strength.
2. What is the advantage of applying the Michaelis-Menten kinetics method?
3. How do you investigate the shear modulus of fiber in soil-cement?
4. From Abram's Law, explain the effect of water to cement ratio (W/C) in soil-cement.
5. Discuss the optimum amount of OPC content in soil-cement by bender element testing.
6. Explain the normalized UCS ($\frac{q_u}{q_{28}}$) with the curing time (D).
7. Discuss the E and F parameters of our research in comparing with other previous works?
8. According to the Thailand highway standard (UCS > 294 kPa), what is the amount of the OPC and fiber the be used in soil-cement?
9. What are the UCS_{max} and $G_{0\ (max)}$ data by using Michaelis-Menten kinetics method?
10. What is the effect of curing time in soil-cement?

References

Abadel, A. A., Albidah, A. S., Altheeb, A. H., Alrshoudi, F. A., Abbas, H., & Al-Salloum, Y. A. (2021). Effect of molar ratios on strength, microstructure & embodied energy of metakaolin geopolymer. Adv. Concr. Constr, 11(2), 127-140.

Abbas, A., & Shafiee, A. (2014). Shear wave velocity of clayey soils: A review. International Journal of Civil Engineering, 12(3), 234–245.

Achenbach, J. (2012). Wave propagation in elastic solids. Elsevier.

AGAIBY, S. S., & Mayne, P. W. (2015, December). Shear Wave Velocity for Clays. In Deformation Characteristics of Geomaterials: Proceedings of the 6th International Symposium on Deformation Characteristics of Geomaterials, IS-Buenos Aires 2015, 15-18 November 2015, Buenos Aires, Argentina (Vol. 6, p. 358). IOS Press.

Ahn C-H, Kim D-J, Byun Y-H. (2020). Expansion-Induced Crack Propagation in Rocks Monitored by Using Piezoelectric Transducers. Sensors, 20(21):6054. https://doi.org/10.3390/s20216054

Airey, D. W., & Wood, D. M. (1987). An evaluation of direct simple shear tests on clay. Géotechnique, 37(1), 25–35. https://doi.org/10.1680/geot.1987.37.1.25

Alaskar, A., Shah, S. N. R., Keerio, M. A., Phulpoto, J. A., Baharom, S., Assilzadeh, H., & Mohamed, A. M. (2020). Development of Pozzolanic material from clay. Advances in concrete construction, 10(4), 301-310.

Ali, A., Mir, B. A., Gul, N., & Malik, F. Z. (2023). Strength and microstructural behavior of soft soil treated with zeolite nanoparticles. Transportation Infrastructure Geotechnology, 10(6), 1239–1254.

Amaral, M. F., Viana da Fonseca, A., & Rios, S. (2013). Numerical methodology to minimize resolution and sensitivity effects in P-wave measurements. Geotechnical Testing Journal, 36(2), 178–186.

Arabani, M., & Haghsheno, H. (2020). The effect of water content on shear and compressive behavior of polymeric fiber-reinforced clay. SN Applied Sciences, 2(11), 1759.

Arasan, S., Işik, F., Akbulut, R. K., Zaimoğlu, A. S., & Nasirpur, O. (2015). Rapid stabilization of sands with deep mixing method using polyester. Periodica Polytechnica Civil Engineering, 59(3), 405–411.

ASTM International C618. (2019). Standard specification for coal fly ash and raw or calcined natural pozzolan for use in concrete.

ASTM International D1633-17. (2017). Standard test methods for compressive strength of molded soil-cement cylinders.

ASTM International D2166-06. (2006). Standard test method for unconfined compressive strength of cohesive soil.

ASTM International D8295-19. (2019). Standard test method for determination of shear wave velocity and initial shear modulus in soils specimen using bender elements.

Attanasio, A., Pascali, L., Tarantino, V., Arena, W., & Largo, A. (2018). Alkali-activated mortars for sustainable building solutions: Effect of binder composition on technical performance. Environments, 5(3), 35.

Ayeldeen, M., & Kitazume, M. (2017). Using fiber and liquid polymer to improve the behaviour of cement-stabilized soft clay. Geotextiles and Geomembranes, 45(6), 592-602.

Bawadi, N. F., AlHamidi, M. A. A., Mansor, A. F., & Anuar, S. A. (2020, May). Influence of banana fiber on shear strength of clay soil. In IOP Conference Series: Materials Science and Engineering (Vol. 864, No. 1, p. 012099). IOP Publishing.

Biel, O., Rożek, P., Florek, P., Mozgawa, W., & Król, M. (2020). Alkaline activation of kaolin group minerals. Crystals, 10(4), 268.

Bishop, A. W., & Wesley, L. D. (1975). A hydraulic triaxial apparatus for controlled stress path testing. Géotechnique, 25(4), 657–670.

Blake, R. E. (1961). Basic vibration theory. In Shock and vibration handbook (Vol. 1, pp. 2–8).

Blewett, J., Blewett, I., & Woodward, P. (1999). Measurement of shear wave velocity using phase-sensitive detection techniques. Canadian Geotechnical Journal, 36(5), 934–939.

Boonyatee, T. (2009). Determination of shear wave velocity by bender elements using variable path length method. Soils and Foundations, 49(3), 489–494.

Botero, E., Ossa, A., Sherwell, G., & Ovando-Shelley, E. (2015). Stress–strain behavior of a silty soil reinforced with polyethylene terephthalate (PET). Geotextiles and Geomembranes, 43(4), 363-369.

Brignoli, E. G. M., Gotti, M., & Stokoe, K. H. (1996). Measurement of shear waves in laboratory specimens by means of piezoelectric transducers. Geotechnical Testing Journal, 19, 384–397.

Carmona, J. P., Oliveira, P. J. V., & Lemos, L. J. (2016). Biostabilization of a sandy soil using enzymatic calcium carbonate precipitation. Procedia engineering, 143, 1301-1308.

Cascante, G., & Santamarina, C. (1997). Low strain measurements using random noise excitation. Geotechnical Testing Journal, 20(1), 29–39. https://doi.org/10.1520/GTJ11418J

Cascante, G., & Santamarina, J. C. (1996). Interparticle contact and wave propagation. Journal of Geotechnical Engineering, 122(10), 831–839.

Chan, C. M. (2012). Variations of shear wave arrival time in unconfined soil specimens measured with bender elements. Geotechnical and Geological Engineering, 30(2), 461–468.

Chen, C. K., Li, G., Liu, J., Xi, Y., & Nan, J. J. (2023). Shear strength characteristics of basalt fiber-reinforced loess. Scientific Reports, 13(1), 15923.

Chen, M., Shen, S. L., Arulrajah, A., Wu, H. N., Hou, D. W., & Xu, Y. S. (2015). Laboratory evaluation on the effectiveness of polypropylene fibers on the strength of fiber-reinforced and cement-stabilized Shanghai soft clay. Geotextiles and Geomembranes, 43(6), 515-523.

Cheng, L., & Cord-Ruwisch, R. (2014). Upscaling effects of soil improvement by microbially induced calcite precipitation by surface percolation. Geomicrobiology Journal, 31(5), 396-406.

Cheng, L., Cord-Ruwisch, R., & Shahin, M. A. (2013). Optimization of in situ ethereous microbial-induced $CaCO_3$ precipitation (MICP) for ground improvement. Journal of Geotechnical and Geoenvironmental Engineering, 139(1), 1–13.

Cheng, L., Shahin, M. A., & Chu, J. (2019b). Soil bio-cementation using a new one-phase low-pH injection method. Acta Geotechnica, 14(3), 615-626.

Cheng, L., Shahin, M. A., & Cord-Ruwisch, R. (2014). Bio-cementation of sandy soil using microbially induced carbonate precipitation for marine environments. Géotechnique, 64(12), 1010-1013.

Cheng, L., Yang, Y., & Chu, J. (2019a). In-situ microbially induced Ca^{2+}-alginate polymeric sealant for seepage control in porous materials. Microbial Biotechnology, 12(2), 324-333.

Chindaprasirt, P., Daprom, P., Jitsangiam, P., & Horpibulsuk, S. (2021). Role of fly ash on strength properties of rejuvenated soil cement for pavement materials. Civil and Environmental Engineering, 17(2), 583–596.

Choi, S. G., Park, S. S., Wu, S., & Chu, J. (2017). Methods for calcium carbonate content measurement of biocemented soils. Journal of materials in civil engineering, 29(11), 06017015.

Choi, S. G., Wang, K., & Chu, J. (2016). Properties of biocemented, continuously graded sand forming from enzyme-induced carbonate precipitation. Construction and Building Materials, 121, 1–9.

Choi, S., & Lee, K. M. (2019). Influence of Na2O content and Ms (SiO2/Na2O) of alkaline activator on workability and setting of alkali-activated slag paste. Materials, 12(13), 2072.

Chompoorat, T., Likitlersuang, S., Sitthiawiruth, S., Komolvilas, V., Jamsawang, P., & Jongpradist, P. (2021a). Mechanical properties and microstructures of stabilised dredged expansive soil from coal mine. Geomechanics & engineering, 25(2), 143-157.

Chompoorat, T., Likitlersuang, S., Thepumong, T., Tanapalungkorn, W., Jamsawang, P., & Jongpradist, P. (2021b). Solidification of sediments deposited in reservoirs with cement and fly ash for road construction. International Journal of Geosynthetics and Ground Engineering, 7(4), 85.

Chompoorat, T., Maikhun, T., & Likitlersuang, S. (2019). Cement-improved lake bed sedimentary soil for road construction. Proceedings of the Institution of Civil Engineers-Ground Improvement, 172(3), 192-201.

Chompoorat, T., Thanawong, K., & Likitlersuang, S. (2021c). Swell-shrink behaviour of cement with fly ash-stabilised lakebed sediment. Bulletin of Engineering Geology and the Environment, 80(3), 2617-2628.

Chompoorat, T., Thepumong, T., Khamplod, A., & Likitlersuang, S. (2022). Improving mechanical properties and shrinkage cracking characteristics of soft clay in deep soil mixing. Construction and Building Materials, 316, 125858.

Chompoorat, T., Thepumong, T., Taesinlapachai, S., & Likitlersuang, S. (2021d). Repurposing of stabilised dredged lakebed sediment in road base construction. Journal of Soils and Sediments, 21(7), 2719-2730.

ConeTec. (n.d.). Cone penetration testing (SCPTu). Retrieved October 2, 2025, from https://www.conetec.com/services/cone-penetration-testing/scptu

Cong, M., Longzhu, C., & Bing, C. (2014). Analysis of strength development in soft clay stabilized with cement-based stabilizer. Construction and Building Materials, 71, 354-362.

Controls Group. (n.d.). Dynamic triaxial system - DynaTriax EMS. Retrieved October 2, 2025, from https://controls-group.com/product/dynamic-triaxial-system-dynatriax-ems-controls/

Correia, A. A. S., Venda Oliveira, P. J., & Lemos, L. J. L. (2013, September). Prediction of the unconfined compressive strength in soft soil chemically stabilized. In Proc., 18th Int. Conf. on Soil Mechanics and Geotechnical Engineering (pp. 2457-2460). Paris: Presses des Ponts.

Cruz, L., Todorovska, M. I., Chen, M., Trifunac, M. D., Aihemaiti, A., Lin, G., & Cui, J. (2024). For how large soil shear wave velocity the soil-structure interaction effects on a tall building can be neglected?–A case study. Soil Dynamics and Earthquake Engineering, 184, 108845.

Cui, M. J., Lai, H. J., Hoang, T., & Chu, J. (2021). One-phase-low-pH enzyme induced carbonate precipitation (EICP) method for soil improvement. Acta Geotechnica, 16(2), 481-489.

Cui, M. J., Zheng, J. J., Zhang, R. J., Han, J., & Seng, L. Y. (2017). Influence of different soil types on the effect of MICP-treated sand. Geomechanics and Engineering, 12(4), 1–15.

De Muynck, W., De Belie, N., & Verstraete, W. (2010). Microbial carbonate precipitation in construction materials: a review. Ecological engineering, 36(2), 118-136.

DeJong, J. T., Fritzges, M. B., & Nüsslein, K. (2006). Microbially induced cementation to control sand response to undrained shear. Journal of Geotechnical and Geoenvironmental Engineering, 132(11), 1381–1392.

DeJong, J. T., Mortensen, B. M., Martinez, B. C., & Nelson, D. C. (2010). Bio-mediated soil improvement. Ecological engineering, 36(2), 197-210.

Department of Highways of Thailand (DOH), & Japan International Cooperation Agency (JICA). (1998). Manual for design and construction of cement column method (p.75). DOH.

Department of Highways. (1989). Standard for soil cement for highway construction (Subgrade) (DH-S201/2532). Bangkok, Thailand.

Dontriros, S., Likitlersuang, S., & Janjaroen, D. (2020). Mechanisms of chloride and sulfate removal from municipal-solid-waste-incineration fly ash (MSWI FA): Effect of acid-base solutions. Waste Management, 101, 44-53.

Drnevich, V. (1978). Resonant column testing problems and solutions. Dynamic Geotechnical Testing, 654, 384–398. ASTM.

Duraisamy, Y., & Airey, D. (2019). Geomechanical behavior of Bio-cemented sand for foundation works. Sandy materials in civil engineering-usage and management.

Duraisamy, Y., & Airey, D. W. (2015). Shear wave velocity and stiffness of bio-cemented sand. Geotechnical Testing Journal, 38(5), 1–12.

Dyvik, R., & Madshus, C. (1985). Lab measurement of G_{max} using bender elements. In Advances in the art of testing soils under cyclic conditions (pp. 186-196). ASCE.

Ekinci, A., Abki, A., & Mirzababaei, M. (2022). Parameters controlling strength, stiffness and durability of a fibre-reinforced clay. International Journal of Geosynthetics and Ground Engineering, 8(1), 6.

Elimbi, A., Tchakoute, H. K., & Njopwouo, D. (2011). Effects of calcination temperature of kaolinite clays on the properties of geopolymer cements. Construction and Building Materials, 25(6), 2805-2812.

Ezzat, S. M. (2023). A critical review of microbially induced carbonate precipitation for soil stabilization: The global experiences and future prospective. Pedosphere, 33(5), 717-730.

Fang, C., & Achal, V. (2019a). Biostimulation of calcite precipitation process by bacterial community in improving cement stabilized rammed earth as sustainable material. Applied microbiology and biotechnology, 103(18), 7719-7727.

Fang, C., & Achal, V. (2019b). Biostimulation of native ureolytic bacteria for the development of cement-stabilized rammed earth. Construction and Building Materials, 223, 1–10.

Firoozi, A. A., Guney Olgun, C., Firoozi, A. A., & Baghini, M. S. (2017). Fundamentals of soil stabilization. International Journal of Geo-Engineering, 8(1), 26.

Foti, S. (2000). Multistation methods for geotechnical characterization using surface waves \[Doctoral dissertation, Università degli Studi di Genova\].

Gabryś, K., Sas, W., Soból, E., & Głuchowski, A. (2017). Application of bender elements technique in testing of anthropogenic soil–-recycled concrete aggregate and its mixture with rubber chips. Applied Sciences, 7(7), 741.

Ganji, V., Gucunski, N., & Nazarian, S. (1998). Automated inversion procedure for spectral analysis of surface waves. Journal of Geotechnical and Geoenvironmental Engineering, ASCE, 124(8), 757–770.

Ghanei, A., Jafari, F., Mehrinejad Khotbehsara, M., Mohseni, E., Tang, W., & Cui, H. (2017). Effect of nano-CuO on engineering and microstructure properties of fibre-reinforced mortars incorporating metakaolin: Experimental and numerical studies. Materials, 10(10), 1215.

Gomez, M. G., Anderson, C. M., DeJong, J. T., Nelson, S. S., & Lau, X. H. (2017a). Geotechnical and geochemical responses to stimulating native ureolytic microbes for chemical stabilization of a gravelly sand. Water Resources Research, 53(10), 1–18.

Gomez, M. G., Anderson, C. M., Graddy, C. M., DeJong, J. T., Nelson, D. C., & Ginn, T. R. (2017b). Large-scale comparison of bioaugmentation and biostimulation approaches for biocementation of sands. Journal of geotechnical and geoenvironmental engineering, 143(5), 04016124.

Gucunski, N., & Woods, R. D. (1992). Numerical simulation of SASW test. Soil Dynamics and Earthquake Engineering, 11, 213–227.

Guzmán-Aponte, L. A., Mejía de Gutiérrez, R., & Maury-Ramírez, A. (2017). Metakaolin-based geopolymer with added TiO2 particles: physicomechanical characteristics. Coatings, 7(12), 233.

Hamid, H., Chorzepa, M. G., Sullivan, M., Durham, S., & Kim, S. S. (2018). Novelties in material development for massive concrete structures: Reduction in heat of hydration observed in ternary replacement mixtures. Infrastructures, 3(2), 8.

Hardin, B. O., & Black, W. L. (1968). Vibration modulus of normally consolidated clay. Journal of the Soil Mechanics and Foundations Division, ASCE, 94(2), 353–369.

Hardin, B. O., & Drnevich, V. P. (1972). Shear modulus and damping in soils: Measurement and parameter effects. Journal of the Soil Mechanics and Foundations Division, ASCE, 98(6), 603–624.

Hardin, B. O., & Richart, F. E. (1963). Elastic wave velocities in granular soils. Journal of the Soil Mechanics and Foundations Division, ASCE, 89(1), 33–65.

Heisey, J. S., Stokoe, K. H. II, Hudson, W. R., & Meyer, A. H. (1982). Determination of in situ shear wave velocities from spectral analysis of surface waves (Research Report No. 256-2). Center for Transportation Research, The University of Texas at Austin.

Horpibulsuk, S. (2012). Strength and microstructure of cement stabilized clay. Scanning electron microscopy, 439-460.

Horpibulsuk, S., Rachan, R., & Raksachon, Y. (2009). Role of fly ash on strength and microstructure development in blended cement stabilized silty clay. Soils and Foundations, 49(1), 85-98.

Horpibulsuk, S., Rachan, R., Chinkulkijniwat, A., Raksachon, Y., & Suddeepong, A. (2010). Analysis of strength development in cement-stabilized silty clay from microstructural considerations. Construction and building materials, 24(10), 2011-2021.

Horpibulsuk, S., Rachan, R., Suddeepong, A., & Chinkulkijniwat, A. (2011). Strength development in cement admixed Bangkok clay: Laboratory and field investigations. Soils and Foundations, 51(2), 239–251.

Horpibulsuk, S., Shibuya, S., Fuenkajorn, K., & Katkan, W. (2007). Assessment of engineering properties of Bangkok clay. Canadian Geotechnical Journal, 44(2), 173-187.

Iamchaturapatr, J., & Piriyakul, K. (2014). Effect of urease dosages in biocementation process for improving strength of sandy soil. Advanced Materials Research, 931, 698-702.

Iamchaturapatr, J., Piriyakul, K., & Petcherdchoo, A. (2022a). Characteristics of sandy soil treated using EICP-based urease enzymatic acceleration method and natural hemp fibers. Case Studies in Construction Materials, 16, e00871.

Iamchaturapatr, J., Piriyakul, K., & Petcherdchoo, A. (2022b). Use of a piezoelectric bender element for the determination of initial and final setting times of metakaolin geopolymer pastes, with applications to laterite soils. Sensors, 22(3), 1267.

Iamchaturapatr, J., Piriyakul, K., Ketklin, T., Di Emidio, G., & Petcherdchoo, A. (2021). Sandy Soil Improvement Using MICP-Based Urease Enzymatic Acceleration Method Monitored by Real-Time System. Advances in Materials Science and Engineering, 2021(1), 6905802.

Ishibashi, I., & Zhang, X. (1993). Unified dynamic shear moduli and damping ratios of sand and clay. Soils and Foundations, 33(1), 182–191.

Ishihara, K. (1996). Soil behaviour in earthquake geotechnics. Oxford University Press.

Ivanov, V., & Chu, J. (2008). Applications of microorganisms to geotechnical engineering for bioremediation and bioimprovement of soil. Reviews in Environmental Science and Bio/Technology, 7(2), 139–153.

Jamiolkowski, M., Leroueil, S., & Lo Presti, D. C. F. (1991). Design parameters from theory to practice. In Proceedings of the International Conference on Geotechnical Engineering for Coastal Development (pp. 877–917).

Jamsawang, P., Charoensil, S., Namjan, T., Jongpradist, P., & Likitlersuang, S. (2021). Mechanical and microstructural properties of dredged sediments treated with cement and fly ash for use as road materials. Road Materials and Pavement Design, 22(11), 2498-2522.

Jamsawang, P., Poorahong, H., Yoobanpot, N., Songpiriyakij, S., & Jongpradist, P. (2017). Improvement of soft clay with cement and bagasse ash waste. Construction and building materials, 154, 61-71.

Jiang, N. J., Tang, C. S., Hata, T., Courcelles, B., Dawoud, O., & Singh, D. N. (2020). Bio-mediated soil improvement: the way forward. Soil Use and Management, 36(2), 185-188.

Ju, T., Achenbach, J. D., Jacobs, L. J., Guimaraes, M., & Qu, J. (2016). Ultrasonic nondestructive evaluation of alkali-Silica reaction damage in concrete prism samples. Materials and Structures, 50, 1–13.

Kang, G., Tsuchida, T., & Athapaththu, A. M. R. G. (2015). Strength mobilization of cement-treated dredged clay during the early stages of curing. Soils and Foundations, 55(2), 375-392.

Kang, S., Yu, J.-D., Hong, W.-T., & Lee, J.-S. (2021). Estimation of Cavities beneath Plate Structures Using a Microphone: Laboratory Model Tests. Sensors, 21(9), 2941. https://doi.org/10.3390/s21092941

Karl, L. (2005). Dynamic soil properties out of SCPT and bender element tests with emphasis on material damping \[Doctoral dissertation\].

Karray, M. (1999). Utilisation de l\'analyse modale des ondes de Rayleigh comme outil d\'investigation géotechnique in-situ \[Doctoral dissertation, Université de Sherbrooke\].

Karray, M., & Lefebvre, G. (2000). Identification and isolation of multiple modes in Rayleigh waves testing methods. In Use of geophysical methods in construction: Proceedings of the sessions of Geo-Denver 2000 (pp. 80–94). ASCE.

Karray, M., Lefebvre, G., Ethier, Y., & Bigras, A. (2010). Assessment of deep compaction of the Péribonka dam using "Modal-Analysis-of-Surface Wave" (MASW). Canadian Geotechnical Journal, 47(3), 312–327.

Kim, A. R., Chang, I., Cho, G. C., & Shim, S. H. (2018). Strength and dynamic properties of cement-mixed Korean marine clays. KSCE Journal of Civil Engineering, 22(4), 1150-1161.

Kim, J., Lee, J. S., Arnold, C., & Kim, S. Y. (2021a). Evaluation of thawing and stress restoration method for artificial frozen sandy soils using sensors. Sensors, 21(5), 1916.

Kim, D.-J., Yu, J.-D., & Byun, Y.-H. (2021b). Piezoelectric Ring Bender for Characterization of Shear Waves in Compacted Sandy Soils. Sensors, 21(4), 1226. https://doi.org/10.3390/s21041226

Kim, S. Y., Lee, J. S., & Park, J. (2021c). Response of transitional mixtures retaining memory of in-situ overburden pressure monitored using electromagnetic and piezo crystal sensors. Sensors, 21(7), 2570.

Kramer, S. L. (1996). Geotechnical earthquake engineering. Prentice Hall.

L'Heureux, J. S., & Long, M. (2017). Relationship between shear-wave velocity and geotechnical parameters for Norwegian clays. Journal of geotechnical and Geoenvironmental engineering, 143(6), 04017013.

Le, M., & Lee, M. (2014). Bio-mediated soil: a sustainable ground improvement technique. J. Geotek, 9, 30-39.

Lee, J. S., & Santamarina, J. C. (2005). Bender elements: performance and signal interpretation. Journal of geotechnical and geoenvironmental engineering, 131(9),1063-1070.

Lee, J. S., Park, G., Byun, Y. H., & Lee, C. (2020). Modified fixed wall oedometer when considering stress dependence of elastic wave velocities. Sensors, 20(21), 6291.

Leelarungroj, K., Likitlersuang, S., Chompoorat, T., & Janjaroen, D. (2018). Leaching mechanisms of heavy metals from fly ash stabilised soils. Waste Management & Research, 36(7), 616-623.

Lefebvre, G., & Karray, M. (1998). New developments in in-situ characterization using Rayleigh waves. In 51st Canadian Geotechnical Conference, Edmonton, Alberta, Canada (Vol. 2, pp. 821–828).

Li, B. (2015). Geotechnical properties of biocement treated sand and clay (Doctoral dissertation).

Li, M., Wen, K., Li, Y., & Amini, F. (2013). Impact of bacteria and urease concentration on MICP-treated sand. Geotechnical and Geological Engineering, 31(5), 1–11.

Li, X. G., Xu, R. Q., & Rong, X. N. (2012). Assessment of strength development in cement-admixed artificial organic soil with GX07. Journal of Central South University, 19(10), 2999-3005.

Liu, L., Liu, H., Xiao, Y., Chu, J., Xiao, P., & Wang, Y. (2018). Biocementation of calcareous sand using soluble calcium derived from calcareous sand. Bulletin of Engineering Geology and the Environment, 77(4), 1781-1791.

Liu, L., Zhou, A., Deng, Y., Cui, Y., Yu, Z., & Yu, C. (2019). Strength performance of cement/slag-based stabilized soft clays. Construction and Building Materials, 211, 909-918.

Liu, S., Zhu, J., Seraj, S., Cano, R., & Juenger, M. (2014). Monitoring setting and hardening process of mortar and concrete using ultrasonic shear waves. Construction and Building Materials, 72, 248-255.

Liu, Z., Zhang, Y., Jiang, Q., Sun, G., & Zhang, W. (2011). In situ continuously monitoring the early age microstructure evolution of cementitious materials using ultrasonic measurement. Construction and Building Materials, 25, 3998-4005.

Lopes, A. V., Lopes, S. M., & Pinto, I. (2020). Experimental study on the flexural behavior of alkali activated fly ash mortar beams. Applied Sciences, 10(12), 4379.

Ma, G., He, X., Jiang, X., Liu, H., Chu, J., & Xiao, Y. (2021). Strength and permeability of bentonite-assisted biocemented coarse sand. Canadian Geotechnical Journal, 58(7), 969-981.

Ma, Q., Yang, Y., Xiao, H., & Xing, W. (2018). Studying Shear Performance of Flax Fiber-Reinforced Clay by Triaxial Test. Advances in Civil Engineering, 2018(1), 1290572.

Madhyannapu, R. S., Puppala, A. J., Nazarian, S., & Yuan, D. (2010). Quality assessment and quality control of deep soil mixing construction for stabilizing expansive subsoils. Journal of geotechnical and geoenvironmental engineering, 136(1), 119-128.

Michaelis, L., & Menten, M. L. (1913). Die Kinetik der Invertinwirkung Biochemische Zeitschrift\> 49.

Mirzababaei, M., Arulrajah, A., Haque, A., Nimbalkar, S., & Mohajerani, A. (2018). Effect of fiber reinforcement on shear strength and void ratio of soft clay. Geosynthetics International, 25(4), 471-480.

Mirzababaei, M., Arulrajah, A., Horpibulsuk, S., & Aldava, M. (2017). Shear strength of a fibre-reinforced clay at large shear displacement when subjected to different stress histories. Geotextiles and Geomembranes, 45(5), 422-429.

Miura, N., Horpibulsuk, S., & Nagaraj, T. S. (2001). Engineering behavior of cement stabilized clay at high water content. Soils and foundations, 41(5), 33-45.

Mohamed, N., Hafez, N., Medhat, E. M., & Sharaky, A. (2021). Stabilization characteristics of different loose sandy soils using microbial-induced calcite precipitation. Walailak Journal of Science and Technology (WJST), 18(9), 9129-17.

Mok, Y. J., Sanchez-Salinero, I., Stokoe, K. H., Roesset, J. M. (1988, June). In situ damping measurements by crosshole seismic method. In Earthquake Engineering and Soil Dynamics II-Recent Advances in Ground-Motion Evaluation (pp. 305-320). ASCE.

Nakagawa, K., Soga, K., & Mitchell, J. K. (1996). Pulse transmission system for measuring wave propagation in soils. Journal of Geotechnical Engineering, 122(4), 302–308. https://doi.org/10.1061/(ASCE)0733-9410(1996)122:4(302)

Nakayenga, J., Cikmit, A. A., Tsuchida, T., & Hata, T. (2021). Influence of stone powder content and particle size on the strength of cement-treated clay. Construction and Building Materials, 305, 124710.

Nas, M., & Kurbetci, S. (2018). Durability properties of concrete containing metakaolin. Advances in concrete construction, 6(2), 159.

Natali Murri, A., Medri, V., Papa, E., Laghi, L., Mingazzini, C., & Landi, E. (2017). Porous geopolymer insulating core from a metakaolin/biomass ash composite. Environments, 4(4), 86.

Naveena, P. C., Mamatha, K. H., & Dinesh, S. V. (2013). Prediction of strength development in stabilized sandy clay at high water contents. Int J Geol, 7(1), 9-23.

Nazarian, S., & Stokoe, K. H. II. (1985). In-situ determination of elastic moduli of pavement systems by Spectral-Analysis-of-Surface-Waves method (Practical aspects) (Research Report No. 368-1F). Center for Transportation Research, The University of Texas at Austin.

Nazarian, S., Stokoe, K. H. II, & Hudson, W. R. (1983). Use of spectral analysis of surface waves method for determination of moduli and thicknesses of pavement systems. Transportation Research Record, 930, 38–45.

Nontananandh, S., Boonyong, S., Yoobanpot, T., & Chantawarangul, K. (2004). Strength development of soft marine clay stabilized with cement and fly ash. Agriculture and Natural Resources, 38(4), 539-552.

Özkılıç, Y. O., Beskopylny, A. N., Stel'makh, S. A., Shcherban, E. M., Mailyan, L. R., Meskhi, B., \... & Madenci, E. (2023). Lightweight expanded-clay fiber concrete with improved characteristics reinforced with short natural fibers. Case studies in construction materials, 19, e02367.

Palumbo, G., Iadicicco, A., Messina, F., Ferone, C., Campopiano, S., Cioffi, R., & Colangelo, F. (2017). Characterization of early age curing and shrinkage of metakaolin-based inorganic binders with different rheological behavior by fiber Bragg grating sensors. Materials, 11(1), 10.

Pan, X., Chu, J., Yang, Y., & Cheng, L. (2020). A new biogrouting method for fine to coarse sand. Acta Geotechnica, 15(1), 1-16.

Park, C. B., Miller, R. D., & Xia, J. (1999). Multichannel analysis of surface waves. Geophysics, 64(3), 800–808.

Park, J., Lee, J. S., Won, J., & Kim, J. (2021). Evolution of small strain soil stiffness during freeze-thaw cycle: Transition from capillarity to cementation examined using magnetic and piezo crystal sensors. Sensors, 21(9), 2992.

Patel, A., Singh, K. K., & Singh, D. N. (2012). Application of piezoceramic elements for determining elastic properties of soils. Geotechnical and Geological Engineering, 30(2), 40.

Patel, S. K. (2022). Experimental Investigation of Glass Fiber Reinforced Clayey Soil for Its Possible Application as Pavement Subgrade Material. In New Approaches in Foundation Engineering. IntechOpen.

Patel, S. K., & Singh, B. (2022). Comparison of shear strength characteristics of sandy and clayey soils reinforced with glass fibres. In M. R. A. S. Rahman & S. J. Jaksa (Eds.), Proceedings of the 20th International Conference on Soil Mechanics and Geotechnical Engineering. Australian Geomechanics Society.

Patro, A., & Sahoo, R. R. (2021, September). Strength and microstructure evolution of soft soils by using nano-silica. In Ground Characterization and Foundations: Proceedings of Indian Geotechnical Conference 2020 Volume 1 (pp. 315-325). Singapore: Springer Singapore.

Pereira, P. M., Ferreira, B. F., Oliveira, N. P., Nassar, E. J., Ciuffi, K. J., Vicente, M. A., \... & De Faria, E. H. (2018). Synthesis of zeolite A from metakaolin and its application in the adsorption of cationic dyes. Applied Sciences, 8(4), 608.

Petcherdchoo, A. (2015, May). Service life and environmental impact due to repairs by metakaolin concrete after chloride attack. In Calcined Clays for Sustainable Concrete: Proceedings of the 1st International Conference on Calcined Clays for Sustainable Concrete (pp. 35-41). Dordrecht: Springer Netherlands.

Petcherdchoo, A. (2018). Probability-Based Sensitivity of Service Life of Chloride-Attacked Concrete Structures with Multiple Cover Concrete Repairs. Advances in Civil Engineering, 2018(1), 4525646.

Petcherdchoo, A. (2018). Sensitivity of Service Life Extension and CO_2 Emission due to Repairs by Silane Treatment Applied on Concrete Structures under Time-Dependent Chloride Attack. Advances in materials science and engineering, 2018(1), 2793481.

Petcherdchoo, A., Hongubon, T., Thanasisathit, N., Punthutaecha, K., & Jang, S. H. (2020). Effect of curing time on bond strength between reinforcement and fly-ash geopolymer concrete. Applied Science and Engineering Progress, 13(2), 127-135.

Petcherdchoo, A., Pochalard, S., & Piriyakul, K. (2023). Use of bender element tests for determining shear modulus of fly-ash and cement admixed Bangkok clay with considering unconfined compressive strength. Case Studies in Construction Materials, 18, e02040.

Petcherdchoo, A., Wungsumpow, C., Pochalard, S., & Piriyakul, K. (2026). MICP treatment techniques for sandy soil stabilization through shear wave velocity monitoring. *Discover Sustainability*.

Phojan, W., Luepongpattana, S., Wonglakorn, N., Thumrongvut, J., Tabyang, W., Keawsawasvong, S., & Suksiripattanapong, C. (2023). Mechanical and environmental characteristics of high calcium fly ash geopolymer stabilized soft Bangkok clay contaminated with zinc sludge. Case Studies in Chemical and Environmental Engineering, 8, 100480.

Phutthananon, C., Tippracha, N., Jongpradist, P., Tunsakul, J., Tangchirapat, W., & Jamsawang, P. (2023). Investigation of strength and microstructural characteristics of blended cement-admixed clay with bottom ash. Sustainability, 15(4), 3795.

Pickering, D. J. (1970). Anisotropic elastic parameters for soil. Geotechnique, 20(3), 271–276. https://doi.org/10.1680/geot.1970.20.3.271

Piriyakul, K. (2006). Anisotropic stress-strain behaviour of Belgian Boom clay in the small strain region (Doctoral dissertation, Ghent University). https://biblio.ugent.be/publication/470294

Piriyakul, K. (2009). Small strain stiffness of kaolinite clay. The Journal of KMUTNB, 19(3), 291–296.

Piriyakul, K. (2010). A development of a bender element apparatus. The Journal of King Mongkut's University of Technology North Bangkok, 20(2), 363–369.

Piriyakul, K. (2013). Application of the non-destructive testing method to determine the Gmax of Bangkok clay. Applied Mechanics and Materials, 418, 157-160.

Piriyakul, K. (2013). Strength development of soft Bangkok clay mixed with cement. Advanced Materials Research, 813, 391-394.

Piriyakul, K., & Haegeman, W. (2005). Automated K_0 consolidation in stress path triaxial cell for bender element testing. Geotechnical Testing Journal, 28(1).

Piriyakul, K., & Iamchaturapatr, J. (2013). Biocementation through microbial calcium carbonate precipitation. The Journal of Industrial Technology, 9(3), 195-218.

Piriyakul, K., & Iamchaturapatr, J. (2014). Horizontally mounted bender elements for measuring shear modulus in soaked sand specimen. Advanced Materials Research, 931-932, 496–500.

Piriyakul, K., & Iamchaturapatr, J. (2017). Deep soil mixing method for the bio-cement by means of bender element test. In Advances in Laboratory Testing and Modelling of Soils and Shales (pp. 375-381). Cham: Springer International Publishing.

Piriyakul, K., & Iamchaturapatr, J. (2017). Effect of mixing patterns for bio-cement. Key Engineering Materials, 728, 396-401.

Piriyakul, K., & Pochalard, S. (2013). Using shear wave velocity to determine the cementation effect of soft Bangkok clay mixed with cement and fly ash. In Multiphysical Testing of Soils and Shales (pp. 311-316). Berlin, Heidelberg: Springer Berlin Heidelberg.

Piriyakul, K., Petcherdchoo, A., Punthutaecha, K., & Phoo-ngernkham, T. (2026). Unconfined compressive strength and small-strain shear modulus of soft marine clay improved by ordinary Portland cement and polyester fibers with modeling by Michaelis-Menten kinetics. Journal of Road Engineering.

Pochalard, S., Promsang, K., Wungsumpow, C., & Piriyakul, K. (2025a). Enhancement of initial shear modulus in cement and fly ash admixed Bangkok clay out of bender element test. Discover Sustainability, 6(1), 781.

Pochalard, S., Promsang, K., Wungsumpow, C., & Piriyakul, K. (2025b). Innovation of compacted cement sand mixed with industrial waste from the refuse-derived fuel (RDF) power plant and glass fiber for green road construction. Discover Sustainability, 6(1), 632.

Pochalard, S., Wungsumpow, C., & Piriyakul, K. (2025c). Enhancement of compressive strength in cement admixed bangkok clay with glass fiber and bottom ash for eco-friendly functional road materials. Mechanics of advanced composite structures, 12(Special Issue 2: Mechanics of Advanced Fiber-Reinforced Composite Structures), 279-292.

Por, S., Nishimura, S., & Likitlersuang, S. (2017). Deformation characteristics and stress responses of cement-treated expansive clay under confined one-dimensional swelling. Applied Clay Science, 146, 316-324.

Poulos, H. G. (2022). Use of shear wave velocity for foundation design. Geotechnical and Geological Engineering, 40(4), 1921-1938.

Reinhardt, H. W., & Grosse, C. U. (2004). Continuous monitoring of setting and hardening of mortar and concrete. Construction and building materials, 18(3), 145-154.

Ricciotti, L., Molino, A. J., Roviello, V., Chianese, E., Cennamo, P., & Roviello, G. (2017). Geopolymer composites for potential applications in cultural heritage. Environments, 4(4), 91.

Richart, F. E., Hall, J. R., & Woods, R. D. (1970). Vibrations of soils and foundations. Prentice-Hall.

Saadeldin, R., & Siddiqua, S. (2013). Geotechnical characterization of a clay–cement mix. Bulletin of Engineering Geology and the Environment, 72(3), 601-608.

Santamarina, J. C., Klein, K. A., & Fam, M. A. (2001). Soils and waves: Particulate materials behavior, characterization and process monitoring. John Wiley & Sons.

Schaeffer, K., Bearce, R., & Wang, J. (2013). Dynamic modulus and damping ratio measurements from free-free resonance and fixed-free resonant column procedures. Journal of Geotechnical and Geoenvironmental Engineering, 139(12), 2145–2155.

Shirley, D. J., & Hampton, L. D. (1978). Shear-wave measurements in laboratory sediments. The Journal of the Acoustical Society of America, 63(2), 607-613.

Sidik, A. S., Canakci, H., Kilic, I. H., & Celik, F. (2014). Bio-mediated soil improvement of local soils. International Journal of Civil, Environmental, Structural, Construction and Architectural Engineering, 8(1), 1–5.

Solorza, S., Álvarez-Borrego, J., & Chaparro-Magallanez, G. (2012). Pattern recognition of digital images by one-dimensional signatures. In Fourier Transform-Signal Processing. IntechOpen.

Stabnikov, V., Jian, C., Ivanov, V., & Li, Y. (2013). Halotolerant, alkaliphilic urease-producing bacteria from different climate zones and their application for biocementation of sand. World Journal of Microbiology and Biotechnology, 29(8), 1453-1460.

Stabnikov, V., Naeimi, M., Ivanov, V., & Chu, J. (2013). Formation of water-impermeable crust on sand surface using biocement. Cement and Concrete Research, 52, 1–10.

Storrer, O., Van den Boeck, M., & Van Impe, W. F. (1986). A numerical model analysing free torsion pendulum results. In International Symposium on Numerical Models in Geomechanics (Vol. 2, pp. 265–273).

Studer, J. A., Koller, M. G., & Laue, J. (2008). Bodendynamik. Springer Berlin Heidelberg.

Sukmak, P., Horpibulsuk, S., & Shen, S. L. (2013). Strength development in clay–fly ash geopolymer. Construction and building Materials, 40, 566-574.

Sukmak, P., Sukmak, G., Horpibulsuk, S., Kassawat, S., Suddeepong, A., & Arulrajah, A. (2021). Improved mechanical properties of cement-stabilized soft clay using garnet residues and tire-derived aggregates for subgrade applications. Sustainability, 13(21), 11692.

Suksiripattanapong, C., Sakdinakorn, R., Tiyasangthong, S., Wonglakorn, N., Phetchuay, C., & Tabyang, W. (2022). Properties of soft Bangkok clay stabilized with cement and fly ash geopolymer for deep mixing application. Case Studies in Construction Materials, 16, e01081.

Sullivan, M.S.; Chorzepa, M.G.; Hamid, H.; Durham, S.A.; Kim, S.S. Sustainable materials for transportation infrastructures: comparison of three commercially-available metakaolin products in binary cementitious systems. J. Infrastructures. 2018, 3, 1-20.

Szymkiewicz, F., Barrett, A. G., Marino, J. P., Le Kouby, A., & Reiffsteck, P. (2015, June). Assessment of strength and other mechanical properties of the deep mixing material. In DFI Deep Mixing Conference 2015 (pp. 10-p).

Takeda, H., Hashimoto, S., Yokoyama, H., Honda, S., & Iwamoto, Y. (2013). Characterization of zeolite in zeolite-geopolymer hybrid bulk materials derived from kaolinitic clays. Materials, 6(5), 1767-1778.

Tang, Y., Xu, G., Yan, Y., Fu, D., Qu, C., Li, Z., & Chaima, E. (2018). Thermal cracking analysis of microbial cemented sand under various strains based on the DEM. Advances in Materials Science and Engineering, 2018(1), 7528746.

Tataranni, P., Besemer, G. M., Bortolotti, V., & Sangiorgi, C. (2018). Preliminary research on the physical and mechanical properties of alternative lightweight aggregates produced by alkali-activation of waste powders. Materials, 11(7), 1255.

Teachavorasinskun, S., & Lukkunaprasit, P. (2004). A simple correlation for shear wave velocity of soft Bangkok clays. Géotechnique, 54(5), 323–326.

Thai Polyester Co., Ltd. (2024, May 5). Polyester staple fiber (PSF). http://www.thaipolyester.com

Thailand Board of Investment. (2017). Report for Thailand: Textile industry. https://www.boi.go.th/upload/content/Textile_5a3b8121275a0.pdf

Thailand Department of Highways. (1989). Standard for highway construction (Subgrade) (DH-S201/2532). Bangkok: Department of Highways.

Tokimatsu, K., Tamura, S., & Kojima, H. (1992). Effects of multiple modes on Rayleigh wave dispersion characteristic. Journal of Geotechnical Engineering, ASCE, 118(10), 1529–1543.

Tsuchida, T., & Tang, Y. X. (2015). Estimation of compressive strength of cement-treated marine clays with different initial water contents. Soils and Foundations, 55(2), 359-374.

Tuladhar, R., Yamazaki, F., Warnitchai, P., & Saita, J. (2004). Seismic microzonation of Greater Bangkok area using microtremor observations. Earthquake Engineering and Structural Dynamics, 33(2), 211–225

Umar, M., Kassim, K. A., & Chiet, K. T. P. (2016). Biological process of soil improvement in civil engineering: A review. Journal of Rock Mechanics and Geotechnical Engineering, 8(5), 767-774.

Vali, K.S.; Murugan, S.B. Effect of different binders on cold-bonded artificial lightweight aggregate properties. J. Adv. Concr. Constr. 2020, 9, 183-193.

Van Impe, W. F. (1977). De vrije wringingsproef; een belangrijke bijdrage tot de studie van het gedrag van funderingen unter invloed van grondtrillingen.

van Paassen, L. A., Ghose, R., van der Linden, T. J., van der Star, W. R., & van Loosdrecht, M. C. (2010). Quantifying biomediated ground improvement by ureolysis: large-scale biogrout experiment. Journal of geotechnical and geoenvironmental engineering, 136(12), 1721-1728.

Vegere, K., Vitola, L., Argalis, P. P., Bajare, D., & Krauklis, A. E. (2019). Alkali-activated metakaolin as a zeolite-like binder for the production of adsorbents. Inorganics, 7(12), 141.

Vichan, S., & Rachan, R. (2013). Chemical stabilization of soft Bangkok clay using the blend of calcium carbide residue and biomass ash. Soils and Foundations, 53(2), 272-281.

Vichan, S., Rachan, R., & Horpibulsuk, S. (2013). Strength and microstructure development in Bangkok clay stabilized with calcium carbide residue and biomass ash. Science Asia, 39(2), 186-193.

Viggiani, G., & Atkinson, J. H. (1995). Interpretation of bender element tests. Géotechnique, 45(1), 149–154.

VJ Tech. (n.d.). An introduction to direct simple shear testing. Retrieved October 2, 2025, from https://www.vjtech.co.uk/an-introduction-to-direct-simple-shear-testing/

Wang, X. Y., & Lee, H. S. (2019). Microstructure modeling of carbonation of metakaolin blended concrete. Advances in concrete construction, 7(3), 167-174.

Wang, Y., Soga, K., DeJong, J. T., & Kabla, A. J. (2014). Effects of microbial-induced carbonate precipitation on the mechanical properties of sand. Géotechnique, 64(12), 1–11.

Wang, Z., Zhang, N., Ding, J., Lu, C., & Jin, Y. (2018). Experimental Study on Wind Erosion Resistance and Strength of Sands Treated with Microbial-Induced Calcium Carbonate Precipitation. Advances in materials science and engineering, 2018(1), 3463298.

Wang, Z., Zhang, N., Lin, F., Ding, J., & Yang, H. (2019). Thermal Conductivity of Dry Sands Treated with Microbial-Induced Calcium Carbonate Precipitation. Advances in Materials Science and Engineering, 2019(1), 4562958.

Warnitchai, P., Sangarayakul, C., & Ashford, S. A. (2000). Seismic hazard in Bangkok due to long-distance earthquakes. In Proceedings of the 12th World Conference on Earthquake Engineering (pp. 1–8). Auckland, New Zealand.

Wongchittaphok, C., & Jamieson, I. A. (2018). Proposed waste management guidelines for the fast fashion industry in Thailand (Doctoral dissertation, Thammasat University).

Wungsumpow, C., Pochalard, S., & Piriyakul, K. (2025). Utilizing fly ash from municipal solid waste and polypropylene fiber to improve the flexural properties of compacted cement sand. Discover Sustainability, 6(1), 726.

Xiao, Y., Chen, H., Stuedlein, A. W., Evans, T. M., Chu, J., Cheng, L., \... & Aboel-Naga, H. M. (2020). Restraint of particle breakage by biotreatment method. Journal of Geotechnical and Geoenvironmental Engineering, 146(11), 04020123.

Yan, Z., Gowthaman, S., Nakashima, K., & Kawasaki, S. (2022). Polymer-assisted enzyme induced carbonate precipitation for non-ammonia emission soil stabilization. Scientific reports, 12(1), 8821.

Yang, D., Xu, G., & Duan, Y. (2020). Effect of particle size on mechanical property of bio-treated sand foundation. Applied Sciences, 10(22), 8294.

Yang, Y., Chu, J., Xiao, Y., & Liu, H. (2022). Influence of particle size on the engineering properties of MICP-treated sand. Geomechanics and Engineering, 28(2), 1–12.

Yao, K., Li, N., Chen, D. H., & Wang, W. (2019). Generalized hyperbolic formula capturing curing period effect on strength and stiffness of cemented clay. Construction and Building Materials, 199, 63-71.

Ylmén, R., Jäglid, U., Steenari, B. M., & Panas, I. (2009). Early hydration and setting of Portland cement monitored by IR, SEM and Vicat techniques. Cement and Concrete Research, 38, 1336–1342.

Yoobanpot, N., Jamsawang, P., Poorahong, H., Jongpradist, P., & Likitlersuang, S. (2020a). Multiscale laboratory investigation of the mechanical and microstructural properties of dredged sediments stabilized with cement and fly ash. Engineering Geology, 267, 105491.

Yoobanpot, N., Jamsawang, P., Simarat, P., Jongpradist, P., & Likitlersuang, S. (2020b). Sustainable reuse of dredged sediments as pavement materials by cement and fly ash stabilization. Journal of Soils and Sediments, 20(10), 3807-3823.

Yu, X., & Gao, Y. (2018). Biocomposite cement-based mortar. Sustainable Construction and Building Materials.

Zeevaert-Wiechers, L. (2000). Importancia del módulo dinámico de rigidez del suelo en el análisis de los problemas de estabilidad por la acción de las ondas sísmicas. Ingeniería Investigación y Tecnología, 1(4), 173–179.

Zeng, C., Veenis, Y., Hall, C. A., Young, E. S., van Der Star, W. R., Zheng, J. J., & Van Paassen, L. A. (2021). Experimental and numerical analysis of a field trial application of microbially induced calcite precipitation for ground stabilization. Journal of Geotechnical and Geoenvironmental Engineering, 147(7), 05021003.

Zhang, L., Li, Y., Wei, X., Liang, X., Zhang, J., & Li, X. (2024). Unconfined compressive strength of cement-stabilized Qiantang River silty clay. Materials, 17(5), 1082.

Zhu, J., Cao, J. N., Bate, B., & Khayat, K. H. (2018). Determination of mortar setting times using shear wave velocity evolution curves measured by the bender element technique. Cement and Concrete Research, 106, 1-11.

Index

A

Abram's Law 8-20, 8-23, 8-24
Alkali-activated mortars 5-1
Anisotropic Media 2-9
ASTM D1633–17 7-4, 8-6
ASTM D8295–19 3-4, 4-15, 4-36, 6-8, 7-4, 8-6, 8-7
Attenuation of Shear Waves 2-11, 2-12

B

Bangkok Clay 1-10, 4-10, 4-16, 4-18, 4-19, 4-20, 4-22, 4-25, 7-1, 7-3, 7-4, 7-6, 7-9, 7-10, 7-12, 8-1, 8-2, 8-3, 8-4, 8-5, 8-6, 8-7, 8-9, 8-12, 8-15, 8-17, 8-20, 8-23
Bender Element Test (BET) 1-8, 1-12, 6-8, 7-4, 8-7
Binders 1-10, 5-1, 5-2, 8-1
Biocementation process 6-3, 6-4, 6-5, 6-9, 6-25, 6-26
Bioclogging 6-1, 6-2, 6-12,
Biostimulation 6-3
Body waves 1-1

C

Calcium Carbonate Precipitation 6-1, 6-4
Calcium Oxide 7-10, 8-5
Calcium Hydroxide 7-10, 7-15
Calibration of bender elements 4-5
California Bearing Ratio (CBR) 5-14
CCR (Calcium Carbide Residue) 7-2
CSH (Calcium Silicate Hydrate) 7-15
Cementation effect 4-22
Chemical compositions 6-25, 7-3, 8-3, 8-4
Cone Penetration Testing 1-7, 3-22, 3-35
Cross-anisotropy model 2-9
Cross-hole testing 3-17
Cyclic simple shear test 3-7
Cyclic triaxial test 3-1, 3-2, 3-5, 3-6, 3-36

D

Damping 1-8, 1-10, 2-11, 2-12, 2-17, 3-1
Damping ratio 2-11, 3-1, 3-6, 3-8, 3-9, 3-11, 3-12, 3-17, 3-28
Data analysis and interpretation 1-10, 4-26, 4-36
Deep Mixing Columns (DMC) 8-1
Down-hole testing 3-17, 3-22

Dynamic parameters 2-11, 3-1

E

Elastic waves 1-1, 2-3
Energy Dispersive X-ray 8-5
Energy loss 2-17

F

Finite Element Method 7-14
Fiber 1-10, 5-1, 5-2, 8-1, 8-2, 8-3, 8-6, 8-7, 8-8, 8-9, 8-10, 8-11, 8-12, 8-15, 8-16, 8-17, 8-18, 8-21, 8-23, 8-24
Fiber reinforcement 8-2
Free Torsion Pendulum Test 3-10, 3-11, 3-35
Fly Ash 1-8, 5-1, 7-1, 7-2, 7-3, 7-4, 7-6, 7-8, 7-9, 7-10, 7-12, 7-13, 7-15, 7-17, 7-18, 8-1, 8-2

G

Geomaterials 1-1, 1-4, 1-8, 1-9, 1-10, 1-11, 1-12, 2-1, 2-2, 2-10, 2-11, 3-1, 3-10, 3-23, 4-1, 5-2
Geopolymeric Materials 1-10, 5-1, 5-3
Ground improvement 4-35, 5-1, 6-1, 6-2, 6-8, 8-1, 8-2

H

Hall effect 3-16
Heterogeneous media 1-10, 2-9, 2-17

I

Injection technique 6-10, 6-21, 6-25, 6-26
Initial Shear Modulus 1-4, 3-4, 3-9, 4-1, 4-2, 4-10, 4-14, 4-15, 4-18, 4-26, 4-27, 4-28, 4-29, 4-30, 4-31, 4-32, 4-33, 4-34, 4-35, 4-36, 5-2, 6-8, 6-21, 7-2, 7-4, 7-6, 7-7, 7-8, 7-13, 7-17, 8-7, 8-23
Initial Setting Time 5-2, 5-5, 5-6, 5-7, 5-8, 5-10, 5-11, 5-12
Isotropic media 2-3

K

K_0 consolidation 3-13, 3-14
Kaolin 5-1, 5-2, 5-3, 5-5, 5-7

L

Lamé coefficients 2-6
Liquidity Index 7-1, 7-3, 8-3
Liquid Limit 4-10, 4-22, 5-6, 7-1, 7-3, 7-4, 7-17, 8-3, 8-5, 8-6, 8-23
Liquefaction potential 1-4, 1-7, 1-9
Love waves 1-1

M

Multichannel analysis of surface waves 3-1
Metakaolin Geopolymer 5-2, 5-3, 5-5, 5-6, 5-7, 5-8, 5-12, 5-14, 5-15, 5-16
Michaelis constant 8-8
Michaelis–Menten Kinetics 8-9, 8-24
Microbially Induced Calcite Precipitation 6-1, 6-3
Morphology 6-2, 6-22

N

Near Field Effect on Shear Wave 4-4
Non-Destructive Testing 4-21, 5-2

O

Optimum Moisture Content 5-14, 7-2, 8-2
Ordinary Portland Cement 1-10, 7-2, 7-3, 7-4, 7-10, 7-12, 7-13, 8-1, 8-3, 8-4, 8-5, 8-6

P

Primary Wave 1-1
Particle size distribution 6-5, 6-6, 7-10
Polyethylene Terephthalate 8-1
Piezoelectric sensors 3-3, 5-2, 5-15
Plastic Limit 5-5, 7-3, 8-3, 8-5
Poisson's ratio 2-6, 2-8, 2-9, 2-11, 2-17, 3-28
Polyester Fiber 8-2, 8-3, 8-6, 8-7, 8-9, 8-10, 8-11, 8-12, 8-15, 8-17, 8-21, 8-23
Pozzolanic reactions 7-1, 7-2, 7-4, 7-10, 7-15

R

Rayleigh wave 1-1, 1-3, 3-21, 4-26
Reflection 2-1, 2-3, 3-1, 3-2, 3-18, 3-19, 3-20, 3-35
Refraction 2-1, 2-3, 3-1, 3-2, 3-18, 3-19, 3-35, 3-36
Resonant Column Test 1-4, 3-1, 3-2, 3-8, 3-35

S

S-wave 1-1, 1-2, 1-4, 2-1, 2-2, 2-3, 2-8, 2-17, 2-18, 3-17, 3-18, 3-20, 3-22, 5-12, 6-8
Spectral Analysis of Surface Waves 1-6, 3-21, 3-35
Seismic Cone Penetration Test 1-7, 3-22
Shallow Soil Mixing 8-1
Shear Modulus 1-4, 1-5, 1-8, 1-11, 2-2, 2-6, 2-9, 2-10, 2-11, 2-14, 2-15, 2-17, 3-1, 3-4, 3-6, 3-8, 3-9, 3-11, 3-23, 3-35, 4-1, 4-2, 4-10, 4-14, 4-15, 4-18, 4-19, 4-21, 4-22, 4-26, 4-27, 4-28, 4-29, 4-30, 4-31, 4-32, 4-33, 4-34, 4-35, 4-36, 5-2, 6-8, 6-21, 7-2, 7-4, 7-6,

7-8, 7-11, 7-13, 7-17, 8-2, 8-3, 8-7, 8-8, 8-17, 8-23, 8-24
Shear modulus of fiber 8-8, 8-24
Shear Strain 1-5, 2-11, 3-1, 3-2, 3-5, 3-8, 3-12, 3-36
Shear Wave Velocity 1-4, 1-6, 1-9, 1-10, 1-11, 1-12, 2-2, 2-8, 2-10, 2-11, 2-14, 2-15, 2-16, 2-18, 3-1, 3-2, 3-4, 3-9, 3-22, 3-23, 3-24, 3-28, 3-35, 4-1, 4-2, 4-3, 4-10, 4-14, 4-15, 4-16, 4-17, 4-18, 4-19, 4-20, 4-21, 4-22, 4-26, 4-27, 4-28, 4-29, 4-30, 4-31, 4-32, 4-33, 4-34, 4-35, 4-46, 5-2, 5-6, 5-7, 5-8, 5-9, 5-10, 5-11, 5-12, 5-15, 5-16, 6-2, 6-3, 6-6, 6-8, 6-12, 6-13, 6-14, 6-15, 6-16, 6-17, 6-18, 6-19, 6-20, 6-25, 7-2, 7-4, 7-6, 7-8, 7-13, 7-17, 8-2, 8-7, 8-23
Signal Processing 1-10, 3-23, 4-3, 4-26, 4-35
Site Characterization 1-10, 4-16
Stiffness 1-4, 1-5, 1-7, 1-9, 1-10, 2-10, 2-11, 3-1, 3-9, 3-23, 3-35, 4-19, 4-21, 4-22, 4-35, 6-1, 6-2, 6-3, 6-4, 6-8, 6-12, 7-1, 7-2, 7-4, 8-3, 8-7, 8-15
Stress Path Triaxial Test 3-13
Surface percolation technique 6-10
Surface waves 1-1, 1-6, 3-1, 3-21, 3-35, 4-26

T

Thermal Treatment 5-3
Transverse motion 2-1, 2-2, 2-10
Travel Time 1-8, 3-2, 3-18, 3-22, 4-2, 4-10, 4-18, 6-8

U

Unconfined Compressive Strengt 4-35, 6-1, 6-2, 7-1, 7-4, 7-6, 7-8, 7-9, 7-10, 7-11, 7-13, 7-17, 8-5, 8-6, 8-7, 8-23
Urea hydrolysis 6-3, 6-4, 6-6, 6-24

V

Vicat needle apparatus 5-4

W

Water to Cement Ratio 8-20
Wave propagation 1-1, 1-10, 1-11, 1-12, 2-1, 2-2, 2-3, 2-6, 2-10, 2-17, 2-18, 3-20, 4-26, 4-35, 5-2
Waveforms 4-4, 4-10, 4-14, 4-36

X

X-Ray Diffractometer 6-10, 6-24

Y

Young's Modulus 2-8, 2-9, 2-10, 2-11, 2-14, 2-16, 2-17, 3-9

